A THERMODYNAMIC APPROACH TO SURFACE RUNOFF

Zur Erlangung des akademischen Grades eines

DOKTORS DER INGENIEURWISSENSCHAFTEN
(Dr.-Ing.)

von der KIT Fakultät für
Bauingenieur-, Geo- und Umweltwissenschaften des

Karlsruher Instituts für Technologie (KIT)

genehmigte

DISSERTATION

von

Samuel Schroers

Tag der mündlichen Prüfung

11/05/2023

Referent: Prof. Dr.-Ing. Erwin Zehe

Korreferent: Prof.dr.ir. Hubert Savenije

A THERMODYNAMIC APPROACH TO SURFACE RUNOFF

SAMUEL SCHROERS

A new perspective on the co-evolution of geomorphology and runoff from hillslopes to rivers

Institue of Water and River Basin Management
Karlsruhe Institute of Technology

July 2023 –

To Jenny and Selva.

Who are beyond anything I could dream of.

ABSTRACT

In this thesis we follow the idea of seeing the highly complex inter-actions of water and the solid earth materials from a thermodynamic viewpoint. In such a perspective one acknowledges that detailed knowledge about each individual process might not just be very com-plex but that it can only be approximately known. This seems to be particularly true for dynamics of dissipative systems, such as hydrody-namics in hydrological systems. For these complicated situations one tries to separate and if possible, answer different kind of questions that don't require precise knowledge of the dynamics of each particle or molecule. The solutions to these problems are called universal. In the case of a hydrological system, such universality has been ex-pressed in laws or principles such as Horton's laws, Hack's law, the principle of minimum (or maximum) dissipation and others, but so far these empirically found concepts have at best a blurry physical basis. Consequently, it was our intention to provide with this work a thermodynamic framework for surface runoff in a geomorphological context. It shall encompass a universal energy-centered scheme that can be used to give empirical laws a new meaning. The individual pro-cesses, involved in surface runoff and erosion were integrated in time and space as part of an open thermodynamic system. Here we focused on the interface of hydrology and geomorphology, an area which has intrigued many and has already been the subject of thermodynamic concepts in the past. Therefore, we analyzed three typical hydrological systems, differently delineated in time and space: 1) The hillslope for steady state runoff conditions, 2) The hillslope for event-based time horizons, and 3) the river- and drainage network of an entire catchment for a hydrological year. The thesis is structured in parallel to this classification in space and time.

In chapter II we present the thermodynamic framework for the case of a dissipative system that is invariant in time. The theoretical derivation shows that the dissipation of free energy of surface runoff along a flow path on hillslopes results in a point of maximum free energy, therefore separating the hillslope conceptually in a part of net energy increase and another of net energy decrease. In the second part of the chapter, we show that the location of this maximum is related to the structural adaptations of the hillslope surface. Micro- and macro-topography in the form of rills shifts the location up- or downstream. We hypothesized that the direction is related to a thermodynamic equilibrium with maximum dissipation rates of the entire hillslope system. We therefore analyzed a set of experiments of surface runoff on hillslope plots in the Weiherbach catchment and found that if sep-

arating a sheet- and rill flow component hillslopes indeed seem to self-organize into a state of maximum power, where the influx of free energy is dissipated at the maximum rate. Subsequently, Chapter III is an extension of chapter II, in that we extended the steady state case to an analysis of transient events. We therefore included the derivatives in time of the free energy fluxes and presented simulations of transient rainfall- surface runoff events by numerically solving the full Saint-Venant equations. The theoretical scenarios showed that the relative dissipation of surface runoff events is largest for hillslope profiles that from up- to downslope exponentially decline in slope and reversely, it is smallest for hillslope profiles that exponentially increase in slope. We followed from this, that hillslope structure rearranges in time and space to increase the relative dissipation of surface runoff events, or differently stated the system evolves through intermittent events into a state where the provided free energy of rainfall is dissipated as fast as possible. We subsequently confirmed this finding for observations of surface runoff in the Weiherbach catchment and furthermore also found that erosion was largest on hillslopes where relative dissipation was smallest. We concluded that the magnitude of free energy of surface runoff that is not dissipated is directly related to the amount of sediment eroded. Hillslopes that show larger relative dissipation rates are therefore closer to a thermodynamic equilibrium when free energy is dissipated faster. These "older" hillslopes correspond to smaller efficiencies of surface runoff, which means that the runoff dynamics are damped at a higher degree due to the formation of structure within the system. In chapter IV we adapt this perspective to entire river networks. In the first part of the chapter we first showed that the free energy dynamics of a surface runoff and related erosion in a watershed can be boiled down to three efficiencies of free energy conversion: 1) The percentage of free energy that is converted from rainfall to discharge, basically an energetic runoff coefficient, 2) the efficiency that relates the gradient of potential energy in discharge to kinetic energy, expressed by the hydraulic radius, and 3) the ratio of kinetic energy of water and of transported sediment particles, expressed as the sediment concentration. We then analyzed the world largest river network the Amazon basin within this energy-centered concept and found distinct patterns of energy conversion efficiencies. In the second part of this chapter we closed this thesis by drawing parallels between models of turbulence, landscape evolution and population growth. We argued that the drainage network relates to turbulence as well as chaos theory. All three systems are deterministic up to a certain degree but highly complex and rich in information if a certain energy threshold is passed. We showed by analysis of the largest terrestrial river networks that Horton's laws of stream area and length relate to one-dimensional maps such as Feigenbaum's bifurcation diagram of

the logistic map. We find Feigenbaum values δ and α below 0.1% and 8% difference to the precise values.

ZUSAMMENFASSUNG

In dieser Arbeit verfolgen wir die Idee, die hochkomplexen Wechselwirkungen zwischen Wasser und der Erde aus einer thermodynamischen Sicht zu betrachten. In dieser Perspektive gesteht man ein, dass das Detailwissen über jeden einzelnen Prozess nicht nur sehr komplex ist, sondern auch nur annähernd bekannt sein kann. Dies scheint insbesondere für die Dynamik dissipativer Systeme zu gelten, wie z. B. die Hydrodynamik in hydrologischen Systemen. Für diese komplizierten Situationen versucht man, Fragen zu beantworten, die keine genaue Kenntnis der Dynamik jedes einzelnen Teilchens oder Moleküls erfordern. Die Lösungen für diese Probleme werden als universell bezeichnet. Im Falle eines hydrologischen Systems wurde eine solche Universalität in Gesetzen oder Prinzipien wie den Hortonschen Gesetzen, dem Hackschen Gesetz, dem Prinzip der minimalen (oder maximalen) Dissipation und anderen ausgedrückt, aber bisher haben diese empirisch gefundenen Konzepte bestenfalls eine verschwommene physikalische Grundlage. Es war daher unsere Absicht, mit dieser Arbeit einen thermodynamischen Rahmen für den Oberflächenabfluss in einem geomorphologischen Kontext zu schaffen. Er soll ein universelles, energiezentriertes Schema umfassen, mit welchem den empirischen Gesetzen eine neue Bedeutung verliehen werden kann. Die einzelnen Prozesse, die am Oberflächenabfluss und an der Erosion beteiligt sind, wurden in Zeit und Raum als Teil eines offenen thermodynamischen Systems integriert. Dabei liegt unser Fokus auf der Schnittstelle von Hydrologie und Geomorphologie, einem Gebiet, welches bereits in der Vergangenheit Gegenstand thermodynamischer Konzepte war. Hierfür analysierten wir drei charakteristische hydrologische Systeme, die zeitlich und räumlich unterschiedlich abgegrenzt sind: 1) den Hang für stationäre Abflussbedingungen, 2) den Hang für ereignisbezogene Zeithorizonte und 3) das Fluss- und Entwässerungsnetz eines gesamten Einzugsgebiets für ein hydrologisches Jahr. Die Arbeit ist dementsprechend parallel zu dieser Einteilung in Raum und Zeit aufgebaut.

In Kapitel II wird der thermodynamische Rahmen für den Fall eines zeitlich invarianten, dissipativen Systems vorgestellt. Die theoretische Herleitung zeigt, dass die Dissipation der freien Energie des Oberflächenabflusses entlang eines Fließweges auf einem Hang zu einem Punkt maximaler freier Energie führt, wodurch der Hang konzeptionell in einen Teil mit Netto-Energiezuwachs und einen anderen mit Netto-Energieabfall unterteilt wird. Im zweiten Teil des Kapitels zeigen

wir, dass die Lage dieses Maximums mit den strukturellen Anpassungen der Hangoberfläche zusammenhängt. Die Mikro- und Makrotopographie in Form von Rinnsalen verschiebt den Ort flussaufwärts oder flussabwärts. Wir stellten die Hypothese auf, dass die Richtung mit einem thermodynamischen Gleichgewicht mit maximalen Dissipationsraten des gesamten Hangsystems zusammenhängt. Im Folgenden analysierten wir daher eine Reihe von Experimenten zum Oberflächenabfluss auf Hangparzellen im Weiherbach-Einzugsgebiet und fanden heraus, dass sich Hänge bei der Trennung von "Sheet-„ und Rillenströmungskomponenten tatsächlich in einen Zustand maximaler Leistung befinden. Diese beobachtete Organisation des Oberflächenabflusses führt dazu, dass ein Zufluss freier Energie mit maximaler Geschwindigkeit abgebaut wird.

Kapitel III ist eine Erweiterung von Kapitel II, indem wir den stationären Fall auf eine Analyse instationärer Ereignisse ausdehnen. Es wurden daher die zeitlichen Ableitungen der freien Energieflüsse miteinbezogen und Simulationen von instationären Regenfällen und Oberflächenabflüssen durch numerische Lösung der vollständigen Saint Venant-Gleichungen durchgeführt. Die theoretischen Szenarien zeigten, dass die relative Dissipation von Oberflächenabflussereignissen bei Hangprofilen am größten ist, deren Neigung von oben nach unten exponentiell abnimmt, und dass sie umgekehrt bei Hangprofilen, deren Neigung exponentiell zunimmt, am kleinsten ist. Daraus folgerten wir, dass sich die Hangstruktur zeitlich und räumlich erneuert, um die relative Dissipation von Oberflächenabflussereignissen zu erhöhen. Anders ausgedrückt, das System entwickelt sich durch intermittierende Ereignisse hin zu einem Zustand, in dem die bereitgestellte freie Energie des Niederschlags so schnell wie möglich dissipiert wird. Wir haben diesen Befund anschließend für Beobachtungen des Oberflächenabflusses im Weiherbach-Einzugsgebiet bestätigt und darüber hinaus festgestellt, dass die Erosion an den Hängen am größten ist, an denen die relative Dissipation am geringsten ist. Wir kamen außerdem zu dem Schluss, dass die Größe der freien Energie des Oberflächenabflusses, die nicht abgeführt wird, direkt mit der Menge des erodierten Sediments zusammenhängt. Hänge, die größere relative Dissipationsraten aufweisen, befinden sich daher näher an einem thermodynamischen Gleichgewicht, wenn die verfügbare freie Energie schneller dissipiert wird. Diese "älteren"Hänge entsprechen einer geringeren Effizienz des Oberflächenabflusses, was bedeutet, dass die Abflussdynamik aufgrund der Strukturbildung innerhalb des Systems stärker gedämpft wird.

In Kapitel IV übertragen wir diese Perspektive auf Flussnetzwerke. Im ersten Teil des Kapitels haben wir zunächst gezeigt, dass die Dynamik der freien Energie des Oberflächenabflusses und der damit verbundenen Erosion in einem Einzugsgebiet auf drei Wirkungsgrade der Umwandlung freier Energie zurückgeführt werden kann: 1)

den Prozentsatz der freien Energie, der von Regen in Abfluss umgewandelt wird, ähnlich einem erweiterten Abflusskoeffizienten, 2) den Wirkungsgrad, der den Gradienten der potenziellen Energie im Abfluss mit der kinetischen Energie in Beziehung setzt, ausgedrückt durch den hydraulischen Radius, und 3) das Verhältnis der kinetischen Energie des Wassers und der transportierten Sedimentpartikel, ausgedrückt als Sedimentkonzentration. Anschließend analysierten wir in diesem Rahmen das größte Flussnetz der Welt im Amazonasbecken. Im zweiten Teil dieses Kapitels schlossen wir diese Arbeit ab, indem wir Parallelen zwischen Modellen für Turbulenz, Landschaftsentwicklung und biologischen Modellen für Populationswachstum zogen. Hier argumentierten wir, dass das Flussnetzwerk sowohl mit Turbulenz als auch mit der Chaostheorie von nichtlinearen dynamischen Systemen in Verbindung gebracht werden kann. Alle drei Systeme sind bis zu einem gewissen Grad deterministisch, wobei gleichzeitig hochkomplex und reich an Informationen, sobald eine bestimmte Energieschwelle überschritten wird. Wir haben durch Analyse der größten terrestrischen Flussnetzwerke gezeigt, dass die Horton'schen Gesetze der akkumulierten Gebietsfläche und -länge mit dem Feigenbaum-Bifurkationsdiagramm der logistischen Gleichung in Beziehung stehen. Wir finden die Feigenbaum-Konstanten δ und α mit weniger als 0,1% und 8% Unterschied zu den genauen, theoretischen Werten.

The great river flows from the mountains to the sea.
I am the river,
the river is me.

— *Maori proverb*

ACKNOWLEDGMENTS

CONTENTS

LIST OF TABLES

Part I

INTRODUCTION

INTRODUCTION

1.1 MOTIVATION

Hydrology is a geoscience which is principally concerned with the circulation of the earth's fresh water. Dingman (2015) categorized Hydrology into the three groups of:

1. The movement of water on and under the earth

2. The interactions of water and earth materials

3. The biological processes as well as human developments which influence the former

A more recent community approach classified the most pressing unsolved problems in Hydrology into seven groups Blöschl et al. (2019), which are:

- Time variability and change

- Space variability and scaling

- Variability of extremes

- Interfaces in hydrology (hillslope-riparian-stream-groundwater)

- Measurements and data

- Modelling methods

- Interfaces with society

Both classifications are seemingly subjective choices as there is no physical boundary between any of these classes. In fact, it is evident that they interact to form a single earth system with fluxes of water and energy (Kleidon (2016)). It is however common sense in the community to scale the system to the size of the process of interest. Specifically, the closure of the mass balance equation has been described as the holy grail of hydrology (Beven (2006)). Because the mass balance is always the starting point for scientific hydrology, it is most reasonable to evaluate the terms at a scale where mass fluxes can be estimated and measured, the so-called control volume, or as Horton (1931) put it:

Any natural exposed [three-dimensional] surface may be considered as a [control volume] on which the hydrologic cycle operates. This includes, for example, an isolated tree, even a single leaf or twig of a growing plant, the

roof of a building, the drainage basin of a river-system or any of its tributaries, an undrained glacial depression, a swamp, a glacier, a polar ice-cap, a group of sand dunes, a desert playa, a lake, an ocean, or the earth as a whole.

A conceptual control volume with in- and outflows is represented in Fig. 1.1. Across its boundaries, fluxes of mass, momentum, and energy can be stored and released so that for a system with conserved quantities, three basic conservation equations can be derived:

- Conservation of mass

- Conservation of momentum

- Conservation of energy

Figure 1.1: The earth as a conservative system with influxes of mass, momentum and energy (J_{in}), outfluxes therof (J_{out}) and storage S (after Kleidon (2016))

In the following we outline how these conservation laws have been used to describe and predict the hydrologic cycle. From this review it will become clear that there is a clear focus on the first and second law, while the conservation of energy is mostly underrepresented in hydrological sciences. This might be due to practicality as well as difficulties of many unsolved problems with the conservation of mass and momentum. Also, with hydrology having a record of being an engineering science with a high degree of solving practical problems, e.g., related to flooding or droughts, few had the aspiration to delve beyond the long-established concepts. Or as Kirchner (2006) put it, there has been a focus on *mathematical marionettes* instead of *getting the right answers for the right reasons*. We recognize however that the era of artificial intelligence has only begun, and artificial networks are often already far better predictors of runoff than existing physics-based

models (Kratzert et al. (2019); Gauch et al. (2021)). It is consequently in hydrology as well as other scientific areas a somewhat conundrum on how to go forward and develop in an age where abstract math will be (is) used to tackle practical problems. Here we argue that such models, although highly capable of predicting outcomes from limited observations fail to explain the underlying process. Feynman famously said in one of his lectures that mathematics is interested in the structure of the reasoning, and that physics provides meaning to the structure's details. He therefore argues that although powerful mathematical tools provide ready-to-use solutions, humans will always want to understand the connection between the details of a structure (e.g., a model) and the real world.

In this work we clearly focus on the latter, and we therefore have two objectives: First, we want to show that the conservation of energy is a useful concept to describe the interaction between surface runoff and the landscape, and second, we mean to provide some pathways forward, going beyond classical mass and momentum dynamics of watersheds. In doing so we show some new perspectives on established concepts at the interface of hydrology and geomorphology.

In the second chapter of this work, we start at the hillslope scale, analyzing the spatial steady state distribution of surface runoff energy. In the third chapter we then release the steady state assumption and describe the transient energy balance of surface runoff on hillslopes and which insights can be drawn for erosion in the context of landscape evolution. Finally, in the fourth chapter we explore the energy dynamics of surface runoff for large rivers, but also extend this analysis to the entire river network. In this thesis we therefore transition spatially from smaller to larger scales, while at the same time separating steady states from transient states.

1.2 THE USE OF CONSERVATION LAWS AT DIFFERENT SCALES

In the following we want to briefly outline how the three conservation equations are used in hydrology on different scales and subsequently evaluate unused potentials.

1.2.1 *Mass balance*

For the simplest system the mass balance, in the case of water also referred to as water balance can be written as

$$influx - outflux = change\ in\ storage \tag{1.1}$$

E.g., hydrologists differentiate fluxes of the water cycle for a watershed at a most basic level as $P + GW_{in} - (Q + ET + GW_{out}) = dS$ (Dingman (2015)) With the influxes being precipitation P and groundwater inflow GW_{in}, and the outfluxes as runoff Q, evapotranspiration ET as well

as groundwater outflow GW_{out}. In sum they change the storage S of the system. More elaborate and detailed process differentiations have been proposed but the closure of the water balance remains an unsolved problem in hydrology (Beven (2006)). However, different models and process conceptualizations on different scales have proven to be applicable for the developed purpose and specific scale (E.g.). Locally the water balance is used to describe the flow of water, here presented by the the continuity equation of incompressible flow (cf. Navier-Stokes equation, Frisch (1995)):

$$\nabla \vec{u} = -r \tag{1.2}$$

Where r is the rainfall rate in units of mass per unit time but could also be any type of source of water such as in- or exfiltration across the boundaries of the control volume, while $\vec{u}$ is a mass flux in three dimensions. There are many other important applications of the mass balance in hydrology, e.g., processes which are associated with sediment erosion, transport, and deposition. In this case the mass balance is typically used to describe the evolution of height of the bed-layer z in time (Exner's equation, cf. Chen, Darbon, and Morel (2014)):

$$\frac{dz}{dt} = s \nabla \vec{q_s} \tag{1.3}$$

q_s is a three-dimensional sediment flux in $kg\ s^{-1}$ and s is a constant describing the packing density of the particles. Associated is its use to estimate the development of a substance which is dissolved or transported within the water, expressed by the advection-diffusion equation (Chanson (2004)):

$$\frac{dc}{dt} = D \nabla^2 c - v \nabla c \tag{1.4}$$

In this case the equation represents a one-dimensional flow flied with a concentration c in $kg\ m^{-3}$, a velocity v in $m\ s^{-1}$ and no source or sinks. The diffusion term is linear and represents Fick's basic law of molecular diffusion with a diffusion coefficient D in $m^2\ s^{-1}$ (Fick (1855)). There are many other applications of the mass balance in hydrology, however there are four principle use cases which as outlined above are 1) the water balance at the catchment scale, 2) the water balance of runoff for a defined cross-section, 3) the sediment continuity equation, and 4) the advection- diffusion equation for mass transport.

1.2.2   *Momentum balance*

For the watershed water cycle the momentum balance is usually not directly applied at this scale. However, single processes are represented by the momentum balance, e.g., the impact of rainfall on soil

particle deposition and therefore erosion (e.g., Schmidt (1996)). Most importantly the momentum balance is applied to represent viscous flow on the surface of the landscape in the form of overland flow on hillslopes and as discharge in the drainage network. The full equation (Navier Stokes momentum balance equation, cf. Frisch (1995)) reads

$$\frac{d\vec{v}}{dt} = -(\vec{v}\nabla\vec{v} + \nabla\frac{p}{\rho}) + \nu\nabla^2\vec{v} + f \tag{1.5}$$

Where $\vec{v}$ is the vector of a flow field's velocity in $m\ s^{-1}$, ρ the fluid density in $kg\ m^{-3}$, ν the kinematic viscosity in $m^2 s^{-1}$, p is the fluid pressure in Pa and f external force in $m\ s^{-2}$. For the use in hydrology and the watershed scale this equation is at least reduced to the Saint-Venant equation (cf. Krylova, Antipova, and Perevozkin (2017) for a rigorous mathematical derivation and assumptions) under the following assumptions:

- Water is an incompressible fluid

- Pressure distribution is considered to be hydrostatic

- Vertical acceleration of water is considered negligible

- Bed slope is considered to be mild

- Effects of boundary friction can be taken into account with flow resistance laws derived for steady flows (e.g., Manning's equation)

- Boussinesq approximation is valid (ignoring forces caused by differences in density)

Depending on the intended use this equation can then be further reduced to the diffusion wave (without acceleration) or the kinematic wave (without acceleration and pressure gradient) equation, which reads for one dimension:

$$\underbrace{\frac{dv}{dt} + v\frac{dv}{dx} - \frac{v}{A_C}q_{lat} + \underbrace{g\frac{dh}{dx}\underbrace{-g(I_e - I_0) = 0}_{kinematic\ wave}}_{diffusion\ wave}}_{hydrodynamic\ wave} \tag{1.6}$$

where A_C is the wetted cross-section in m^2 for a water depth h in m, q_{lat} lateral water sources in $m^2\ s^{-1}$, g acceleration due to gravity in $m\ s^{-2}$ and I_e, I_0 energy and bed slope.

1.2.3   *Energy balance*

The conservation of energy in classical watershed hydrology comes mainly into play when estimating evaporation. The classical example is the Penman equation (Penman (1948)) which is a combination of the energy balance for vaporization of water, a sink term for vapor removal and heat flux into or from the soil. As originally assumed by Penman (1948), soil heat flux over longer periods can often be neglected so that the energy balance reads:

$$R_n = E_v + K_a \tag{1.7}$$

Where R_n is the net radiant energy available at the surface, E_v the energy which is used in evaporation (flux of latent heat), and K_a the energy which is used for heating the air (sensible heat flux). In terms of surface runoff the energy balance has been applied by Bagnold (1966) for estimating the work a river enacts on its underlying bed material. For steady state the loss of energy per unit flow path and per unit time is called stream power Ω in *watt m^{-1}*:

$$\Omega = \rho g Q I_e \tag{1.8}$$

Leopold and Langbein (1962) have extended the idea of discharge losing energy along a flow path and included the second law of thermodynamics to explain the most likely configuration of the profile of a river by hypothesizing that a river maximizes entropy production. Therefore, they imagined the river as a chain of heat engines (cf. Fig. 1.2) where each heat engine represents an open thermodynamic system. In dynamic equilibrium the system does not increase entropy within its boundaries (cf. Prigogine (1955)) but the produced entropy is exported. In the case of surface runoff this is accomplished by dissipation of energy into heat. The authors then concluded that if a river maximizes entropy production, the energy slope must decrease exponentially along the flow path to fulfill the equation:

$$\frac{dH}{dx} \frac{1}{H} = constant \tag{1.9}$$

Where H represents the energy which can be used as mechanical work in the system of length dx (also called free energy, iii). In a nutshell, the conservation of mass and momentum are primarily used in hydrology to describe the quantitative dynamics of the water cycle. Although evaporation (and transpiration) and dissipation of energy play a crucial role in this, both processes are represented by semi-empirical parameters which are difficult to estimate (cf. air and stomata resistances in Penman-Monteith equation, or roughness parameter in Manning's equation (Dingman (2015))) and are usually only well-defined for steady state conditions where a continuous force (or gradient) is applied (cf. Emmett (1970); Phelps (1975)). We therefore believe that an

energy centered perspective in hydrology holds untapped potential to understand the water cycle beyond a static state. In particular, we think that the first and second law of thermodynamics provide a useful starting point for deriving more meaningful descriptions and models for surface runoff in the context of geomorphological development.
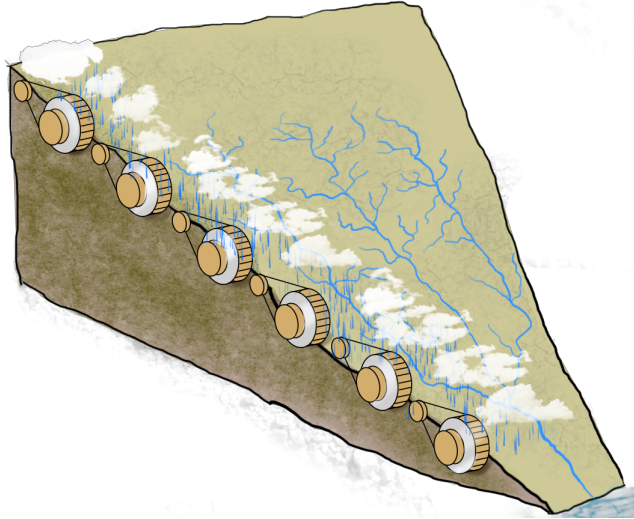
Figure 1.2: : Schematic of a river network as a chain of heat engines, represented by individual prony brakes (after Leopold and Langbein (1962))

1.3 THE INTERACTION OF SURFACE RUNOFF AND LANDSCAPE: STRUCTURE

The notion that structural formation of a watershed can be generalized is at least as old as Playfairs law from the beginning of the 19th century (cited in Horton (1945)):

Every river appears to consist of a main trunk, fed from a variety of branches, each running in a valley proportioned to its size, and all of them together forming a system of vallies, communicating with one another, and having such a nice adjustment of their declivities that none of them join the principal valley either on too high or too low a level.

E. Horton was probably one of the first to focus on this organization of a river's main trunk, branches and ever smaller subbranches. He viewed the watershed as a physical system that organizes its internal structures like hillslopes and drainage channels through the forces of the hydrological cycle, giving birth to the hydrophysical perspective (Horton (1945)). Within the watershed as a control volume, Horton could show that especially the river network that is created by surface runoff adheres to specific laws, today still known as the Horton laws of stream number and stream length (cf. iv).

Horton also found that the spatial extension and density of the drainage network relates to runoff from the basin. A higher stream density is typically observed for areas with more rainfall, whereas smaller stream densities are found for areas with less rainfall. This is striking as the mass balance of a system is therefore somehow imprinted into the structure of the system. Today, almost any physics-based model which intends to predict runoff by spatial and temporal analysis of the water balance is principally concerned with the representation of structure of the system. A very famous and often cited example is K. Beven's and M. Kirkby's Topmodel (Beven and Kirkby (1979)), which inspired a whole generation of hydrologists (Beven et al. (2021)) and is based on a topographic (structural) index which was developed by Kirkby (1975). Kirkby (1971) also elaborated on the general formation of hillslope structures by applying the conservation equation of sediment:

$$M + D_{chem} = -\frac{dz}{dt} \tag{1.10}$$

Where M is the rate of mechanical lowering, D_{chem} the rate of chemical lowering and z the elevation at a given location along the hillslope. Kirkby then evaluated for the transport limited case of erosion typical hillslope profiles which relate to the boundary conditions (soil physical constitution and rainfall regime, cf. sect- ii). Later on, Willgoose, Bras, and Rodriguez-Iturbe (1991) extended this sediment continuity equation to thw whole catchment, accounting for tectonic uplift U and diffusive erosion ($D\frac{d^2z}{dx^2}$,with D as a diffusion constant in $m^2\ s^{-1}$):

$$\frac{dz}{dt} = U + \frac{1}{\rho}q_s + D\frac{d^2z}{dx^2} \tag{1.11}$$

Here the term q_s describes fluvial sediment transport. For this model to work one needs to specifically implement a threshold for channel initiation (Dietrich, Wilson, and Reneau (1986)) which accounts for the more diffusive erosion on hillslopes. Therefore, this model was subsequently modified and improved, leading to an equation which mirrors the previously presented advection-diffusion equation 1.4 and is currently the basis for landscape evolution modelling (Perron, Dietrich, and Kirchner (2008); Bonetti et al. (2020)):

$$\frac{dz}{dt} = U + KA^m|\nabla z| + D\nabla^2 z \tag{1.12}$$

Fluvial sediment transport does no longer have to be distinguished by additional contraints but is represented as a term that depends on upslope accumulated drainage area A and the constants K and m. Based on this work, Perron, Kirchner, and Dietrich (2009) found that the equation can be written in its non-dimensional form and a number Pe, similar to a Peclet number can be found in landscape evolution models. Pe represents the relative contribution of advective and diffusive

erosion and was recently compared to the Reynoldsnumber (Hooshyar et al. (2020)) which describes the relative contribution of inertial and viscous forces of viscous flow. Interestingly, Perron, Kirchner, and Dietrich (2009) have shown that a *Pe* number of 1, where diffusive and advective forces are almost equal relates to a characteristic length which corresponds to the mean valley spacing of the landscape.

1.4 A THERMODYANMIC EXPLANATION FOR STRUCTURE

As indicated in the previous section, the interaction of surface runoff and landscape is in essence a fingerprint of free energy dissipation, resulting in all kinds of structural adaptations from small to large scales (Leopold and Langbein (1962); Howard (1990); Rodriguez-Iturbe et al. (1992), Cheraghi et al. (2018)). Prigogine (1978) referred to the structures which result within thermodynamic systems as dissipative structures. Dissipative structures, such as eddies in turbulent flows (Frisch (1995)), rill-networks on hillslopes (Cheraghi et al. (2018); Schroers et al. (2022)), or wave-like patterns on alluvial riverbeds (Kleidon (2016)) enhance dissipation and therefore allow systems to operate far from a thermodynamic equilibrium. As dissipation rates of a system are altered, the energy balance is affected as well, which feeds back on the structures. Such feedbacks consequently lead to an evolution of dynamics of the system through the growth of dissipative structures. The main point here is that the dissipative structures of the system not only enhance the internal dynamics but at the same time limit them, as their growth alters the energy fluxes and their associated gradients themselves. This interplay of growth of dissipative structures and a parallel depletion of the gradient which drives the creation of these, leads to a state which has been termed by Gilbert (1876) as dynamic equilibrium. A state which describes a system in equilibrium whose environment changes, causing the system itself to move to a new equilibrium position (Thorn and Welford (1994)). Prigogine (1978) describes this evolution of a system as evolutionary feedback of instabilities which increase entropy production of the system. Kleidon et al. (2013) give the example of a hillslope which initially is homogeneuos and even, without eroded rills. Eventually, a rainfall event might cause the displacement of some sediment and therefore increase the gradient at a particular location, which in turn results in further erosion. Such instabilities lead to fluctuations in the system which produce more entropy, fueled by the growth of dissipative structures. Prigogine (1978) termed these dynamics "order through fluctuations".

The evolution of runoff and the formation of structure in hydrological systems can therefore be linked to thermodynamic theory. Although, this was already noted by Leopold and Langbein (1962), approximating the energy and entropy balance of a system is still a task for rebels

in engineering sciences. As Thorn and Welford (1994) point out, the measurement and observation of energy, not to speak of entropy in the field is an almost impossible task. However, we intend to be somewhat rebellious in the following chapters of this thesis.

Part II

SURFACE RUNOFF ON HILLSLOPES - STEADY STATES

This study is published in the scientific journal Hydrology and Earth System Science (HESS). The remainder of part II is a reprint of:

2

MORPHOLOGICAL CONTROLS ON SURFACE RUNOFF: STEADY-STATE ENERGY PATTERNS, MAXIMUM POWER STATES AND DISSIPATION REGIMES

ABSTRACT.   Recent research explored an alternative energy-centred perspective on hydrological processes, extending beyond the classical analysis of the catchments water balance. Particularly, stream flow and the structure of river networks have been analysed in an energy-centred framework, which allows the incorporation of two additional physical laws: 1) the conservation of energy and 2) that entropy of an isolated system cannot decrease (1st and 2nd law of thermodynamics). This is helpful for understanding the self-organized geometry of river networks and open catchment systems in general. Here we expand this perspective, by exploring how hillslope topography and the presence of rill networks control the free energy balance of surface runoff at the hillslope scale. Special emphasis is on the transitions between laminar, mixed and turbulent flow conditions of surface runoff, as they are associated with kinetic energy dissipation as well as with energy transfer to eroded sediments. Starting with a general thermodynamic framework, we analyse in a first step how typical topographic shapes of hillslopes, representing different morphological stages, control the spatial patterns of potential and kinetic energy of surface runoff and energy dissipation along the flow path during steady states. Interestingly, we find that a distinct maximum in potential energy of surface runoff emerges along the flow path, which separates upslope areas of downslope potential energy growth from downslope areas where potential energy declines. A comparison with associated erosion processes indicates that the location of this maximum depends on the relative influence of diffusive and advective flow and erosion processes. In a next step, we use this framework to analyse the energy balance of surface runoff observed during hillslope-scale rainfall simulation experiments, which provide separate measurements of flow velocities for rill- and for sheet flow. To this end, we calibrate the physically based hydrological model Catflow, which distributes total surface runoff between a rill- and a sheet flow domain, to these experiments and analyse the spatial patterns of potential energy, kinetic energy and dissipation. This reveals again the existence of a maximum of potential energy in surface runoff as well as a connection to the relative contribution of advective and diffusive processes. In case of a strong rill flow component, the potential energy maximum is located close to the transition zone, where turbulence or at least mixed flow may emerge.

Furthermore, the simulations indicate an almost equal partitioning of kinetic energy into the sheet and the rill flow component. When drawing the analogy to an electric circuit, this distribution of power and erosive forces to erode and transport sediment corresponds to a maximum power configuration.

2.1   INTRODUCTION

Surface runoff in rivers and from hillslopes is of key importance to biological, chemical, and geomorphological processes. Landscapes, habitats, and their functionalities are coupled to the short and long-term evolution of rainfall-runoff systems. As we live in a changing environment it has been of mayor interest to explain the development of runoff systems and how ecological (Zehe, Blume, and Blöschl (2010); Bejan and Lorente (2010)), chemical (Zhang and Savenije (2018); Zehe et al. (2013)) and geomorphological (Leopold and Langbein (1962); Kirkby (1971); Yang (1971); Kleidon et al. (2013)) processes organize in time and space. Here we focus on the energy balance of surface runoff particularly at the hillslope scale using a thermodynamic framework. Typically, the momentum balance of surface runoff and stream flow is strongly dominated by friction, which is usually characterized by the flow laws of Darcy-Weißbach, Manning or Chezy (Nearing et al. (2017)). Consequently, hydraulic estimates of flow velocities rely on the semi-empirical parameters of these laws, which in essence express the ability of a system to dissipate free energy via friction into heat and thus to produce entropy (Zehe and Sivapalan (2009)). A thermodynamic perspective appears hence as the natural choice for deeper understanding of how the mass, momentum and energy balances of surface runoff are controlled by and interact with the landscape, and how short and long-term feedbacks determine the co-development of form and functioning of hydrological systems (Paik and Kumar (2010); Singh (2003)).

2.1.1   *Thermodynamics in landscape evolution and optimal channel networks*

Leopold and Langbein (1962) were among the first to introduce thermodynamic principles in landscape evolution. Representing a one-dimensional river profile as a sequence of heat engines with prony brakes (see Fig. 2.1), they showed that the most likely distribution of potential energy per unit flow along a rivers course to the sea follows an exponential function. Their main hypothesis was that stream flow performs least work, or equivalently, that the production of entropy per flow volume is constant. Yang (1976) extended this principle and termed it minimum stream power and detailed how flow velocity, slope, depth and channel roughness of a stream should adjust to mini-

mize stream power. In his work about optimal stream junction angles, Howard (1990) also assumed that stream power is minimized, while Rodriguez-Iturbe et al. (1992) proposed that optimal channel networks (OCN) minimize overall energy dissipation. The authors postulated three principles: (1) the principle of minimum energy expenditure in any link of the network, (2) the principle of equal energy expenditure per unit area, and (3) the principle of minimum total energy expenditure in the entire network. Subsequent work of these authors (Rodriguez-Iturbe et al. (1994); Ijjasz Vasquez et al. (1993)) revealed that application of these principles yielded three-dimensional drainage networks in accordance with Horton's laws of stream number and stream lengths (Smart (1972)). In climate research, Paltridge (1979) proposed the principle of maximum entropy production. He showed that a simple two box model allowed a successful reproduction of the steady state temperature distribution on Earth, which maximizes entropy production, expressed as the product of the heat flow and the driving temperature difference. Kleidon et al. (2013) argued that maximum entropy production in steady state is equivalent to a maximization of power, which means that the flow extracts free energy at a maximum rate from the driving potential energy gradient. The authors applied the maximum power principle to river systems and proposed that they develop to a state of maximum power in sediment flows: While the driving geopotential gradient is depleted at the maximum rate, the associated sediment export maximizes with the same rate. Furthermore, the authors relate maximum power in the river network to minimum energy expenditure, as minimum dissipation implies that a maximum of potential energy can be converted into kinetic energy of the water and sediment flux.

2.1.2 *Surface runoff and hillslope morphology and the role of energy conversions*

Though surface runoff on hillslopes is governed by the same physics as stream flow, there are also important differences. Overland flow is an intermittent threshold response to rainfall events (Zehe and Sivapalan (2009)) caused either by infiltration excess (Horton (1945), Beven (2004)) or saturation excess (Dunne and Black (1970)). Surface runoff flows along a partially saturated soil and may hence either accumulate downslope or re-infiltrate. Downslope re-infiltration implies an export of water mass and thus potential energy into the soil (Zehe et al. (2013)), and the related decline in flow depth reduces shear stress which affects the momentum balance. Overland flow is typically very shallow compared to the roughness elements, which makes the use of the above-mentioned flow laws even more challenging (Phelps (1975)), and it manifests either as diffusive sheet flow or advective flow in rill networks. Due to the transient nature of overland and sediment

flows, rill networks are generally transient but they develop in a self reinforcing manner (Gomez, Darboux, and Nearing (2003); Rieke-Zapp and Nearing (2005); Berger et al. (2010)). Micro rills emerge at some critical downstream distance on the hillslope (cf. Horton's "belt of no erosion" Horton (1945)) and continue in parallel for some length before they merge into larger rills (Schumm, Harvey, and Watson (1984)). Sometimes these rills split apart before converging into larger gullies (Achten et al. (2008); Faulkner (2008)) and finally connecting to a river channel. This transitional emergence of a structured drainage network was firstly stated in Playfair's Law (cited in Horton (1945)) and has since then been observed in a variety of studies (Emmett (1970); Abrahams, Parsons, and Wainwright (1994); Evans and Taylor (1995)). Motivated by the similarity to river networks and surface rill networks, several experimental studies explored whether rill networks grow towards and develop as least energy structures in accordance with the theory of optimal channel networks (Gomez, Darboux, and Nearing (2003); Rieke-Zapp and Nearing (2005); Berger et al. (2010)). The studies of Rieke-Zapp and Nearing (2005) and Gomez, Darboux, and Nearing (2003) revealed that the emergence of rill networks and their development implies indeed a reduction of energy expenditure, which has previously been shown for stream channel networks (Ijjasz Vasquez et al. (1993)). In line with these findings, Berkowitz and Zehe (2020) proposed that rill flow reduces the volume specific dissipative energy loss due to a larger hydraulic radius compared to sheet flow, which is equal to smaller rills merging into a larger as noted by Parsons, Abrahams, and Luk (1990).

The possible optimization of river or rill network geometries through the interplay of surface runoff, erosion and deposition of soils/ sediments is the first point that motivates an analysis from a thermodynamic perspective. The second point relates to the transition from laminar to turbulent flow conditions, which was already corroborated by Emmett (1970) in a set of comprehensive field and laboratory experiments to investigate hydraulics of overland flow. As laminar flow converts more potential energy into kinetic energy per unit volume than turbulent flow, it is of interest whether and how this transition relates to the emergence of rills and their optimization. Parsons, Abrahams, and Luk (1990) measured the hydraulic properties of overland flow on a semiarid hillslope in Arizona and attributed the observed downslope decrease in the frictional flow resistance to the accumulation of surface flow in fewer, but larger rills. This is similar to a transition of inter-rill flow, from here onwards referred to as sheet flow (Dunne and Dietrich (1980)), to rill flow. More recently a concept emerged that upholds a theory of a slope-velocity equilibrium (Govers, Takken, and Helming (2000); Nearing et al. (2005)), proclaiming that physical and therefore hydraulic roughness adapts such that flow

velocity is a unique function of the overland flow rate independent of slope.

2.1.3 *Objectives and hypotheses*

In the light of this concise selection of studies, we propose that an energy centred perspective on overland flow on hillslopes might be helpful to better understand the co-evolution of hillslope form and functioning and whether those (and other) hydrological systems evolve towards a meta-stable, energetically optimal configuration (Zehe et al. (2013); Kleidon, Renner, and Porada (2014); Bejan and Lorente (2010)). Following the work of Kleidon (2016), we develop the general thermodynamic framework and explain how surface runoff along rivers and hillslopes fit into this setting (2.2). We argue that despite the similarity of hillslope surface runoff and river runoff, morphological adaptations and the related degree of freedom of both systems, manifest at distinctly different scales. Mature river elements are mainly fed by the upstream discharge and local base flow, while hillslope elements receive substantial water masses during runoff events through local rainfall and upslope runon. This causes an interesting trade-off along the overland flow path, where mass grows downslope due to flow accumulation, while geopotential height declines. We hypothesize that these antagonistic effects lead to a peak in potential energy of overland flow at a distinct point on the hillslope. This implies an upslope area, where the potential energy of overland flow is growing due to flow accumulation (though water is flowing downslope) before it starts declining in downslope direction. From a thermodynamic perspective, the ability of surface runoff to perform work increases up to the point of maximum potential energy and is then depleted through a cascade of energy conversion processes. Our second hypothesis is thus, that this build-up of potential energy occurs under laminar flow conditions with a low degree of freedom for morphological changes, while the location of potential energy maximum coincides with the emergence of turbulent flow, and with a maximum degree of freedom for morphological changes, including the emergence of rills.

The first application of our framework tests hypothesis 1, by exploring how typical shapes of hillslope topography in combination with different width functions control the spatial patterns of potential and kinetic energy of surface runoff and energy dissipation along the flow path during steady states. As these shapes represent different morphological hillslope stages (Kirkby (1971)), shaped by erosive forces of previous surface runoff events (Rieke-Zapp and Nearing (2005)), we expect differences in the energy balance, including the location of the potential energy maximum. The second application of our framework tests hypothesis 2, by analysing the energy balance

of surface runoff observed during hillslope scale rainfall simulation experiments in the Weiherbach catchment (Scherer et al. (2012)). The experiments provide measurements of eroded sediments and total runoff including sheet and rill flow velocities at the lower end of the irrigated stripes, and therefore present an opportunity to explore how rills and rill networks affect the energy balance of surface runoff. For that purpose, we calibrated an extended version of the Catflow model (Zehe et al. (2001)), which accounts for the transition from sheet to rill flow, to these experiments, and analysed the spatial patterns of potential energy, kinetic energy and dissipation with respect to the transition from laminar to turbulent flow based on simulated flow depths and velocities.

2.2 THEORY

2.2.1 *Free energy balance of hillslopes as open thermodynamic rainfall-runoff systems*

To frame surface runoff processes into a thermodynamic perspective we define the surface of a hillslope as an open thermodynamic system (OTS; Kleidon (2016)). In this sense, the hillslope exchanges mass, momentum, energy and entropy with its environment (Fig. 2.1). Rainfall adds mass at a certain height and thus free energy in the form of potential energy along the upper system boundary. Mass and free energy leave the system at the lower boundary due to surface runoff or via infiltration as subsurface flow (Zehe et al. (2013)). To express energy conservation of surface runoff, we start very generally with the first law of thermodynamics in the following form:

$$\frac{dU}{dt} = \frac{d(H)}{dt} + \frac{dW}{dt} \tag{2.1}$$

Eq. 2.1 states that a change in the internal energy U [*Joule*] of a system consists of change in heat H in joule plus the amount of work W in joule performed by the system. Here, the performed work dW remains part of the internal energy, as in an open environmental system work is usually performed in the system and does not leave it as it is the case for heat engines (Kleidon (2016)). Note that the capacity of a system to perform work is equivalent to the term "free energy". Solving Eq. 2.1 for the change in free energy/work reveals hence that a change in heat is associated with a dissipative loss of free energy and production of thermal entropy. The latter reflects the second law of thermodynamics, which states that entropy is produced during irreversible processes. The free energy of surface runoff at any point on the hillslope corresponds to the sum of its potential and kinetic energy if we neglect pressure work (i.e., assuming constant pressure) and mechanical work (i.e., no shaft work such as pumps and turbines).

We apply Eq. 2.1 to balance both potential and kinetic energy of surface runoff separately and subdivide the hillslope into lateral segments along the horizontal flow path x (Fig. 2.1), with a given width b and express energy fluxes in *watt* m^{-1}. Note that differences between in- and outflux of free energy in a hillslope element imply that these are either converted into another form of free energy or are dissipated. The potential energy balance of surface runoff depends on the topographical/ geopotential elevation of the hillslope element, on the corresponding mass inputs due to rainfall and upslope runon, on the mass losses due to infiltration and downslope runoff and on the energy conversion into kinetic energy (Eq. 2.2). In our notion potential energy of infiltration excess surface runoff is converted into kinetic energy of overland flow, while kinetic energy is partly dissipated via friction into heat (Eq. 2.3), and another part is transferred into erosion and sediment transport. Note that in our two-box scheme (Fig. 2.1) we consider total energies of fluid flow (mean velocity, though possibly turbulent) and the kinetic energy balance residual D_f does not separate energy transfer to sediments from frictional dissipation. We can thus write the potential and kinetic energy balance equations for any segment of the hillslope in watt per meter:

$$\frac{dE_f^{pe}(x)}{dt} = J_{f,in}^{pe}(x) - J_{f,out}^{pe}(x) + J_{P,in}^{pe}(x) - J_{Inf,out}^{pe}(x) - P_f(x)$$
$$= J_{f,net}^{pe}(x) + J_{Peff,net}^{pe}(x) - P_f(x)$$

(2.2)

$$\frac{dE_f^{ke}(x)}{dt} = P_f(x) - D_f(x) + J_{f,in}^{ke}(x) - J_{f,out}^{ke}(x)$$
$$= P_f(x) - D_f(x) + J_{net}^{ke}(x)$$

(2.3)

Fluxes with superscript *pe/ke* relate to potential energy and kinetic energy, respectively. The subscript f relates to surface runon and runoff, subscript *inf* to infiltration and subscript P to precipitation (see table 2.2). Equations 2.2 and 2.3 balance changes of potential energy of runoff E_f^{pe} and its kinetic energy E_f^{ke}, also expressed in terms of the net energy fluxes across the segment boundary $J_{(f,net)}^{pe}, J_{(f,net)}^{ke}, J_{Peff}^{pe}$. P_f is the transfer from potential to kinetic energy and D_f summarizes the frictional dissipation rate and the work needed for sediment detachment and transport as well as energy that is used to generate turbulent kinetic energy. While dissipation means free energy is lost as heat, kinetic energy transfer to the sediment is not dissipated, as it creates macroscopic motion. Along similar lines, one could separate turbulent kinetic energy from kinetic energy of the mean flow when

including turbulent velocity fluctuations. By combining Eq. 2.2 and 2.3 the total free energy balance of a hillslope segment becomes:

$$\frac{dE_f^{pe}(x,t)}{dt} + \frac{dE_f^{ke}(x,t)}{dt} =$$

$$J_{f,net}^{pe}(x,t) + J_{f,net}^{ke}(x,t) + J_{Peff,net}^{pe}(x,t) - D_f(x,t)$$

(2.4)

The change in total free energy of overland flow in a segment is equal to the sum of net energy fluxes minus dissipation. In the case of steady state $((dE_f^{pe}(x,t))/dt = (dE_f^{ke}(x,t))/dt = 0)$, the dissipation term D_f can be determined as residual of the steady state energy balance. Before we further elaborate on this in section 2.3, we reflect on the relation between the energy balance residual, frictional dissipation, and the related flow laws.
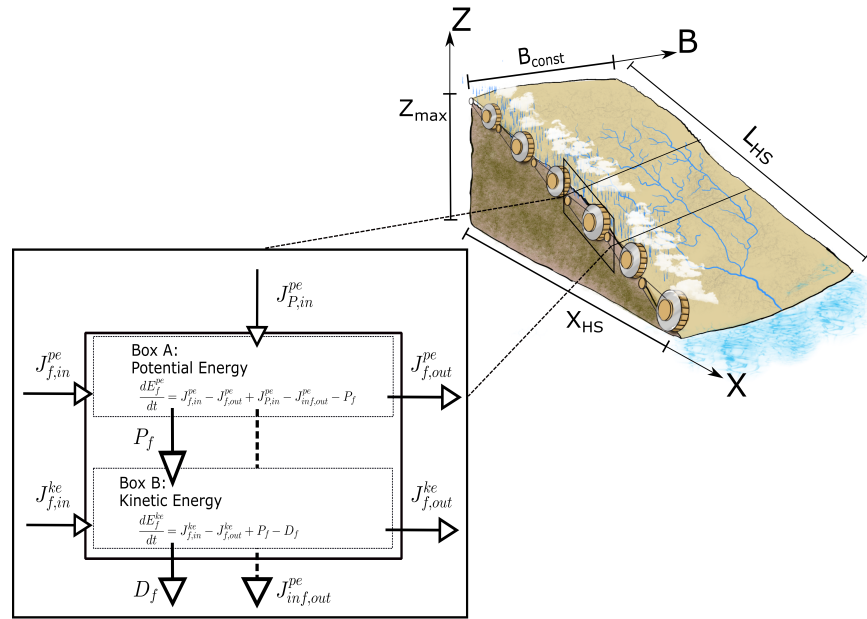
Figure 2.1: Hillslope open thermodynamic system with spatial division into sub-OTS as a two box open thermodynamic system. Each control volume (sub-OTS) is represented by a prony brake

2.2.2 *The energy balance residual and frictional dissipation at the hillslope scale*

Here, we focus on conversion of potential energy into kinetic energy, because the former controls the hierarchy of possible energy conversion in surface runoff. We neglect the subsequent kinetic energy transfer to sediments and turbulent velocity fluctuations and refer to D_f simply as the dissipation of kinetic energy. The concept could be extended to account for phase transitions from laminar to turbulent flow as well as for kinetic energy transfer to eroded sediment particles.

In these cases, D_f needs to be separated into the energy fluxes that a) convert kinetic energy of mean flow into turbulent kinetic structures, b) transfer energy to sediment motion and c) frictional dissipation, while at the same time one needs to include the energy balance of eroded sediments.

For laminar flow the downslope accumulation of runoff leads to a steeper vertical velocity gradient, which might surpass a critical threshold Reynolds number to create turbulent flow structures (expressed as the relation of inertia to viscous forces). These convert kinetic energy of the mean flow into kinetic energy of small-scale velocity fluctuations, and thereby reduce the kinetic energy and thus velocity of the mean flow. Turbulence in turn provides the power and force to detach and lift sediment particles, which also need to be accelerated (in the simplest case) to the mean flow velocity. Both erosion processes feed again on the kinetic energy of the mean flow, while particle detachment feeds also on kinetic energy of rain drops. In the light of these thoughts, one can expect D_f to be larger for turbulent than for laminar flow, when using the mean flow velocities to calculate E_f^{ke}, and D_f should also be larger in the case of erosion and sediment transport. Both processes extract kinetic energy and consequently reduce mean flow velocities, as corroborated by Ali et al. (2012) for energy transfer to sediments in experiments of runoff on erodible beds. This energy transfer has implications for the inverse estimate of roughness coefficients from rainfall simulation experiments (also for those we use in section 4). The important point to stress here, is that in general an increase of an observed (apparent) resistance to flow due to a reduced mean flow velocity can but must not necessarily imply that a larger frictional dissipation is the underlying cause.

Govers, Takken, and Helming (2000) summarize the methods, which are still in use today for estimating how frictional dissipation controls steady state runoff velocities as a function of roughness, essentially representing the degree of free energy loss from the mean flow. Most approaches focus on the generalization of a friction coefficient in time and/or space for a given surface area where runoff occurs, which is expressed by a general friction law that relates unit width discharge q to flow depth d and topographic slope I_0:

$$q = c_1 d^{c_2} \sqrt{I_0} \tag{2.5}$$

Where c_1 and c_2 are coefficients, which vary for Manning-Strickler (Manning's n), Chezy (C) and Darcy-Weißbach (f) (Singh (2003), 2.1).

Although it is known that friction coefficients on hillslopes vary with the degree of roughness element inundation (Lawrence (1997)), as well as sediment transport concentrations and are transient (Abrahams, Parsons, and Wainwright (1994)), mean flow velocities are in practice estimated by using constant values. Without additional information about the flow regime and transport process, these coefficients

LAW	c_1	c_2
Manning-Strickler	1/n	5/3
Chezy	C	3/2
Weißbach	$2\sqrt{2g/f}$	3/2

Table 2.1: Coefficients of general friction law

provide, as explained above, an uncertain estimate of frictional energy dissipation of free energy into heat and related entropy production (Govers, Takken, and Helming (2000)). Furthermore, experiments by Govers (1992) for rill flow as well as by Nearing et al. (2017) for sheet flow indicate that friction coefficients vary across the hillslope during steady state. They even seem to be spatially organized, as these studies found that mean runoff velocity can be solely estimated by the runoff rate, independent of topographic slope or rainfall intensities. For the analysis presented in sect. 3, we use one of these empirical formulae which was developed by Nearing et al. (2017) for surface runoff on stony hillslopes:

$$v = 26.39 q^{0.696} \tag{2.6}$$

Eq. 2.6 implicitly incorporates variable friction coefficients, as flow velocity v is a unique function of unit width discharge q. The advantage of Eq. 2.6 is that we can back-calculate the spatial distribution of potential energy without estimating frictional dissipation as a lumped constant, such as it is the case in Eq. 2.5. Obviously, this formula might not be applicable to hillslopes with different soil properties and vegetation, but thoughtful design of future experiments might reveal that the hypothesized independence of flow velocity is generalizable. For the analysis of the rainfall simulation experiments in section 4, the derivation of a similar empirical formula is beyond the data this study has at hand. This implies that absolute values of frictional dissipation rates presented section 4 are uncertain. But they are nevertheless a useful starting point, as our focus lies on their spatial patterns and the relative differences depend on macroscale properties (measured velocities and runoff rates of rill and sheet flow in this case), which are well captured by these experiments. So even without explicit inclusion of the energy transfers between mean flow and turbulent structures or sediment particles, the analysis of the spatial distribution of potential energy is helpful to understand constraints of runoff and morphological process as well as the sensitivity to different hillslope forms or the presence of rill networks

SYMBOL	UNIT	DESCRIPTION
U	kgm^2s^{-2}	internal energy of a thermodynamic system
W	kgm^2s^{-2}	available energy to perform work by the thermodynamic system
H	kgm^2s^{-2}	thermal energy of the thermodynamic system
$E^{pe/ke}$	kgm^2s^{-2}	Potential- or kinetic energy of the water flow
$J^{pe/ke}_{f,in/out}$	$kgms^{-3}$	Potential- or kinetic energy flux entering or leaving the system
$J^{pe}_{P,in}$	$kgms^{-3}$	precipitation entering the system as potential energy flux
$J^{pe}_{inf,out}$	$kgms^{-3}$	infiltration leaving the system as potential energy flux
P_f	$kgms^{-3}$	power to create kinetic energy of system
D_f	$kgms^{-3}$	dissipation of free energy of flow into different kind of energy
v	ms^{-1}	velocity of runoff, parallel to bed slope
ρ	kgm^{-3}	density of water with value of 1000
g	ms^{-2}	gravitational acceleration with value of 9.81
v	m^2s^{-1}	Kinematic viscosity with value of 10^{-6}
Q	m^3s^{-1}	discharge
h	m	water height above channel bank (h=z+d)
b	m	hillslope width
b_r	m	Bottom width of trapezoidal rill cross-section
q	m^2s^{-1}	Unit width discharge
I	mmh^{-1}	rainfall infiltration excess intensity
d	m	water column depth of surface runoff
n	$m^{-1/3}s$	Manning coefficient
C	$ms^{-1/3}$	Chezy coefficient
f	—	Darcy-Weißbach coefficient
I_0	—	topographic slope
z	m	geopotential of bed level to reference level
X_{HS}	m	Dlength of hillslope, parallel to reference surface
L_{HS}	m	length of hillslope, parallel to bed level
R	m	hydraulic radius
A	m^2	wetted area of discharge
τ	$kgm^{-1}s^{-2}$	bed shear stress
C_f	—	Flow accumulation coefficient of Catflow model
α, β, γ	$radians$	Angles of Catflow hillslope surface
Re	—	Reynolds number of surface runoff
k	—	Relative roughness
Q_{sed}	kgs^{-1}	Sediment discharge
C_{sed}	kgm^{-3}	Sediment concentration
d_{50}	μm	Mean sediment particle diameter

Table 2.2: Overview of the different symbols used in this study

2.2.3   *The steady state energy distribution of surface runoff and transitions between flow regimes*

We come back to the steady state free energy balance of surface runoff (Eq. 2.4), which allows an estimation of the term D_f as energy balance residual. For convenience, we express the energy fluxes on the right-hand side by the hydrological variables overland flow rate Q in $m^3 s^{-1}$, mean flow velocity v in ms^{-1}, infiltration excess intensity I in mmh^{-1} (difference between rainfall intensity and infiltration rate), and water height above the channel bed h in m (see Appendix A.1.1 for derivation):

$$D_f(x) = J^{pe}_{f,net}(x) + J^{pe}_{Peff,net}(x) + J^{ke}_{f,net}(x)$$

$$= \rho g(-\frac{dQ(x)}{dx}h(x) - \frac{dh(x)}{dx}Q(x) + I(x)h(x)b(x)/(3.6*10^6))$$

$$-\frac{1}{2}\rho(\frac{dQ(x)}{dx}v(x)^2 + 2v(x)\frac{dv(x)}{dx}Q(x)) \quad (2.7)$$

Where ρ is the density of water, and g is gravitational acceleration. The terms in the first bracket reveal the antagonistic effects of a downslope growing discharge due to flow accumulation and the decline in topographic elevation on potential energy. As stated in our first hypothesis, we expect that this trade-off leads to a local potential energy maximum. While the existence of such a maximum can in fact already be confirmed by a re-analysis of the experiments of Emmett (1970) (Fig. 2.2, sect. 3.), the existence of such a maximum is usually not discussed in the case of stream flow. This is because Eq. 2.7 simplifies in streams to Eq. 2.8, as kinetic energy fluxes are much smaller than potential energy fluxes and with increasing discharge the mass balance gets more and more dominated by upstream runon while precipitation input becomes marginal:

$$D_f(x) = -Q(x)\rho g\frac{dh(x)}{dx} \quad (2.8)$$

In the literature Eq. 2.8 is also called stream power (Bagnold (1966)) and is used to calculate the force τ in Nm^{-2} that acts on bed material per unit area ("shear stress", with d in m, as depth of water column) for river discharge:

$$\tau(x) = \frac{D_f(x)}{v(x)b(x)} = -d(x)\rho g\frac{dh(x)}{dx} \quad (2.9)$$

Mostly $\frac{dh}{dx}$ is approximated by topographic slope, leading on hillslopes to an underestimation of the driving water level gradient in flat terrain and an over-estimation of the gradient on steep slopes (Govers, Takken, and Helming (2000)). This is also related to the experimental findings of Ali et al. (2012), who concluded that sediment transport capacity is weakly correlated to calculated bed stress and attributed this finding

to the transfer of energy to the detachment of sediment. It is therefore evident that the approximation of lost energy by topographic slope and fixed roughness parameters alone cannot provide closure for the energy balance of surface runoff, and a closer look at involved energy conversion processes seems necessary. After the upslope onset, surface runoff accumulates as very shallow, laminar sheet flow (Dunne and Dietrich (1980)), which is, according to Eq. 2.9, yet too small to trigger erosion and perform significant work to the hillslope surface. Resistance to flow at this stage relates to the individual drag force of exposed sediment particles, leading to an increase of roughness for larger flow depths (Lawrence (1997)). As soon as the particles are inundated the kinetic energy of overland flow can be enlarged or even maximized as a further increase of flow depth results in a reduction of local roughness. Here the flow is still laminar, meaning that mean flow velocities and kinetic energies in the mean flow are larger than for turbulent flow. With further increase of flow accumulation and flow depth, the velocity profile in the boundary layer becomes steep enough to create turbulence, so less potential energy is converted into kinetic energy of the mean flow, which lets resistance to the mean flow appear larger. In fact, the reduced kinetic energy of the mean flow is also due to the increase of kinetic energy of turbulent structures, which in turn provide the necessary power to erode the surface and deplete the topographic gradient by redistribution of soil material through rill networks.

Rill structures form on event to seasonal timescales due to a fast positive feedback (Rieke-Zapp and Nearing (2005)). On a longer timescale the redistribution and export of soil material restructures entire topographic hillslope profiles such that typical shapes can be attributed to a dominant erosion process (Kirkby (1971); Beven (1996)). The latter change in space along the flow path, and therefore in close connection to the flow regimes (Shih and Yang (2009); cf. Fig. 2.2). At the upslope divide erosion is mostly influenced by gravity, resulting in soil creep. With flow accumulation in downslope direction, the particles eroded by raindrop splash can be transported by surface runoff, until surface runoff becomes turbulent and can erode and transport particles as soil wash. The spatial organization of transition processes (also called threshold processes) can be described by the relative contribution of internal and external forces. Turbulence emerges when gravitational (external) force surpasses a certain threshold in relation to viscous (internal) forces. Similarly, soil wash erosion relates to externally induced bed stress by runoff while soil creep depends on internal resistance factors of the soil matrix. We therefore propose, as stated in our second hypothesis, that both process transitions are linked through their external forcing, which is attributed to the energy gradient of surface runoff. The distribution of surface runoff energy and its gradient provide therefore insights on erosional as well as flow regimes.

In the following we apply our framework to test our hypotheses on two related temporal and spatial scales. In section 3, we analyse the distribution of energy at the macroscale, representing the hillslope as an open thermodynamic system which adapts morphologically to the distribution of gradients and fluxes on long timescales. To this end we analyse steady state runoff on typical hillslope profiles that reflect according to Kirkby (1971) dominant erosion processes "soil creep", "rain splash" and "soil wash". In section 4 we analyse the energy balance of surface runoff observed during short term rainfall simulation experiments, where runoff concentrates in rills and distributes energy into a sheet- and a rill domain.

In both sections we explore how the transition of flow regime and erosion processes on hillslopes relate to the distribution of energy and its local maximum. We want to stress that we speak of laminar flow if there is a clear dependence between flow Reynolds number of surface runoff and friction coefficient (Phelps (1975)). For purpose of comparison with earlier studies of hydraulics of surface runoff (Emmett (1970); Parsons, Abrahams, and Luk (1990)) we calculate flow Reynolds number Re as per Eq. 2.10, relating the characteristic length of surface runoff to flow in a fully filled circular pipe. Here, v represents the depth averaged flow velocity, R the hydraulic radius and ν is the kinematic viscosity with a value of $10^{-6}m^2s^{-1}$.

$$Re = \frac{4vR}{\nu} \tag{2.10}$$

2.3 TOPOGRAPHIC CONTROLS ON THE SURFACE RUNOFF ENERGY BALANCE TERMS - A FIRST-ORDER ASSESSMENT

To clarify and test our hypothesis, we digitized results of rainfall runoff experiments on hillslope plots from Emmett (1970) and plotted potential energy E_f^{pe} and specific potential energy $E_f^{pe,SP}$ ($E_f^{pe,SP} = E_f^{pe}/Q$) (Fig. 2.2, upper part) in parallel to a sketch of surface runoff on a hillslope and the related flow and erosion process transitions (Fig. 2.2, lower part). E_f^{pe} and $E_f^{pe,SP}$ were calculated from measured water depth above outlet reference level and mean flow velocity.

The accumulation of mass along a declining geopotential leads to a maximum of potential energy in space, dividing the flow path into a section where energy is gained (Fig. 2.2, arrow a) and a section where energy is depleted (Fig. 2.2, arrow b). In between these two sections (Fig. 2.2, area highlighted in grey), depletion of potential energy is balanced by the energy influxes of runoff accumulation and rainfall. Volumetric energy $E_f^{pe,SP}$ as well as its gradient decrease along the flow path. Or differently stated, the energy expenditure per unit discharge decreases in downstream direction (solid blue line). This is very much in line with the previously mentioned principles of Rodriguez-Iturbe et al. (1992) and Yang (1976) of minimum stream power in river streams.

To our knowledge a separation of the runoff system into an energy production and energy depletion zone has not been investigated so far but could have consequences on our understanding on the transitional formation of runoff and erosion processes on hillslopes. The transition
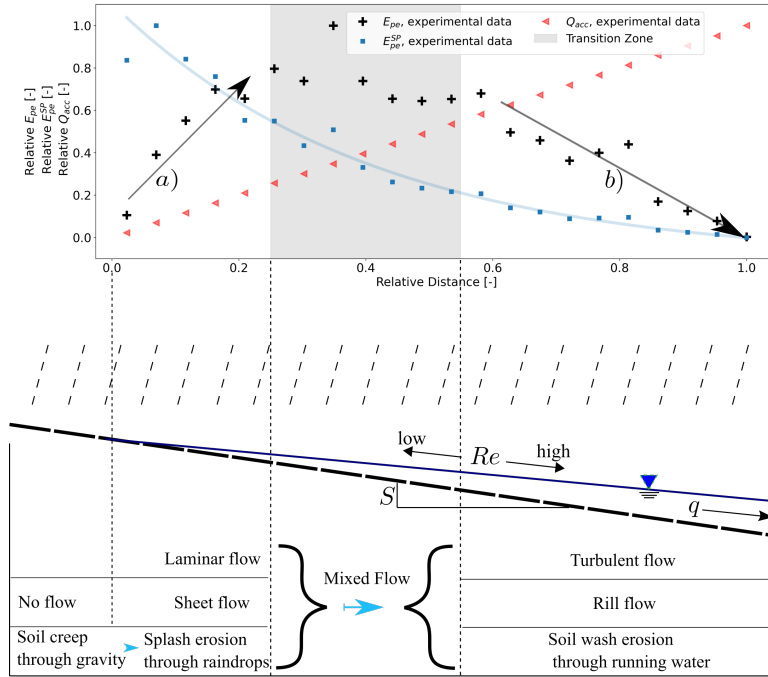
Figure 2.2: Upper Part: Digitized results from rainfall simulation experiments at New Fork River 1 (Emmett (1970)), expressed as normalized potential energy E_f^{pe}, specific potential energy $E_f^{pe,SP}$, and Reynolds number Re; Lower Part: Simplification of overland flow processes on hillslopes (modified after Shih and Yang (2009)) as a function of Reynolds number Re and distribution of potential energy

from a laminar into a turbulent flow regime is indicated by ranges of critical Reynolds-number Re_c, which depend on the type of flow as well as relative friction. While the Re_c of circular pipe flow is roughly 2300 (Schlichting and Gersten (2017)), Emmett (1970) determined in field and laboratory experiments Re_c of sheet flow between 1500 to 6000. Later Phelps (1975) pointed out that for sheet flow over rough surfaces Re_c depends on relative friction k, that is the size of an average sediment particle to the depth of the flow. He showed that for k values of 0.5, Re_c can be as low as 400. For the results presented in Fig. 2.2, Re was calculated with average depths and mean velocities along the slope direction and increased linearly up to 1368 at the lower end of the experimental plot. As however an analysis of the flow patterns suggests, local Re at points where flow converges into rills is likely to be much larger. A transition from laminar to turbulent flow regime in rills is therefore likely to correspond in Fig. 2.2 to a flow path distance within the highlighted transition zone between increase and decrease of potential energy (mixed flow).

2.3.1   *Typical hillslope forms and width functions*

In this section, we explore how typical hillslope configurations and effective rainfall forcing, control runoff accumulation and related energy conversions. We distinguish three typical hillslope forms, which are related to a dominant erosion process (Kirkby (1971)). Equation (2.11) defines the distribution of geopotential along a representative flow path. The coefficients m_1 and m_2 describe the relative contributions of accumulated discharge and topographic slope to sediment transport ($Q_{sed} \propto Q^{m_1} S^{m_2}$). According to Kirkby (1971) the region $m_1 < 1$ is therefore related to a hillslope profile that was formed by diffusive erosion processes (soil creep or rain splash), whereas the region $m_1 > 1$ corresponds to more advective erosion processes with higher sediment transport capacities (soil wash, river flow). We can therefore use these empirical coefficients to describe the transition of one regime (diffusive erosion/ transport) into another (advective erosion/ transport), if appropriate boundary conditions (rainfall and infiltration rates, vegetation, etc.) allow for long enough feedback to reach steady state.

$$Z(x) = Z_{max}(1 - (x/X_{HS})^{(1-m_1)/(1+m_2)}) \qquad (2.11)$$

A rough relation between coefficients m_1 and m_2 and corresponding erosion regions is shown in Fig. 2.3a (after Kirkby, 1990; cited in Beven (1996)). For selection of the coefficients that we use to relate hillslope form and sediment erosion/ transport regime, we digitized the upper and lower limits and computed a mean curve from which we extracted the coefficients m_1 and m_2 in accordance to ranges indicated by Kirkby (1971). In our example, all hillslopes start at Z_{max}=10 m , the maximum geopotential in meter above stream bank, and end at zero at the hillslope end (X_{HS}=100 m , cf. Fig. 2.3b), depleting all available geopotential gradients on the hillslope. We then combine these forms with three different width distributions, which are either constant (const), converging (conv) or diverging (div) (Fig. 2.3c). In our analysis we keep the projected area constant at 5000 m^2 for all configurations, which results in an equal total surface runoff from all hillslope forms for a given effective rainfall intensity. Finally, we computed steady state surface runoff for effective rainfall intensities of 5-, 10-, 20- and 50- $mmhr^{-1}$ (Fig. 2.3d). The differently dotted lines in Fig. 2.3c, and d represent the three hillslope width distributions and show their influence on runoff accumulation. For all combinations of runoff accumulation and hillslope topography, we computed the steady state spatial distribution of water mass and flow velocity using 2.6. From the computed hydraulic variables, we then calculated the distribution of potential energy flux J_f^{pe} and kinetic energy flux J_f^{ke} (see Appendix A.1.1).
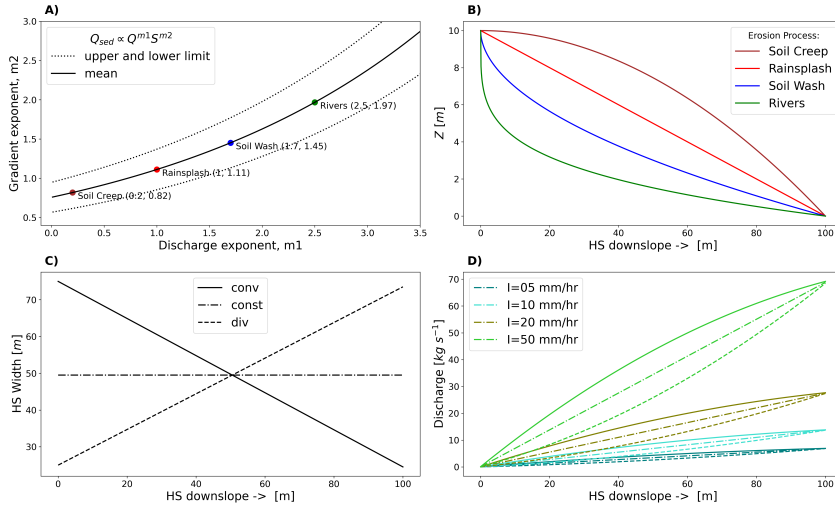
Figure 2.3: a) Discharge (m_1) and gradient (m_2) exponent (after Kirkby 1990, cited in Beven (1996)) for characterizing sediment transport capacity; b) Typical hillslope (and river) profiles as result of dominant erosion process (Kirkby (1971)); c) Assumed width distributions along flow path; d) Resulting steady state discharge along the hillslope for different rainfall infiltration excess intensities. The line types in panel d correspond to the width functions in panel c.

2.3.2   *Spatial maxima of potential energy*

Generally, we found that the trade-off of downslope mass accumulation and declining geopotential leads to a distinct potential energy maximum, which has a clear dependence on the slope form, width function and strength of rainfall forcing (Fig. 2.4). This implies that the hillslope can be sub-divided into three classes of spatial energy dynamics:

1. $(dE_f^{pe}(x))/dx > 0$

2. $(dE_f^{pe}(x))/dx = 0$

3. $(dE_f^{pe}(x))/dx < 0$

Within the first interval potential energy flux increases along the flow path, as the additional mass from rainfall adds more energy to the sub-OTS than flows out. At a certain distance (interval 2), energy outflux equals energy influx through precipitation plus upstream inflow and we observe an energetic maximum. Within the third interval, energy outflux is continuously larger than energy influx, effectively depleting the accumulated geopotential of interval 1. Fig. 2.4a shows that the
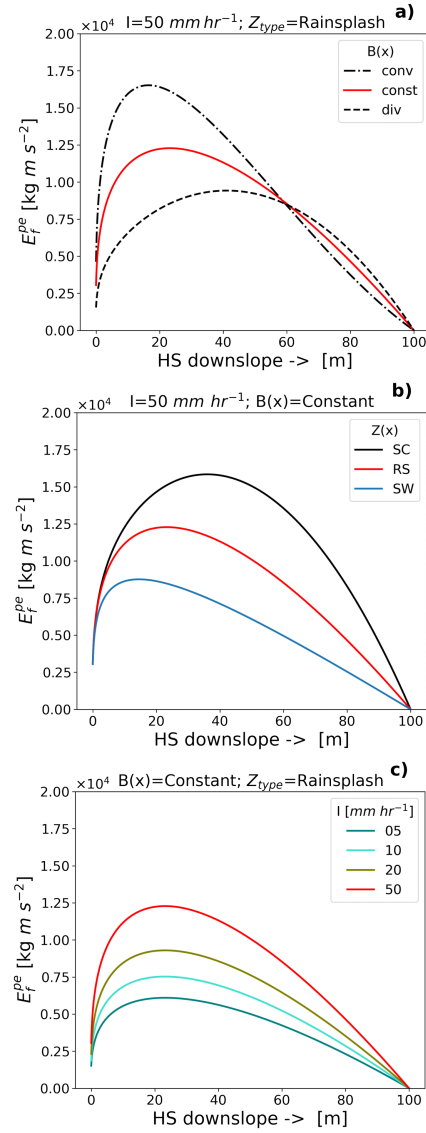
Figure 2.4: Distribution of potential energy E_f^{pe} per unit length (*Joule* m^{-1}) as a function of a) hillslope width b) geopotential distribution (form) and c) rainfall intensity I

location of the energetic maximum moves upslope when changing the width function from divergent (div), over parallel (const) to convergent (conv). The magnitude of the absolute value of the maximum increases in a similar fashion. The distribution of geopotential from top to bottom clearly influences the location and size of maxima (Fig. 2.4b). Hillslope profiles which are formed by soil creep (SC) show the maximum of E_f^{pe} farthest downslope, whereas profiles related to rainsplash (RS) and soil wash (SW) erosion reach the maximum potential energy farther upslope. As potential energy has dissipated at the end of the hillslope, this implies that SC profiles dissipate more energy on shorter flow path distance than RS or SW profiles (indicated by the gradient of E_f^{pe} in Fig. 2.4b). If dissipation is proportional to bed stress

(see discussion) this means that for the same amount of energy input across the hillslope larger bed stresses occur on SC profiles while in comparison SW profiles relate to lower relative bed stress.

Similarly, an increasing rainfall infiltration excess intensity I increases the magnitude of the energy maxima while it does not affect their location (Fig. 2.4c). Increasing energy maxima imply steeper energy gradients resulting in more power during the energy conversion processes. We thus state that the distribution of potential energy in space is a function of hillslope width, form and rainfall intensity and seems to go hand in hand with the morphological stages of hillslope forms.

2.3.3 *Topographic control of energy conversion rates*

To estimate the relative amount of influx energy that is converted into the energy balance residual D_f we compute for each hillslope form the accumulated energy residual $D_f^{acc}(xl) = \int_{x=0}^{xl} D_f(x)dx$ (watt) divided by accumulated steady state energy input $J_{in}^{acc}(xl) = \int_{x=0}^{xl} J_{Peff,net}^{pe}(x)dx$ (*watt*) along the flow path:

$$\frac{D_f^{acc}(xl)}{J_{in}^{acc}(xl)} = \frac{J_{f,net}^{pe,acc}(xl) + J_{in}^{acc}(xl) + J_{f,net}^{ke,acc}(xl)}{J_{in}^{acc}(xl)} \tag{2.12}$$

If no other mass affecting processes are considered, $J_{in}^{acc}(xl)$ is the accumulated energy influx due to rainfall at flow path distance xl. Further we do not consider upslope runon at the hillslope top in steady state $J_{f,net}^{pe,acc}(xl) = -J_{f,out}^{pe}(xl) = -\rho Q(xl)h(xl)g$ and $J_{f,net}^{ke,acc}(xl) = -J_{f,out}^{ke}(xl) = -\rho Q(xl)v(xl)^2/2$ so that Eq. 2.12 becomes:

$$\frac{D_f^{acc}(xl)}{J_{in}^{acc}(xl)} = 1 - \frac{J_{f,out}^{pe}(xl) + J_{f,out}^{ke}(xl)}{J_{in}^{acc}(xl)} \tag{2.13}$$

Equations 2.12 and 2.13 describe at each point along the flow path how much energy of the upslope accumulated potential energy from rainfall is neither conserved as kinetic nor potential energy of the mean flow. The ratio D_f^{acc}/J_{in}^{acc} is therefore a thermodynamic descriptor that can be used to estimate the dissipation per power, i.e., energy input, independent of absolute flow path lengths, rainfall rates and geopotential gradient. Similarly, the ratio $J_{f,out}^{ke}/J_{in}^{acc}$ describes the relative magnitude of upslope accumulated input energy that is converted into kinetic energy at each cross section along the flow path.

Fig. 2.5a reveals a distinct pattern of D_f^{acc}/J_{in}^{acc}. For SW hillslope forms the ratio is continuously larger than for RS and SC forms. Regardless of absolute energy influx, SW hillslope forms convert relatively more influx energy into D_f than RS or SC forms. Similarly, but to a much smaller degree than profile form, hillslopes with converging

widths dissipate relatively more energy on less flow path lengths compared to constant or diverging widths. For all forms, J_{in}^{acc} is almost completely dissipated at the end of the hillslope ($D_f^{acc}(X_{HS}) \approx J_{in}^{acc}(X_{HS})$) and only a minor part of J_{in}^{acc} is converted into kinetic energy (Fig. 2.5b and c: $J_{f,out}^{ke} / J_{in}^{acc} < 0.002$). SW hillslope forms convert a larger part of the influx energy into kinetic energy than RS and SC forms and the same hierarchy is found in converging, to constant and to diverging hillslope widths (Fig. 2.5c). The function of kinetic energy along the flow path is convex, which relates to increasing production of kinetic energy per energy influx.

2.3.4 *Discussion*

In this section we related the spatial distribution of slope (hillslope form) to the distribution of potential and kinetic energy of surface runoff. As form is also connected to the dominant erosion process, an analysis of energy dissipation provides a link between erosion process and thermodynamic principles. In a first step we digitized surface runoff experiments by Emmett (1970) and we showed that the distribution of potential energy results in a distinct flow path distance with maximum potential energy. Up to this point the system net accumulates energy and only undergoes a net loss of energy after this location. The distribution of these zones of energy production and energy depletion seems to be related to the transition of the system from one type of flow regime to another. Magnitude and distribution of energy are relative to a level of null energy at the hillslope end, and therefore represent an assumed equilibrium state of the land-water system at the hillslope scale. From a larger perspective the accumulated discharge at the end of the hillslope can perform work within the context of the whole catchment, which has been discussed previously (cf. Rodriguez-Iturbe et al. (1992); Kleidon et al. (2013)). For an analysis of these equilibrium state hillslopes, we relied on established semi-empirical descriptions of hillslope forms and related erosion processes (Kirkby (1971)) and we assumed that surface runoff on equilibrium hillslopes has dissipated all potential energy at the downslope end (usually the channel bank). The resulting steady state distribution of potential energy of surface runoff was then calculated by a friction law that was established for stony hillslopes in Arizona (Nearing et al. (2017)) but in essence expresses the tendency of a hillslope surface to spatially organize friction as a function of slope and has previously been established with different parameters for rill flow (Govers (1992)). We note that these studies were concerned with surfaces which had little to no vegetation influencing the resistance to erosion of the soil particles, meaning that morphological adaptations were predominantly due to surface runoff. In a similar fashion we did not account for vegetation and infiltration but should mention that

these processes would certainly affect the here presented steady state energy balance and its residual. Therefore, we stress that the presented distribution of potential energy is meant to approximate steady state runoff on equilibrium hillslopes with respect to frictional adaptation without vegetation and situations with significant infiltration excess runoff.

The resulting distributions reveal that on hillslope forms which relate to diffusive erosion (SC slope forms), $E_f^{pe,max}$ of surface runoff is found farther downslope, but with relatively larger magnitude than for forms related to advective erosion (SW). The net energy depletion zone on SC slopes depletes therefore for the same runoff more energy on shorter flow path distance than SW or RS slope forms, which implies larger bed stress. Energetically, this can be expressed as relative accumulated dissipation per energy influx D_f^{acc}/J_{in}^{acc}. Interestingly we find that hillslope forms that relate to soil wash convert a larger part of the energy influx into D_f than RS and SC related forms. This means that although absolute bed stress is larger for SC formations, SW forms maximize work per input energy, and are therefore more dissipative in relative terms. This makes sense as D_f incorporates energy needed for sediment detachment and transport and is in line with the theory that SW forms maximize kinetic energy per energy influx (Leopold and Langbein (1962)). From a thermodynamic perspective this corresponds to an increase of entropy, as energy can be distributed across more energetic states if the ratio D_f^{acc}/J_{in}^{acc} is larger. Similarly, the distribution of the derivative of D_f^{acc}/J_{in}^{acc} is almost uniform for SW forms (cf. grey, straight line in Fig. 2.5a), which relates to the equal energy expenditure hypothesis of optimal channel networks (Rodriguez-Iturbe et al. (1992)), as well as to a constant production of entropy per unit discharge (Leopold and Langbein (1962)).

Our assessment is based on an empirical relation between flow velocity and unit discharge and therefore does not provide closure to the energy balance. However, the Eq. 2.6 implicitly incorporates a spatial organization of relative friction (cf. 2.2.3) which in accordance with our results seems to be supported by thermodynamic theory. Reversely, we show that maximum power and equal energy expenditure per unit discharge for surface runoff on hillslopes should result in friction laws like the ones proposed by Govers (1992) and Nearing et al. (2017). In fact, the proposed slope-velocity equilibrium by Nearing et al. (2005) seems to be a natural outcome of the equal energy expenditure, maximum power and maximum entropy concepts.

Finally, we want to point out that along a similar line of thoughts Hooshyar et al. (2020) have recently shown that logarithmic mean elevation profiles of landscapes resemble the logarithmic mean velocity profile in wall bounded turbulence. The authors concluded that these logarithmic profiles are a consequence of dimensional length-scale independence, and therefore apply to different dynamical systems,

possibly also to the much smaller hillslope scale. As these profiles were observed at an intermediate region and therefore are spatially transient, we believe they might relate to the here proposed transition from energy production to energy depletion, inspired by the well-known energy cascade of turbulent kinetic energy (Tennekes and Lumley (1972)).
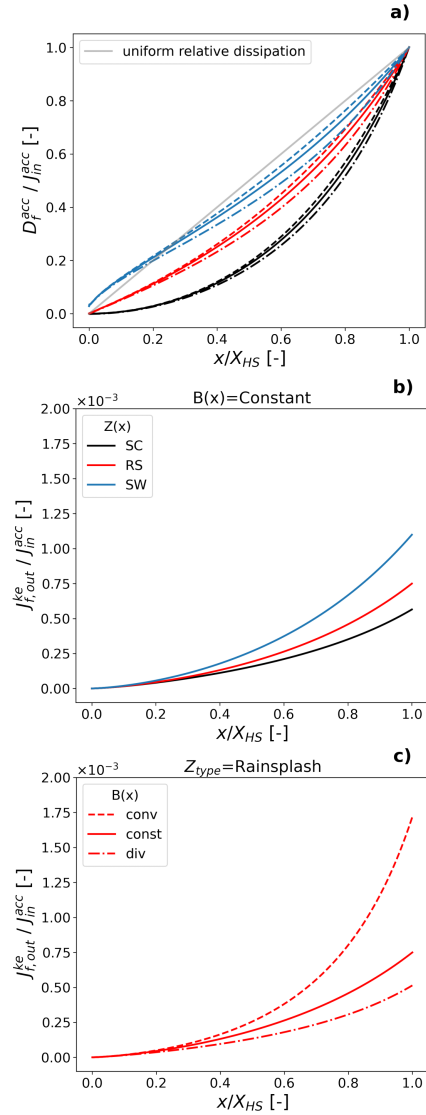
Figure 2.5: Spatial distribution of the ratio of a) accumulated dissipation and accumulated energy influx; b) kinetic energy outflux and accumulated energy influx for constant hillslope width but varying hillslope forms; c) kinetic energy outflux and accumulated energy influx for hillslope form related to rainsplash but varying hillslope width distributions.

We now explore the spatial distribution of potential energy in sheet and rill overland flow, which was observed during rainfall-runoff experiments carried out in the Weiherbach catchment (Gerlinger (1996)). Therefore, we built an extension to the physical hydrological model Catflow, which allows the accumulation of flow from sheet flow areas into rills (Catflow-Rill). As these experiments were performed on 12 m plots with a uniform slope they correspond to the rain-splash dominated hillslope type, as shown in Fig. 2.3b.

2.4.1 *Study area and experimental data base*

The Weiherbach catchment is an intensively cultivated catchment which is almost completely covered with loess up to a depth of 15 m (Scherer et al. (2012)). It is located in the Kraichgau region northwest of Karlsruhe in Germany. Because of the hilly landscape, the intensive agricultural use and the highly erodible loess soils, erosion is a serious environmental problem in the Kraichgau region. The Weiherbach itself has a catchment area of 6.3 km^2 and is around 4 km long. Elevation ranges from 142 m to 243 m above sea level; the slopes are long and gentle in the west, and short and steep in the eastern part of the catchment. The climate is semi-humid with a mean annual temperature of 10 °C (Scherer (2008)). More than 90% of the catchment area is arable land or pasture, 7% are forested and 2.5% are paved (farmyards and roads). Severe runoff and erosion events are typically caused by thunderstorms in late spring and summer, when Hortonian overland flow dominates event runoff generation (Zehe et al. (2001)). A comprehensive hydro-meteorological dataset as well as data on soil hydraulic properties, soil erosion, tracer and sediment transport are available for the Weiherbach (Scherer et al. (2012); Schierholz, Schäfer, and Kolle (2000)).

Here we analyse 31 rainfall simulation experiments (Gerlinger (1996); cf. Appendix A.1.4), which were performed to explore formation of overland flow and the erodibility of the loess soils (Scherer et al. (2012)). The rainfall simulators were designed to ensure both realistic rainfall intensities and kinetic energies on plots of 2 m by 12 m size. Rainfall intensity of experiments ranged between 34.4 to 62.4 $mm\ h^{-1}$. Runoff and sediment concentrations in overland flow samples were derived from samples taken during the experiments. We categorized an experiment as reaching steady state discharge if during the last time quarter, the relative change of discharge between measurements stays below 10% measurement error (Fig. 2.6a). Likewise, we proceeded to classify measured sediment concentrations (Fig. 2.6b). The final steady

state classification of each experiment per discharge and sediment concentration can be found in the supplemental data to this study. All but 5 experiments were classified as reaching steady state discharge (Fig. 2.6a) while only 9 were classified as reaching steady state sediment concentrations (Fig. 2.6b). This means that only experiments which reached steady state runoff as well as sediment concentrations can be considered as being truly in an energetic steady state (7 out of 31, cf. Appendix A.1.4). The different sites were characterized according to their antecedent soil moisture, soil texture and organic content in the upper 5-10 cm (Scherer et al. (2012)). Additionally, surface roughness (Manning's n) was estimated from the falling limb of the observed hydrograph (Engman (1986); Govers, Takken, and Helming (2000)). Observed rill flow velocities $v_{RF,obs}$ were measured by upslope tracer injection and correspond to the time it took until the peak of tracer concentration reached the plot outlet, while reported sheet flow velocities $v_{SF,obs}$ have been back calculated from measured runoff rates. Further details on the experimental setup are provided by Gerlinger (1996), Seibert et al. (2011), and Scherer et al. (2012). A first analysis of the data already reveals that experimental sites with a larger Manning's n correspond to a smaller ratio $v_{rat} = v_{SF,obs}/v_{RF,obs}$, suggesting that a larger roughness leads to stronger accumulation of runoff in rills. As will be shown, this in turn relates to the portioning of kinetic energy between sheet and rill domain.

2.4.2 *Model and model setup*

Next, we present an extension to the Catflow model (Zehe et al. (2001)), accounting for a dynamic link between sheet- and rill flow of surface runoff. The model has previously been extended, incorporating water-driven erosion (Scherer (2008)) and has been shown to successfully portray the interplay of overland flow, preferential flow and soil moisture dynamics from the plot to small catchment scales (Graeff et al. (2009); Loritz et al. (2017); Zehe et al. (2005); Zehe et al. (2013)).
A catchment is represented in CATFLOW by a set of two-dimensional hillslopes (length and depth), which may be connected by a river network. Each hillslope is discretized using curvilinear orthogonal coordinates; the third dimension is represented by a variable width. Subsurface water dynamics are described by Richard's equation, which is solved numerically by an implicit mass-conservative Picard iteration scheme. The simulation time step for soil water dynamics is dynamically adjusted to achieve an optimal change of the simulated soil moisture, which assures fast convergence of the Picard iteration. Soil hydraulic properties are usually parameterized using the van Genuchten-Mualem model (Mualem (1976); van Genuchten (1980)), but other options are available. Enhanced infiltrability due to activated macropore flow is conceptualized through enlarging the soil hydraulic
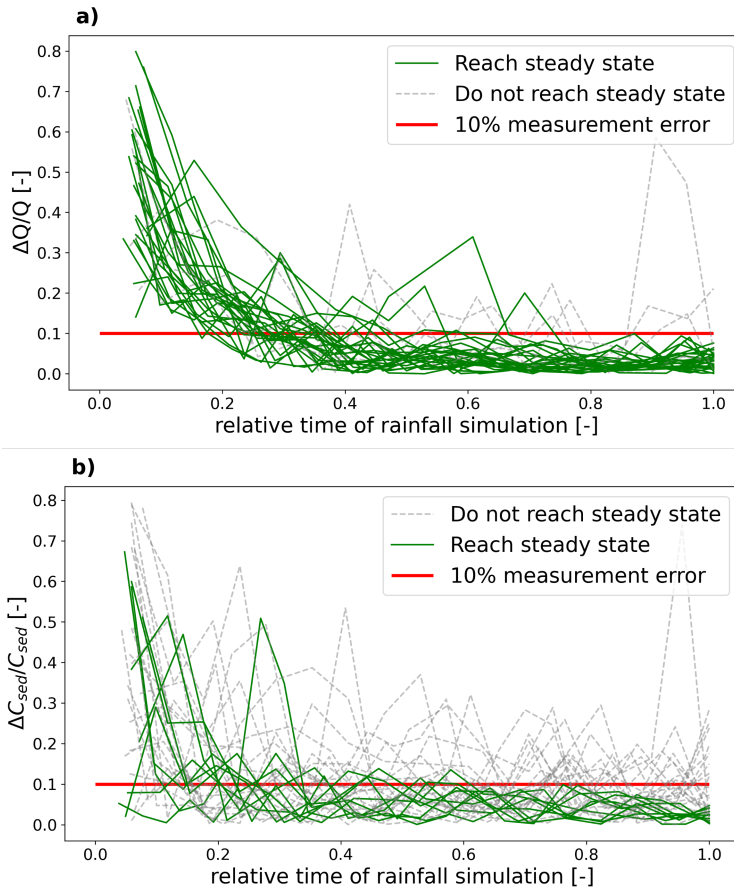
Figure 2.6: Classification of rainfall simulation experiments, green lines reach steady state during 0.75-1.0 of relative time of rainfall simulation: a) Relative change of discharge; and b) Relative change of sediment concentration

conductivity by a macroporosity factor f_{mak}, when a soil moisture threshold is exceeded. This approach is motivated by the experimental findings of Zehe and Flühler (2001a) and Zehe and Flühler (2001b) in the Weiherbach catchment and has been shown to be well suited for predicting rainfall-runoff dynamics (Zehe et al. (2005)) as well as tracer transport at the plot and the hillslope scales (Zehe and Blöschl (2004); Zehe et al. (2001)).

Representation of overland flow in Catflow and Catflow-Rill

Overland flow is simulated in Catflow-Rill with the diffusion wave equation, which is numerically solved using an explicit upstreaming scheme, a simplification of the Saint-Venant equations for shallow water flow, for details of the numerical scheme we refer to Scherer (2008). Flow velocity is calculated with Manning's equation (Eq. 2.5). The previous Catflow model assumes sheet flow only. To incorporate a rill domain that dynamically interacts with sheet flow, we conceptualise

the hillslope surface similar to the open book catchment (Wooding (1965)) as an open book hillslope (Fig. 2.7). In this configuration water may accumulate in a trapezoidal rill of width B_r in the middle of the open book hillslope with width B_{HS} and downslope length L_{HS}. Rainfall is added proportionally to the projected area along the flow path in both domains, resulting in spatially distributed sheet flow Q_{SF} and rill flow Q_{RF}. The link is established by a flow accumulation coefficient C_f (Eq. 2.14). This is visualized in 2.7 by the angle γ (in radians) between the vectors $\overrightarrow{Q_{RF}}$ and $\overrightarrow{Q_{SF}}$, which manifest at each point on the sheet flow surface the tendency of a volume water to flow downslope the hillslope gradient α or to follow the secondary flow accumulation gradient β (Eq. 2.15).

$$dQ_{link}(x) = Q_{SF}(x)C_f(x) \tag{2.14}$$

$$tan(\gamma) = \frac{\overrightarrow{Q_{RF}}}{\overrightarrow{Q_{SF}}} = \frac{\alpha}{\beta} \tag{2.15}$$

The maximum amount of flow which is transferred per unit flow path length from the sheet domain into the rill domain is then given by:

$$C_{f,max} = \gamma 2/\pi \tag{2.16}$$

However, depending on the configuration of the open book hillslope, we need to account for a flow path length L_{FC}, where flow accumulation becomes constant and maximum:

$$L_{FC} = B_{HS}tan(\gamma) \tag{2.17}$$

From hillslope top to the flow path length L_{FC}, the flow accumulation coefficient is linearly interpolated between $C_f(x = 0) = 0$ until $C_f(x = L_{FC}) = C_{f,max}$.

Model setup and calibration of flow accumulation

From the experimental database Scherer et al. (2012) created Catflow simulation setups, which were calibrated to reproduce runoff by adapting the macroporosity factor to scale infiltration capacity. The hillslopes were parameterized and initialized using observed data on average topographic gradient, plant cover, soil hydraulic functions, surface roughness, soil texture, and antecedent soil moisture. The models were driven by a block rain of the respective intensity and duration of the experiment. From here onwards subscript "sim" relates to the results of the presented calibrated numerical simulations. Hillslopes were discretized on a 2D numerical grid with an average lateral distance of 60 cm and vertically increasing distances starting with 1 cm at the surface and ending with 5 cm on the soil bottom. This resulted
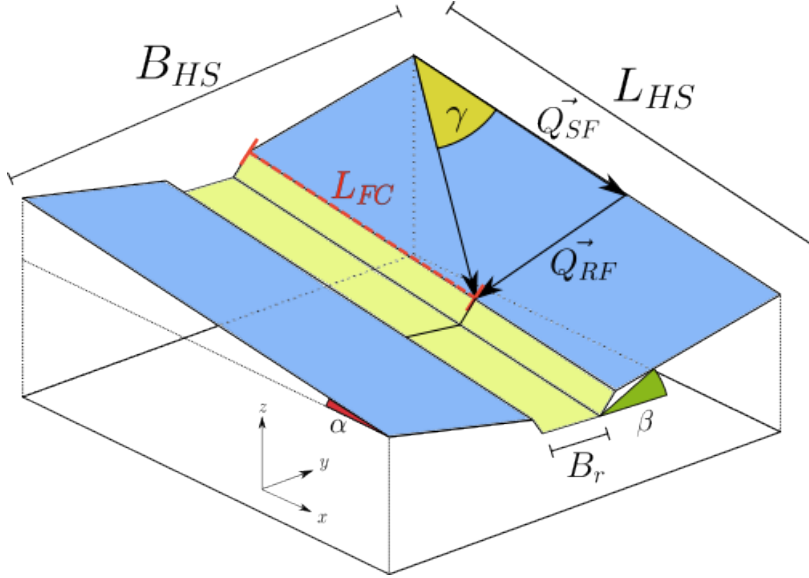
Figure 2.7: Representation of overland flow domains in Catflow-Rill as open book hillslope: Sheet flow domain (blue area) and Rill flow domain (yellow area).

TYPE	k_s [m s^{-1}]	θ_s [-]	Ψ_r [-]	α_s [m^{-1}]	n_s [-]	γ_s [-]
Calcaric regosol	$6.803*10^{-7}$	0.444	0.066	0.51	2.24	0.71

Table 2.3: Soil hydraulic parameters of Van Genuchten-Mualem model for simulated hillslopes, namely saturated hydraulic conductivity k_s, saturated soil moisture θ_s, residual soil moisture Ψ_r, reciprocal air entry point α_s, as well as soil hydraulic form parameters n_s and γ_s

in 21 x 29 computational points for 12 m long, 2 m wide and 1 m deep hillslope plots. Soil hydraulic parameters of the Van Genuchten-Mualem model were reported by Schäfer (1999), who conducted a soil hydraulic parameter campaign within the Weiherbach catchment and classified five homogeneous soil types. From these, parameters from the calcaric regosol soil type were used for the presented simulations (Scherer (2008)) in accordance with the location of the experimental plots within the catchment (see Table 2.3). Grain size distributions are available with mean particle diameters d_{50} between 20 to 70 μm (Scherer (2008); Appendix A.1.4).

To match the observed flow velocities, we adjusted the flow accumulation coefficient C_f, starting at 0.001 and incrementing in 0.001 steps, compared the steady state values of $v_{RF,sim}$ and $v_{RF,obs}$ and stopped the incrementation of C_f when the residual of both values was below 1% of $v_{RF,obs}$ (cf. Fig. 2.8b and d). Fig. 2.8 shows the result of selected calibration iterations for the representative experiments lek-2 and oek2-4 to highlight the sensitivity to flow accumulation. For experiment lek-2 (slope=0.163) significant rill flow was reported (Ger-

linger (1996)) with steady state rill runoff velocities ($v_{RF,obs}$=0.239 ms^{-1}) almost double the average sheet flow velocities ($v_{SF,obs}$=0.122 ms^{-1}). Contrarily, during experiment oek2-4 (slope=0.151) little to no rill flow was observed, manifesting in almost equal surface runoff velocities of $v_{SF,obs}$=0.142 ms^{-1} and $v_{RF,obs}$=0.15 ms^{-1} .For both hillslopes the calibration produced good results after few incrementing steps. For lek-2 this resulted in C_f=0.018 and for oek2-4 in C_f=0.0032 (Fig. 2.8a and c). Total mass is conserved as total simulated discharge $Q_{tot,sim}$ ($Q_{tot} = Q_{RF} + Q_{SF}$) stays constant independent of C_f for all simulations, while discharge in the rill domain grows with C_f. Except for the onset of surface runoff, $Q_{tot,sim}$ stays with 10% error tolerance bands of measured total discharge $Q_{tot,obs}$ for both experiments (compare Fig. 2.8a and c grey bands). While the observed rill flow velocities are matched well for both sites (lek-2 $v_{RF,sim}$=0.238 m s^{-1}, oek2-4 $v_{RF,sim}$= 0.15 m s^{-1}), computed sheet flow velocities exhibit small deviations from the observed values. One reason might be the approach to calculate of v_{SF} indirectly from measured total discharge and v_{RF} (Gerlinger (1996)), and the likely larger measurement errors. The final simulated steady state value of v_{SF} is however for both experiments within a 10% error margin, which is tolerable in the light of measurement uncertainty.

2.4.3 *Simulation results*

Flow accumulation in rills

Figure 2.9 shows that calibrated rill flow velocities match the observed values for all 31 experiments well (Fig. 2.9a). We also note that magnitude of rill flow velocity is correlated to flow accumulation, ranging from smallest $v_{RF,obs} = 0.11 \ ms^{-1}$,$C_f = 0.002$ to largest $v_{RF,obs} = 0.3 \ ms^{-1}$,$C_f = 0.024$. In line with the observations, simulated rill flow velocities are not correlated to slope (Appendix A.1.2). The resulting $v_{SF,sim}$ are close to observed sheet velocities, with 23 out of 31 lying within 10% measurement error (Fig. 2.9b, grey band). Outliers can partly be explained by classification of experiments reaching steady state runoff Q^{SS} and/or steady state sediment concentrations C_{Sed}^{SS} (cf. sect. 4.1 Fig. 2.6) and experiments which should be considered not steady state (Q^{NSS} and/or C_{Sed}^{NSS}, compare Fig. 2.9b). Simulations with largest inconsistency between $v_{SF,sim}$ and $v_{SF,obs}$ are either classified as Q^{NSS}(Fig. 2.9b, marker "x") or C_{Sed}^{NSS} (Fig. 2.9b, coloured red), or both. In general, the proposed flow accumulation model slightly underestimates sheet flow velocities. Finally, we find a strong correlation between C_f and the ration of sheet to rill flow velocity $v_{rat} = v_{SF,sim}/v_{RF,sim}$(Fig. 2.9c), which can be represented as a power law $v_{rat} = 0.11 * C_f^{-0.38}$ ($R^2 = 0.82$). In parallel we also find that Manning's n is positively correlated to C_f as well as v_{rat} (cf. Fig. 2.9c and Appendix A.1.2). Largest friction coefficients are therefore related to highest flow accumulation but lowest v_{rat} values.

Dissipation and erosion

In a similar fashion to comparison of relative dissipation along the typical hillslope profiles in 2.3.3, we calculate the kinetic energy export at the hillslope end in relation to the potential energy influx by rainfall and compare the relative contributions of rill flow and sheet flow. However, we can only confidently evaluate this for simulated experiments, which can be classified as steady state (for discharge and sediment concentrations; cf. Fig. 2.6) and where $v_{SF,sim}$ matches $v_{SF,obs}$ sufficiently well (Fig. 2.9b). Considering all these requirements results in only 5 out of 31 simulations for which we can confidently compare relative dissipation rates to potential energy influx by rainfall as defined in Eq. (2.18). Consequently, as we analyse energy relative to hillslope outlet, potential energy is assumed to be completely dissipated or exported as kinetic energy at the hillslope end, so that Eq. (2.13) can be written as:

$$D_f^{acc}/J_{in}^{acc} = 1 - J_{f,out}^{ke}/J_{in}^{acc} \tag{2.18}$$

J_{in}^{acc} implicitly incorporates rainfall intensity, slope and area of the hillslope and normalizes dissipation rates for comparison among
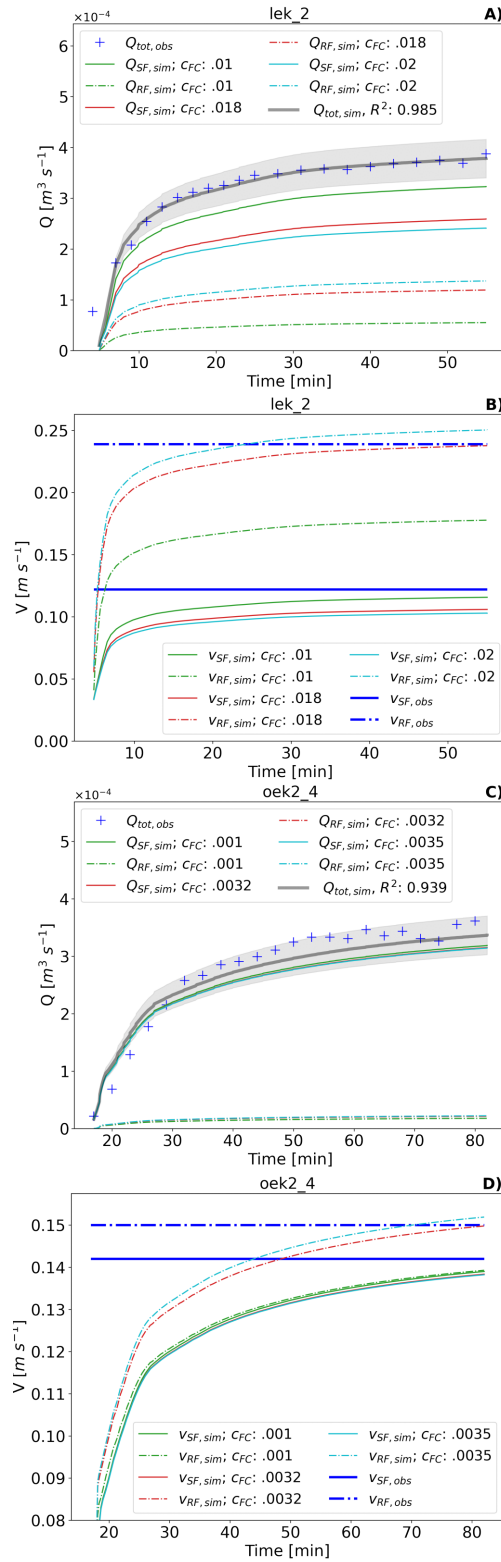
Figure 2.8: Results of calibrations runs for experiments lek-2 and oek2-4 :
a) and c) Calibrated total discharge $Q_{sim,tot}$, measured discharge
$Q_{tot,obs}$ (incl. grey 10% error band) and computed contributions
of sheet flow $Q_{SF,sim}$ and rill flow $Q_{RF,sim}$; b) and d) Observed rill
and sheet-flow velocities $v_{RF,obs}$ and $v_{SF,obs}$ and calibration runs
for different flow accumulation coefficients C_f
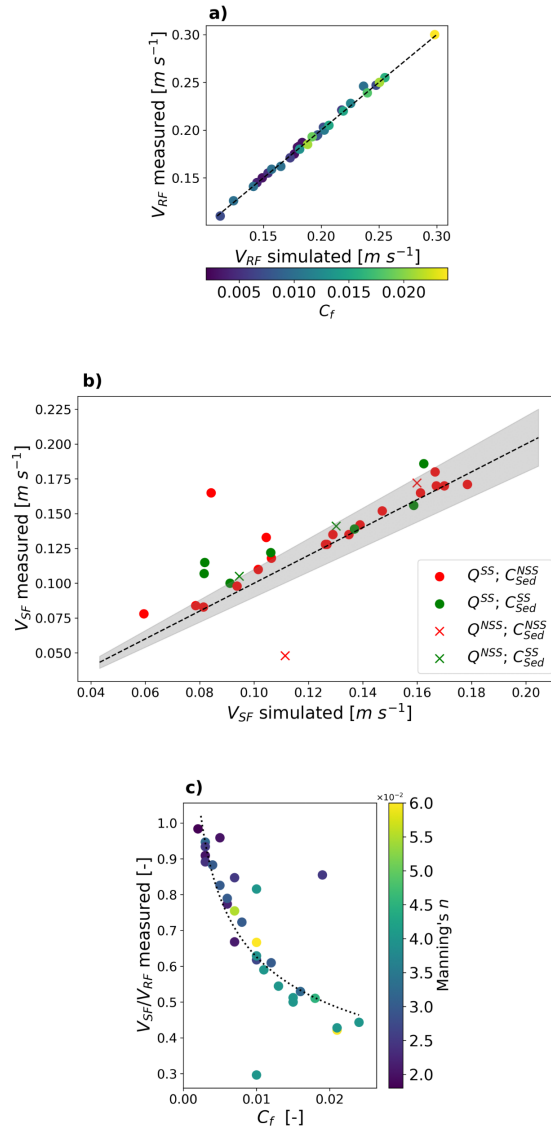
Figure 2.9: Results of calibration of flow accumulation to observed rill flow velocities: a) $v_{RF,sim}$ vs. $v_{RF,obs}$; b) $v_{SF,sim}$ vs. $v_{SF,obs}$; and c) C_f vs. $v_{rat} = v_{SF,sim}/v_{RF,sim}$

the selected experiments. Fig. 2.10a plots $J_{f,out}^{ke}/J_{in}^{acc}$ for the 5 trusted experiments (marked as "+", high confidence) as well as for the 26 remaining simulations (marked as circle, low confidence). For each simulation we plotted the relative contribution of sheet flow F_{SF} (blue) and rill flow F_{RF} (black) against flow accumulation coefficient, which sum up to total relative conversion rates of potential to kinetic energy. As the kinetic energy flux is proportional to Q^3(cf. Eq. (A5)b, $J_{f,out}^{ke} = f(Q^3)$), we analytically express F_{SF} and F_{RF} as cubic functions of accumulated discharge ($F_{RF/SF}(C_f)=a_1 C_f^3 + a_2 C_f^2 + a_3 C_f + a_4$) with C_f determining Q_{RF} and Q_{SF}. Fig. 2.10a presents for each domain F_{RF} and F_{SF} the fitted cubic function as well as their sum, which represents the total relative rate of kinetic energy export at the hillslope outlet as function of flow accumulation in the rill domain. It is interesting to note that both functions also capture a significant portion of points which have been ruled out due to lower confidence, and consequently were not included in the fit. As F_{SF} declines and F_{RF} increases with flow accumulation, total normalized kinetic energy export exhibits a distinct minimum value for C_f values in the range of 0.011 to 0.012 (Fig. 2.10a). This also corresponds to the region where relative kinetic energy export of rill flow $J_{RF,out}^{ke}$ and sheet flow $J_{SF,out}^{ke}$ are equal. According to Eq. (2.18) this equally means that the relative dissipation rate is maximized in this range of C_f values.

Spatial distribution of energy and flow regimes

The calibrated CATFLOW-Rill models also provide an estimate of the spatial distribution of energy for the rill- and the sheet- domains. Fig. 2.11a and b show the spatial distribution of potential energy E_f^{pe} (joule m^{-1}) and kinetic energy E_f^{ke} in each domain for an experiment with significant rill flow (lek-2, cf. Fig. 2.8). First, we note that both approaches of runoff calculation ($C_f = 0$ "and" $C_f = C_{calib}$) result in a local maximum of potential energy and that most energy is stored within the sheet flow domain. The rill simulation increases potential energy within the rill domain and decreases E_f^{pe} in the sheet flow domain. This happens non-linearly, meaning relatively more energy is transferred from the sheet to the rill flow domain downslope than upslope. As a result, the location of maximum potential energy is shifted in upslope direction and decreases in magnitude. The accumulation of runoff in rills leads to an increase of E_f^{ke} in the rill domain and contrarily a decrease of E_f^{ke} in the sheet domain in flow direction (Fig. 2.11b). For the calibrated experiment lek-2 kinetic energies of the two domains approach each other in downslope direction and are almost equal at the hillslope end. As potential energy is up to 1000 times larger in magnitude than kinetic energy, the sum of free energies $E_f = E_f^{pe} + E_f^{ke}$ is essentially equivalent to E_f^{pe}. We further find that
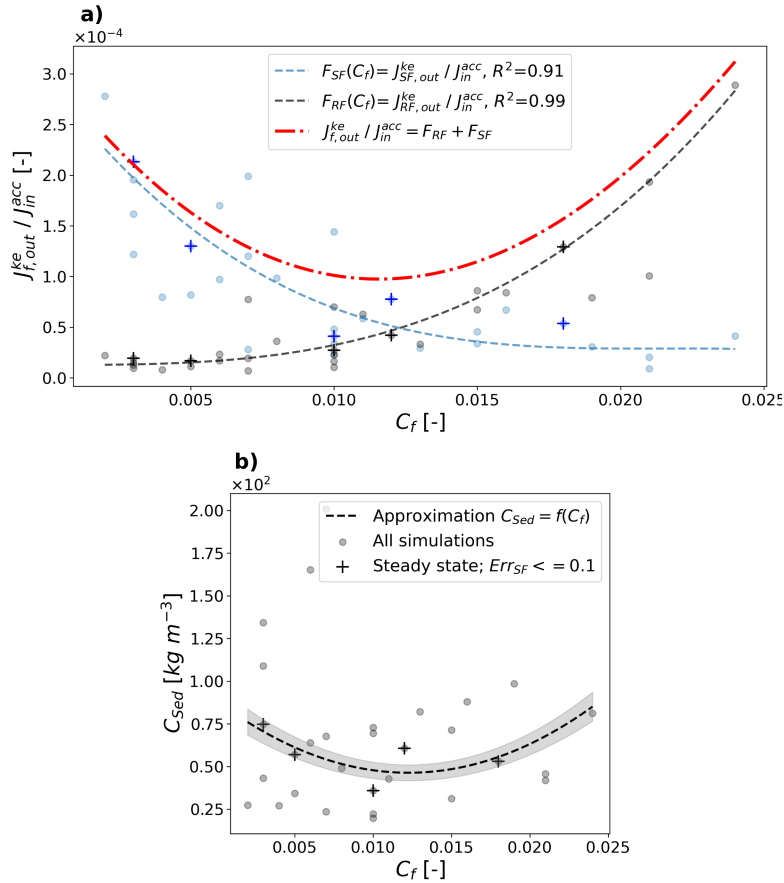
Figure 2.10: : a) Relative flux of kinetic energy at the hillslope outlet as a function of flow accumulation for rill domain (F_{RF}) and sheet domain (F_{SF}) as well as total relative flux ($F_{RF} + F_{SF}$); b) Measured sediment concentrations at hillslope outlet plotted against flow accumulation parameter C_f, simulations with $Err_{SF} = |v_{SF,sim} - v_{SF,obs}|/v_{SF,obs}$ below 10% and classified steady state are marked with "+".

the accumulation of flow in a rill reduces the total amount of energy being stored on the hillslope.

By comparing five experiments classified as steady state (cf. Fig. 2.10), we find that E_f^{pe} is shifted farther upslope for simulations with a) higher maximum potential energy and b) more runoff in rills (Fig. 2.12a). The latter becomes evident by estimation of Reynolds numbers of rill flow at the flow path length of maximum potential energy. Largest Re are found for energy distributions with the maximum occurring farther upslope and smallest Re are related to energy maxima appearing farther downslope. Computed Reynolds numbers at these maximum points range from 600 to 2100, which implies that the transition to turbulent or at least mixed flow regime is possible. Interestingly, the ratios of kinetic energy in sheet- to rill domain declines downslope and the gradient of the curve increases (Fig. 2.12b) when the location
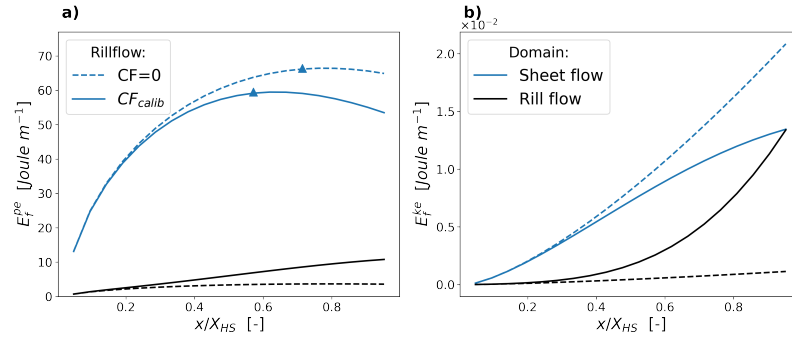
Figure 2.11: Spatial distribution of a) E_f^{pe} (maximum marked as Δ) and b) E_f^{ke} for calibrated rainfall runoff simulation "lek-2", separated into sheet- and rill flow

and magnitude of $E_f^{pe,max}$ is moving upslope. We observed that for one out of five experiments the ratio reached unity ($E_{SF}^{ke}/E_{RF}^{ke} = 1$), while for the others kinetic energy export in the sheet domain is dominant. We can therefore conclude, that from the presented simulations only experiments with significant rill flow approached unity within the 12m plot lengths, while the plot length is too small for a final conclusion on experiments with less flow accumulation.
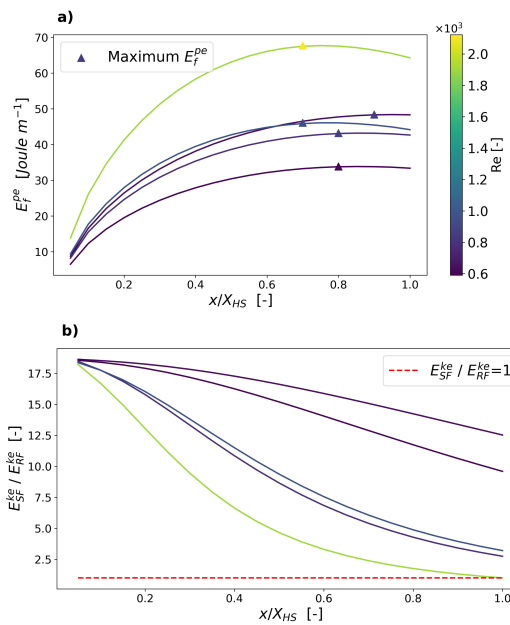
Figure 2.12: Spatial distribution of a) E_f^{pe} and b) E_{SF}^{ke}/E_{RF}^{ke} for considered experiments in the Weiherbach catchment (compare Appendix A.1.4); results are coloured by Re at hillslope distance of $E_f^{pe,max}$)

2.4.4 *Discussion*

Our approach to model the accumulation of surface runoff by a single rill and the calibration of a flow accumulation parameter resulted in partly good approximations of observed rill and sheet flow velocities and therefore justifies the presented simplification of surface runoff across two domains. Although the model uses a single friction coefficient (Manning's n), which is a simplification (cf. 2.2.3), flow accumulation in a rill and the opposite, flow dispersion of sheet flow led to spatially varying hydraulic radii, which imply variable friction along the hillslope. Manning's n which was determined for each experiment (Gerlinger (1996)) is therefore closely related to flow accumulation and the ratio of sheet vs. rill flow velocity. Our results show that a larger friction coefficient leads to relatively more flow accumulation in rills, a phenomenon which was also observed in field experiments by Abrahams, Parsons, and Shiu-Hung (1990). Some of the simulations performed poorly on estimating sheet flow velocity (cf. Fig. 2.9b and c), this can partly be explained by classification of experiments reaching steady state discharge and sediment concentrations during the interval of rainfall simulation. Other outliers could be related to tilling, which is common on the hillslopes in the Weiherbach catchment. We conclude that for such conditions, experiments would have to be conducted for much longer durations, allowing for imprinted topographical structures of farming practices to be reversed and natural rill networks to emerge. Rieke-Zapp and Nearing (2005) applied to laboratory plots of 4 by 4 meters rainfall with maximum duration of 90 minutes and results suggest that rills have not reached an equilibrium steady state. Although the field plots have certainly been impacted by previous rain events and are therefore closer to an equilibrium state than a plane of laboratory sand, in retrospective it is not possible to judge the degree of perturbation due to farming. Nevertheless, the experiments clearly indicate that sheet- and rill flow velocity are not a function of slope but depend on flow accumulation. Lowest flow velocities were observed for simulations with lowest C_f coefficient and correlate up to largest observed flow velocity and largest calibrated C_f (Fig. 2.9a; Appendix A.1.2). This is in line with the postulated slope-velocity theory on hillslopes (Govers, Takken, and Helming (2000); Nearing et al. (2005)), and to our belief, is the result of a feedback between friction coefficient and flow accumulation from sheet flow to flow in threads and then in rills.

Analysis of relative dissipation of energy per influx energy by rainfall reveals that surface runoff across rill and sheet domain is related to the existence of a maximum power state. For the analysed experiments we distinguished those which reached steady state discharge and sediment concentrations and calculated the kinetic energy per

influx energy that leaves the plot. For rill flow it can be shown that kinetic energy export increases with flow accumulation, while kinetic energy of sheet flow decreases with growing C_f. As expected, kinetic energy flux of both domains can be approximated by cubic functions of C_f. The sum of both represents the total outflux of kinetic energy per potential energy input, which is characterized by a distinct range of flow accumulation that minimizes normalized kinetic energy export. Within this range kinetic energy of both domains is approximately equal and dissipation, expressed as the energy balance residual, is maximum (cf. Fig.2.10a). This finding is very similar to theoretical elaborations by Kleidon et al. (2013) on surface runoff and sediment export at the catchment scale, with an accumulation of channel flow from overland flow areas in a certain number of channels. As the number of channels grows, the distance of overland flow into the channel decreases, resulting in an optimal channel number with minimum dissipation. The difference between our and Kleidon's argumentation is that tectonic uplift and the depletion of slope gradient is negligible on the small hillslope plots in the Weiherbach catchment. In contrast to the study by Kleidon et al. (2013) sediment export should therefore not be maximized but minimized, with metastable hillslopes being related to hillslopes with minimum to no erosion. An assessment of observed sediment concentrations on the experimental plots indeed seems to indicate that minimum C_{sed} might be related to minimum total kinetic energy per influx energy and therefore maximum relative dissipation (cf. Fig. 2.10b). In this sense the formation of rills is thermodynamically an expression of maximization of dissipation per influx energy from rainfall.

For the analysis of flow regime transitions (cf. hypothesis two), we plotted the Reynolds number of rill flow at the flow path distance where potential energy is maximum (cf. Fig. 2.12a). While some Re exceed the critical threshold for turbulence, others are below the value proposed by Emmett ($1500 < Re < 6000$). Yet, these low Re numbers might still relate to the onset of turbulent flow regime as reported mean particle diameters are very small ($20 < d50 < 70 \ \mu m$, cf. Appendix A.1.4) resulting for very shallow runoff depths in high relative roughness and consequently turbulent flow regime at lower Re. Although spatially distributed mean water depths were not part of the experimental data set, the results of the calibrated simulations clearly indicate that the distribution of potential energy relates to the transition from laminar to turbulent flow regime in downslope direction.
Potential energy in this section is based on a relative calculation of potential energy with the null level of the 12 m plots at the outlet of the Weiherbach catchment, which makes the results (Fig. 2.12) comparable. We argue that surface runoff on hillslopes in its simplest case can be

separated into sheet and rill flow and that the distribution of flow within both domains approaches over time a maximum power state (cf. Fig. 2.10a). At this state dissipation per driving gradient is maximized, while the ratio of kinetic energies approach unity. We found that two of the truly steady state as well as seven other experimental sites cluster in this area. In fact, we see very strong similarities to a maximum power state of an electrical circuit where the load resistance (in the case of surface runoff: the inverse of rill conveyance) has adjusted to meet the source resistance (the inverse of sheet flow conveyance, cf. Appendix A.1.3). This finding can also be corroborated from Fig. 2.10a, with minimum total flux of kinetic energy being related to equal fluxes of kinetic energy (and therefore also equal kinetic energies) across both surface runoff domains.

2.5 SUMMARY AND CONCLUSION

In this study we linked well-known processes of surface runoff (Shih and Yang (2009)), and erosion (Kirkby (1971); Beven (1996)) to thermodynamic principles (Kleidon (2016)) and theories derived thereof (Leopold and Langbein (1962); Rodriguez-Iturbe et al. (1992)). The geomorphological development, surface runoff and the dominant erosion process co-evolve. We could show that an approach to account for the energy conversion and dissipation rates is a helpful unifying concept. The core of this concept are the residuals of the observable, free energy fluxes and particularly their spatial distribution, which is key to evaluate empirical friction laws of surface runoff velocities in a thermodynamic framework. Although we do not provide a full closure of the energy balance of surface runoff, we were able to test and corroborate two hypotheses about the distribution of potential and kinetic energy of surface runoff and the related transition from laminar to turbulent flow, on two related hillslope scales. Hypothesis one states that surface runoff systems can be separated into an area of production- and an area of depletion of energy. Our second hypothesis relates the typical transitioning of flow (laminar to turbulent) and erosion (diffusive to advective type) regime to these zones.

In line with our first hypothesis, we showed that hillslopes as mass-accumulating systems are characterized by a distinct energetic behaviour: The trade-off between downslope mass gain and geopotential loss along a runoff flow path leads to a maximum of potential energy. We found that the location and magnitude of this maximum is a function of hillslope form and accumulated surface runoff. Specifically, we analysed the influence of typical hillslope macro-topographical profiles with a fixed accumulated runoff for the spatial pattern of overland flow energy. We found that hillslope forms which relate to diffusive erosion processes (soil creep SC) have an energetic maximum located farther downslope than hillslope profiles related to advective

erosion (soil wash SW). One might therefore be inclined to relate maximum dissipation rates to the former hillslope type SC as for our example more energy is depleted on a shorter flow path. However, in relative terms we see that SW forms have much larger dissipation rates than RS or SC forms, implying that dissipation is increased and even maximized as relative dissipation per unit flow path is close to unity. At the same time, SW forms also increase kinetic energy per influx energy, a criterium proposed by various authors for maximization of power (Kleidon et al. (2013)) as well as maximum entropy production (Leopold and Langbein (1962)). Referring to our second hypothesis, we interpret these findings as results of the transition of dominant energy conversion process of surface runoff. Hereby we present a theory why laminar flow regime should be related to sheet flow and mixed / turbulent flow is related to concentrated flow in rills and channels. For the second application of this study, we create an extension to the numerical model Catflow, which allows an adjustment of flow accumulation, by separating runoff into sheet and rill flow and dynamically linking both one dimensional flow domains. The calibration to observed rill and sheet flow velocities from rainfall simulation experiments in the Weiherbach catchments revealed distinct flow accumulation coefficients, which clearly relate to the distribution of kinetic energy of and the relative contribution to surface runoff from both domains. In fact, we showed that maximum relative dissipation rates are achieved when kinetic energy exports from both domains are equal. This can be interpreted as a maximum power state with minimum production of total kinetic energy and related experiments therefore result in minimum sediment concentrations.

For those experiments that reached an energetic steady state, our simulations show that the build-up of potential energy on hillslopes is likely to occur under laminar flow conditions, while decrease of potential energy along the flow path seems to be related to concentrated rill flow with Re reaching values which classify as mixed or turbulent flow regime. We evaluated the Re at the flow path distance with maximum free energy in the simulated rill domain and found that values range between 600 to 2300, which classifies as the beginning of mixed and turbulent flow, depending on relative roughness. Although the rill model is a simplification of surface runoff, the well-matched rill and sheet flow velocities suggest that the model captures both runoff processes effectively. The results therefore present a valid estimate of the onset of mixed and turbulent flow by relating flow concentration to the distribution of energy production and depletion zones along the hillslope. The measurements at hand are certainly not comprehensive enough to allow a final conclusion whether a maximum of free energy defines the onset of a turbulent flow regime, but specifically designed and carefully measured experiments might reveal further insight on this. We would like to stress that the theory presented here applies to

conditions where erosion is predominantly driven by surface runoff and not limited by vegetational and geological controls.

Our final comment is aimed at the common picture of runoff as a fixed volume of water losing energy by friction (e.g., Bagnold (1966)). We think that we have shown that this picture should be revised because a loss of mean flow energy does not necessarily imply an equal increase in production of heat but can also be translated into velocity fluctuations of turbulence or lift and accelerate sediment particles. All this affects real dissipation rates and needs to be considered if one ever attempts to depart from empirical friction laws of channel flow for estimation of surface runoff on hillslopes.

Part III

SURFACE RUNOFF ON HILLSLOPES - TRANSIENT EVENTS

This study is published in the scientific journal Hydrology and Earth System Science (HESS). The remainder of part III is a reprint of:

3

SURFACE RUNOFF ON HILLSLOPES- TRANSIENT EVENTS

ABSTRACT   Surface runoff over time shapes the morphology of the landscape. The resulting forms and patterns have been shown to follow distinct rules, which hold throughout almost all terrestrial catchments. Given the complexity and variety of the earth's runoff processes, those findings have inspired researchers for over a century, and they resulted in many principles and sometimes proclaimed laws to explain the physics that govern the evolution of landforms and river networks. Most of those point to the 1st and 2nd law of thermodynamics, which describe conservation and dissipation of free energy through fluxes depleting their driving gradients. Here we start with both laws but expand the related principles to explain the coevolution of surface runoff and hillslope morphology by using measurable hydraulic and hydrological variables. We argue that a release of the frequent assumption of steady states is key, as the maximum work that surface runoff can perform on the sediments relates not only to the surface structure but also to "refueling" of the system with potential energy by rainfall events. To account for both factors, we introduce the concept of relative dissipation, relating frictional energy dissipation to the energy influx, which essentially characterises energy efficiency of the hillslope when treated as an open, dissipative power engine. Generally, we find that such a hillslope engine is energetically rather inefficient, although the well-known Carnot limit does not apply here, as surface runoff is not driven by temperature differences. Given the transient and intermittent behaviour of rainfall runoff, we explore the transient free energy balance with respect to energy efficiency, comparing typical hillslope forms that represent a sequence of morphological stages and dominant erosion processes. In a first part, we simulate three rainfall-runoff scenarios by numerically solving the shallow water equations and we analyse those in terms of relative dissipation. The results suggest that older hillslope forms, where advective soil wash erosion dominates, are less efficient than younger forms which relate to diffusive erosion regimes. In the second part of this study, we use the concept of relative dissipation to analyse two observed rainfall runoff extremes in the small rural Weiherbach catchment. Both flood events are extreme, with estimated return periods of 10000 years and produced considerable erosion. Using a previously calibrated, distributed physics-based model, we analyse the free energy balance of surface runoff simulated for the 169 model hillslopes and determine the work that was performed on the eroded sediments. This reveals, that relative

dissipation is largest on hillslope forms which relate to diffusive soil creep erosion, and lowest for hillslope profiles relating to advective soil wash erosion. We also find that power in surface runoff and power in the complementary infiltration flux are during both events almost identical. Moreover, there is a clear hierarchy of work, which surface runoff expended on the sediments and relative dissipation between characteristic hillslope clusters. For hillslope forms that are more energy efficient in producing surface-runoff, on average a larger share of the free energy of surface runoff performs work on the sediments (detachment and transport) and vice versa. We thus conclude that the energy efficiency of overland flow during events does indeed constrain erosional work and the degree of freedom for morphological changes. We conjecture that hillslope forms and overland dynamics coevolve, triggered by an overshoot in power during intermittent rainfall runoff events, towards a decreasing energy efficiency in overland flow. This implies a faster depletion of energy gradients during events, and a stepwise downregulation of the available power to trigger further morphological development.

3.1   INTRODUCTION

Water-rock interactions, chemical weathering and fluvial erosion have relentlessly shaped our Earth over the past 3.8 billion years (Wolman M. G. and Miller J. P. (1960)). By performing physically work on the land surface, overland flow erodes and transports sediments, thereby shaping landforms and fluvial networks with distinct characteristics at almost any scale. Prominent examples thereof are expressed in Horton's laws of stream number, area and length (Shreve (1966)) or Hack's law about the upslope contributing catchment area and maximum stream length (Hack J. T. (1957)). Moreover, there is a distinct relation between the size and return period of flood peaks and the channel cross section (Leopold and Maddock T. (1953)), as well as shape and extend of the flood plain and sediment transport (Dunne et al. (1998)). At the hillslope scale, one can depending on the morphological age of the system observe typical hillslope forms. These reflect the dominant erosion processes of diffusive soil creep, rain splash and advective soil wash (Kirkby (1971) or Bonetti et al. (2020)). Thus, on the catchment as well as hillslope scale, surface runoff dynamics and geomorphic features are co-organized in a highly complex manner. Due to the complexity of these interactions and their multiple scale dependent manifestations many concepts to explain the co-evolution of surface runoff and landscape morphology are of semi-empirical nature. This implies that they partly rely on "tuning" parameters, which capture the relation between fluid flow and channel or hillslope geometry, as well as physical properties for a particular environmental and hydro-climatological setting and scale (Wolman and Gerson (1978); Beven

(1981)). However, despite of these obstacles, there has been continuous research to discover the seemingly hidden physical laws governing and constraining the co-development of form and functioning of the earth's hydrologic systems (Leopold and Langbein (1962); Yang (1971); Riggs (1976); Wolman and Gerson (1978); Dietrich et al. (1982); Howard (1990); Rodriguez-Iturbe et al. (1992); Perron, Kirchner, and Dietrich (2009)).

In line with the idea that morphological changes of the land surface require physical work (Wolman M. G. and Miller J. P. (1960)), these studies relate observed spatial patterns to the directed evolution of the system (river network, catchment or hillslope) towards a steady state optimum configuration. For these cases, optimality refers in some sense to the dissipation of free energy in an open system, leading in the context of a stream to the local maximization of stream power (Kleidon et al. (2013)) and to the minimum (free) energy expenditure of average discharge in the stream network as a whole (Rodriguez-Iturbe et al. (1992)). On the hillslope scale Zehe, Blume, and Blöschl (2010) and Zehe et al. (2013) showed that macropore flow patterns relate to maximum free energy dissipation and correspond to maximum entropy production (Leopold and Langbein (1962)). The fundamental reason why free energy can be dissipated and hence be lost to the process dynamics, arises from the 2nd law of thermodynamics. The latter states that entropy cannot be consumed, but it is produced during irreversible processes. At a very basic level this implies that fluxes deplete their driving gradients (and that water flows downslope). Although energy is conserved and cannot disappear due to the 1st law of thermodynamics, free energy is not a conserved property, but is dissipated during irreversible processes due to the related production of entropy. Free energy is basically energy without entropy, and the free energy of a flow system is thus equivalent to its capacity to perform work to steepen a concentration gradient (Zehe et al. (2021)) or to create motion in form of coupled water and sediment fluxes (Bagnold (1966)). Frictional dissipation during the latter implies production of heat through production of entropy, which increases the average kinetic energy of the molecules in the riverbed or the hillslope surface materials. As heat corresponds to a random isotropic motion of molecules it cannot be converted (back) into work to generate overland flow by cooling down the riverbed. While this would be consistent with energy conservation, it would violate the second law as it required consumption of entropy. Any increase in entropy of an isolated environmental system goes hence on the expense of a reduction of available free energy and the system's capacity to perform work. This implies that the system ends in a dead state called thermodynamic equilibrium where all gradients have been depleted, corresponding to minimum free energy and maximum entropy. Open thermodynamic systems may however prevail

in an organized state far away from the entropy maximum, if there is an external feedback sustaining a net influx of free energy to perform the necessary work to act against the depletion of gradients and to export the entropy produced during irreversible processes (Zehe et al. (2021)). In the following we want to clarify this aspect for surface runoff and related ideas of thermodynamic optimality, which appear to be contradictory at first sight.

The potential energy of water molecules and the related flux of potential energy is clearly larger at the upstream/upslope end of its flow path where the atmosphere re-delivers water via rainfall to the land, than at its downstream/ downslope outlet where water runs off to the sea/ or the river. This free energy difference is characterized by the geopotential gradient along the hillslope/ river course on one hand and the downstream/downslope accumulation of runoff/water mass on the other hand (Schroers et al. (2022)). Both factors jointly determine the maximum amount of work the system could perform in a mechanical sense (Gillett (2006)). We thus speak of the free energy of surface runoff. However, as pointed out by previous studies (Schroers et al. (2022); Loritz et al. (2019)) only a minute amount of this free energy is actually converted into work i.e., the kinetic energy of the coupled water and sediment flux, while the vast majority has dissipated at the downstream/downslope outlet. Recalling the concept of energy efficiency, which relates the work per time i.e., the power produced by a heat engine/ power plant to the energy influx, surface runoff has a very low energy efficiency, at least during steady state flow conditions. This is striking, because the energy efficiency of surface runoff is not limited by the well-known Carnot limit. The latter is generally valid for heat engines, and it also limits turbulent fluxes of sensible heat in the atmosphere (Kleidon and Renner (2018); Conte et al. (2019)). Runoff is however not driven by a temperature gradient but a gradient in geopotential. Rainfall and tectonic uplift distribute water and sediments against the geopotential gradient, thereby maintaining a permanent disequilibrium in the coupled water and sediment cycles in river basins by "refueling the catchment engine". These open systems can hence evolve towards an optimal configuration far from the entropy maximum (Kleidon (2016)): the periodic and intermittent input of free energy by rainfall results in co-adaptive development of the internal structure and the space-time pattern of water and sediment fluxes. In this context Leopold and Langbein (1962) put the river in analogy to a chain of heat engines and showed that maximization of entropy production by stream flow must result in an exponential geo-potential profile of a river's course through the landscape, which can indeed be found for many rivers (Langbein (1964); Tanner (1971)). While this study is certainly a landmark and the analogy is appealing, the reasoning is not fully consistent, as runoff

is not driven by temperature gradients and the Carnot limit does not constrain energy efficiency. Later onwards, Yang (1971) introduced the minimum stream power theory, which was placed on the minimum entropy production concept proposed by Prigogine and Wiame (1946) in physical chemistry. Rodriguez-Iturbe et al. (1992) extended this work to the theory of optimal channel networks by postulating three principles: (1) the principle of minimum energy expenditure in any link of the network, (2) the principle of equal energy expenditure per unit area, and (3) the principle of minimum total energy expenditure in the entire river network. These principles apply to steady state and thus average discharge conditions, which assures that the constraints of a closed catchment water balance is fulfilled. The inconsistency here is that bank full discharge corresponds according to Wolman M. G. and Miller J. P. (1960) to the two to ten years flood and not to average discharge. If the channel is formed by fluvial erosion, this implies that the kinetic energy balance of the sediments is not included in this theory, as average discharge is less than bank full discharge. In a later work Wolman and Gerson (1978) extended the idea to effective landscape forming events and added the notion that dynamic thresholds determine the effectiveness of a runoff event, leading to event sequencing (Beven (1981)).

More recently, Kleidon et al. (2013) applied the maximum power principle, originally proposed by Lotka (1922), to river systems and proposed that those develop to a state of maximum power in the coupled water and sediment flux. They argued, while the driving geopotential gradient is depleted at the maximum rate, the associated sediment export maximizes with the same rate. The weakness of this analysis was to treat the catchment as runon-runoff system, where water is added at the uppermost stream segment as a constant discharge along the course of a river. Catchments are however mass accumulative because they receive their rainfall in a spatially distributed manner, resulting in downstream growth of stream flow (Schroers et al. (2022)). This means that in the upper part of the slope/catchment potential energy of surface runoff grows in downslope direction to a local maximum and declines afterwards. Moreover, maximum power in the combined sediment-water flux does in steady state correspond to maximum entropy production. This idea hence seems to contradict the idea of minimum energy expenditure assuming minimum entropy production.

These apparent contradictions can be explained by at least two pitfalls that emerge, when working with the analogy to heat flows and entropy production in geosciences. First, there exist at least three forms of physical entropy (not to mention information entropy), (cf. Popovic (2017)) namely thermal entropy produced by depletion of temperature gradients, molar entropy produced by mixing and depletion of

chemical potential and geo-potential gradients, and radiation entropy produced by radiative cooling (Kleidon (2016), Zehe et al. (2021)). And second, a proper definition of entropy production requires a clear definition of the system and its boundary, otherwise "Nobody really knows what entropy is" (Von Neumann, cited in Tribus and McIrvine (1971)). In this light, minimum energy expenditure refers to the production of thermal entropy through friction, which shall be minimized in the entire network. Minimum dissipation results in maximum power of stream flow, as energy is conserved. This implies in turn a maximum flux of water (and sediments) and thus maximum production of molar entropy. We therefore very much agree with e.g. Kleidon (2016) that an exact definition of the system and a proper terminology which kind of entropy is produced in which part of the system, resolves these apparent contractions.

In line with these thoughts, we propose here that the concepts of free energy, work and energy efficiency are much more suited for analyzing the interplay of (land-) form (-s) and functioning of overland flow systems. Starting point is our previous work (Schroers et al. (2022)), which revealed that the aforementioned morphological stages and related typical hillslope forms, do not only reflect the transition of the dominant erosion processes from diffusive soil creep, over mixed behavior to advection dominated soil wash (Kirkby (1971)), but are also a manifestation of a hierarchy of energy efficiency of overland flow. This can be explained by the fact that a change of the longitudinal hillslope profile affects not only the driving geo-potential gradient, but also the amount of rainfall that is locally intercepted by the projected area on the horizontal axis. We defined relative dissipation as dissipated fraction of free energy of overland flow, normalized by energy influx due to precipitation. Relative dissipation was largest for hillslope profiles relating to soil wash erosion and minimum for profiles where soil creep dominates. This suggests that hillslope forms develop towards smaller energy efficiency in overland flow, meaning that a larger fraction of the energy influx is dissipated for hillslopes which are closer to a dynamic equilibrium than for hillslopes which are far away from an equilibrium. In consideration of the effectiveness concept of hydrological events, coined by Wolman and Gerson (1978), relative dissipation also captures the notion of dynamical thresholds (cf. Beven (1981)) and beyond that gives us a useful starting point for a thermodynamic evaluation of these. We furthermore showed that the emergence of rills increases the power and thus the energy efficiency in steady state overland flow, but also relates to larger friction coefficients which in turn limit overall energy efficiency. This feedback resulted in maximum relative dissipation or equivalently minimum relative free energy at the outlet and showed a correlation with sediment transport rates. Here we step beyond this analysis by releasing the steady state

assumption, which is rarely fulfilled during natural rainfall events. This is particularly true for hillslopes because overland flow events are intermittent. It is important to extend our concept to transient conditions, because in steady state dissipation in overland flow is almost equal to the power input. Structural development needs however work and thus an overshoot in power, meaning a certain resistance threshold must be exceeded for effective erosion events (Wolman M. G. and Miller J. P. (1960)).

Steady state hydraulic conditions imply time invariant flow depths (Chow (1959)). This is seldomly achieved in natural streams and practically non-existent for overland flow and surface runoff on hillslopes (cf. Dunne and Dietrich (1980); Emmett (1970)). Yet, most laboratory (Giménez and Govers (2002); Rieke-Zapp and Nearing (2005)) and field experiments (Nearing et al. (1997)) studying surface runoff on hillslopes have been set up in a way to reach steady state conditions and conclusions are drawn from adaptations to this state. Time is even more important, when considering the interaction of the water fluid with sediments. For rivers it is well known that sediment transport is directly coupled to unsteady state flood waves, which trigger the detachment of larger particles leaving smaller particles unprotected and prone for transport (Gob, Bravard, and Petit (2010)). Similar behaviour was shown by Kinnell (2020) for hillslopes, where the onsets of particle detachment and transport are distinctly linked to different points in time during surface runoff events. Importantly, steady states considering coupled fluid and sediment fluxes differ considerably from those dealing only with fluid flow. This is firstly due to the transport mechanism which governs sediment travel times and can lead to much slower sediment particle velocities than water flow. And secondly, transient loads of suspended particles imply a changing fluid density, even if fluid and particle velocities would not change with time. A true steady state is therefore not achieved until the slowest moving particle detached at the point farthest from the discharge point is discharged at the outlet and a continuous steady sediment transport is reached. This requires obviously periods of time invariant rainfall, otherwise transport and therefore time of concentration of sediment discharge might be altered.

This study has hence two objectives. First, we expand our thermodynamic framework for analysing the free energy balance of transient surface runoff and sediment flows using measurable hydraulic flow parameters. To this end, we simulate surface runoff events using the above mentioned characteristic 1D hillslope profiles, which relate to different dominant erosion and relative dissipation regimes. We use the 1D shallow water equations for this purpose, because they do not rely on a quasi-steady state momentum balance, and we apply a finite

difference McCormack time diminishing variation (TVD) scheme to numerically solve it. The benefit from this is a more accurate simulation of flow velocities and thus kinetic energy, which assures a more reliable calculation of the transient free energy balance of surface runoff, as well as the related energy efficiency to test our hypothesis about a power maximum in time. In a second part of the paper, we apply our theory to two rainfall runoff extremes observed in the Weiherbach catchment. To this end we employ an existing setup of the Catflow model (Zehe et al. (2005)), representing the catchment by 169 typical hillslopes, accounting for the pattern of crops and their roughness, and an interconnected river network. We use this simulated surface runoff for comparing relative dissipation and erosion patterns between characteristic hillslope types. Although the morphological development in the Weiberbach catchment has been affected by anthropogenic land use, we hypothesize that specific hillslope morphologies show distinct fingerprints of relative dissipation and power of transient surface runoff as well as sediment transport.

3.2 THEORY

3.2.1 *The hillslope as open thermodynamic system*

The theory and applications of this paper are an extension to our first publication (Schroers et al. (2022)) regarding steady state dissipation regimes. Therefore, we present here the final equations only and refer to our study for details. In general, we represent the hillslope surface as an open thermodynamic system (OTS) (Kleidon (2016), Zehe et al. (2013)), which exchanges mass, momentum, energy, and entropy with its environment. The boundaries of the system are a subjective choice, depending on the type and objectives of the analysis and are defined here as the hillslope surface without its subsurface soil structure (compare e.g., Zehe et al. (2013)), starting at the topographic divide upslope and ending at the drainage channel downslope. Within these boundaries, we set surface runoff into a thermodynamic perspective and apply the first and second law of thermodynamics, which constitute that energy is conserved and entropy of an isolated system can only grow (Kondepui and Prigogine (1952)). We start with the assumption that a hillslope can be defined as a spatially integrated OTS, here denoted by the subscript HS (cf. Fig. 3.1).
Energy dynamics of this OTS black box are therefore driven by a single representative influx of potential energy $J^{pe}_{HS,in}(t)$ in watt, on hillslopes in the form of rainfall, which leads to spatial gradients of geopotential of water. Over a certain flow path distance LHS, these gradients are then converted into kinetic energy $E^{ke}_{HS}(t)$ in Joule (surface runoff) and heat, which is composed of changes in temperature and entropy. These

spatial dynamics in time lead to Eq. 3.1, with net potential energy flow $J^{pe}_{HS,net}(t)$ (watt) (Eq. 3.3), either increasing potential energy of the system $E^{pe}_{HS}(t)$ or powering the creation of another type of energy $P_{HS}(t)$ (watt). Eq. 3.2 details how $P_{HS}(t)$ either leads to the creation of kinetic energy or dissipation $D_{HS}(t)$. Additionally, net kinetic energy flow $J^{ke}_{HS,net}(t)$ accounts for the net gain or loss of kinetic energy flow of the system. Eq. 3.1 to 3.4 are a simplification of surface runoff, as we do not consider other types of energy than potential and kinetic energy of water. For the here presented applications however all other energy types can be considered negligible.

$$\frac{dE^{pe}_{HS}(t)}{dt} = J^{pe}_{HS,net}(t) - P_{HS}(t) \tag{3.1}$$

$$\frac{dE^{ke}_{HS}(t)}{dt} = P_{HS}(t) - D_{HS}(t) - J^{ke}_{HS,net} \tag{3.2}$$

$$J^{pe/ke}_{HS,in}(t) - J^{pe/ke}_{HS,out}(t) = J^{pe/ke}_{HS,net}(t) \tag{3.3}$$

In combination Eq. 3.1 and 3.2 lead to Eq. 3.4, which relates in- and output of energy of a system with the energy stored within the system.

$$\frac{dE^{pe}_{HS}(t)}{dt} + \frac{dE^{ke}_{HS}(t)}{dt} = J^{pe}_{HS,net}(t) + J^{ke}_{HS,net}(t) - D_{HS}(t) \tag{3.4}$$

For a rainfall runoff event the black box OTS (Fig. 3.1, Eq. 3.4) of a hillslope surface can be further simplified. We assume that the system receives on its upper end a constant potential energy inflow $J^{pe}_{HS,in}(t)$ and releases a time dependent energy outflow at the lower end. We assign the lower end a bed level of zero, which makes the specific geopotential of the lower boundary flux only dependent on the water depth. In this case we regard the potential energy which enters the system much larger than the potential energy which leaves the system and therefore also $J^{pe}_{HS,out}(t)$ (watt) to be negligible. The kinetic energy flow at the inflow boundary is also assumed to be zero and temporal gradients are abbreviated by dot notation (e.g.,$dE^{pe}_{HS}/dt = \dot{E}^{pe}_{HS}$) so that we can write the reduced equation 3.4 as:

$$D_{HS}(t) = J^{pe}_{HS,in}(t) - \dot{E}^{pe}_{HS}(t) - J^{ke}_{out}(t) - \dot{E}^{ke}_{HS}(t) \tag{3.5}$$

Each of the terms of Eq. 3.5 shall be derived from integration of spatially distributed hydraulic flow variables. For a detailed calculation of spatially distributed steady state dynamics, we refer to Schroers et al. (2022), and for the derived transient system a summary is presented in Appendix A.1.1.

From Eq. 3.5 we deduce that a transient system has several degrees of freedom to in- or decrease dissipation rates (or free energy respectively), whereas a steady state system can only adjust the outflux of kinetic energy (J_{out}^{ke}). For the transient case, the influx potential energy can also be converted into potential and kinetic energy, stored within the system itself. For a constant energy influx, power can e.g., be maximized through minimization of increases in E_{HS}^{pe}, meaning less influx energy is converted into potential energy and more into kinetic energy. It is therefore possible that a system maximizes power whilst also minimizing dissipation. It is tempting to think that this simplification holds for discrete timesteps, but as natural systems are highly transient it seems more likely that total dissipation in time or a maximum value during a concrete time-interval might be optimized. If a system receives a certain amount of energy influx, it is therefore clear that optimization must happen through adjustment of the internal spatial structure which determines temporal derivatives of free energy conversion rates. Previously (Schroers et al. (2022)) we assumed the system to be in steady state and analysed the local adjustment of free energy conversion rates. Dissipation can be minimized by geomorphological adaptations of the hillslope surface optimizing loss of energy per wetted cross section. For a transient event we integrate over a spatial domain and have an additional degree of freedom as energy can be stored in time. We therefore expect that the structure of hillslopes is not a result of a steady state but rather an outcome of many transient events (cf.Wolman and Gerson (1978)), during which free energy gradients are depleted as fast as possible.

3.2.2   *Relative Dissipation of surface runoff*

As hillslopes vary spatially in vertical as well as horizontal length scales and surface runoff events vary in time, absolute values do not represent relative dynamics of the energy balance and need to be normalized for comparison. Starting with Eq. 3.5, we first calculate the accumulated dissipation D_{HS}^{acc} (joule, Eq. 3.6) for an event from $t = 0$ to tl and then normalize by the influx of energy $J_{HS,in}^{acc} = \int_{t=0}^{tl}(J_{HS,in}^{pe}(t))dt$ which is accumulated at time tl (Eq. 3.7).

$$D_{HS}^{acc} = \int_{t=0}^{tl}(J_{HS,in}^{pe} - \dot{E}_{HS}^{pe} - \dot{E}_{HS}^{ke} - J_{HS,out}^{ke})dt \tag{3.6}$$

$$\hat{D}_{HS}(t) = \frac{D_{HS}^{acc}}{J_{HS,in}^{acc}} = 1 - \frac{\int_{t=0}^{tl}(J_{HS,in}^{pe}(t) - \dot{E}_{HS}^{pe}(t) - J_{out}^{ke}(t) - \dot{E}_{HS}^{ke}(t))dt}{J_{HS,in}^{acc}} \tag{3.7}$$

$\hat{D}_{HS}$ is dimensionless (*joule joule*$^{-1}$) and represents a thermodynamic descriptor for a spatially defined system which can be analysed
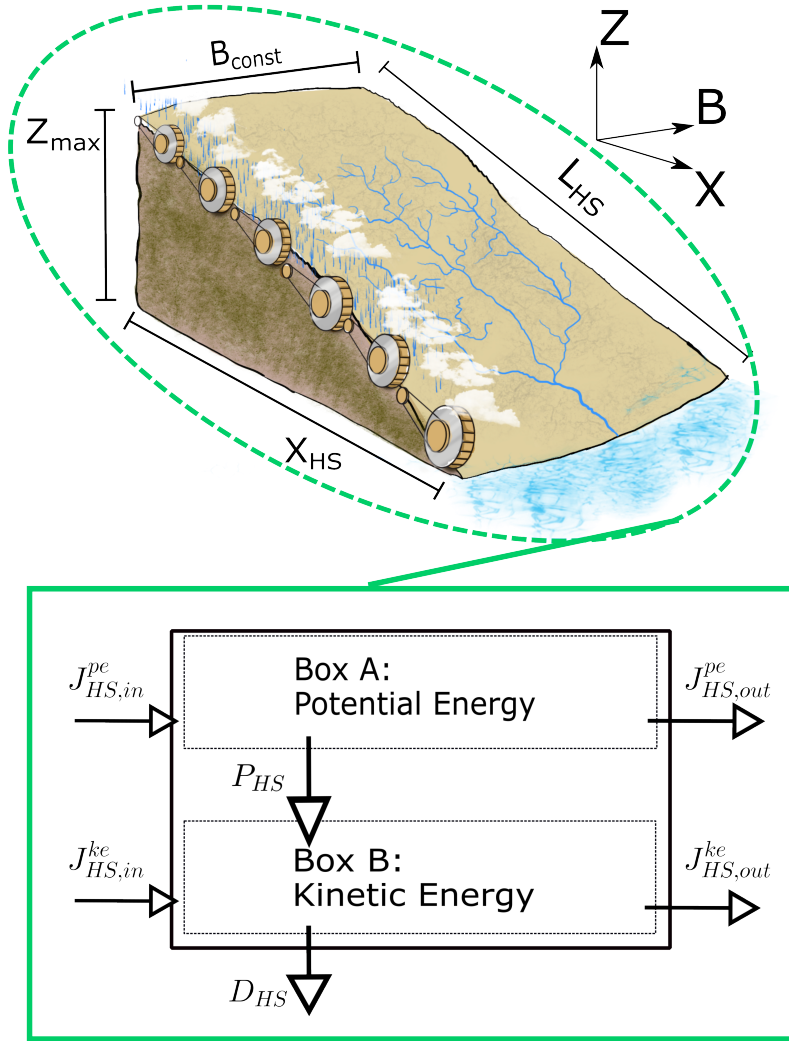
Figure 3.1: Representation of energy conversion processes of surface runoff on hillslopes for a spatially integrated system

in time for a given rainfall-runoff event. In the following we apply Eq. 3.7 for comparison of relative dissipation rates for characteristic hillslope profiles. The energy influx normalization is useful as it allows a comparison of different transient rainfall-runoff events independent of absolute rainfall rates and vertical as well as horizontal hillslope lengths. The second term on the right side of Eq. 3.7 can also be termed energy efficiency of overland flow, a larger value leads to less relative dissipation and reversely a lower value increases $\hat{D}_{HS}$. Maximum relative dissipation is therefore related to minimum energy efficiency. Additionally we define relative stored energy $\hat{E}_{HS} = \int_{t=0}^{tl} (\hat{E}_{HS}^{pe} + \hat{E}_{HS}^{ke})/(J_{HS,in}^{pe}) dt$ as well as relative energy flux at the hillslope foot as $\hat{J}_{HS} = \int_{t=0}^{tl} (J_{HS,out}^{ke})/(J_{HS,in}^{pe}) dt$, leading to a shortened version of Eq. 3.7: $\hat{D}_{HS} = 1 - \hat{E}_{HS} - \hat{J}_{HS}$.

3.3   ENERGY EFFICIENCY OF TRANSIENT OVERLAND FLOW AS A FUNCTION OF HILLSLOPE FORM AND EROSION PROCESS

In this first part of the study, we test our hypothesis that the evolution of landscape forms is directly linked to energy efficiency of transient overland flow events. In its simplest form, the distribution of geopotential gradients can be related to prevalent erosion processes, ranging from very diffusive erosion regimes (soil creep, rain splash) to more advective flow regimes (soil wash, river flow) (Kirkby (1971)). These erosion regimes are per definition directly linked to the effectiveness of overland flow to erode and transport soil particles. Soil creep related hillslopes are therefore likely to have seen significant overland flow less frequently and on smaller magnitudes, while the opposite can be said of hillslopes related to soil wash. This hierarchy should consequently translate into differences in energy conversion rates, resulting in some optimization with regard to overland flow on soil wash related profiles. To test this idea, we use the existing theory about erosion processes and hillslope form to construct characteristic 1D hillslopes and analyse overland flow scenarios on these within the context of energy efficiency. Transient overland flow is modelled by numerically solving the 1D Saint Venant equations through a McCormack scheme (Liang, Falconer, and Lin (2006)) on a space time grid.

3.3.1   *Erosion process and hillslope form*

Quantitative geomorphological modelling is concerned with the development of landforms, given some initial and idealized boundary conditions (e.g. Willgoose, Bras, and Rodriguez-Iturbe (1991); Perron, Kirchner, and Dietrich (2009)). Typically, the form of a hillslope is being modelled by solving partial differential equations of sediment and water mass conservation, coupled by semi-empirical transport laws (Beven (1996)). The parameters of these laws are usually derived from data and reach explicatory value by relating certain parameter combinations to prevalent erosion- and transport processes. In its simplest form sediment transport capacity C is at least dependant on accumulated discharge and local gradient $C = Q^m S^n$. Although the range of (m, n) combinations is broad, we assume the ranges, mentioned by Kirkby (1990, cited in Beven (1996)) to represent the underlying erosion- and transport processes (Fig. 3.2a). With the model provided by Kirkby (1971), the erosion processes of diffusive soil creep, rain splash, soil wash, and advective river transport result in typical 1D hillslope profiles given by Eq. 8 and shown in Fig. 3.2b. The profiles reflect also the theory from Tarboton, Bras, and Rodriguez-Iturbe (1992) that within a catchment context hillslope processes can be attributed

to convex profiles (more diffusive than advective erosion processes) and channels to concave profiles.

$$Z_{typ}(x) = Z_0 * (1 - (\frac{x}{x_{HS}})^{(1-m)/(1+n)})$$ (3.8)

Eq. 3.8 is valid for the transport limited case and a hillslope with a close to constant width along the flow path.
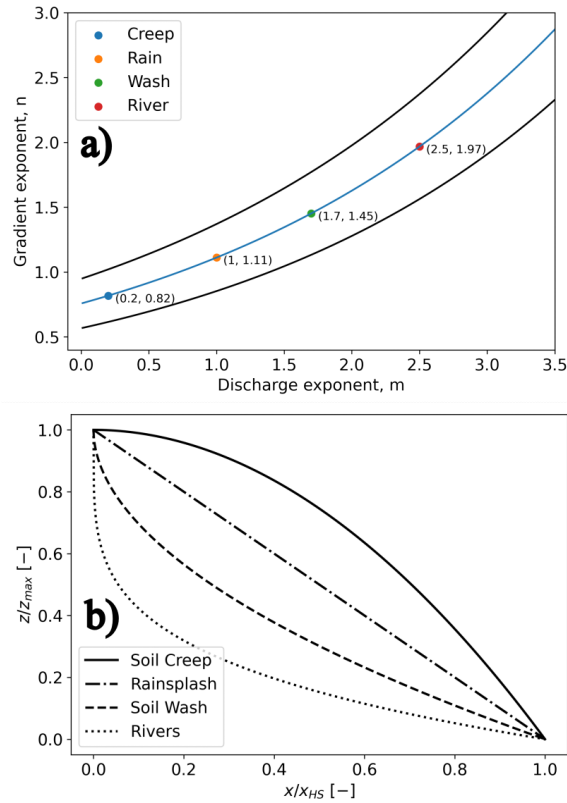
Figure 3.2: a) Parameter ranges for typical erosion processes (Beven (1996)); b) Resulting 1D profiles for highlighted parameter combinations

In our previous study we have already shown that convex profiles maximize dissipation of surface runoff per input flux of energy (precipitation) whilst also showing maximum rates of kinetic energy export at the downslope end. This is possible as kinetic energy is on a scale of 1000 times smaller than influx potential energy, therefore not significantly affecting the overall energy balance of a hillslope profile. In this context we extend this steady state analysis to account for the transient state of surface runoff and analyse maximum power and total work during a full surface runoff event. For simulation of these rainfall-runoff events, we implemented a solver of the 1D St. Venant equations for viscous flow and analysed the hydraulic variables on a space-time grid. The events were simulated for soil creep (SC) and soil wash (SW) profiles as their distributions of geopotential gradient show largest differences.

3.3.2   *Numerical model for transient surface runoff*

The simulation of surface runoff on 1D hillslope profiles, related to the erosion processes was done by numerical approximation of the system of equations, known as the shallow water equations. In this study we solve the conservative form of the 1D mass and momentum equations:

$$\frac{\delta X}{\delta t} + \frac{\delta F}{\delta x} = S \tag{3.9}$$

where

$$X = \begin{bmatrix} H \\ q \end{bmatrix} \quad F = \begin{bmatrix} q \\ \frac{\beta q^2}{H} + \frac{gH^2}{2} \end{bmatrix} \quad S = \begin{bmatrix} I \\ gH\frac{\delta z}{\delta x} + gq|q|\frac{n^2}{H^{7/3}} \end{bmatrix}$$

We applied a finite difference time variation diminishing (TVD) Mac-Cormack scheme, which is presented in Liang, Falconer, and Lin (2006). In this study we adjusted the source term by including the rainfall rate I in $m\ s^{-1}$ and we approximated the friction term by the Manning-Strickler equation (Das and Bagheri (2015)) with the Manning coefficient n in $m\ s^{-1/3}$ instead of the originally proposed Chezy formula. H is the total water column depth in meters, g is the acceleration due to gravity (here 9.81 $m\ s^{-2}$) and q the discharge per unit width in $m^2\ s^{-1}$. β is the correction factor for the non-uniform vertical velocity profile, which has been set to equal 1.0 for a uniform velocity distribution. Due to the influence of the water depth on the friction term, small and zero water depths cause numerical instabilities and correct wetting-drying algorithms must be applied to insure stability of the numerical scheme (Liang, Lin, and Falconer (2007)). We applied similar to Vincent, Caltagirone, and Bonneton (2001) an algorithm which sets the water depth during each computation time step to a minimum of 10^{-5} m and no mass flux (q=0) at these points. The TVD term is included only at the inner computation points, excluding the boundary and the so-called ghost points, which are needed for the calculation of no boundary flux at the hillslope top (solid wall boundary) and the bottom outflow of the accumulated discharge (transmissive wall boundary, cf. Causon and Mingham (2010)). In the following we briefly outline the MacCormack Scheme (MacCormack (1969)) with the additional TVD term (Liang, Falconer, and Lin (2006)):

$$X_i^p = X_i^j - (F_i^j - F_{i-1}^j) * \frac{\Delta t}{\Delta x} + S^j * \Delta t \tag{3.10a}$$

$$X_i^c = X_i^j - (F_{i+1}^p - F_i^p) * \frac{\Delta t}{\Delta x} + S^p * \Delta t \tag{3.10b}$$

$$X_i^{j+1} = \frac{X_i^p + X_i^c}{2} TVD(X_i^j) \tag{3.10c}$$

The superscripts p and c denote the predictor and corrector steps, while j and i represent the discretization in time and space. It is important to note that the spatial flux term F is discretized backwards in the predictor time step and discretized forward in the corrector time step. The main benefits of this two-stage scheme are that one can solve regions with sharp gradients through the inclusion of the TVD term and that the source term is computationally efficiently treated, whilst maintaining second-order accuracy, in time and space. The complete implementation of the scheme, including transmissive and solid wall boundary conditions is presented as python script in the supplemental code to this publication (Appendix A.2).

3.3.3 *Averaging in time and space*

Depending on the space and time discretization we can analyse how much of the energy influx by rainfall was converted into free energy of overland flow and how much has dissipated. It is however not trivial to disentangle energy fluxes in space and time, and less so to analytically average over both domains to describe the nature of transient energy conversion rates. On the one hand, averaging over the time domain is typically accompanied by setting time derivatives to zero and allows us to analyse the steady state spatial distribution of energy (Schroers et al. (2022)). On the other hand, averaging over the space domain leads to a black box system where we are unaware of the internal spatial distributions and only express the temporal evolution of the system (e.g., Kleidon et al. (2013)).

As the partial differential equations of the underlying movement of water (mass and momentum balances) are numerically approximated on a space-time grid, only an average of the energy fluxes in both domains provides an estimate for an entire hillslope and event. In this section, to introduce the reader to the general dynamics of transient surface runoff, we spatially lump the entire hillslope into one OTS which is transient in time. In section 4 of this study, we extend this concept and double average in space as well as in time. Fig. 3 shows the space-time grid, where at the computation points (circles) the hydraulic variables H and q are calculated. An exemplary OTS is discretized in space with length dx and temporal conversion dynamics of energy for a time interval with length dt. Spatial derivatives of Eq. 3.4 $J_{f,net}^{pe}, J_{f,net}^{ke}$ are averaged in time (dt) and temporal derivatives $\frac{dE_{pe}}{dt}, \frac{dE_{ke}}{dt}$ are averaged in space (dx), leading to a double averaging of power and dissipation of surface runoff (Fig. 3.3). For calculation of space- and time derivatives between computation points i (j) and $i+1$ ($j+1$) we apply forward differencing, which reads $\frac{df(y)}{dy} = \frac{f^{i+1}(y) - f^i(y)}{dy}$, where y is the averaged variable in time $\widetilde{q}, \widetilde{H}$ or space $\bar{q}, \bar{H}$. Eq. 3.4 forms the basis for an analysis of surface runoff in space and time. Depending
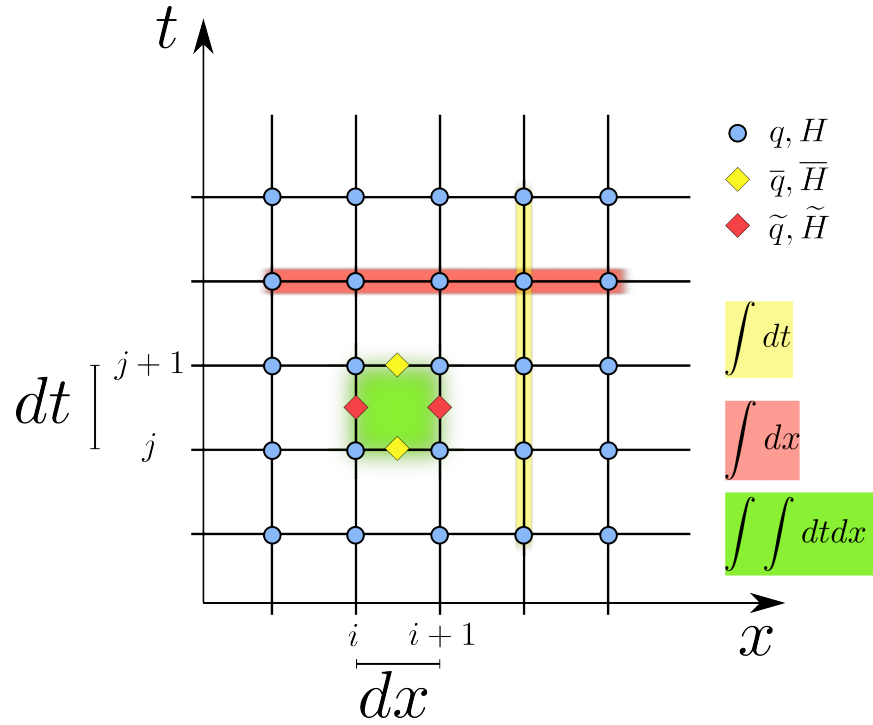
Figure 3.3: Discretization of energy conversion dynamics in space (x) and time (t). q and H are evaluated on nodes (blue circles), energy conversion in time is integral over space (red) [$Watt$], in space is integral over time (blue) [$J\ m^{-1}$] and total energy converted is calculated as space-time integral (green) [J].

on the system and the rainfall-runoff event we define spatial and temporal boundaries to calculate the total converted energies. For a defined OTS this allows for calculation of power and dissipation by integration: Either for the whole OTS (Fig. 3.3 red area) in W, for the whole event (Fig. 3.3, blue area) in $J\ m^{-1}$, or for a specified duration and distance, averaged in time and space (Fig. 3.3, green area) in J.

3.3.4   *Scenarios and results*

To highlight the different transient behaviours of characteristic hillslopes we compare the hillslope form which is related to advective soil wash erosion (SW) with the one which relates to diffusive soil creep (SC). We ran three simulation scenarios on each hillslope, differing in block rainfall rates (100 $mm\ hr^{-1}$ and 50 $mm\ hr^{-1}$) as well as length of rainfall time interval (120s and 360s) (cf. Fig. 3.4). Based on the calculated hydraulic results we then proceeded to calculate the transient energy balance averaged in space over the hillslope length. Finally, the residual of the energy balance is interpreted as the total amount of dissipated energy in time and is analysed relative to the accumulated influx of energy by rainfall (D_{HS}, cf. Eq. 3.7), which allows

a thermodynamic description of a temporally transient rainfall-runoff event.

Scenarios

The three analysed scenarios have been computed by the described numerical implementation of the 1D shallow water equations, the simulated hydrograph of each scenario is plotted in Fig. 3.4. In the first and third scenario (S1 and S3) both hillslope forms reach steady state (approximated as $\dot{Q} = 0$, if $\frac{\Delta Q}{Q} < 0.01$), where SW-hillslope forms reach steady state in less time than SC-hillslope forms. Scenario S2 describes a case without a steady state runoff regime. For all cases it is apparent that SC forms react faster to rainfall for the rising as well as the falling limb of the hydrographs. Interestingly, different rainfall rates lead to different time intervals until the runoff can be described as steady state (cf. S1 and S3), with higher rainfall rates leading to a relative faster reaction of the hillslope and a longer interval of steady state runoff conditions. This relates to the nonlinear character of the simulated shallow water equations, as water accumulates faster on the surface, average runoff velocities grow as well.

Energy conversion dynamics

In the presented transient framework, an influx of energy may either lead to an increase of stored potential energy $\dot{E}_{HS}^{pe}$, an increase of kinetic energy $\dot{E}_{HS}^{ke}$, or an increase of the outflux of kinetic energy $J_{HS,out}^{ke}$ (Fig. 3.1). If these energy fluxes are positive the energy is not dissipated and instead maintained as free energy of surface runoff. $\dot{E}_{HS}^{pe}$ and $\dot{E}_{HS}^{ke}$ contribute to the stored energy on the hillslope during the rising limb of the hydrograph, recede to zero when reaching steady state and dissipate during the falling limb of the hydrograph ($\dot{E}_{HS}^{pe} < 0$, $\dot{E}_{HS}^{ke} < 0$). For all simulated scenarios the total energy which is stored and released is larger for SC than for SW profile forms (Fig. 3.5a and b). The shortest interval to reach steady state is achieved for SW hillslopes and largest rainfall rates (S1), and contrarily the longest time interval for reaching steady state is related to SC hillslope forms and smallest rainfall rates (S3). Scenario S2 does not reach steady state runoff and follows the energy dynamics of S1 during the rising limb of the event (both have equal rainfall rates). As however less energy has been stored on the hillslope for S2 than for S1, less energy is dissipated during the falling limb of S2 than of S1. For potential energy most energy is created at the beginning of the event, with small runoff depths and little to no flow. Most internal kinetic energy $\dot{E}_{HS}^{ke}$ is produced when flow depths rise (and therefore $\dot{E}_{HS}^{pe}$ falls) whilst the output of kinetic energy $J_{HS,out}^{ke}$ still hasn't reached it's maximum. $J_{HS,out}^{ke}$ is linked to the observed runoff at the downslope end of the hillslope profile and is for all three scenarios larger for SC than for
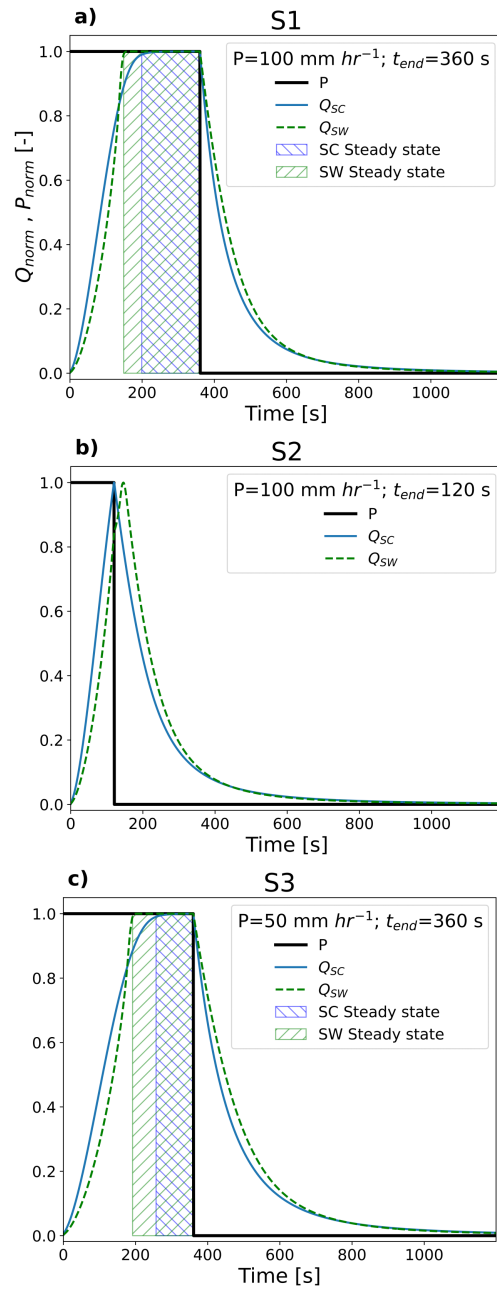
Figure 3.4: Block rainfall scenarios and simulated hydrographs for SC- and SW- related 1D hillslope profiles
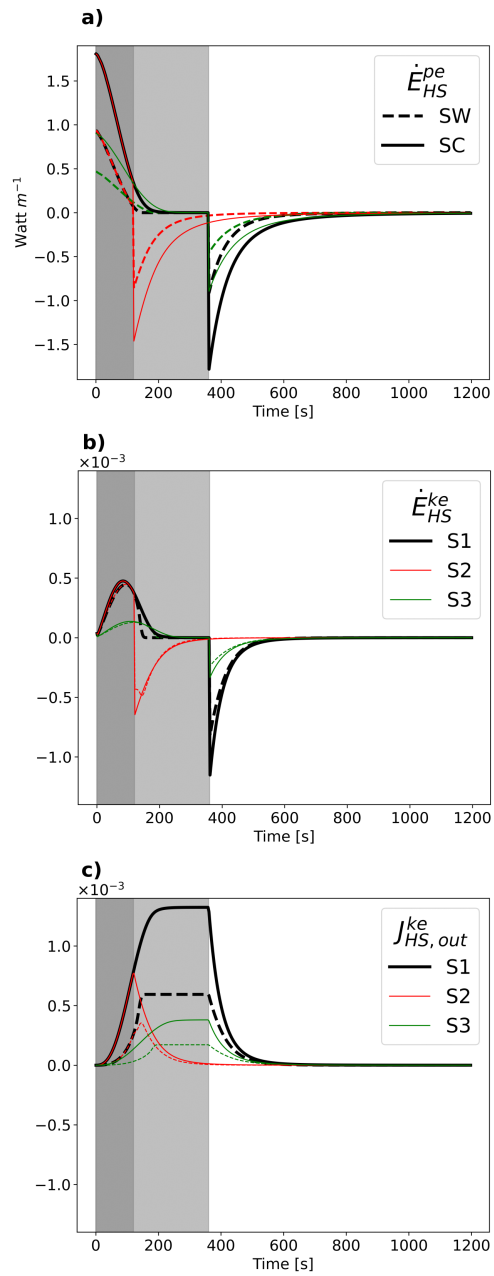
Figure 3.5: Simulated temporal dynamics of spatially lumped a) stored potential energy; b) stored kinetic energy and c) kinetic energy outflux in watt per meter flow width for SW- and SC- related 1D hillslope profiles.

SW hillslope forms (Fig. 3.5c). This export of energy from the system is linked to the internal work from overland flow on the system, the longer it takes for the hillslope system to reach a steady state value of $J^{ke}_{HS,out}$ the more energy is available to perform work on the surface structures. This reflects our notion that certain hillslope morphologies are more likely to experience an overshoot in power and consequently more work which is generated by surface runoff.

Dissipation and energy efficiency

As outlined in the previous section, we approximate the dissipated energy integrated over the hillslope length as the energy residual of the computed hydraulic variables q and H (cf. Appendix A.1.1). The temporal evolution of dissipation D_{HS} in watt per meter flow width for all simulated scenarios is plotted in Fig. 3.6a. In absolute terms dissipation rates are for each simulated scenario larger for SC than for SW hillslope forms. This result is independent of the transient temporal evolution of D_{HS}, maximum dissipation rates relate to the fully developed steady state and are at each point in time larger for SC than for SW hillslope profiles. In this setup SW forms receive less
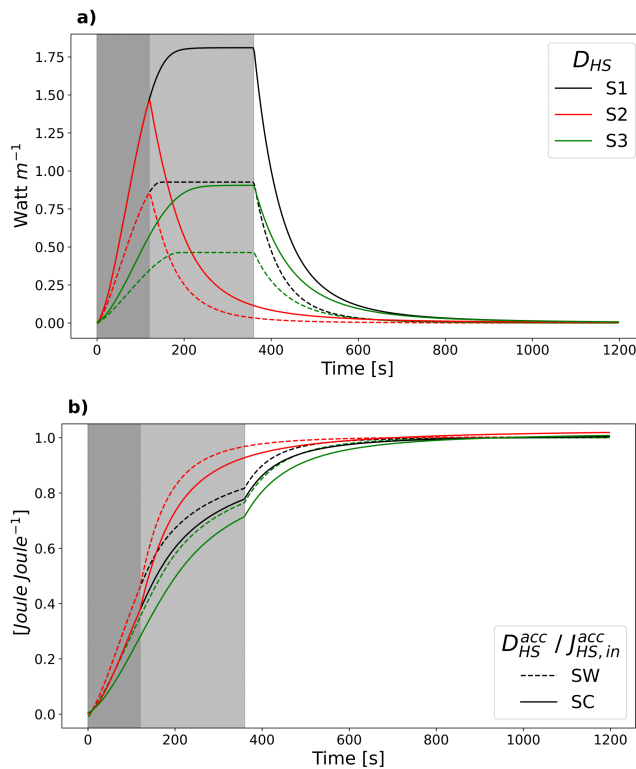
Figure 3.6: Computed transient results of a) absolute dissipation D_{HS} and b) relative dissipation $\hat{D}_{HS}$ for scenarios S1, S2, S3 on hillslope profiles realted to soil wash (SW) and soil creep (SC)

influx of energy than SC forms and dissipation rates therefore need to be normalized by the influx of potential energy by rainfall to evaluate

how much relative free energy is dissipated per hillslope type and scenario. We therefore computed D^{HS}, the fraction of accumulated dissipation D_{HS}^{acc} per accumulated influx energy $J_{HS,in}^{acc}$ (Fig. 3.6b, cf. Eq. 3.6). This thermodynamic descriptor represents at each point in time the amount of energy which has already dissipated from the accumulated influx of free energy, a higher value means that friction is relatively larger and the runoff process less energy efficient. At the end of the event this descriptor is close to 1 as almost all influx energy has dissipated at $t_{end} = 1200s$. In Fig. 3.6b we plotted relative dissipation D^{HS} for the simulated hillslope profiles and scenarios. For all scenarios D^{HS} is larger during the transient runoff event for SW than for SC hillslope profiles. This result is the opposite of the absolute values of dissipation and highlights the effect of normalizing energy conversion rates. Interestingly, larger rainfall rates (scenario S1) lead to larger relative dissipation rates than smaller rainfall rates (scenario S3). This means that although larger rainfall rates lead to higher kinetic energy production $J_{HS,out}^{ke}$ (Fig. 3.5c), kinetic energy rates are much smaller than dissipation rates, allowing relative dissipation rates to be highest for largest rainfall rates and SW hillslope profiles. Scenario S2 without steady state runoff conditions leads to larger D^{HS} values during the falling limb of the hydrograph, with a larger fraction of energy being dissipated at any point in time during the rainfall runoff event than for S1 or S3.

3.3.5 Discussion

In this first part of the study, we highlight the connection between surface runoff, dissipation of its free energy and the evolution of surface morphology. We argue in line with Wolman and Gerson (1978) and Beven (1981) that such events in nature are highly intermittent and transient in time, leading to the question how this can be interpreted within an optimality context such as has been proposed by many (cf. Singh (2003), for an overview). Therefore, we put forward the concept of relative dissipation of free energy or equivalently energy efficiency of surface runoff, which is similar to Carnot's theorem of maximum work which can be extracted from heat flow (Kondepui and Prigogine (1952)). This idea was applied to surface runoff on characteristic 1D hillslope profiles which are related to diffusive soil creep erosion and advective soil wash erosion. Interestingly our results show that the latter (SW) results in less energy efficiency of surface runoff, or differently stated a larger fraction of the provided free energy by rainfall is dissipated than for SC hillslope types (cf. Fig. 3.6b). This means that there is relatively more energy available for work on the surface of SC profiles (be it in the form of detachment or transport of sediment particles). This reflects the generally accepted theory of the evolution of hillslope profiles (Kirkby (1971)) and river profiles (Leopold and

Langbein (1962)) towards concave distributions of geopotential, e.g., a falling energy slope along the flow path. Although we do not specifically account for energy of sediment particles, we derive a simple starting point for a thermodynamic interpretation of erosion regimes and resulting geopotential distributions. The simulated scenarios also hint at the evolution of runoff response. If relative dissipation rates are analyzed on an event scale, our results show for the same hillslope, shorter but more intense runoff events maximize relative dissipation and minimize energy efficiency.

We stress that these scenarios are only adequate for situations where infiltration is negligible as a loss of mass affects the transient energy balance. Furthermore, we did not touch small scale geomorphological adaptations such as rills. We showed in our previous study (Schroers et al. (2022)) for steady state overland flow that rill processes are linked to the distribution of dissipation rates and therefore affect the energy balance. The development of rills is however transient (Rieke-Zapp and Nearing (2005)) and reflects our notion that structural adaptations are a result of an overshoot of power. As a starting point it is therefore important to understand during which situations such an overshoot is more likely and transient structural adaptations will occur. The here proposed transient, event-based perspective highlights that larger rainfall rates and shorter rainfall overland flow events lead to larger relative dissipation rates- which is somewhat counterintuitive as flow velocities and kinetic energy increase as well. The reason for this effect is that larger flow depths increase flow velocities and therefore facilitate during the transient state a faster depletion of the influx of potential energy through rainfall, while relatively less free energy is stored on the hillslope. In terms of energy efficiency of overland flow this means that long duration, small intensity rainfall overland flow events are most efficient, in contrast to short, high intensity rainfall overland flow events where a larger fraction of the provided free energy dissipates faster. Following this logic, structural patterns on hillslopes should organize over time to decrease efficiency. This means that if we would apply the same event to a hillslope surface twice, the first event will produce smaller relative dissipation rates than the second. Simultaneously, the kinetic energy of surface runoff would increase for the second event as the provided energy gradients are depleted faster. The latter coincides with the theory about minimization of energy expenditure (Rodriguez-Iturbe et al. (1992)) as well as experimental results on the plot scale (Rieke-Zapp and Nearing (2005)).

This can also be explained with the maximum power principle (Lotka (1922); Kleidon (2016)) which states that the open thermodynamic system organizes its internal structure to deplete the driving gradients at the maximum rate. In the case of runoff on a hillslope

this would imply that given no other constraints, the hillslope erodes towards a configuration which reacts for the same rainfall event faster with larger runoff rates. The maximum power would be achieved once the runoff approaches the shortest possible runoff response and largest runoff rate. Obviously, this is an extreme case which cannot be achieved in nature as geology, soil composition and vegetation constrain the runoff response, but this example helps to understand the evolution of the interaction between runoff and erosion. In the second part of this study, we build on these theoretical results, but extend the concept to real world hillslopes and observed runoff responses in the Weiherbach catchment and analyze whether erosion and the evolution of surface runoff is indeed linked to maximum power of surface runoff.

3.4 APPLICATION TO SURFACE RUNOFF EVENTS IN THE WEIHERBACH CATCHMENT

Following our argumentation from the previous section, we apply the developed theory about energy efficiency of overland flow to observed rainfall runoff events in the Weiherbach catchment. The catchment has been subject to intensive monitoring which includes data about erosion and sediment transport, allowing in addition to overland flow for an analysis of erosion patterns within the presented energy efficiency framework.

3.4.1 *The Weiherbach catchment and the flash floods of 1994/1995*

The hilly Weiherbach catchment lies in the Kraichgau, which is in the south-west of Germany (Fig. 3.4.1). The latter has a size of 3.45 km^2 and has been a hydrological observatory of for more than three decades (Plate and Zehe (2008)). The result is a rich data set with multiple continuous time series of discharge, precipitation, climate parameters as well as soil humidity. Furthermore, several measurement campaigns yielded a spatially distributed set of soil hydraulic parameters (Zehe et al. (2001)), Manning-Strickler values of the principal land uses as a function of plant growth stage (Gerlinger (1996)), and annual cycles of morphological as well as physiological plant parameters. Sediment concentrations measurements at the two discharge measurement stations allowed balancing of total sediment loads (Scherer (2008)). Approximately ninety percent of the catchment is agricultural land use, of which the principal plant cultivations are wheat, corn, turnip and sunflower (cf. Fig. 3.4.1b). The two largest runoff events were recorded on the 27th of June 1994 and on the 13th of August 1995 - in the following we will focus on these two events only and we will therefore refer to them as event 1 and event 2 or by year only (cf. table 3.1). Both events were caused by a convective precipitation event with
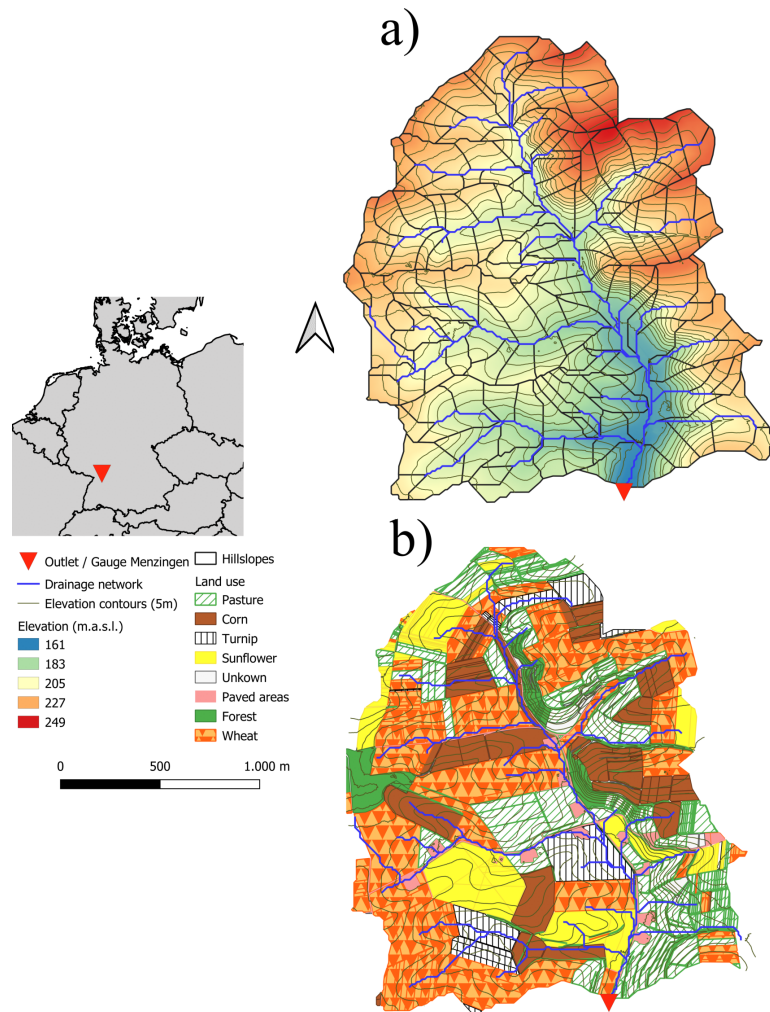
Figure 3.7: The Weiherbach catchment: a) Observed drainage network, surface elevation and derived hillslopes (cf. Zehe et al., 2001); b) Land use patterns during the monitoring period (Scherer, 2008)

a return period of 200a according to the KOSTRA data set (Junghänel, Ertel, and Deutschländer (2010)). However, the discharge peaks of both floods lie well above the 10000-year flood of 3.3 m^3 s^{-1} (BW-Abfluss, cf. Blatter et al. (2007)). A more detailed analysis of the event runoff generation can be found in Zehe et al. (2005), while for the study at hand we conclude that the recurrence intervals of peak discharge suffice to consider them effective in terms of landscape formation (cf. Beven (1981)), as corroborated by the considerable amounts of eroded sediments.

3.4.2 *Model description and calibration*

The model we used is an extended version of the physically based model CATFLOW (Maurer (1997); Zehe et al. (2001)) which incorporates a sediment erosion module (Scherer (2008)). In brief, the model

Event	Date	I_{cum}	I	QP	RC	$\bar{\theta}$	T_I	T_{QP}	M_{sed}
-	-	[mm]	[mm h^{-1}]	[m^3 s^{-1}]	[-]	[-]	[a]	[a]	[t]
1	17.06.1994	78.3	22	7.9	0.12	0.25	200	>10^4	1800
2	13.08.1995	73.2	23	3.2	0.07	0.26	>100	10^4	500

Table 3.1: Hydrological variables for extreme events of 1994 and 1995

subdivides a catchment into several hillslopes and a drainage network, where each hillslope is discretized into a two-dimensional vertical grid. The widths of the elements vary from the top to the foot of the hillslope. For each hillslope, the model simulates the soil water dynamics and solute transport based on the Richards equation in the mixed form as well as a transport equation of the convection diffusion type. The equations are numerically solved using an implicit mass conservative Picard iteration (Celia, Bouloutas, and Zarba (1990)) and a random walk (particle tracking) scheme. The simulation time step is dynamically adjusted to achieve an optimal change of the simulated soil moisture per time step which assures fast convergence of the Picard iteration. The hillslope module can simulate infiltration excess runoff, saturation excess runoff, lateral water flow in the subsurface and return flow. However, in the Weiherbach catchment only infiltration excess runoff contributes to storm runoff and lateral flow does not play a role at the event scale. What is important is the redistribution of near surface soil moisture in controlling infiltration and surface runoff. As the portion of the tile drained area in the catchment is smaller than 0.5%, we didn't account for tile drains in the simulation. The here presented setup of the Weiherbach catchment is based on simulations and results from Zehe et al. (2005), who subdivided the catchment into 169 hillslopes in relation to land use and soil patterns (cf. Fig. 3.4.1a). The total soil depth represented by the model was 2m, Manning roughness coefficients for the hillslopes and channels were taken from the mentioned experimental database (Gerlinger, 1997), while relative distribution of macroporosity at the hillslope scale was measured by Zehe (1999). The latter scales the total infiltration capacity during rainfall events in relative terms of the soil hydraulic conductivity, after the soil water content increases field capacity. The model was calibrated by stepwise increasing of macroporosity variability (Zehe et al. (2005)) for event one and two (table. 3.1), yielding Nash-Sutcliff model efficiencies of 0.97 (event 1) and 0.98 (event 2) at the downstream gauge in Menzingen (Fig. 3.8a and Fig. 3.8b). The main storm runoff generation mechanism for both events is infiltration excess runoff, which is routed in the model on the hillslopes into the channel, both based on the advection-diffusion approximation to the one-dimensional Saint-Venant equations. Individual surface runoff responses of each hillslope Q_{HS}^i , mean of all hillslopes Q_{HS}^m and for both events can be seen in Fig. 3.8. For reasons of briefness, we refer

to Maurer (1997) or Zehe et al. (2001) and Zehe et al. (2005) for more details on model structure and model equations, as well as the parameters of the river network. Sediment erosion and transport is modelled
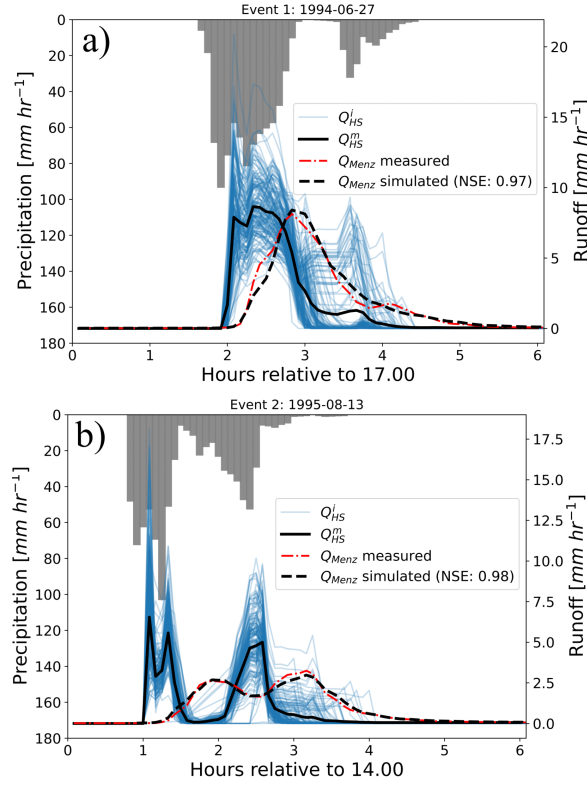
Figure 3.8: Observed precipitation and catchment discharge response, simulated surface runoff at hillslope scale Q_{HS} as well as simulated river discharge Q_{Menz} for a) the event of 1994-06-27 and b) the event of 1995-08-13.

using the steady state sediment continuity equation (Eq. 3.12). Sediment transport capacity follows an adjusted concept from Wischmeier and Smith D.D. (1978), treating sediment detachment and transport as individual processes. Potential erosion epot ($kg \ m^{-2} \ s^{-1}$) is simulated in CATFLOW-SED (Scherer et al. (2012)) by a semi-empirical approach that bilinearly accounts for detachment by rainfall momentum flux mr ($N \ m^{-2}$) as well as overland flow shear stress τ ($N \ m^{-2}$) (cf. Eq. 3.10c).

$$e_{pot} = p_1(\tau + p_2 m_r - f_{crit}); if \ e_{pot} < 0, e_{pot} = 0 \qquad (3.10c)$$

The resisting forces acting against detachment are characterised by two empirical parameters: the erosion resistance f_{crit} ($N \ m^{-2}$) as well as the erodibility parameter p_1 (-), scaling the growth of the detachment rate in case the attacking forces exceed the threshold f_{crit}. The parameter p_2 (-) weighs the momentum flux of rainfall against shear stress from overland flow. The empirical parameters were determined

for conventionally tilled loess soils using data from rainfall simulation experiments performed in the laboratory (Schmidt (1996)) and at erosion plots in the field (Scherer et al. (2012)). Sediment transport is modelled with the approach from Engelund and Hansen (1967) empirically relating a dimensionless transport intensity to dimensionless stream intensity and consequently allowing for a calculation of transport capacity based on hydraulic overland flow conditions. Sedimentation of suspended particles is accounted for depending on Reynolds number and the particle size, characterizing their buoyancy. At each timestep CATFLOW-SED then balances sediment transport for each overland flow element based on the stationary form of the sediment continuity equation (Eq. 3.12).

$$\frac{\delta q_s}{\delta x} = \Psi(x, t) \tag{3.12}$$

Where q_s is sediment mass flow per unit width in $kg\ m^{-1}\ s^{-1}$, Ψ net detachment/ sedimentation of sediments from overland flow in $kg\ m^{-2}\ s^{-1}$, x length coordinate in meter and t time step in seconds. For more details on the implementation and model equations we refer to Scherer et al. (2012) and Scherer (2008). The sediment transport model was able to simulate total erosion for both flash floods with an absolute error of 8% (see table 3.1), which is within the error margin of the observations. As previously mentioned, deposition and erosion patterns for individual hillslopes indicate that especially convex shaped slopes with highly erodible crop types result in high erosion rates (Fig. 3.4.1). In the Weiherbach catchment these slope types are located in the east.

3.4.3 Transient energy and power

Surface runoff

We estimated for both events the evolution of potential and kinetic energy on each hillslope as well as the kinetic energy export from the hillslope (cf. Eq. 3.6 and Eq. 3.7). $\dot{E}_{HS}^{pe}$ makes up by far the largest portion of free energy at any point in time, while $\dot{E}_{HS}^{ke}$ and $J_{HS,out}^{ke}$ can be considered negligible for the hillslope energy balance (cf. Fig. 3.9). For the event in 1994 $\dot{E}_{HS}^{pe}$ shows three positive and three negative peaks with very limited periods of time independence at roughly 2.5 h to 3.3 h (Fig. 3.9a). For $\dot{E}_{HS}^{pe}$ as well as $\dot{E}_{HS}^{ke}$ positive values represent an increase of free energy that is stored on the hillslope and thus an overshoot in power, while negative values indicate that stored free energy is decreasing (Fig. 3.9a and 3.9b). In contrast to the internal free energies, $J_{HS,out}^{ke}$ increases on average to a certain level and maintains this flux until the end of the rain event (Fig. 3.9c). From an external perspective the system therefore seems to reach steady state but is internally in a transient unsteady state. At this

stage it is interesting to mention, that Zehe et al. (2013) quantified
the power in soil water fluxes during these events and evaluated their
dependency on macroporosity, which resulted in values of 1-2 *watt*
m^{-2} per hillslope. This translates with a mean hillslope area of 20000
m^2 into approximately 2-4 x 104 *watt* per hillslope, which is of the same
scale as the sum of the here presented free energy fluxes $\dot{E}_{HS}^{pe}$, $\dot{E}_{HS}^{ke}$
and $J_{HS,out}^{ke}$. Event 2 in 1995 (Fig. 3.10) shows similar energy dynamics
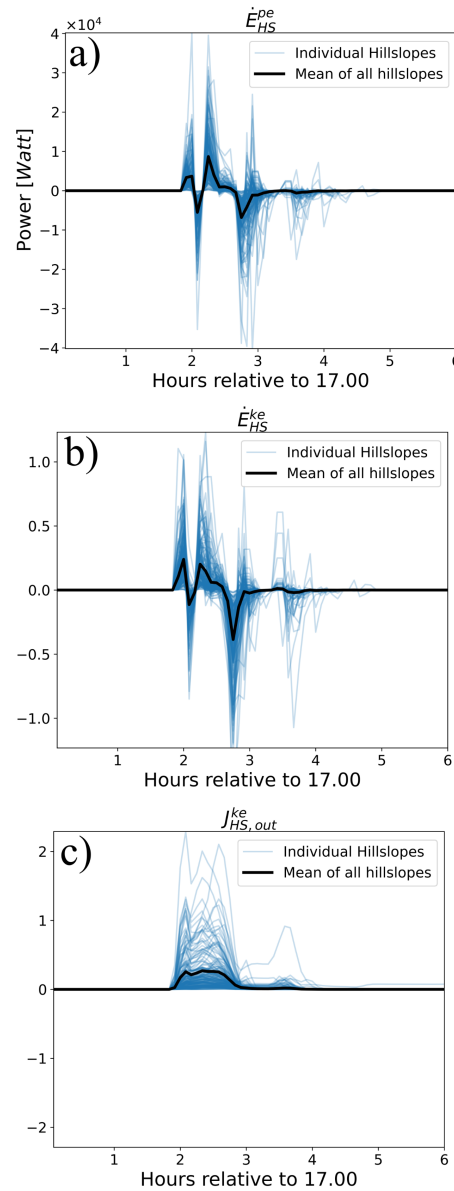
Figure 3.9: Calculated free energy dynamics for the surface runoff event 1
on 1994-06-27 of changes in a) potential energy $\dot{E}_{HS}^{pe}$, b) kinetic
energy $\dot{E}_{HS}^{ke}$ and c) energy out flux $J_{HS,out}^{ke}$

but with lower magnitude and lesser maximum runoff rates. The
maximum peak of $\dot{E}_{HS}^{pe}$ is not mirrored by a negative counterpart (Fig.
3.10a), indicating that large amounts of stored surface water infiltrates

rather than contribute to further surface runoff. Its effect can also be seen from the dynamics of $J^{ke}_{HS,out}$ (Fig. 3.10c) which has on average 3 peaks with a dip in power between peak one and two, although energy influx from rainfall is maintained almost constant during this period (cf. Fig. 3.8b). Using the energy influx J^{in}_{HS} we calculated D_{HS}
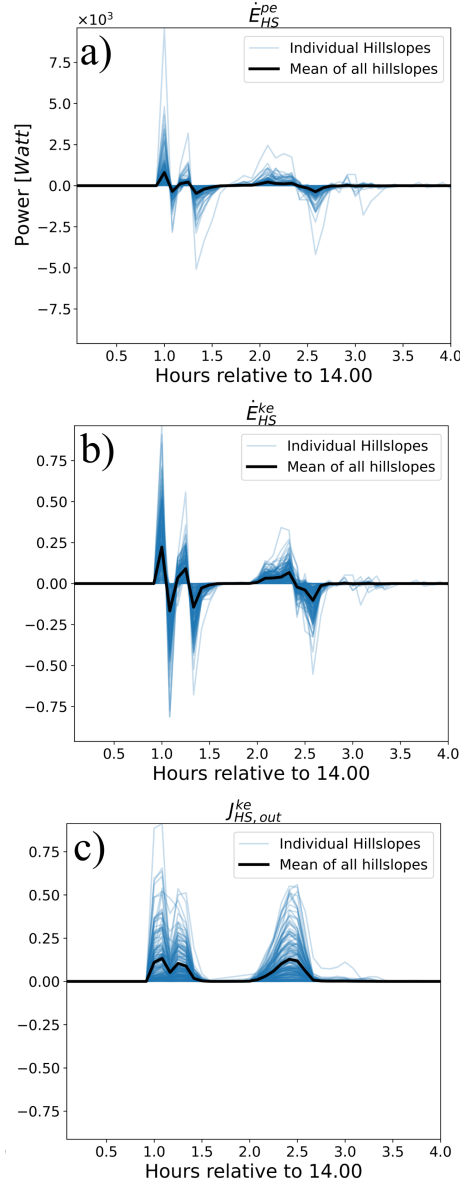
Figure 3.10: Calculated free energy dynamics for the surface runoff event 2 on 1995-08-13 of changes in a) potential energy $\dot{E}^{pe}_{HS}$, b) kinetic energy $\dot{E}^{ke}_{HS}$ and c) energy out flux $J^{ke}_{HS,out}$

for each hillslope (Eq. 3.5), event, and as average of all profiles (Fig. 3.11). D_{HS} is very dynamic and is for both events unsteady, with a global maximum occurring at the beginning of an event and followed by one or more subsequent smaller local maxima. We also note that

the spread of D_{HS} between individual hillslopes is large, especially at the points in time of maxima.
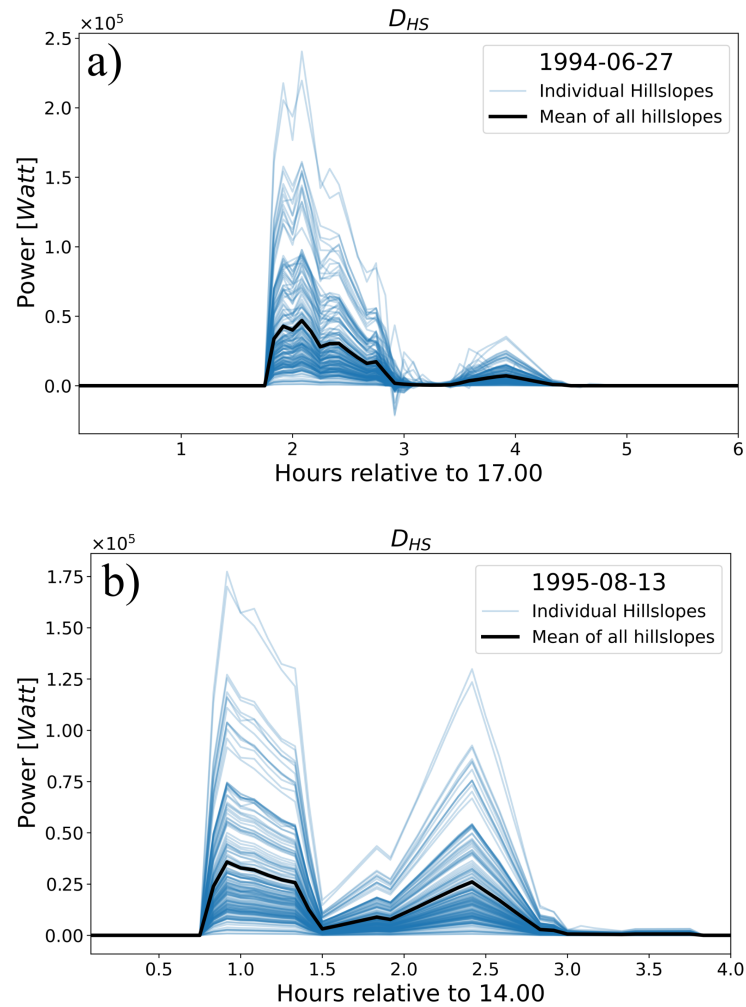
Figure 3.11: Temporal dynamics of dissipation D_{HS} for individual hillslopes and mean of all hillslopes for a) event 1 and b) event 2

Sediment transport

For both simulated events the model was able to reproduce observed total sediment transport at the gauge Menzingen (cf. table 3.1). To estimate the average work of overland flow on sediments we analyse the accumulated spatial erosion- and deposition patterns on each hillslope at the end of both events. We approximate the average kinetic energy that would be necessary to transport a given mass of sediment m_{sed} (kg) for a representative length l_{rep}, which represents the average distance a sediment particle was transported during the time interval of overland flow t_{sed}. We calculate l_{rep} by weighting of the downslope distance of each computation segment s to the hillslope end with its related eroded or deposited sediment mass $m_{sed,s}$ in kg (Eq. 3.13). The

sum of eroded and deposited sediment over all hillslope segments results in total eroded mass per hillslope $m_{sed,HS}$.

$$l_{rep} = \frac{\Sigma_{s=1}^{s_{end}}(l_s m_{sed,s})}{\Sigma_{s=1}^{s_{end}} m_{sed,s}} \qquad (3.13)$$

The time interval during which overland flow was acting on bed material t_{sed} was calculated from simulation results of each hillslope as the period of overland flow with mean overland flow depths larger than $1\ mm$. Total expended energy per unit area $e_{sed,HS}$ ($J\ m^{-2}$) is finally calculated for each hillslope as:

$$e_{sed,HS} = \frac{1}{2} \frac{m_{sed,HS}}{A_{HS}} \left(\frac{l_{rep}}{t_{sed}}\right)^2 \qquad (3.14)$$

Where A_{HS} is the hillslope area in m^2 and $m_{sed,HS}$) the eroded sediment mass in kg. Fig. 3.12a shows the simulation results for accumulated erosion per hillslope segment after the 1994 event (cf. Scherer (2008)). Negative values represent areas of deposited sediment whereas positive values indicate the erosion of soil. Erosion was large on highly erodible soils with little plant coverage such as sunflower or corn fields (cf. Fig. 3.4.1b). A difference between convex and concave hillslope profiles was visible, as the former allow for deposition of sediment at the hillslope feet due to a declining topographic gradient. Note that hillslope form is incorporated in the estimated average expended energy on sediments as negative erosion (mostly deposition at the hillslope foot) reduces l_{rep} (cf. Eq. 3.13) and $e_{sed,HS}$ (cf. Eq. 3.14). $e_{sed,HS}$ therefore, not only reflects the influence of soil erodibility due to land use and soil characteristics, but also implicitly informs on driving geopotential gradients. This can be seen by comparing the spatial patterns of erosion (Fig. 3.12a) and related expended energy $e_{sed,HS}$ (Fig. 3.12b): While absolute erosion rates are seemingly randomly scattered throughout the catchment, $e_{sed,HS}$ is clearly largest on the eastern slopes of the catchment and to a lesser extent present on the western slopes (Fig. 3.12b). In the following we will make use of this information about geopotential gradients and analyse the east-west pattern with respect to energy efficiency of overland flow.

3.4.4 *Energy efficiency of characteristic hillslope forms*

The calculations of transient energy and power for both calibrated rainfall runoff events provide an estimate of energy efficiency of overland flow for each hillslope in the Weiherbach catchment. These energy efficiencies are linked to the geomorphological development stage of each hillslope, facilitating an interpretation of geomorphology within the energy balance of surface runoff. To this end, we cluster the hillslopes into groups, representing the typical hillslope profile groups SW, RS, and SC, as introduced in sect. 3.3.1 and detailed below. subsubsection*Clustering hillslope forms To cluster the 169 hillslope profiles,

a)

b)
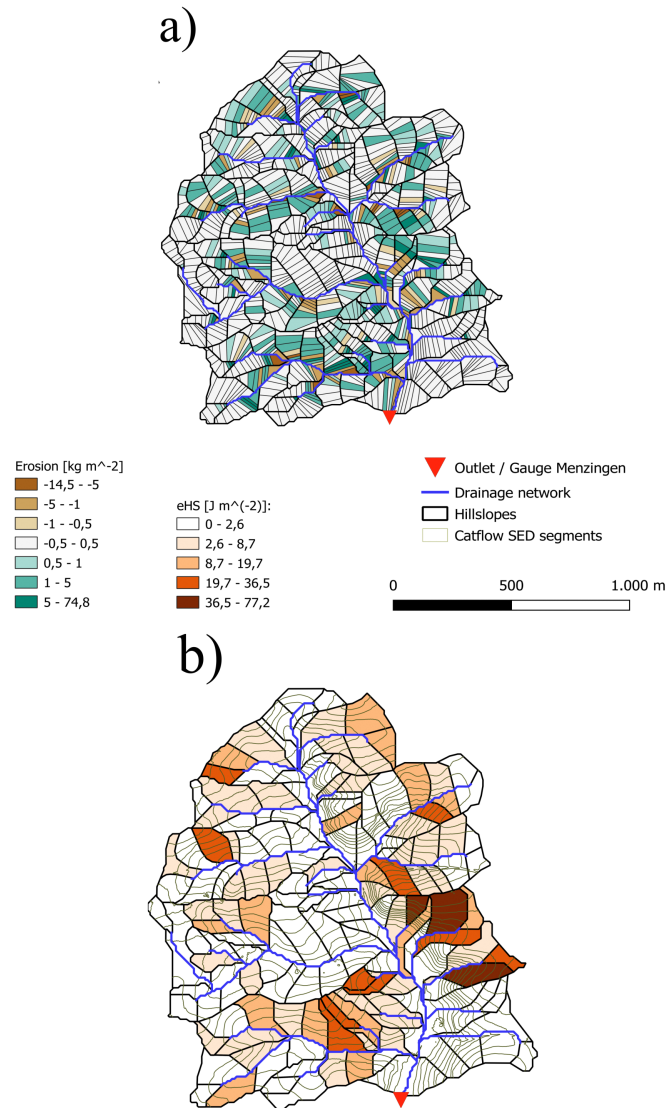
Figure 3.12: a) simulated erosion and b) approximated expended energy on erosion per hillslope for the 1994 event

each one is normalized in its vertical and horizontal length and then plotted as a single point into a three-dimensional space, consisting of the axis: 1) Mean vertical height, 2) Percentage length of negative curvature, 3) Horizontal length coordinate of maximum slope. The same procedure is applied to the normalized characteristic hillslope profiles SW, RS and SC from sect 3.3.1 forming cluster centroids. This allows clustering of model hillslopes according to their minimum Euclidian distance in the parameter space and resulted in 27 hillslopes being classified as SC type, 129 profiles as RS type and 13 belonging to SW (Fig.3.13a). This confirms the perception that most erosion can be attributed to a combined impact of kinetic energy by rain splash plus shear stress of overland flow accumulation. The classification also showed that 27 hillslopes which can be related to soil creep lie

mostly in the eastern part of the Weiherbach catchment (cf. Fig.3.13b), where highest erosion rates were simulated. In the next section we do not only confirm this general erosion pattern but also show that highest erosion rates coincide with highest relative dissipation rates and therefore maximum work which overland flow performed on the sediments.
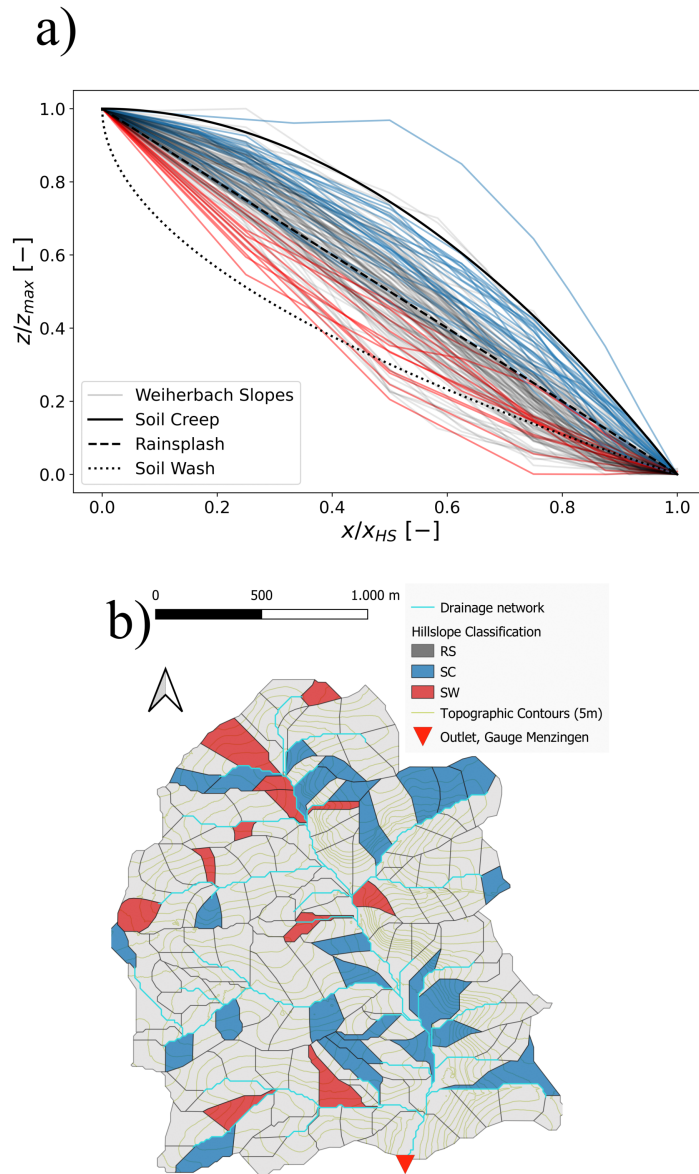
Figure 3.13: Classification of Weiherbach hillslope profiles into forms related to soil creep (blue), rain splash (a) grey, b) white), and soil wash (red).

Relative dissipation patterns and energy efficiency of surface runoff

For both events we plot the hillslope clusters for calculated total dissipated energy as well relative dissipated energy (Fig. 3.14). In both

cases we find distinct differences between SC, RS and SW hillslope types. In absolute terms, more energy is dissipated for both events on SC profiles than RS and SW types, while SW types show lowest dissipated energy levels. Contrarily, relative dissipated energy is highest for SW hillslope types and lowest for SC classified profiles. $\hat{D}_{HS}$ values ranging from 91% to 99% indicate that almost all energy has been dissipated or has been transferred to the sediments at the end of the rainfall event at $t_{end} = 5h$. SC hillslopes receive larger quantities
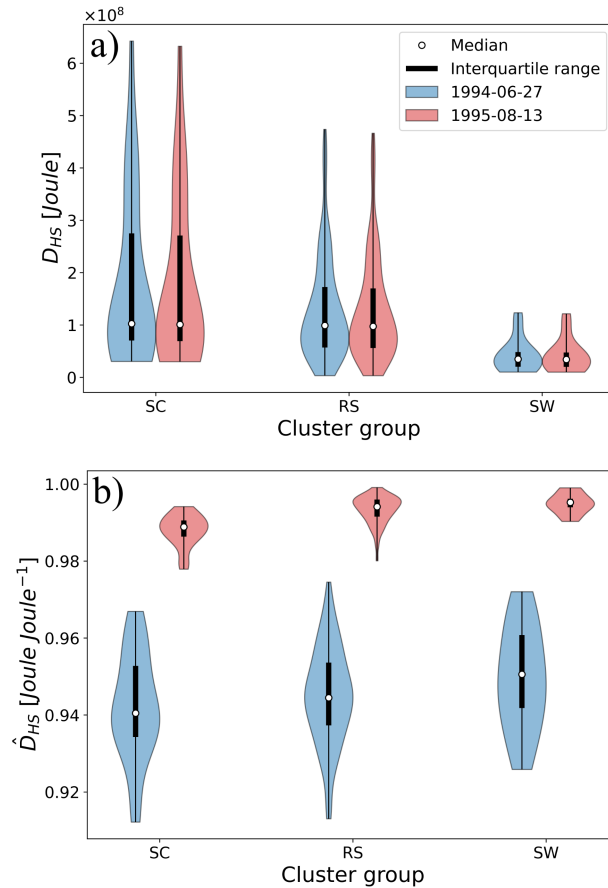
Figure 3.14: Clusters of geomorphological hillslope types (SC, RS, SW) and a) dissipated energy D_{HS} as well as b) relative dissipation $\hat{D}_{HS}$ for runoff events 1 and 2

of energy influxes through rainfall but in comparison to SW profiles dissipate a smaller portion of this energy. Both events show similar total dissipated energy levels, which is due to very similar total rainfall volumes. Fig. 3.14b however shows that although total energy influx and dissipation is similar, relative dissipation is larger for the 1995 event than for the 1994 event. This difference arises from the larger surface runoff rates of the latter (due to less infiltration (cf. Zehe et al. (2005)) at its peak up to three times larger, cf. Fig. 3.8), leading to more kinetic energy of surface runoff at the outlet.

Similarly, we compare relative free energies $\hat{E}_{HS}$ and relative outflux

energies $\hat{J}_{HS,out}$ of the three hillslope types (Fig. 3.15). Fig. 3.15a shows the maximum values of transient relative free energy that is not dissipated during each surface runoff event for all simulated hillslopes (cf. Eq. 2.7b). The results indicate a tendency of SW and RS profiles to lead to less relative free energy in comparison to SC hillslope profiles. Relative free energy $\hat{E}_{HS^{max}}$ mirrors $\hat{D}_{HS}$, highlighting the connection between maximum free energy that is stored in time on the hillslope and total dissipated free energy over the whole event.

Compared with each other, the 1994 event generates larger relative kinetic and potential energy fluxes than the 1995 event, with less total runoff volume. $\hat{E}_{HS}$ of the 1994 event is therefore much larger than during the 1995 event.

Free energy during a transient event consists of the stored potential and kinetic energy as well as the energy outflux at the hillslope end. An analysis of the latter (Fig. 3.15b) reveals that there is only a small difference between the three hillslope types and between events. This means that for the analysed events hillslope geomorphology seems not to be imprinted in kinetic energy export at the hillslope outlet. These findings imply that during a surface runoff event, the largest differences between hillslope types can be observed in the pattern of free energy components along the flow paths, and not locally, e.g., at the hillslope end. These results differ from our previous analysis of steady state runoff, where SW hillslope types increased the relative kinetic energy outfluxes in comparison to RS and SC profiles (Schroers et al. (2022)). As the latter did not account for infiltration processes, we hypothesize that distributed infiltration in the catchment levels out these differences.

Erosion patterns

Mean erosion rates e_m ($kg\ m^{-2}$) and accumulated erosion e_{tot} (tonnes) for both events have been calculated by summing total sediment-erosion and deposition of each hillslope. Similarly, we calculated the runoff coefficient RC_{HS} of overland flow for each hillslope. For the 1994 event e_{tot} ranges between 0 to 90 tonnes per hillslope and RC_{HS} lies between 0.05 and 0.52, while for the 1995 event the corresponding ranges are 0-45 tonnes for e_{tot} and 0.02 to 0.16 for RC_{HS} (cf. Fig. 3.16). While there is no correlation between these variables for neither of both events, we find a clear relation to the hillslope profile type. For both events eroded sediment is smallest for profiles related to soil wash (SW) and largest for SC type profiles. Note that for the 1994 event the averaged eroded sediment per hillslope profile type e_m is smallest ($e_m = 1.4 tonnes$) for SW, intermediate (10.2 tonnes) for RS and largest (23 tonnes) for SC profile (Fig. 3.16a). The same pattern is observed for the event of 1995 (Fig. 3.16b). e_{tot} on SW profile types accounts for only around 1% (18 tonnes) of total erosion in the catchment during the 1994 event and 3% (20 tonnes) during the 1995 event. Interestingly, the
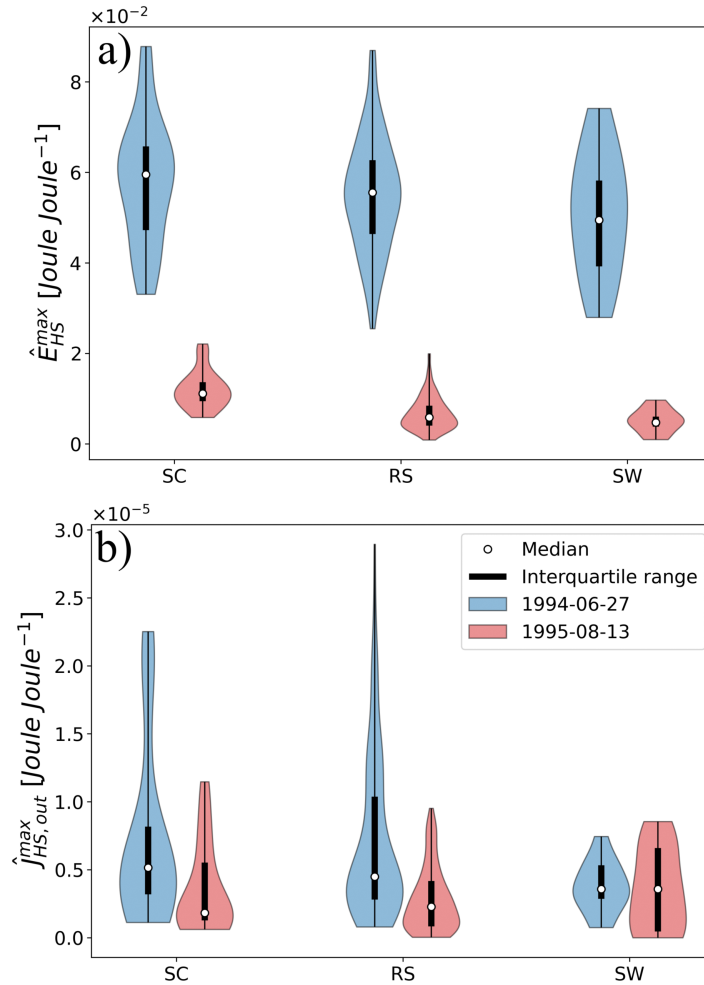
Figure 3.15: Clusters of geomorphological hillslope types (SC, RS, SW) and maximum a) relative stored free energy $\hat{E}_{HS}$ as well as b) relative free energy flux $\hat{J}_{HS,out}$ at the hillslope foot for runoff events 1 and 2

largest difference of eroded sediment between both events is observed on SC and RS profiles while mean as well as total eroded sediment of SW profiles is almost equal for both events. With respect to total runoff volumes, the results convey, that hillslopes with runoff coefficients in the medium range determine almost the entire erosion. For the event of 1994, hillslopes with $0.06 < RC_{HS} < 0.17$ account for 92% of total eroded sediment mass, while for the event of 1995, 95% of eroded mass occurred on hillslopes with $0.042 < RC_{HS} < 0.095$. Above and below these ranges none to very little erosion occurred. It is also noteworthy that for both events not only largest amounts of eroded sediment coincide with medium range runoff coefficients, but also that most hillslopes operate in this range.

For both events we then computed relative dissipation of overland flow and plotted the result against average expended energy on sediment transport per unit area for each individual hillslope (Fig. 3.17).
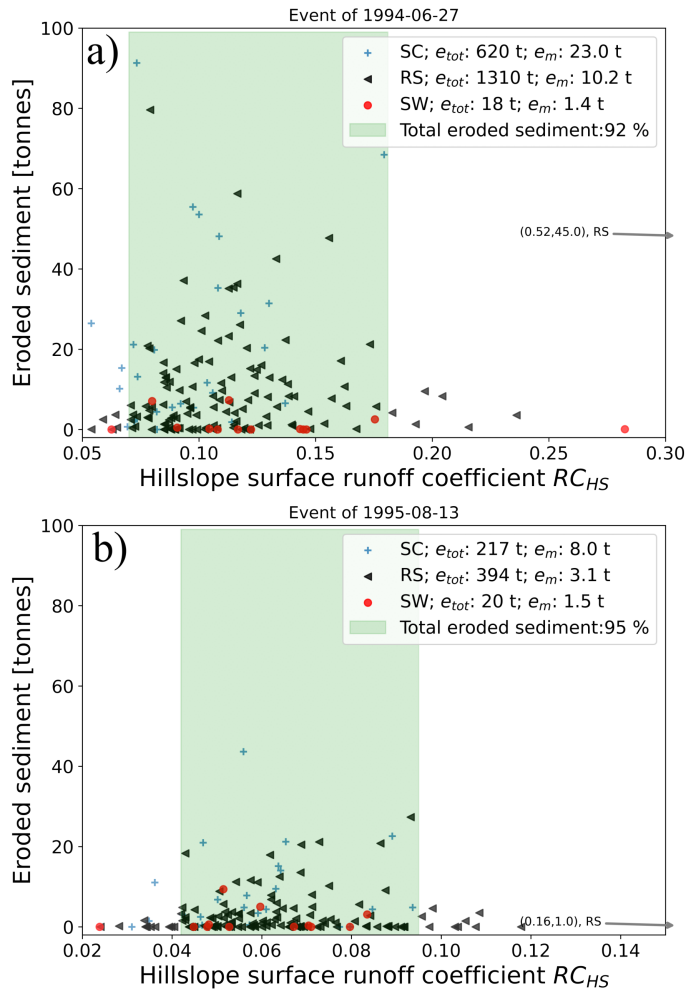
Figure 3.16: Simulated surface runoff coefficient RC_{HS} vs. eroded sediment for each hillslope of a) event in 1994 and b) event in 1995 for each hillslope and hillslope cluster (SC, RS, SW)

We highlighted the medium ranges of relative dissipation $\hat{D}_{HS}$ and kinetic energy of the sediments e_{HS} for each hillslope cluster with kernel colour coding, which indicates a hierarchal structure of expended energy on sediment transport: e_{HS} decreases from SC- to RS- to SW profile types. This marked difference can be seen for both events (Fig. 3.17a and b) and is highlighted by the mean expended energy on sediment transport per cluster group $e_{HS,m}$. Relative dissipation is as expected for both events and all hillslopes close to one, which suggests that most input energy is dissipated during the runoff process. Mean relative dissipation $\hat{D}_{HS,m}$ is generally smaller for the 1994 event than for the 1995 event where less overland flow occurred. For both events $\hat{D}_{HS,m}$ increases with changing hillslope type from SC to RS to SW, but this hierarchy is more pronounced for the 1995 event. We conclude that the results indicate a clear pattern of relative dissipated energy of overland flow and expended energy on sediment transport: On aver-

age, from SC, to RS, to SW $\hat{D}_{HS}$ increases and e_{HS} decreases. In plain words, if relatively more energy of the influx energy is dissipated, less energy is available for erosion and sediment transport. A decrease of energy efficiency (equals increase of $\hat{D}_{HS}$) in overland flow is therefore related to a decrease of expended energy on sediment transport.
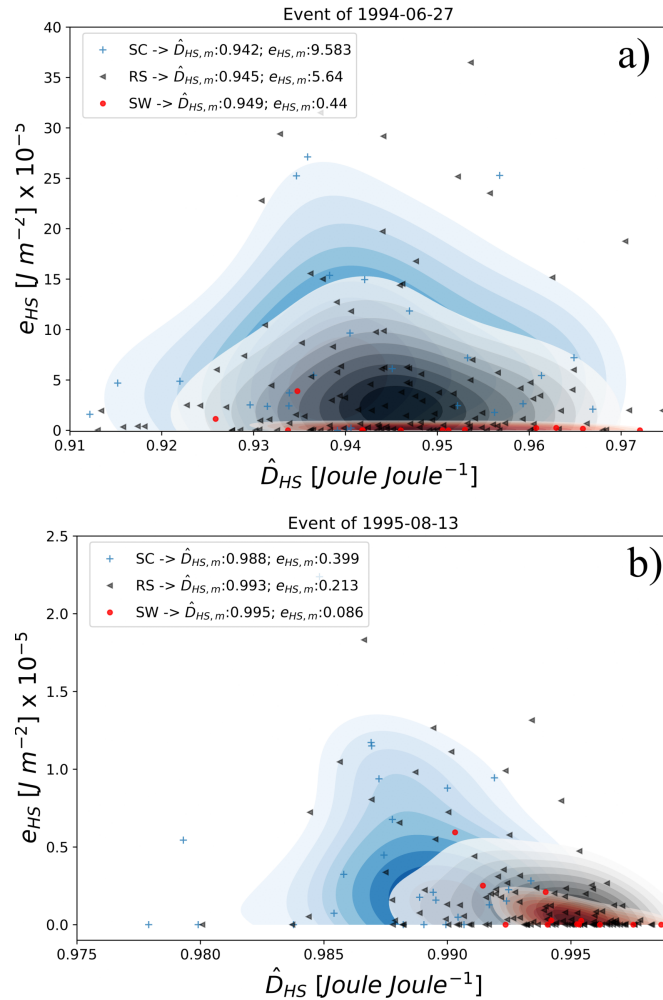
Figure 3.17: Relative dissipated energy $\hat{D}_{HS}$ vs. total expended energy for sediment erosion e_{HS} of a) the event in 1994 and b) the event in 1995 for each hillslope and hillslope cluster (SC, RS, SW)

3.4.5 *Discussion*

In this second part of the study, we have explored a range of concepts to connect runoff generation process, erosional regimes, and geomorphological evolution of hillslopes in a thermodynamic framework. We put the focus on the analysis of two extreme rainfall runoff events, which were observed in the Weiherbach catchment. This certainly raises the question how representative these events are- given their

rare occurrence. We argue however, in line with Wolman and Gerson (1978) and also Beven (1981) that only certain events contribute to effective landscape formation. Those events must be extraordinary as an overshoot in power is needed to exceed a threshold and trigger significant erosion and structure formation (Zehe and Sivapalan (2009)). Our analysis of the surface runoff during these two extreme events clearly shows, that driving downward, dissipative cascade of energy conversions from potential energy to kinetic energy and work on the sediment should be seen within a transient framework, as neither the mass nor the momentum balance during overland flow events is at steady state. We found that the resulting power of surface runoff is of the same order as power of water infiltration into the soil via macropores (cf. Zehe et al. (2013)). This might imply that surface and subsurface flow coevolve into a maximum power state where dissipation and power are equally distributed between complementary domains or more precisely flow paths (cf. Schroers et al. (2022)).

We then connected the energy balance and energy efficiency of surface runoff events to the geomorphological forms of the derived hillslope systems. While this rests on the assumption that the delimited hillslopes represent homogeneous dynamics, we are confident that this is the case as those are defined by topography as well as land use, the main controls of infiltration rate and surface runoff (Zehe et al. (2001)). Most hillslopes were classified as profiles relating to rain splash erosion, and only few as soil creep or soil wash profile. We find a clear hierarchy relating relative dissipation, thus energy efficiency to erosion rates. $\hat{D}_{HS}$ is largest on SW then RS and smallest on SC profiles, indicating that SW profiles are conserving the least percentage of the energy influx by rainfall while SC profiles are most efficient in generating power in surface runoff. The energy efficiency of overland flow $1 - \hat{D}_{HS}$ therefore constrains the effectiveness of a rainfall runoff event to change land forms and trigger landscape evolution (cf. Wolman M. G. and Miller J. P. (1960)). A larger value indicates that more potential energy is conserved as free energy, which implies that overland flow acts with larger average forces and can perform more work on the surface materials (overshoot in power for structure formation). The 1995 event on average resulted in larger $\hat{D}_{HS}$ values than the 1994 event, which explains the higher erosion rates of the latter (cf. table 3.1: $M_{sed}^{1994} = 1800 tonnes$ vs. $M_{sed}^{1995} = 500 tonnes$). Importantly, as accumulated rainfall amounts are almost equal for both events (cf. table 3.1: $I_{cum}^{1994} = 78.3mm$ vs. $I_{cum}^{1995} = 73.2mm$), this difference relates not to differences in energy influxes by rainfall. This is indicated by almost equal absolute dissipated energy (Fig. 3.14a) and can also not be deduced from kinetic energy fluxes at the hillslope feet (Fig. 3.15b). The difference between both events arises from storage rates of free energies within the hillslope systems in the form of potential and kinetic energies. Importantly, energy storage and therefore effectiveness of a

surface runoff event relate to transient conditions. Although we found that runoff coefficients and total erosion amounts were not correlated, largest erosion rates were found for hillslopes with a medium RC_{HS}. This is somewhat surprising as one would think that highest RC_{HS} values would also result in largest erosion rates. However, our results give evidence that larger RC_{HS} values are related to hillslope profiles which are closer to a dynamic equilibrium, store less free energy and therefore produce less erosion. The maximum work surface runoff can perform on the sediments relates to the potential flux in overland flow and thus on runoff and the specific geopotential gradient (cf. Schroers et al. (2022)). As the concept of relative dissipation captures both, we found a strong relation between mean $\hat{D}_{HS}$ and the average work / free energy expended on sediments e_{HS} (detachment and transport) for the three analyzed hillslope classes (Fig. 3.17). Clearly most work on the eroded sediments was performed on SC- and RS- and only very little on SW hillslopes. In terms of efficiency, we find that SC profiles are on average more efficient in power generation of surface runoff ($1 - \hat{D}_{HS}$ is larger), which implies that more work can be performed on sediments (e_{HS} is larger), while SW profiles are less efficient ($1 - \hat{D}_{HS}$ smaller, e_{HS} smaller).

This finding is in line with a general pattern, characterizing the co-evolution of surface runoff dynamics, erosion and hillslope geomorphology, which holds for various climatological as well as geological settings (Perron, Kirchner, and Dietrich (2009)). More generally, the evolution of the hillslope system towards less energy efficiency is consistent with the idea of maximization of dissipation and therefore entropy production (cf. Leopold and Langbein (1962)).

3.5 SUMMARY AND CONCLUSION

In this study we established a connection between morphological hillslope forms and their efficiency to power generation of overland flow from the energy input during rainfall events. We expanded the thermodynamic framework relating the steady state free energy balance of surface runoff to hillslope forms and the presence/ absence of a rill network (Schroers et al. (2022)) to a) transient conditions and b) included the expended energy/ work performed on erosion and sediment transport. Releasing the steady state assumption, essentially implies that the free energy balance of surface runoff, which constrains the maximum work surface runoff can perform on the sediments, relates to slope, form and structure of the hillslope and at the same time to the "refuelling" of the open system with potential energy during rainfall events. To account for both factors, we introduce the concept of relative dissipation, relating frictional energy dissipation to the energy input, which characterises energy efficiency of the hillslope when treated as open, dissipative power engine. We explored the transient

free energy balance in terms of its energy efficiency, comparing typical hillslope forms, representing a sequence of morphological stages and related dominant erosion processes (Kirkby (1971)) A first analysis, based on simulated synthetic events, suggested that older hillslope forms, where advective soil wash erosion regimes dominates, are less energy efficient in generating power during overland flow events, when compared to younger forms with diffusive erosion regimes. In the time domain we found that shorter, more intense events result in lower energy efficiencies than longer, lower intensity events. Given no other constraints (tectonic activity, geology, plants, climate, land use, etc.), this might imply that morphology organizes in time through erosion to facilitate faster and more intense runoff rates, for instance by forming rill- (Schroers et al. (2022)) and river networks. Both increase the power available for downstream sediment transport (Kleidon et al. (2013); Berkowitz and Zehe (2020)), while the local slope declines.

In the second part of the study, we tested whether similar behaviour can be found for extreme flood events in runoff and erosion rates, observed in the Weiherbach catchment. We used a previously calibrated physical model (Catflow, cf. Zehe et al. (2001)) to calculate relative dissipation, work and free energies of surface runoff and erosion for both extreme rainfall runoff events in 1994 and 1995. Surprisingly, we found a clear hierarchy of declining energy efficiencies with increasing morphological age for the three hillslope forms. Younger hillslopes, characterized by diffusive soil creep erosion receive largest free energy influxes from rainfall but dissipate in comparison to soil wash hillslope types less of this input, leaving relatively more free energy available for erosion and sediment transport. While this was found for both events, we highlight that the hillslope system is generally energetically rather inefficient, although the well-known Carnot limit does not apply here.

We conclude that the energy efficiency of overland flow during events does indeed constrain erosional work and the degree of freedom for morphological changes. We conjecture that hillslope forms and overland dynamics coevolve, triggered by overshoot in power during intermittent rainfall runoff events, towards a decreasing energy efficiency in overland flow. This means a faster depletion of energy gradients during events, and a stepwise downregulation of the available power to trigger further morphological developments, and this also implies the emergence of quasi-steady, metastable configurations, which optionally might maximize power in water and sediment fluxes, when averaged in space and time.

Part IV

SURFACE RUNOFF FROM RIVERS AND THEIR
NETWORKS

SURFACE RUNOFF IN RIVERS AND THEIR NETWORKS

4.1 INTRODUCTION

Rivers and their spatio-temporal discharge dynamics determine human development and decay. Even 3000 BC, during the time of the Mesopotamian civilization understanding the physical nature of rivers and water flow was of utmost importance for irrigation of food crops as well as consumption (Macklin and Lewin (2015)). One of the oldest civilizations found in South America, the city of Caral in today's Peru was founded near the river and in the region pre-inca civilizations poured extensive resources into the building of channel and storage systems, on the surface as well as underground (Ochoa-Tocachi et al. (2019)). Around the end of the 19th century, industrialization allowed humans to modify the river structure and discharge dynamics on ever greater scales, which led due to necessity and chance, to the slow emergence of a physical understanding of the water dynamics (Brown (2002)). Foremost, Horton (1945) characterized catchments as physical systems which create structures that can be found in all terrestrial catchments, today known as Horton's laws of stream number, area, length, and slope (Shreve (1966)). His hydro-physical approach led to a new perspective of stream networks, resulting in many descriptive studies of structural patterns (Strahler (1957); Schumm, Harvey, and Watson (1984)) of river morphology. Meanwhile, researchers also developed concepts that point to the cause of structure itself. Apart from statistical approaches (Shreve (1966)), those are based on fundamental physical laws of conservation of mass, momentum, and energy (cf. Bagnold (1966)). While mass conservation is mostly studied for understanding quantities of the water cycle of whole systems (Hydrology), the momentum balance plays a more local role for flow dynamics (Hydraulics) and in a catchment context is used for describing travel times of runoff. As conservation of mass and momentum is already highly complex and in practice very challenging, conservation of energy as represented by the first law of thermodynamics, has seemingly been too abstract at the catchment scale. However, as the hydrological cycle of our earth requires roughly 1.3×10^{24} Joule per year, equivalent to 40 million major power stations (Walling, 1987; cited in Knighton (1998)), thermodynamic concepts might yet be useful to understand how and why this energy is dissipated. For example, Leopold and Langbein (1962) showed that by application of the first and second law of thermodynamics fluvial erosion must lead to exponential river

profiles. Also, energy in fluvial systems is represented as potential-, kinetic-, and thermal energy (Knighton (1998)), but only potential and kinetic energy can perform mechanical work. They are therefore also referred to as free energy, which in a river takes the form of

- work done against viscous shear and turbulence

- work done against friction at the channel boundary

- work done in eroding the channel boundary

- work done in transporting the sediment load

The energy which is required for each of these is drawn from the geopotential difference between water upstream and downstream, leading to a cascade of energy conversions. These conversion processes are however limited by the respective gradients, e.g., the velocity gradient close to the channel bed which determines bed shear stresses. Hence for better understanding on how hydrological systems organize in time and space, we believe it is useful to identify reliable concepts of free energy, work and dissipation at this scale. In the following chapter we first analyse general dynamics of free energy in the largest terrestrial river network, the Amazonas River. We do this by analysing first and second order data sets of runoff, sediment transport and morphology, which enables us to approximate free energy and dissipation throughout the entire basin. In a second part we use the findings as a baseline for a new concept of fluvial dynamics which manifests in structural patterns, such as the Horton laws and others. Here we extend our perspective beyond the Amazonas River to the 18 largest river networks of the earth by area, covering in total 25% of global continental landmass. Finally, we hypothesize that the catchment scale dynamics of free energy can be represented by a thermodynamic system which transitions from a chaotic, high entropy state into an organized, low entropy state.

4.2 FREE ENERGY, DISSIPATION, AND WORK OF A RIVER NETWORK - A CASE STUDY OF THE AMAZONAS

4.2.1 *Theory*

Free energy, dissipation and sediment transport along a river's flow path

In analogy to the previous chapters, we begin at the hillslope scale, where rainfall enters the flow system as energy influx. Although kinetic energy of rainfall is an important driver of erosion (Wischmeier and Smith D.D. (1978)), we neglect this part of the energy balance as it represents only a minor part of the free energy which is added by rainfall to the entire system. The free energy influx at each point of the catchment J_{in}^{pe} in *Watt* m^{-2} can therefore be calculated as the product of rainfall mass ρI multiplied by its geopotential with respect to the catchment outlet gh :

$$J_{in}^{pe} = \rho I g z \tag{4.1}$$

Where ρ in $kg\ m^{-3}$ represents the density of water, g the acceleration through gravity in $m\ s^{-2}$, z is the vertical distance to the sea level in m, and I is the rainfall intensity in $m\ s^{-1}$. The total flux into a certain area J_P in *Watt* is then computed by integration of J_{in}^{pe} over the accumulated upstream area:

$$J_P = \int_{A=0}^{A=A_{cc}} J_{in}^{pe} dA \tag{4.2}$$

This influx of potential energy powers the flow of water through the landscape, which in turn is composed of potential as well as kinetic energy:

$$J_f^{pe} = \rho g Q z \tag{4.3}$$

$$J_f^{ke} = \frac{1}{2}\rho Q v^2 \tag{4.4}$$

Both free energy fluxes of Eq. 4.3 and 4.4 are in *Watt*, Q is the accumulated discharge in $m^3\ s^{-1}$, and v the average flow velocity in $m\ s^{-1}$. The free energy which is lost from the water molecules between an up- and a downstream cross section of the flow path Ω in *Watt* m^{-1} is represented by Eq. 4.5 with I_e as the free energy gradient (cf. Schroers et al. (2022)).

$$\Omega = \rho g Q I_e \tag{4.5}$$

Eq. 4.5 assumes further that the system is in steady state (cf. ii). As mentioned before, the energy which is lost from the water is largely dissipated by internal viscous shear and turbulence into heat, but a smaller portion is maintained as free energy fluxes of sediment transport, which can be calculated by Eq. 4.3 and Eq. 4.4 as J_{sed}^{pe} and J_{sed}^{ke}, when accounting for the density of sediments ρ_{sed}.

Free energy and sediment fluxes of the Rhine, a system out of equilibrium

With these concepts in mind, we draw a connection between the main energy fluxes of water and matter in our landscape, which we want to present exemplary for the reach of the River Rhine from Constance in Germany to Lobith in the Netherlands, close to the sea level of the North Sea. We chose this stretch of the river due to the good data basis and the direct relation between sediment transport and free energy loss (Asselman (1999)). Upstream of the gauge at Constance lies lake Constance, a sediment trap, where almost all sediment from the Alps is deposited (Frings et al. (2019)), while downstream of the gauge at Lobith, the River Rhine diverges into the lower Rhine and the Waal River. Between these two gauges the river has first been straightened and consolidated, particularly for flood protection during early summer floods but also for agricultural land use (Tulla (1825)), and later the section was impounded for generation of electricity. This progress of civilization has brought new problems, especially regarding sediment transport, which needs to be actively managed in the river Rhine (Vollmer S. and Goelz E. (2006)). As outlined above, flowing water represents a flux of free energy which converts through a cascade of energy conversions into heat and free energy of sediment, which implies that an enforced alteration of this flux necessarily affects the free energy balance. On first sight, the free energy balance of the river system is like the one of a hillslope surface (cf. iii), mass accumulates while losing geopotential along the flow path. However, the difference in terms of discharge accumulation along a river flow path is that rainfall contributes to a much smaller amount than on hillslopes, as almost all water is gained through inflow from large stream tributaries at confluences. Fig. 1a shows this for the River Rhine and its largest confluences for mean annual discharge (cf. LUBW (2022)). Unlike hillslopes, discharge is not accumulated homogeneously but flow increases erratically at confluences. This sudden increase of mass and momentum leads to a variety of flow phenomena, which often manifest in downstream changes of channel geometry. Most strikingly, the inflows increase the sediment flux (Fig. 4.1b) which can only be achieved if more free energy is available for the transport. For the River Rhine it seems that we can distinguish flow regimes with close to constant sediment flux but a net loss of free energy (Fig. 4.1b, grey areas) and a regime with an increasing sediment flux which is accompanied by a constant net free energy flux (Fig. 4.1b, green area). This example shows very generally that a river's capacity to transport a certain mass of sediment corresponds to an expense of net free energy, whereas an increase in sediment flux must be accompanied by an alteration of the river's free energy balance. Additionally, flow and sediment transport organize over time to build structures at confluences (e.g.,Ribeiro et al. (2012)), which has been related to optimality approaches (Howard (1990)). Here, we leave aside the complexity of

these local hydraulic adaptations as we intend to analyse the river network on a much larger scale, at which those processes blend into a much more general free energy balance. We hypothesize, that at the scale of river networks the accumulation and depletion of free energy along a flow path reflects different flow regimes, manifesting in distinct morphological adaptations. However, for a more thorough analysis of feedbacks between natural energy fluxes and resulting structural adaptations, the example of the Rhine is not applicable as the flow system has undergone too many anthropogenic alterations. This led to a system which we judge as being in disequilibrium as its structural pattern needs to be actively managed (addition of free energy by human activity) to maintain its current state.
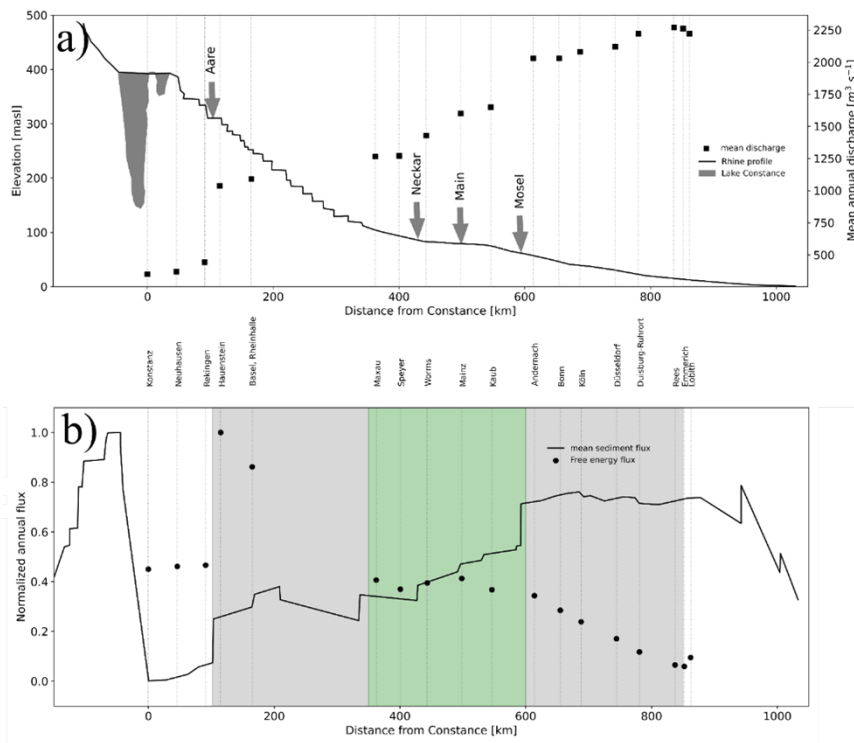
Figure 4.1: a) Profile of the Rhine River , mean annual discharge (LUBW (2022)) and major tributaries; b) Mean annual sediment flux and mean annual free energy flux in *Watt Watt*$^{-1}$ at discharge gauging stations (after Frings et al. (2019))

Efficiency of flow and transport

Each energy flux is driven by a gradient of energy. If we assume that in the cascade of energy conversion processes, one flux is driven by a single gradient, we can specify a simplified hierarchy of energy conversions from rainfall to sediment transport (Fig. 4.2) At the catchment level, potential energy influx of rainfall is the driving power of maintaining a gradient of geopotential along the flow paths, providing the initial power that drives water flow. Along a certain distance, some
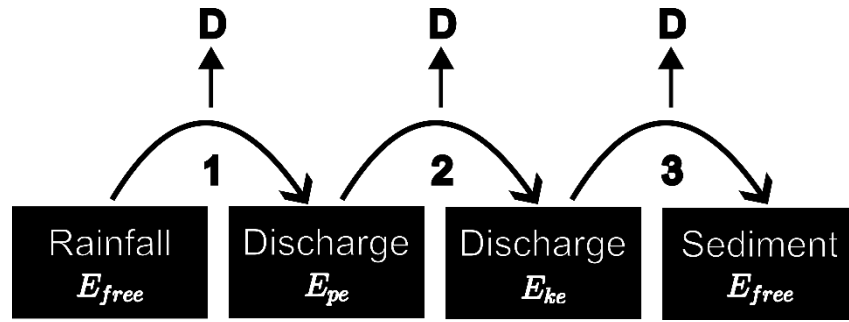
Figure 4.2: Cascade of free energy conversion

part of the accumulated potential energy will dissipate through a cascade of energy conversion processes, and another will remain as potential energy of discharge (Fig. 4.2, level 1). On the next lower level, this discharge relates to a gradient of geopotential, thereby leading to a mass flux and associated kinetic energy of the flow (Level 2). This kinetic energy in turn produces a gradient within the flow itself, as water molecules in the vertical water column closer to the surface of the stream move with a faster velocity than particles close to the bed level. This spatial gradient of kinetic energy leads to a transfer of mean flow energy into turbulent kinetic energy, which provides the force to lift sediment particles, as well as a transfer of kinetic energy to accelerate the particles and transport them downstream (Level 3). Regarding these complexities, we represent the first level of energy conversion (Rainfall to discharge) and the third level of energy conversion (Discharge to sediment) as a black box system, as we are only aware of the influx and outflux of free energy but are unaware of the internal energy conversion cascade. The second level however presents a clear relation between the gradient of potential energy and the resulting kinetic energy flux. In the following we analyze the efficiencies of the three presented energy conversion levels by setting the resulting energy flux in the case of a black box system into relation with the driving energy influx (level 1 and 3), or in case of a direct energy conversion, relating the resulting flux with its driving gradient (level 2).

LEVEL 1: EFFICIENCY OF RAINFALL TO DISCHARGE ENERGY CONVERSION   At each point within a catchment, the accumulated influx of energy by rainfall J_P is given as the area integral of rainfall intensity and geopotential height (Eq. 4.2). Subsequently at each point of the catchment (system) the relative flux of free energy per upstream energy influx E_P is represented by Eq. 4.6.

$$E_P = \frac{J_f^{pe}}{J_P} \tag{4.6}$$

E_P is essentially an extension of a runoff coefficient, relating energy outflux from discharge to energy influx from rainfall.

LEVEL 2: EFFICIENCY OF GEOPOTENTIAL GRADIENT TO KINETIC ENERGY CONVERSION   The resulting flux of kinetic energy from discharge is at each point along the flow path the result of the driving gradient of geopotential energy:

$$E_Q = \frac{J_f^{ke}}{\Omega} = \frac{\frac{1}{2}\rho Q v^2}{\rho g I_e Q} = \frac{v^2}{2g I_e} \tag{4.7}$$

With a formula which links average flow velocity and driving gradient, such as the Darcy-Weißbach formulation:

$$I_e = \frac{f v^2}{R_H 8g} \tag{4.8}$$

Eq. 4.7 can be written as:

$$E_Q = \frac{4R_H}{f} \tag{4.9}$$

E_Q expresses the efficiency of runoff to turn a geopotential difference into free energy in the form of a kinetic energy flux.

LEVEL 3: EFFICIENCY OF KINETIC ENERGY OF DISCHARGE TO KINETIC ENERGY OF SEDIMENT CONVERSION   Analogous to the kinetic energy flux of discharge, the kinetic energy flux of sediment is calculated as

$$J_{sed}^{ke} = \frac{\rho_{sed} v^2}{2} Q_{sed} \tag{4.10}$$

If we assume equal flow velocities of water and sediment the relative sediment transport efficiency can be expressed as the ratio of sediment flux F_{sed} and water flux F_Q, both in $kg\ s^{-1}$:

$$E_{sed} = \frac{J_{sed}}{J_Q} = \frac{\rho_{sed} Q_{sed}}{\rho Q} = \frac{F_{sed}}{F_Q} \tag{4.11}$$

E_{sed} therefore provides a measure of how much kinetic energy of discharge is converted into kinetic energy of sediment particles and if multiplied by the density of water represents E_{sed} equals the concentration of sediment per water volume in $kg\ m^{-3}$.

In conclusion the three presented efficiencies E_P, E_Q, E_{sed} provide a means for estimating the evolution of the systems energy conversion rates. These efficiencies of energy conversion are directly related to the well-known parameters of the runoff coefficient R_C, the hydraulic radius R_H, the friction coefficient f and sediment concentration C_{sed}. In the following we assimilate spatio-temporal first and second order datasets of precipitation, runoff and sediment transport and analyse the resulting patterns of E_P, E_Q, E_{sed}.

4.2.2   *Study site- The Amazonas a system (yet) in equilibrium*

Water balance

Due to our intention to apply the concepts of free energy and its cascade of conversion processes into thermal heat at the largest terrestrial scale possible, we chose as a case study the over 6 million km2 extensive basin of the Amazon River and its network of tributaries. The Amazon basin covers roughly 40% of South America's land mass, amasses a peak flow of over 300 000 $m^3\ s^{-1}$, and accounts with just over 200 000 $m^3\ s^{-1}$ average annual flow for a fifth of the discharge of all rivers on earth (Beighley et al. (2009)), which is five times larger than that of the Congo basin, the second largest basin on earth (Salati and Vose (1984)). Due to its geolocation along the equator and size the basin's water cycle is influenced by multiple climatic regimes. Although its main atmospheric water influx stems from the Northern Hemisphere trade winds, interannual variations are strongly linked to sea surface temperature of the Atlantic and the Pacific oceans as well as opposing summer and winter periods in its northern and southern basins (Figueroa and Nobre (1990);Marengo (1992)). Although these climatological phenomena lead to substantial spatial and temporal variabilities of precipitation (Espinoza Villar et al. (2009a)) and stream flow (Espinoza Villar et al. (2009b)), the Amazon basin is said to be a system in long-term equilibrium of water, nutrients and energy fluxes (Salati and Vose (1984)). Therefore, at a most basic level the complex water cycle of the Amazon basin can be described by an average of 2200 $mm\ yr^{-1}$ of rainfall (P_a), where roughly one half is evapotranspirated (ET_a) and the other half (Q_a) flows as runoff into the Atlantic (Fassoni-Andrade et al. (2021); cf Fig. 4.4). Most of the rainfall falls in three regions of the basin: Over the north-west P_a exceeds 3600 $mm\ yr^{-1}$, in the centre around 2400 $mm\ yr^{-1}$, and close to the river mouth annual rainfall reaches up to 2800 $mm\ yr^{-1}$ (Marengo (1992); cf. Fig. 4.3a). Interrelated is annual ET_a, which is an important control of rainfall within the basin itself, as up to 50% is recycled locally (Zemp et al. (2017)), and it also influences in the entire continent, with ET_a from the Amazon providing around 70% of the precipitation in south-eastern South America (van der Ent et al. (2010)). The rest of the precipitation reaches the Atlantic Ocean downstream of Obidos with a peak of the flood wave in June (Fig. 4.4b). This peak is the result of the runoff from the opposing rainfall seasons in the north (June-July-August, Solimoes River) and the south (December-January-February, Madeira River) as well as the long travel time for the flood wave to reach Obidos from the Peruvian Andes (Espinoza Villar et al. (2009a)). This dynamic can also be noted by comparison of the annual hydrographs at Manacapuru (Solimoes River) and at Fazenda Vista Alegre (Madeira River), where floods of the latter, southern river peak in March-April, while the main stem at Manacapuru (Solimoes River) peaks in May-June (Fig. 4.4d).
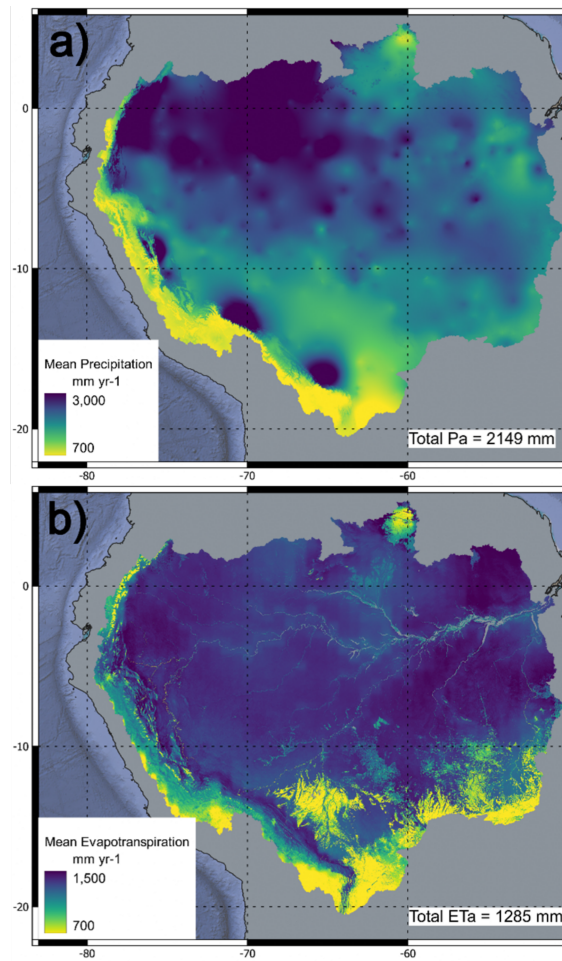
Figure 4.3: Amazon basin, distribution of a) Mean annual precipitation (from Worldclim version 1; Hijmans et al. (2005)) and b) Mean annual evapotranspiration (from MOD16A2/A3; Mu et al. (2007))

Sediment transport

The basin consists of three geomorphological units (Constantine et al. (2014); cf. Fig. 4.4a), which steer sediment fluxes: The main source of sediment flux in the main stem (Solimoes and Amazonas River) are the Andean mountains, a region of high relief consisting of highly erodible sedimentary and volcanic rocks (Dunne et al. (1998)). Accordingly, the Amazon rivers that drain this region carry the highest sediment loads (in the hundreds of $Mt\ yr^{-1}$ per river, e.g., Ucayali, Madeira; Armijos et al. (2020)), followed by rivers which originate in the sedimentary rocks of the Central Through (in the tens of $Mt\ yr^{-1}$ per river, e.g., Purus, Jurua; Filizola and Guyot (2009)). The least amount of sediment is carried by the rivers that drain the relatively plain, low relief shields of the north and the south (e.g., Negro, Tapajos; cf. Fig. 4.4a). Early studies from Sioli (1957) and Gibbs (1967) have shown that mean sediment concentration decreases from source (Ucayali River) to mouth (Amazon River at Obidos), affirming the im-

portance of the Cordillera on Amazonian sediment fluxes. Subsequent measurement campaigns have shed light on the temporal dynamics of sediment transport (Meade et al. (1985)), highlighting the importance of storage and resuspension of sediment in the lower Amazon reach (Manacapuru to Obidos) during the rising and falling stage of the flood wave. Meade et al. (1985) also estimated the mean annual sediment flux F_a at Obidos as 1200 ± 200 $Mt\ yr^{-1}$. This range has since then been confirmed by a modern setup of measurement stations of the HYBAM initiative (F_a=1122 $Mt\ yr^{-1}$; cf. Armijos et al. (2020)). The HYBAM network not only extended our knowledge of annual sediment fluxes from the Amazon basin's major subbasins (cf. stations Fig. 4.4a), but also made it possible to distinguish the distinct signals of fine ($45\mu m < particles <= 65\mu m$) and coarse (particles>65μm) sediment. The latter is important, as the transport of finer sediment is correlated to upstream rainfall rates, whereas coarse sediment transport is a function of discharge regime (Armijos et al. (2020); cf. Fig. 4.4c). This result is related to the water surface gradient which has been shown to be upstream Manacapuru twice as large during the rising limb of the flood wave than during the falling limb, and reversely downstream of Manacapuru largest during the falling limb (Meade et al. (1985)). This potentially provides more power for resuspension and transport of coarser particles during different stages of the flood wave and contribute to a net deposition of 200 $Mt\ yr^{-1}$ of sediment in the channel between Manacapuru and Obidos (Dunne et al. (1998)). Apart from transport and deposition within the channels to the Atlantic, Dunne et al. (1998) have shown that a significant amount of sediment is deposited in the floodplain of the central through. According to the authors, the main processes affecting the net sediment budget of the Solimoes-Amazonas stretch and therefore the sediment exchange between the channel and the floodplain are suspended sediment transport, bank erosion, bar deposition, diffuse and channelized overbank deposition as well as in channel storage. Combined they result in 500 $Mt\ yr^{-1}$ of sediment being deposited on the Amazonian floodplain in Brazil.

4.2.3   *Data collection and assimilation*

For the estimation of energy fluxes and their respective efficiencies, we work with three types of datasets: 1) Flow and sediment transport variables directly measured at gauging stations (Measurement stations), 2) estimates of flow and transport from peer reviewed publications (Studies), and 3) secondary data products, derived from physical, statistical and artificial neural network models (Models).
While the first type represents point measurements that are scattered in time and space, the second type provides estimates of flow and transport for the time interval and region of the study, based on mea-

Figure 4.4: Hydrology and sediment transport of the Amazon Basin: a) Main streams of Amazon River network (HydroSHEDS, 2022), physiographic provinces (after Constantine et al. (2014)) and sediment measurement stations from HYBAM (Armijos et al. (2020)); b) Monthly mean rainfall P_m (WORLDCLIM v1; cf. Hijmans et al. (2005)) and monthly mean discharge Q_m (HYBAM, 2022) in mm $month^{-1}$ at Obidos measurement station; c) Monthly mean concentration of fine sediment C_f and coarse sediment C_c in mg L^{-1} at Obidos station (from Armijos et al. (2020)); d) Monthly mean discharge Q_m in m^3 s^{-1} at Obidos (Amazon River), Manacapuru (Solimoes River) and Fazenda Vista Alegre (Madeira River) measurement stations (HYBAM, 2022).

surements obtained from individual measurement campaigns. The third type contains information distributed in time and space at different resolutions.

For the analysis in the following, we first give an overview of the different types of data and derived data products which were used for this study. We collected freely available data from public sources and reviewed the derived estimates. In this study we assessed the distribution of discharge from the gauging station datasets, we derived spatial distributions of sediment fluxes through combining published estimates and assimilated the data with global model results. The result allows an evaluation of energy dynamics within the entire Amazonian River network.

Measurement Stations

The temporal and spatial distribution of discharge within the Amazon Basin has been subject of numerous measurement campaigns (Meade et al. (1985)). For long term standardized measurements fewer reliable sources exist. At a minimum, each country that is part of the Amazon basin (AB) has appointed an official entity that operates a network of measurement stations that operate under different standards and norms, but not each country makes these measurements publicly available. the measured data on discharge was therefore collected from the following sources:

ANA BRAZIL   The Agencia Nacional de Aguas (ANA) of Brazil is responsible for the implementation of the national hydrometeorological network. This network consists of 4641 monitoring sites throughout Brazil, of which 1874 relate to measurements of transport of water and sediments in rivers and 2767 measure meteorological variables like rainfall and temperature. The database also contains point measurements of sediment concentrations as well as hydraulic variables like water depths, composition of cross sections, and flow velocities. The data is accessible through a web portal, free of charge at https://www.snirh.gov.br/hidroweb/mapa.

ANA PERU   The Agencia Nacional del Agua (ANA) of Peru is responsible for the administration of the national water resources and their management. The country's hydrography is separated into basins that drain into the Pacific Ocean, basins that drain into the Lake Titicaca, and the Amazon region. The online database (https://snirh.ana.gob.pe/observatorioSNIRH/) gives access to over 295 stations within the whole Peru, of which we selected 15 river gauging stations of the Peruvian Amazon basin (cf. Fig. 4.5) for computation

of mean annual discharge.

HYBAM   The observatory for hydro-geochemistry of the Amazonian basin (HYBAM) is operational since 2003, monitoring rivers and water resources in the Amazon. This transboundary effort covers long-term hydrological, sedimentary and geochemical measurements from the Andes Cordillera to the Atlantic Ocean. It consists of 17 stations collecting data to understand the origin and evolution of waters and transported materials. Data can be obtained after registration at https://hybam.obs-mip.fr/data/.

GRDC   The global runoff data center (GRDC), established by the World Meteorological Organization (WMO) provides an archive of over 10000 river gauging stations from 159 countries with time series of daily discharge data up to 200 years old. For the study at hand, we extracted 198 stations within the Amazon basin, of which we used the official record for mean annual discharge as provided by the GRDC. The database does not contain data on sediment transport. Data for regions of interest can be obtained through https://portal.grdc.bafg.de/.

All sources provide free access to continuous as well as point measurements of discharge and sediment transport variables. Fig. 4.5 shows the spatial distribution of the selected measurement stations and data collection sites within the Amazon basin. In total, we work with 59 stations from ANA Brazil, 16 stations from ANA Peru, 14 stations of the HYBAM data set, and 164 of the GRDC database. Several stations are included in more than one dataset, leading to a total of 217 unique gauging stations which were used in this study (cf. Appendix A.3.1, and Fig. 4.5). For discharge we judged the GRDC dataset as the base dataset and excluded overlapping stations from the other datasets.

Studies

The AB has been subject of various sediment measurement campaigns since the 1950s (e.g., Sioli (1957); Gibbs (1967); Schmidt (1972)), but it was only in the 1980s that Meade et al. (1985) reported the first width- and depth- integrated measurements of suspended sediment discharge. These studies had in common that they reported sediment fluxes for the main river of the Amazonas- the Solimoes-Amazonas, which discharges into the Atlantic Ocean. Beyond that, some studies on sediment transport have been conducted within individual sub basins of the Amazonas (e.g., Guyot (1993)). For an estimation of spatially distributed sediment fluxes within the entire Amazon Basin we combined three independent studies on sediment transport from the last 20 years (Dunne et al. (1998); Filizola and Guyot (2009); Armijos
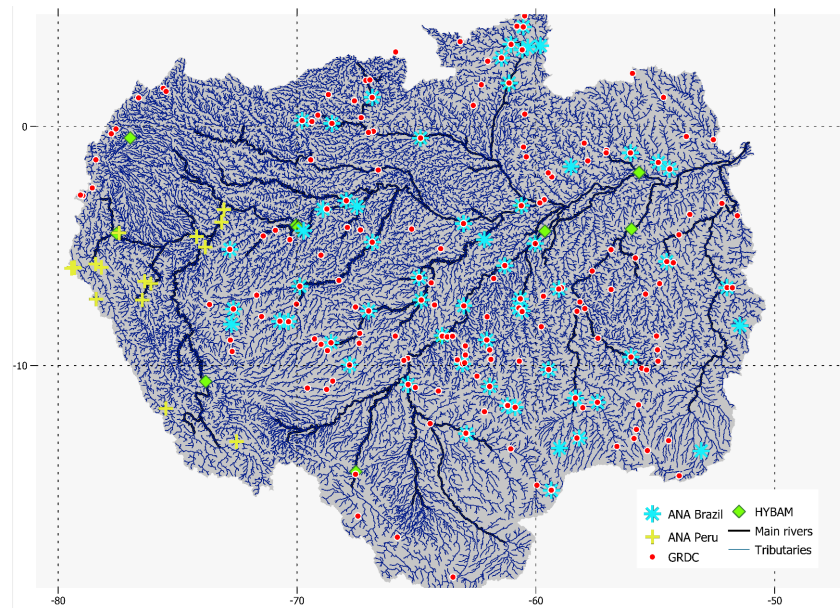
Figure 4.5: Overview of discharge and sediment measurement stations from GRDC, HYBAM, ANA-Peru and ANA-Brazil

et al. (2020)). To our knowledge the estimates from those 3 studies currently represent the most reliable, comprehensive and complete data on sediment transport in the Amazon Basin. The obtained estimates of sediment flux and respective discharge are shown in Appendix A2.

DUNNE ET AL. (1998)   The authors calculated the balance of sediment fluxes for 2100 *km* of the lower Amazon River in Brazil. In their methodology they separated suspended sediment transport from bedload transport and calculated sediment exchange fluxes between the river channel and the floodplain. Their measurements show that bedload transport accounts for roughly 1% of the suspended load, and that roughly 20% of the suspended sediments can be classified as sand (particle diameter > 0.06 *mm*) while the rest is silt and clay (particle diameter < 0.06 *mm*). They estimated similar to Meade et al. (1985) a sediment flux of 1239 *Mt yr*$^{-1}$ at Obidos, and additionally showed that around 500 *Mt* of sediment is net deposited on the Brazilian flood plain every year.

FILIZOLA AND GUYOT (2009)   As part of the HYBAM initiative, Filizola and Guyot (2009) reviewed the Brazilian national data set on flow and transport in the Amazon Basin. The dataset contained more than 2000 sediment samples, which were taken at 60 measurement stations between 1970 and the time of the study. They applied three different techniques (QS1, QS2, QS3) to calculate sediment fluxes from concentrations and compared their results to newer, standardized measurements, concluding that the QS1 technique resulted in most

reliable estimates. Their results (cf. Appendix A2) reconfirmed the importance of upstream sediment influx from the Andean Mountains and indicated net sediment deposition in the constrained floodplains of the lower Amazonas. The authors concluded that the dataset is well suited for estimating the spatial and temporal distribution of sediment fluxes within the basin but limitations due to outdated sediment sampling techniques should be acknowledged.

ARMIJOS ET AL. (2020)   As part of the HYBAM initiative, Armijos et al. (2020) undertook an effort to estimate the influence of rainfall on sediment fluxes within the Amazon Basin. Their database consisted of over 3000 sediment samples, collected every 10 days during 20 years from 1995 until 2014 at five gauging stations of the principal Amazonian rivers. Like Dunne et al. (1998) the measurement approach distinguishes between sand and silt-clay fractions, which the authors found to follow distinct temporal transport dynamics. Armijos et al. (2020) showed that 60% of the total sediment load can be attributed to finer particles which are linked to rainfall, while the coarser rest is linked to discharge regime. Estimated total sediment fluxes are shown in Appendix A2.

Models

We used the HydroATLAS database which combines a range of global model results from the fields of hydrology, physiography, climate, landcover, soils and geology, as well as anthropogenic influences with stream networks (Linke et al. (2019)). In the following we briefly present the underlying models for the variables we used in this study.

HYDROLOGY   The natural discharge in the HydroATLAS dataset is based on the WaterGAP Hydrology Model (WGHM, cf. Döll, Kaspar, and Lehner (2003)). The model computes surface runoff, groundwater recharge and river discharge for spatial resolutions of 0.5°. The results are based on global data sets and was tuned with observed discharge at 724 gauging stations, accounting for 50% of the global land area. Computed long-term mean discharges lie within 1% error range for half of these stations and individual corrections were made for the other half. Consequently, WGHM represents a reliable tool to estimate global long-term water availability at high spatial resolution and was therefore deemed applicable for representing the distribution of mean annual runoff in the Amazon Basin.

PHYSIOGRAPHY AND RIVER NETWORK   The topological representation of the Amazon basin, its subbasins and its stream network in this study is based on the HydroSHEDS database (Lehner, Verdin, and Jarvis (2008), cf. Fig. 4.5). The database was developed by the

Conservation Program of the World Wildlife Fund and is primarily based on NASA's Shuttle Radar Topography Mission (SRTM). The approach for delineation of stream networks and river basins is outlined in Lehner, Verdin, and Jarvis (2008) and can be accessed under www.hydrosheds.org. The elevation profile of each river segment is based on EarthEnv-DEM90 (Robinson, Regetz, and Guralnick (2014)).

CLIMATE   Mean annual precipitation of accumulated catchment areas has been adopted from the Worldclim model (Hijmans et al. (2005)). Worldclim provides interpolated climate surfaces for global land areas at a spatial level of 30 *arc s*. For this study we used distributed mean annual precipitation for the Amazon Basin, which is based on measurements from 1950 until 2000. The model uses a thin-plate smoothing spline algorithm, interpolating mean monthly precipitation values with latitude, longitude and elevation as independent variables. Results are less reliable in mountainous areas where the density of available climate stations tends to be lower than in more accessible terrain.

Data preparation

The collected data on measured discharge and related hydraulic geometry is scattered in time and was aggregated to represent mean annual dynamics for each measurement location. We used the dataset from ANA Brazil for measurements of daily discharge, which was subsampled for each station per year if the time series covers at least 90% (300 days) of the selected year. Subsequently, we calculated an average annual mean of these subsampled daily discharges. Point measurements in time of discharge Q_p, mean flow velocity v_p, river width w_p, as well as mean water depth d_p, are available for a subset of the selected stations (cf. Appendix A.3). In a next step, we calculated wetted cross-section $A_p = Q_p/v_p$ and estimated the wetted perimeter as $P_p = w_p + 2d_p$, which seems to be a reasonable estimate as river widths are on average many times larger than mean water depths. Finally, the hydraulic radius was calculated as $RH_p = A_p/P_p$. For all of these, we fitted power laws with discharge as the dependent variable: $Variable = a(Q_p)^b$

The resulting curves are then used to extend point measurements in time of v_p,w_p,d_p,RH_p to mean daily values v_d,w_d,d_d,RH_d, from which we then computed annual means v_a,w_a,d_a,RH_a. For fitting of power laws we used a technique similar to Kirchner (2009). First, we binned the available data points and calculated a mean of each bin (cf. 4.6). Here we allowed a minimum of 3 and a maximum of 20 data points per bin, while each bin contains an equal amount of data points. In the next step we fitted a linear curve to the bin means on logarithmic axis, from which the coefficients *a* and *b* of the power law can be derived.

For each fitted curve we calculated the coefficient of determination R^2 to the original data, extended the point measurements to the date range of daily discharge and computed a mean annual value for each station. The resulting coefficients and mean annual values are listed in Appendix A3.

Due to the highly dynamical character of the Amazonian rivers as well as the long time series, measurement stations have been recalibrated or rebuild when deemed necessary by the responsible operator. This necessarily leads to differences in absolute values of the measured variables if not adjusted. Moreover, measurement of flow is subject to hysteresis effects of the flood wave. Although the ANA Brazil dataset provides measurements since the 1950s, both aspects lead to significant uncertainties when dealing with such data without further details, and we therefore excluded several measurement stations from the analysis of hydraulic geometry. From the built power curves, we accepted those which resulted with our approach in a R^2 larger than 0.5, which was the case for 23 stations for w_p, 56 stations for d_p, 57 for v_p, and 56 for RH_p out of a total of 60 (cf. Appendix A3).
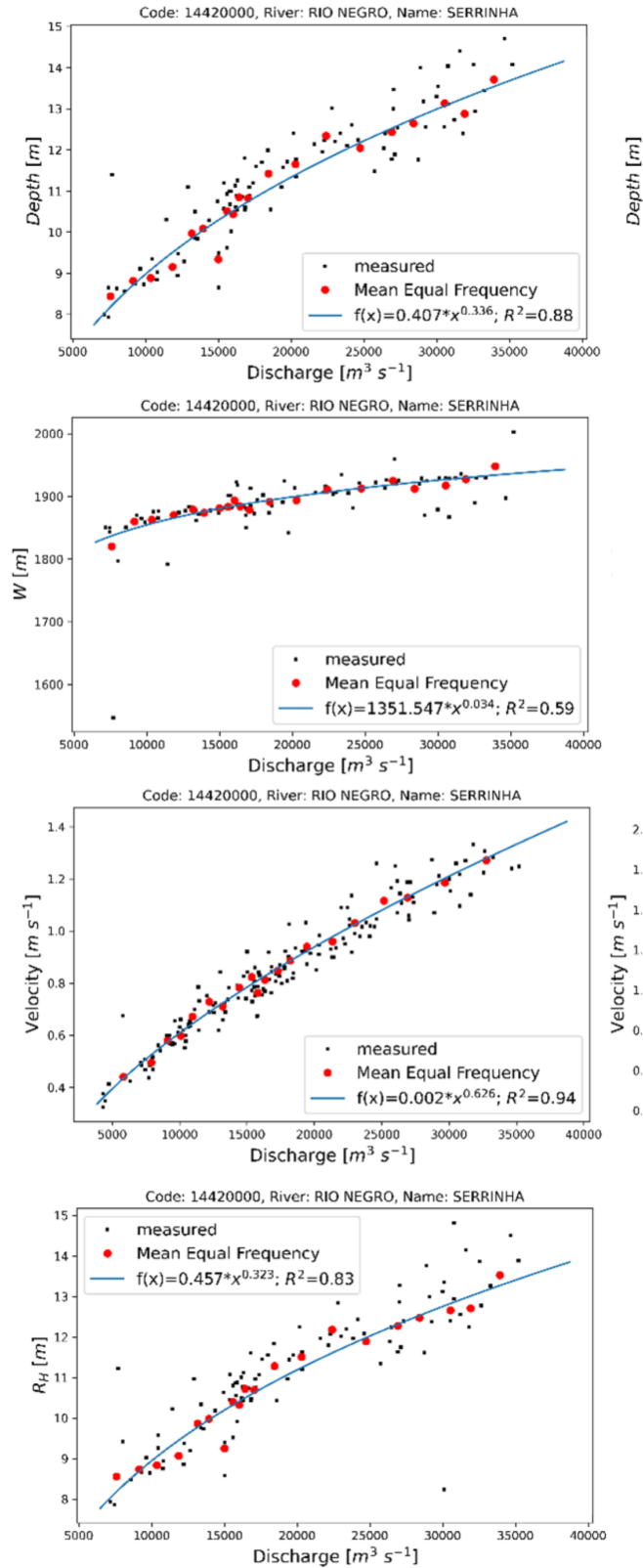
Figure 4.6: Sampled and processed measurements of mean water depth d, river width w, flow velocity v and hydraulic radius R_H vs. discharge at gauging stations Serrinha (Rio Negro).

Data assimilation

To combine the reviewed information about flow and sediment transport, we developed a methodology which is shown in Fig. 4.7. First, we extracted the river network and the relevant attributes of the AB from the HydroATLAS database. In a second step we applied an algorithm that connects individual river segments of the network and the locations with discharge and sediment measurements. The algorithm searches first for the river segment which is closest to the coordinates of the measurement station and then compares accumulated upstream area. If the difference is within 10% the segment is accepted and connected to the measurement station. If the difference is larger than 10% the algorithm moves along the flow path one segment downstream and repeats. Some measurement stations could not be connected, probably due to inaccurate coordinates of the underlying datasets and were either connected manually or discarded if no relation could be found. As a result, each considered measurement location was connected to the HydroATLAS database, relating the measured variables of discharge and sediment transport to stream network descriptors and third-party model results. The connector is represented by an individual stream segment ID and the respective model attributes (cf. Appendix A1 and A2).
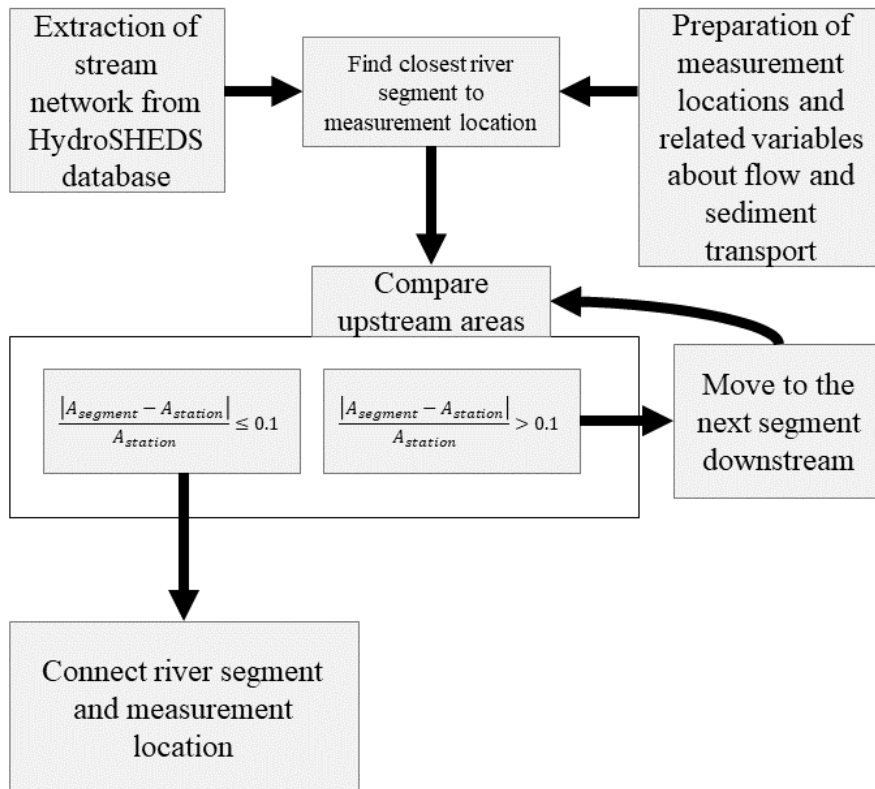
Figure 4.7: Schematic of the applied data assimilation procedure

4.2.4   *Energy dynamics of the largest river in the world- The Amazonas*

Annual mean dynamics of water and sediment flow

For the estimation of annual mean dynamics of discharge and sediment transport we used the processed datasets as presented in Appendix A.3.1 and A.3.2. As pointed out previously, discharge and sediment transport are spatially very heterogeneous, which becomes particularly obvious when comparing specific Amazonian rivers and their subbasins. In Fig. 4.8 and Fig. 4.9, we therefore distinguish at a very basic level between the northern Rio Negro basin, the southern Rio Madeira basin and the main basin of the Amazonas-Solimoes River with its Andean tributaries, the Rio Ucayali, Rio Napo, Rio Maranon as well as the lower tributaries of the Rio Purus, Rio Javari, and Rio Jurua. In rough terms we compare the physiographic units of the northern and southern shield with the Andes including the central through (cf. Fig. 4.4). The assimilated data sets enable us to show mean annual discharge and sediment transport as a function of upstream accumulated area as well as distance downstream until the Atlantic Ocean. Fig. 4.8 shows the computed mean annual discharge Q_a in m^3 s^{-1} (panels a and b), mean annual rainfall of the upstream area P_a in m^3 s^{-1} (panels c and d), and the resulting mean annual runoff coefficient R_a (panels e and f) for each considered measurement station. On average Q_a as well as P_a are both linear functions of upstream catchment area A_{cc} (panels a and c), but there exist marked differences between physiographic regions for Q_a. The Negro Basin (NB) carries the largest mean annual discharge for a given basin area, even larger than Q_a of the same A_{cc} of the main stem (AB), while the Madeira Basin (MB) carries much less discharge for an equal basin area (panel a). This difference can only partly be explained by larger rainfall rates in the NB, as total rainfall differences between NB, AB and MB are smaller than differences in runoff rates. This can be confirmed by comparison of runoff coefficients R_a (panel e), where largest R_a are related to the NB and lowest to the MB. Interestingly, R_a seems to decrease downstream the flow path of the NB but increases along the flow path of the MB. Differences between Q_a of these basins become even more evident when comparing discharges along an increase of distance (instead of area), e.g. the distance downstream to the Atlantic (cf. panels b,d, and f). The NB shows the largest increase per flow path length for both Q_a and P_a from the three basins, the second largest is then the MB and smallest the AB (panels b and d). Although this result hints at the on average larger rainfall rates in the NB than the MB, it is striking that the AB shows the smallest increase in discharge and rainfall per flow path length of all three basins. For all three basins the increase of Q_a and P_a is largest upstream and decreases in downstream flow direction (panels b and d). Along the flow path the variation of runoff coefficients is different for each river (panel f).

Similar to panel e, R_a decreases along the flow path in downstream direction for NB but increases in the MB. For the AB, and therefore the main Amazonas River, overall runoff coefficients first rise from 5000 *km* to 2700 *km* upstream where R_a peaks with almost 0.9 and then decreases until Obidos measurement station (700*km* upstream of the Atlantic Ocean) to a value of 0.5.
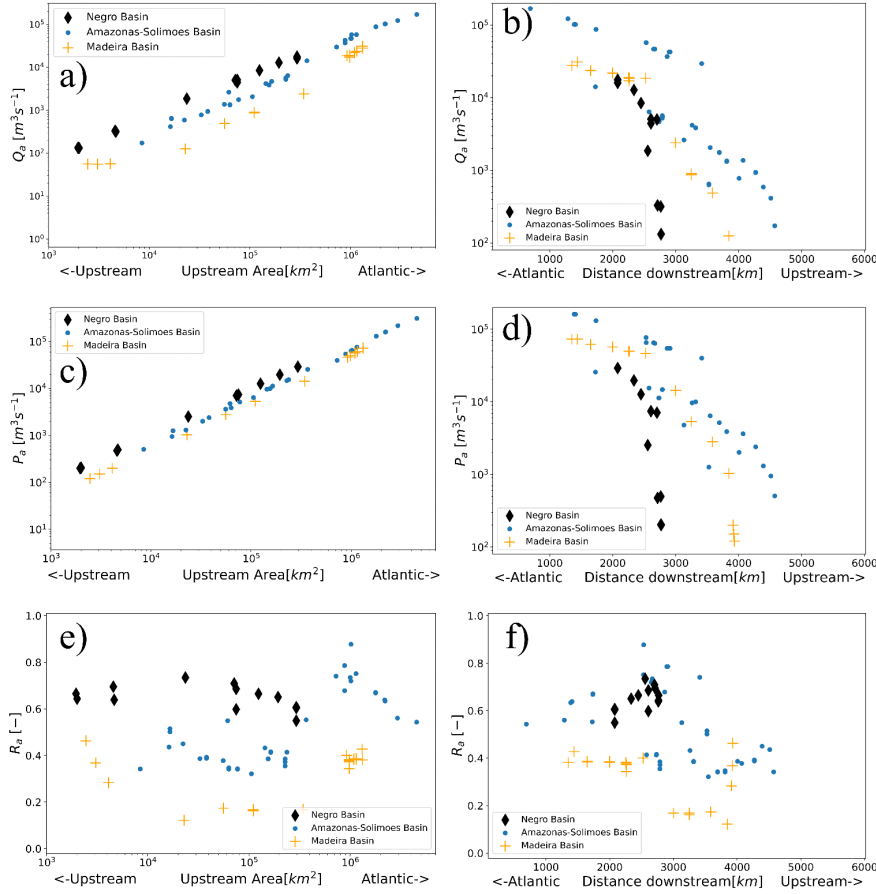
Figure 4.8: Mean annual discharge Q_a, mean annual rainfall in the upstream catchment P_a, and the resulting runoff coefficient R_a vs. upstream accumulated area A_{cc} (a, c , e) and vs. distance downstream to the Atlantic Ocean (b, d , f) for the available measurement stations (cf. Appendix A.3.1).

The reported sediment fluxes are plotted in Fig. 4.9 for downstream distance to the Atlantic Ocean l_{dn} (panel a and c) and for upstream accumulated catchment area A_{cc} (panel b and d). Total sediment flux Q_{Sed} at Obidos is estimated to exceed 1200 *Mt yr^{-1}* (panel a), a result of an almost constant increase along the main stem flow path of the AB. Q_{Sed} increases by similar rates for the MB but stays very low for the NB. In stark contrast, sediment flux increases with increasing A_{cc} for the AB and the MB particularly when surpassing 10^5 *km^2* (panel b). Until this point $Q_{Sed,a}$ has hardly reached 10% of the reported sediment flux at Obidos. From 10^5 *km^2* to 10^6 *km^2* the sediment flux

of the AB increases approximately by a factor of 10, indicating a linear relationship between $Q_{Sed,a}$ and A_{cc} for this part of the AB. Along the flow path in downstream direction sediment yield $Q_{Sed,sp,a}$ of the AB is decreasing (panel c), which highlights the influence of the Andes as main sediment source. However, $Q_{Sed,sp,a}$ of the MB increases in downstream direction until its confluence with the Amazonas River. When sediment yield is plotted against A_{cc} (panel d), largest $Q_{Sed,sp,a}$ is computed for intermediate regions between 10^5 km^2 to $2*10^5$ km^2. Sediment yield rates increase before this point and decrease after. Sediment yield of the NB stays almost constant and very low for all available measurement stations.
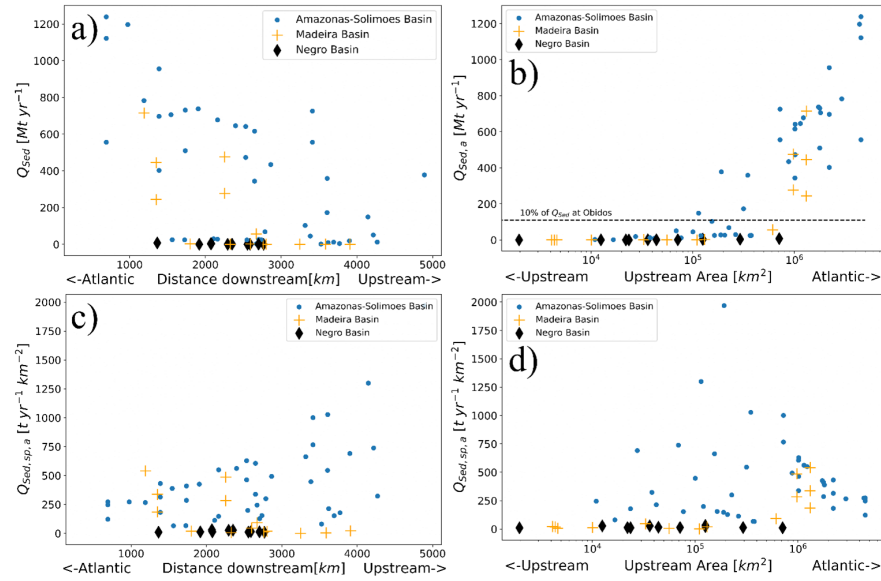
Figure 4.9: Mean annual sediment flux $Q_{Sed,a}$ and mean annual sediment yield $Q_{Sed,sp,a}$ vs. upstream accumulated area A_{cc} (b, d) and vs. distance downstream to the Atlantic Ocean (a, c) for the available measurement stations (cf. Appendix A.3.2)

Distribution of free energy

As outlined in 4.2.1 we represent the four main types of free energy that relate to discharge and sediment transport as annual mean flux (in *watt*) for each available measurement station: 1) Potential energy of rainfall $J_{P,a}$, 2) potential energy of discharge $J_{Q,a}^{pe}$, 3) Kinetic energy of discharge $J_{Q,a}^{ke}$, and 4) kinetic energy of sediment $J_{Sed,a}^{ke}$. Each flux can then be analysed along a flow path distance or as a function of upstream accumulated catchment area. Additionally, we computed specific free energy fluxes per A_{cc} (in *Watt km^{-2}*). The results are shown in its entirety in Appendix A4, in the following we summarize for each type of free energy flux the major findings.

Energy influxes through rainfall are linearly dependent on upstream accumulated area (Fig. 4.10a). A distinction can be drawn between

measurement stations which measure discharge which largely origi-
nates in the Andes or in the Andes foreland and the Amazonian
shields. For a given A_{cc} largest $J_{P,a}$ relates to the Andes and smaller
free energy fluxes to the shields. We estimate the total mean annual
energy influx (its maximum at Obidos) as potential energy by rainfall
as 1.49 x 106 MW, or equivalently 13000 terawatt hours, which is more
than the total primary energy consumption of all South America (cf.
https://ourworldindata.org/). When computed as specific energy
flux per unit area $J_{Q,a,sp}^{pe}$ shows marked differences between the physio-
graphic regions of the AB (Fig. 4.10b). Not surprisingly largest values
are found in the Andean catchments, which decline with decreasing
ldn as most geopotential height is lost between 6000 to 3500 km dis-
tance downstream to the Atlantic. The largest specific energy flux is
observed at Piedra Luisa measurement station in Ecuador with an
annual mean of 1.72 $MW\ km^{-2}$. From the energy influx by rainfall
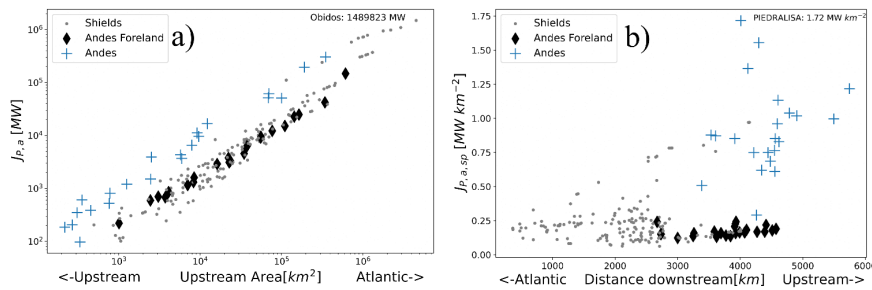
Figure 4.10: Accumulated energy influx in the Amazonas basin as a) total
flux and b) flux per accumulated upslope area

results at each point of the drainage network an energy flux by dis-
charge. This free energy flux can be separated into a flux of potential
energy $J_{Q,a}^{pe}$ and kinetic energy $J_{Q,a}^{ke}$. Fig. 4.11a shows that along the
flow paths of the river network, potential energy first accumulates
until its peak at Nazareth measurement station (close to the border
between Peru, Colombia and Brazil) on the Amazonas-Solimoes River
and only afterwards decreases. Most of the increase is due to accu-
mulation of flow with high geopotential in the Andes, while the net
loss of potential energy is related to the lowland of the AB. $J_{Q,a,sp}^{pe}$
confirms this finding, as almost all energy fluxes above 0.1 $MW\ km^{-2}$
lie within the Andean Cordillera. The specific energy flux is largest at
the beginning of the flow path and decreases until the Atlantic (Fig.
4.11b). Next in the presented free energy cascade 4.2 is the kinetic
energy flux by discharge $J_{Q,a}^{ke}$, which is plotted against d_{dn} in Fig. 4.12a.
Interestingly, throughout most of the network $J_{Q,a}^{ke}$ is very small and
almost constant. There is however a medium range, approximately
between 3000 km to 1500 km distance downstream to the Atlantic,
where much larger values are observed. Peak $J_{Q,a}^{ke}$ is found at Itapeua
measurement station with 158 MW. For $J_{Q,a,sp}^{ke}$ we find a positive trend
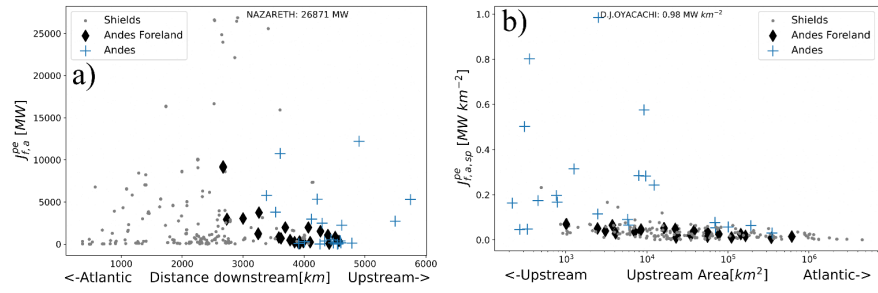
Figure 4.11: Accumulated potential energy flux a) total along flow path distance and b) per unit area for upslope area

with increasing upstream accumulated catchment area (Fig. 4.12b). Smallest fluxes occur upstream for smaller upstream areas and largest specific energy flux occurs farther downstream. Of the four analysed
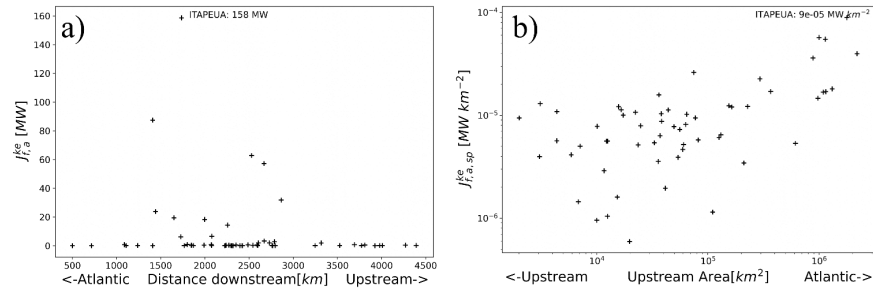
Figure 4.12: Accumulated kinetic energy flux a) total along flow path distance and b) per unit area for upslope area

free energy fluxes, kinetic energy flux of sediments is the smallest. From the initial influx of energy by rain only a miniscule amount remains in the transport of sediment (Fig. 4.13a). $J^{ke}_{Sed,a}$ increases from upstream to downstream, peaking at Obidos with 0.039 MW. $J^{ke}_{Sed,a,sp}$ is largest for an intermedian range at approximately 10^5 km^2 (Fig. 4.13b).
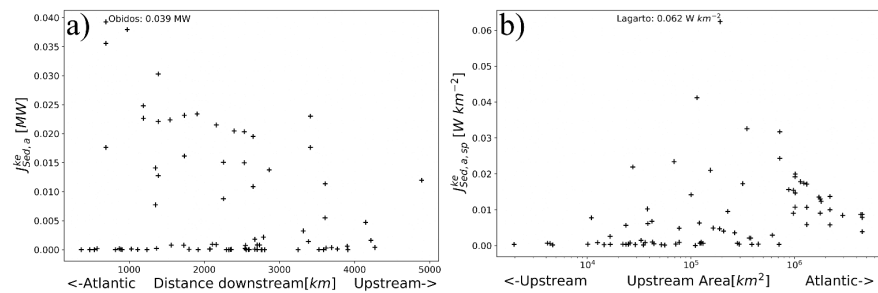
Figure 4.13: Accumulated sediment energy flux a) total along flow path distance and b) per unit area for upslope area

Energy efficiencies of water and sediment transport

From the distribution of free energy fluxes (cf. previous section) the hypothesized efficiencies of energy conversion rates E_P (Rainfall potential energy to discharge potential energy), E_Q (discharge kinetic energy per discharge potential energy gradient) and E_{sed} (Discharge kinetic energy to sediment kinetic energy) can be calculated for the assimilated dataset. E_Q can be converted into the hydraulic radius R_H if we assume that average friction coefficients within the river network stay constant, while E_{sed}, if multiplied by the density of water, represents the average concentration of sediment mass per water volume C_{sed}. We plotted E_P, R_H and C_{sed} against accumulated drainage area (Fig. 4.14a to c) and against distance downstream (cf. Appendix A.3). For E_P we distinguished the main subbasins of the Amazonas, which highlights the large differences in energy efficiency between them. In general terms, energy efficiencies are largest upstream and diminish with increasing A_{cc} until the last measurement station close to sea level and therefore with almost zero energy and minimum E_P. For the stations of the Negro basin, we find much larger energy efficiencies than for the Madeira basin. On the way downstream both decrease in energy efficiency, with minimum levels reached when entering the mainstem of the Amazonas River. The largest E_P is at D.J.Oyacachi station with over 63% of the upslope potential energy influx by rainfall maintained as potential energy of discharge.

The hydraulic radius is plotted against upstream area in Fig. 4.14b. Interestingly R_H increases linearly with A_{cc}, peaking at Itapeua measurement station with an annual average of $38m$. In contrast, C_{sed} sees an increase until roughly $10^5 km^2$ to $3*10^5\ km^2$, where concentration levels peak with $1831\ mg\ L^{-1}$ at Lagarto measurement station. After this peak, concentration levels decline continuously in downstream direction towards the Atlantic Ocean.

4.2.5 *Discussion*

In this section we have estimated the principle free energy fluxes of water and sediment within the Amazon basin. Therefore, we assimilated various data sources and model results into a single dataset consisting of average annual discharge, sediment transport and hydraulic geometries. Our results show that the specific free energy per upland area minimizes along the flow paths in downstream direction. This result was confirmed by analysis of average efficiencies of energy conversion rates, showing an overall decrease of energy efficiency with increasing upstream area. We see that a distinction needs to be drawn between global (within the network) and local (at the cross-section of the measurement station) patterns of energy efficiencies.

More specifically, although the overall energy efficiency E_P decreases
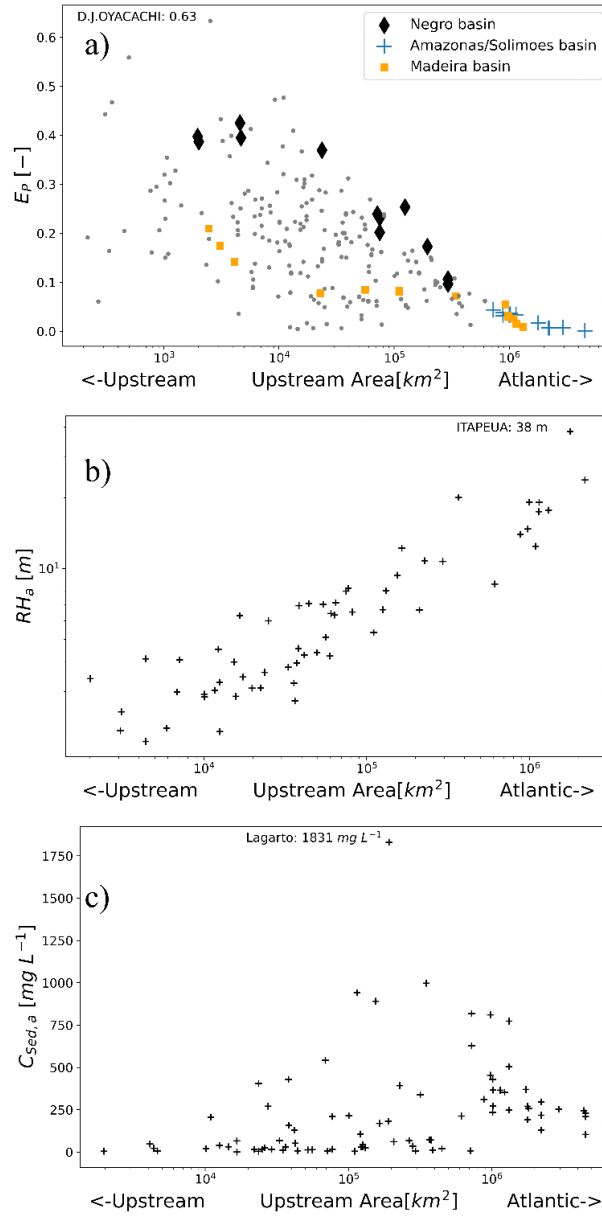
Figure 4.14: Efficiency of converting a) Energy influx to potential energy of discharge, b) Energy gradient of discharge to kinetic energy, c) kinetic energy of discharge to kinetic energy of sediments

in downstream direction, the hydraulic radius, which expresses the efficiency of how much potential energy can be converted into kinetic energy, grows. We hypothesize that this is possible, as kinetic energy fluxes represent only a minute amount of the total free energy flux and therefore do not affect the overall energy efficiency of the catchment. Rather, larger R_H provide the means to decrease potential energy even faster, therefore additionally decreasing E_P. Similarly, C_{sed} decreases along the flow path, therefore dissipating less energy from the kinetic energy of the water, which once more facilitates a faster decrease of E_P with increasing upland area. Apart from these energy conversion rates it is interesting to note the particularities of the energy fluxes which enables this general pattern of E_P decrease. Most strikingly of all, the main free energy flux of the network $J_{f,a}^{pe}$ peaks within a median range of distance downstream to the Atlantic at Nazareth measurement station, while it also linearly accumulates with A_{cc}. This finding signifies a shift of perspective of catchment energy dynamics. The dynamics scale with accumulated area but result along a flow path in a part of the river that net accumulates energy and a part of the river that net dissipates energy.

4.3 THE PERFECT RIVER- AN ANALYSIS OF THREE TRANSCENDENTAL PROPERTIES OF RIVER NETWORKS

4.3.1 *Theoretical background*

In this second part of the case study, we go beyond local free energy dynamics of water and sediment and search for fingerprints of structural equilibria of the whole river network. We have identified three different properties which have previously been related to a river's structural equilibrium in space (Horton (1945), Leopold and Langbein (1962), Stølum (1996)), and which we have already mentioned the hydrophysical approach (Horton (1945)) and the thermodynamic approach (Leopold and Langbein (1962)) in 1 but give a brief review in the following. Additionally, we present Stolum's theory about self-organized criticality. The three concepts have in common that they represent dimensionless properties of stream networks, a powerful tool which can be used to analyse network dynamics in the phase space (Stepinski et al. (2002)). The underlying theory suggests that a dynamical system is attracted to a certain critical state in this phase space, a state we refer to as dynamic equilibrium, and which is defined by the environment. E.g., Glacial networks have been found to show distinctly different channel patterns than fluvial networks (Grau Galofre and Jellinek (2017)).

The first property relates to Horton's method of ordering river networks, refined by Strahler (1957). Today known as the Horton-Strahler stream order, it allows a dimensionless analysis of basic hydrographic

Law	Equation	Usual range	Source
Law of stream numbers	$R_B = \frac{N_\omega}{N_{\omega+1}}$	$3 < R_B < 5$	Horton (1945)
Law of stream length	$R_L = \frac{L_{\omega+1}}{L_\omega}$	$2 < R_L < 3$	Dodds and Rothman (2000)
Law of drainage area	$R_A = \frac{A_{\omega+1}}{A_\omega}$	$3 < R_A < 6$	Schumm, Harvey, and Watson (1984)

Table 4.1: Horton laws (as derived from stream network ordering according to Strahler (1957)) with N_ω as the number of stream segments classified for HS-order ω, L the mean length of a stream segment, and A the mean upstream acccumulated area, cf. Fig.4.20b

properties of stream basins and their drainage networks. When ordering stream segments by this simple method (cf. table 4.1 and Fig. 4.20b) one can derive Horton's laws of stream number R_B, stream length R_L, and drainage area R_A (Shreve (1966)). Several studies showed that Horton's laws hold throughout most terrestrial stream networks (e.g. Knighton (1998); Dodds and Rothman (2000)). The constants of the Horton laws are outlined in table 4.1.

The second property refers to the vertical profile of bed level along the river's flow path. Long it has been observed that the average geopotential height along the flow path decreases exponentially, that is to say, the slope of the riverbed in flow direction decreases towards the outlet of the basin. Different theories exist (e.g. Tanner (1971)) but we refer in this section mainly to the thermodynamic theory from Leopold and Langbein (1962) who conceptualized the river segments as individual thermodynamic systems (heat machines) which maximize overall entropy production (cf. i). The authors showed that the most probable state of a river's flow path is characterized by a spatially uniform value of entropy production, which can only be achieved if the vertical profile is exponentially declining in geopotential height and slope. Maximum entropy production along a flow path is therefore achieved when at each point slope is a linear function of the river's geopotential, or differently stated slope divided by geopotential is constant.

The third analysed property of a river which relates to structural (and therefore energetic) equilibrium refers to a rivers structure in the horizontal plane. The sinuosity S_V of a river describes the typically observed pattern of meanders along a fixed flow path length and for a fixed scale (cf. Eq. 4.12).

$$S_V = \frac{L}{l} \tag{4.12}$$

Where L is the length of the river along its course from a point A to a point B, and l is the shortest length between the same points. Although sinuosity is highly transient in space and time, Stolum put forward a theory that describes the bend creating process of outer bank erosion and the bend cut-off process by inundation and erosion during flood events as a stable cycle. A meander is therefore in a subcritical state if sinuosities are very small, the river has few bends

and flows straight downstream the steepest gradient. Opposed is the supercritical state with large sinuosities and many bends with more cut-off events to be expected. He hypothesized that the scale-independent attractor S_V^{SOC} of this cyclic meandering is a critical state can be described by an average sinuosity of π. He proved his theory of self-organized criticality (SOC) for a numerical model (Fig. 4.15) as well as for the meandering of the Jurua River of the Amazon Basin. In total we therefore distinguish between five non-dimensional
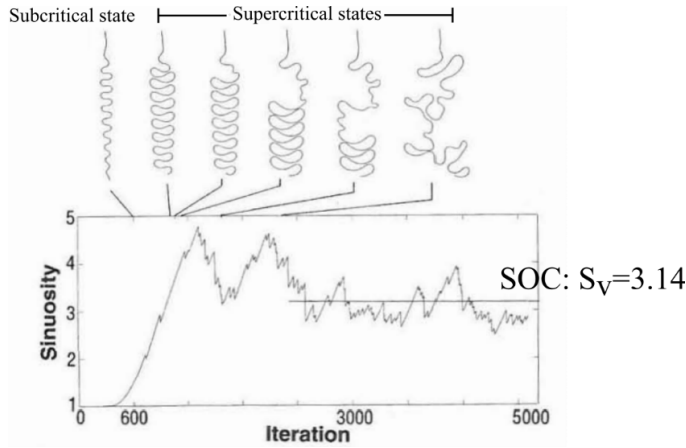
Figure 4.15: Evolution of sinuosity from a numerical model (adjusted from Stølum (1998))

constants, three from the Horton laws (R_A, R_L, R_B) and one each from thermodynamic (cf. Eq. 1.9) and dynamic system theory (S_V^{SOC}). In fact, we hypothesize that all of them are related to mathematical constants that are believed to be transcendental numbers, which persistently occur in the mathematical description of the natural world. These kind of numbers cannot be expressed as the root of a polynomial, meaning they are not algebraic. In the following we scan the structures of the world's largest river networks for these transcendental numbers.

4.3.2 Database

The mentioned constants relate to the 3-dimenional structure of a river network. The HydroSHEDS (Linke et al. (2019)) network provides this information for the network (streams number, area, and length), as well as for the individual flow path extension in the horizontal plane (sinuosity) and the vertical plane (stream profile). Although we acknowledge uncertainties regarding scale and accuracy of the dataset (e.g., streams were derived from a 90m resolution digital elevation model), we assume that the dataset suffices for our purpose of analysing large scale structural patterns, which emerge on a scale of several thousand kilometers of flow path.
We extracted the for each considered basin its network and each

River	Basin Size km^2	Q_a m^3s^{-1}	Ω_{max}
Amazonas	5912919	205604	10
Congo	3705049	39635	9
Niger	2098664	6859	8
Nile	2916802	1934	8
Rio de la Plata	2594295	18311	9
Mississippi	3179496	21894	9
Mackenzie	1795841	9232	9
Ob	2467589	13754	9
Lena	2453574	15803	9
Yenisei	2489751	19719	9
Ganges Brahmaputra	1574223	40392	9
Yangtze	1909199	31067	9
Mekong	774281	15252	8
Amur	1998203	10899	9
Yellow River	761252	1490	8
Murray	775219	256	9
Danube	786749	6745	8
Rhine	163008	2451	7

Table 4.2: The world's largest rivers with data of catchment size, annual mean flow Q_a and largest Strahler number Ω_{max} from Lehner, Verdin, and Jarvis (2008)

stream's topological attributes (coordinates, length, elevation) from the HydroSHEDS database and ordered the rivers according to the Horton-Strahler stream ordering system (Fig. 4.16). Streams with lowest order start where the head basin accumulates at least 10 km^2, resulting in a (terrestrial) maximum order of 10 at the outlet of the Amazon Basin. We repeated this ordering process for all basins of table 4.2, which combined provide roughly 50 percent of the global terrestrial discharge into the oceans and cover 25 percent of the world's land area.

4.3.3   *Fingerprints of structural equilibrium in river networks*

The 18 selected river basins (4.2) were processed and the Horton laws, sinuosities as well as the vertical profiles were sequentially computed. In the following we show this procedure exemplary for the AB, the largest river network on earth and analyse the results of all considered
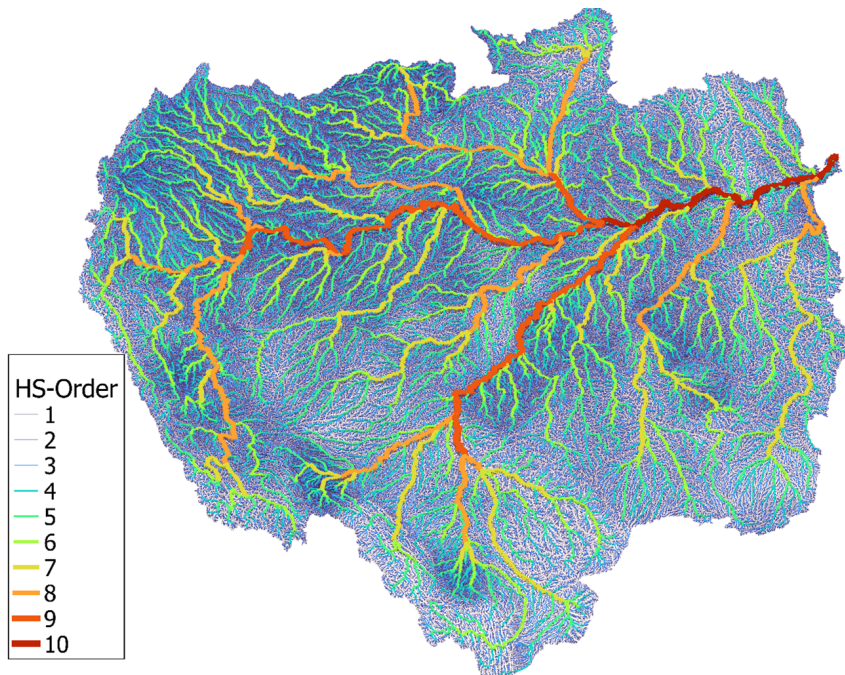
Figure 4.16: Amazonas stream network, ordered by Horton-Strahler system

networks.

The river profile

The first property is based on the principle of maximum entropy production (Leopold and Langbein (1962)). If a river can be approximated by a chain of heat machines, each heat machine (river segment) should produce the same amount of entropy. For this to hold true, slope divided by geopotential height must be a uniform constant. For testing this concept in the AB we selected for each river segment with HS-order of 8 the longest flow paths from upstream to the Atlantic Ocean, resulting in a total of 58 flow paths for the AB (Fig. 4.17a). Each of these flow paths we subsampled into 9 equally long segments, from which we created flow paths to all downstream segments, resulting in $9 + 8 + 7 + 6 + .. + 1 = 45$ sub-segments ($FP_{tot} = n(1 + n)/2$, with n as the number of segments). To each of these sub-segments we fitted then an exponential profile of the form $f(d_{dn}) = a\,e^{(b\,d_{dn})}$ with a and b as parameters, and selected the fitted curves with an R^2 above 0.9 as best fits (Fig. 4.17b). Repeating this step for all 58 flow paths of the AB resulted in sub-segments with near to perfect exponential profiles for distinct subsampled flow path segments. In Fig. 4.17c we plotted the vertical extension of the selected flow paths as well as the best exponential fits in relative lengths for the AB.

According to these results flow paths follow a perfect exponential profile within certain restricted flow path distance and not along the
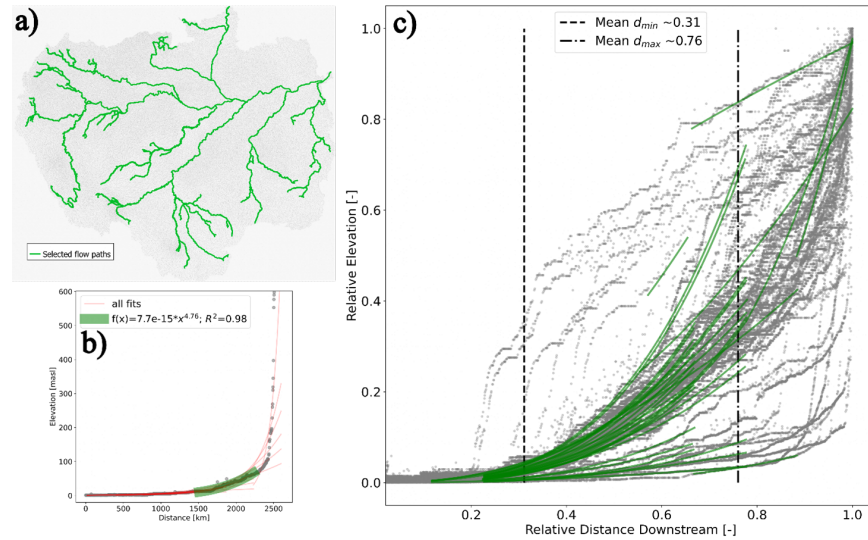
Figure 4.17: a)Selected flow paths Amazon basin, b)Fitted exponential profiles to single flow path, c) Best fit of all flow paths

whole path. For the Amazon basin these exponential profiles start on average at 0.76 of total distance downstream and end at 0.31 of $d_{dn,max}$. We conclude that average vertical profiles follow exponential laws in a strict sense (see above) only within a medium range of flow path distance. For the AB this medium range corresponds to the Andes foreland and the lowland, but not to the Andes themselves and neither to the last 20-30% of flow path distance before entering the Atlantic Ocean. An optimal river profile, in the sense of Leopold and Langbein (1962) is therefore only present within a limited medium range. We hypothesize that this is a result of the build-up of energy in the upper part of a catchment (cf. 4.2), while the medium range relates to the net decrease of energy along the flow path. The last bit before the Ocean shows virtually no topographic slope and is partially influenced by the tide, which could mean that flow in this part is principally the result of inertia and much less due to a defined energy gradient. We repeated this procedure for other rivers from table 4.2, of which we had to exclude several river networks that lie far north due to large uncertainties in the accuracy of geopotential from the underlying digital elevation models. However, from the included river networks we find very similar patterns of elevation profiles (cf. Appendix A.3.5). We conclude that rivers maximize entropy production according to Leopold and Langbein (1962) only within a limited medium range of flow path distance, and we believe that this is the result of the mentioned energy increase and decrease along a rivers flow path.

Sinuosity of the meandering river

Sinuosity S_V was calculated for all river networks along all represented flow paths within the HydroSHEDS data base. As outlined

by Stølum (1998) S_V is a fractal property which scales with the considered segment length. Therefore, we applied like Woolderink et al. (2021) an algorithm that calculates sinuosity of each segment and for increasing length scales. For a representative flow path in the AB we found maximum sinuosities to increase with length scales (Fig. 4.18a) from $17km$ to $901km$, and decreasing with larger length scales. On average largest S_V is observed within $2000km$ to $4000km$ of distance downstream. We also categorized for each considered length scale the resulting S_V with HS-order and calculated mean as well as maximum sinuosity for each HS-order (Fig. 4.18a and Fig. 4.18b). For the AB mean sinuosity increases from HS-order 1 to 8, then peaks at HS-order 8 with a mean value of 1.5 to 1.6 and decreases to 1.2 until the last segment of HS-order 10. Maximum sinuosities for each HS-order are plotted in Fig. 4.18c. Of these, absolute maxima can be related to the proclaimed state of self-organized criticality (SOC) by Stølum (1996), close to a value of π. For the AB we find that the maxima of S_V are indeed close to SOC, especially for HS-order 2,3 and 5. Likewise for computed S_V in downstream direction, maximum values seem to be limited by a value of π (Fig. 4.18a, dashed line). We repeated the described analysis for all river networks of table 4.2 and found similar results for maximum sinuosity. Fig. 4.19a shows the mean sinuosity of all considered river networks against HS-order. The results indicate that the increase of mean S_V up to HS-order 7 to 8 and the subsequent decrease is a general pattern of all networks. Maximum mean S_V we find for HS-order 8 with an average value of 1.5. It is interesting to note that mean values between different networks are very similar for HS-order 1 to 5 and differ greatly for orders above 6. Maximum sinuosities for each HS-order and river network are shown in Fig. 4.19b. Although within each order maximum values are highly variable, it is striking that the mean of these maximum values lies astonishingly close to the theorized state of SOC at $S_V = \pi$ for HS-orders 2 to 7 (0.1% error for HS-order 2 to 5 and 10% error for orders 6 and 7).
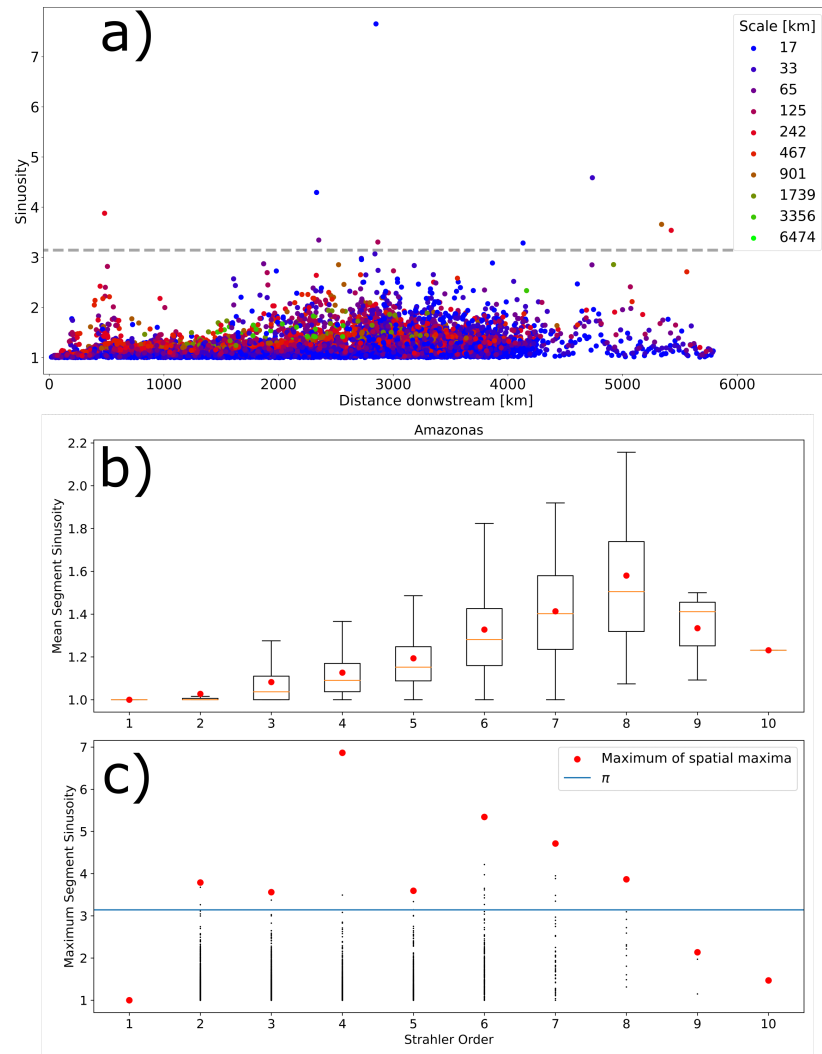
Figure 4.18: a) Sinuosities as a function of scale for the Amazon basin, b) Mean sinuosity and c) maximum sinuosity

Horton laws

We computed total stream number N, mean stream length L, and mean accumulated drainage area A_{cc} for each river network by first finding all stream segments that make up a HS-order segment and second grouping those segments into HS-order bins. Of these bins we then calculated the mean (A_{cc} and L) or the total counts (N). The result can be seen Fig. 4.20 for the Amazonas River network (values normalized by maximum). From the log-linear trends, seen in Fig. 4.20, it becomes clear that the Horton laws are imprinted in the Amazonas network. We repeated these steps for all river basins of table 4.2 and calculated the Horton numbers R_L, R_B, R_A (cf. table 4.1, Fig. 4.21). It is interesting to note that it is only assumed that the Horton numbers are constant throughout terrestrial networks, and that the given ranges refer to a spatial mean which is derived by fitting a linear curve to
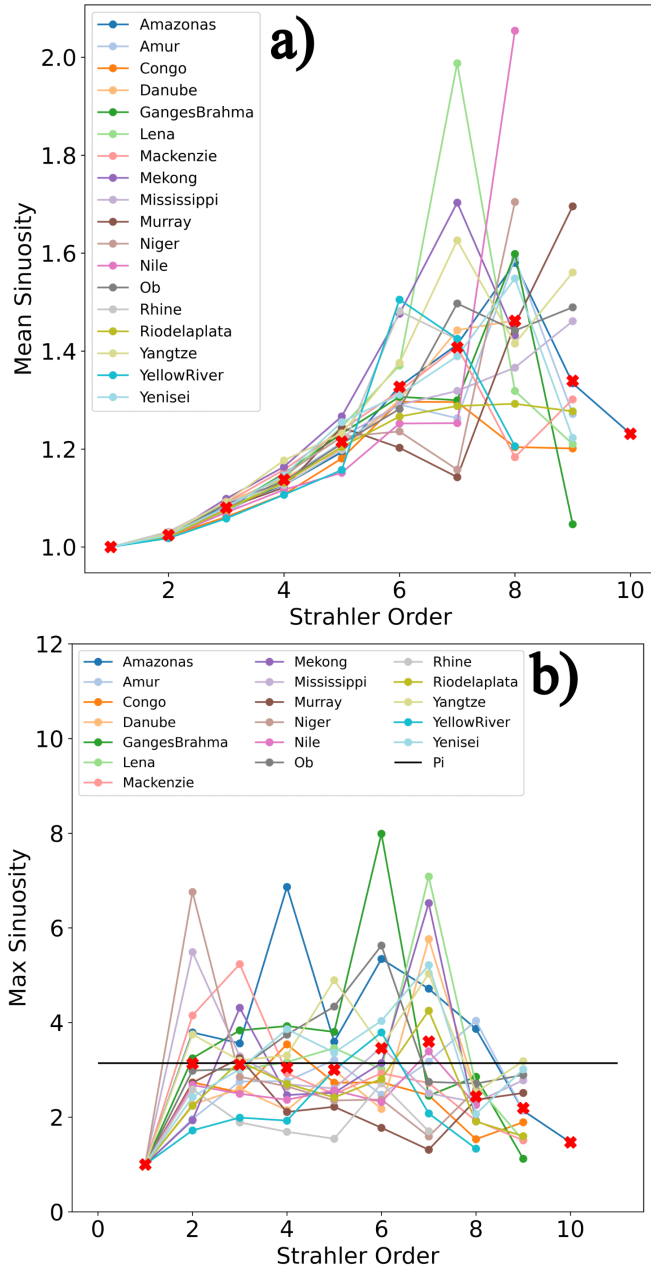
Figure 4.19: World a) Mean sinuosities and b) maximum sinuosities
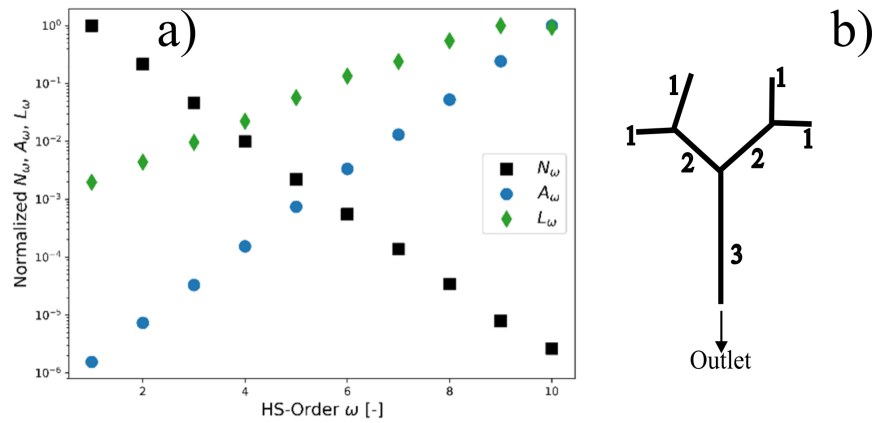
Figure 4.20: a) Normalized stream number N_ω, accumulated drainage area A_ω and stream length L_ω against HS-order ω for the Amazonas River network, b) Example of Horton-Strahler ordering for a network of $\omega = 3$

the log-plot (Fig. 4.20, cf. Appendix A.3.5). Here, we plotted R_L, R_B, R_A against the HS-order for the considered networks instead and computed for each order individual statistics (Fig.4.21). By doing so we find that the ratios of larger orders are quite dispersed, but that with decreasing order the numbers seem to converge (or from up-to downstream diverge). R_B and R_A converge to a number between 4.5 and 4.7 and R_L converges towards a number between 2.4 and 2.6 in upstream direction. In the following section we will explain our hypothesis why we think that these numbers correspond to the Feigenbaum numbers δ and α for 1-dimensional nonlinear maps (cf. Fig.4.22).
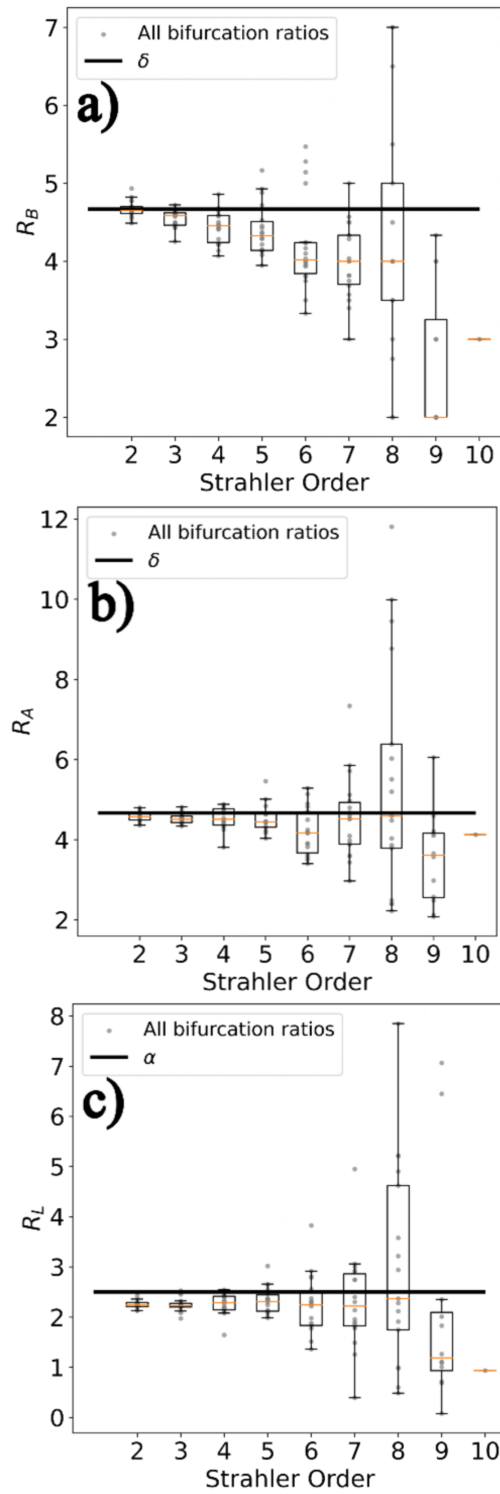
Figure 4.21: Horton numbers a) R_B, b) R_A, c) R_L vs. HS-order for the largest river networks in the world (cf. table 4.2) and corresponding Feigenbaum numbers δ and α

4.4   DISCUSSION: IS THE STRUCTURE OF RIVER NETWORKS CHAOTIC?

In this section we have analysed three non-dimensional properties which relate to the morphology of river networks. We found that for each property exist distinct spatial regions, either expressed as flow path distance or as HS-order, where these properties are close to being constant. The vertical river profile divided by the gradient is found to be constant for a medium range of both, which we hypothesize is most probably due to the pattern of energy increase and decrease along the flow path. A section with an increase of energy along the flow path should therefore not be related to an exponential profile. Exponential profiles might in consequence relate to flow sections where energy decreases (dissipates), which is a major assumption Leopold and Langbein (1962) made when claiming maximum entropy production along a flow path. Along these sections, geopotential decrease is a linear function of geopotential, which can only be the case if the profile relates to the transcendental number e. Similarly, we have shown that maximum sinuosity is limited by the transcendental number π, in fact we computed mean S_V from the largest river networks on earth below 0.1% of difference to π.

Apart from these findings which relate the three-dimensional structure of individual flow paths to some equilibrium state we further hypothesize that the Horton laws and the respective constants relate to the Feigenbaum constants (Fig. 4.22), which were first discovered by Feigenbaum (1978). In a mathematical sense the constants arise from a system of which the dynamics can be described by a nonlinear difference equation. The most famous example is probably the logistic map, popularized by May (1976), an equation which was used to model simple population dynamics in biology:

$$N_{y+1} = rN_y(1 - N_y) \tag{4.13}$$

Where N_y is the relative population in one year and N_{y+1} the relative population of the next year (N between 0 and 1). The value r represents the reproduction rate, while the second term in brackets is thought to capture a density-dependent mortality which is largest when the systems current population is closest to the maximum capacity ($N = 1$). For N to remain bounded within 0 and 1, the growth and decay parameter r has to stay within 0 and 4. The attracted state depends on r, with bifurcations occuring at discrete values (cf. Fig. 4.22). At some point when r surpasses some critical value the attracted state is described as chaos (Gleick (1988)).

Feigenbaum ([1978](#)) found that for all one-dimensional non-linear maps the ratio of the intervals between occuring bifurcations as well as their tines' widths approach in the limit (cf. Fig.[4.22](#)) the constants:

1. $\delta = \lim_{n \to \infty} \frac{n_i}{n_{i+1}} = 4.669201609103...$

2. $\alpha = \lim_{d \to \infty} \frac{d_i}{d_{i+1}} = 2.502907875095...$
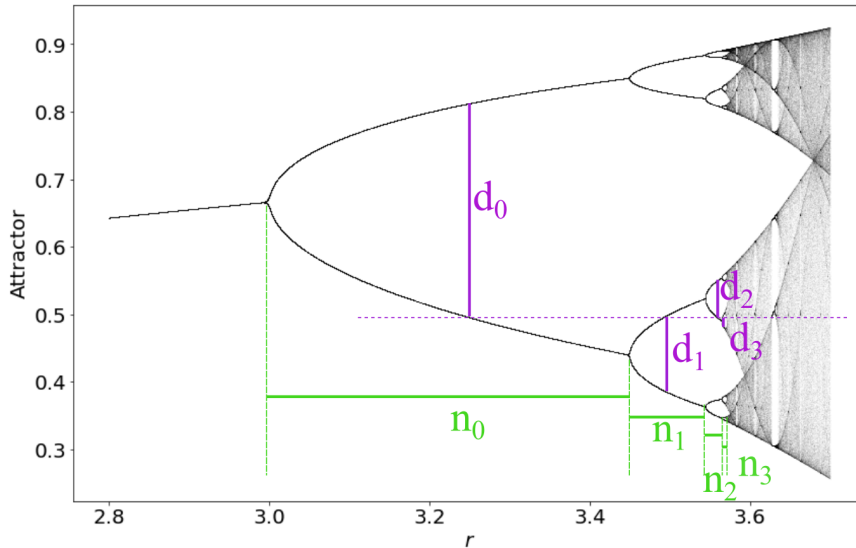
Figure 4.22: Bifurcation diagram of [4.13](#)

In the context of a river network, we put forward the idea that a river basin can also be expressed by a simple nonlinear map such as Eq. [4.13](#). In this case the nonlinearity arises in the spatial domain instead of the temporal domain, and the system transitions along the flow path from a chaotic state into an ordered state. We hypothesize that these nonlinear dynamics can be explained with the entropy balance of the system in space. A chaotic state in the upstream parts of the basin might therefore relate to high entropy and the ordered downstream state at the outlet represents low entropy. However, as mentioned in [iii](#), we must be precise to which type of entropy we refer to. At the upstream part of the river basin, we imagine a river network in a state of high entropy as there are many possible states in which the network might be organized. This means if the upstream accumulated area is small, our knowledge of the structure of the system is small as entropy is high. Slopes may be greater or smaller, while discharge regimes fluctuate more and are therefore less predictable. The more area is accumulated, the more certainty we can express about average dynamics of the runoff system, such as slope or average runoff. For example, in Fig. [4.23](#) we plotted for the AB mean annual runoff coefficients R_a, unit runoff Q_U, and average upstream slope, of each included stream segment against accumulated upstream area A_{cc}. The

spread of each of these variables decreases with increasing A_{cc}, which we think is equal to a decrease of the system's entropy. As entropy cannot disappear, it must be exported by the system's dynamics to its surrounding environment. This happens through mass and momentum export by hydrologic processes, or more generally by dissipation of free energy. In Appendix A.3.6 we outline the parallels between the morphological evolution of a runoff system and May's model of population growth. We recognize that such a model is a gross simplification of the complex water cycle of a hydrological system, however it provides a first starting point to see hydrological processes as nonlinear dynamics of a dissipative system. The here presented analysis of nondimensional properties provides evidence that feedbacks of opposing processes result in a state where the hydrological system fluctuates around a complex equilibrium state. Our analysis shows that this state is characterized by the transcendental numbers e and π, as well as the Feigenbaum constants α and δ. The latter are believed to be transcendental but a mathematical prove is still missing. We highlight the notion of transcendence, as it is striking that this property seems to be necessary to mathematically describe the structures of the natural world. While π and e were derived from shapes that were observed in nature (Archimedes circle (Arndt and Haenel (2001)), Bernoulli's continuous compounding interest (Boyer and Merzbach (1991)), the Feigenbaum constants were first discovered in mathematical theory (Feigenbaum (1978)) before they could be shown to exist in natural phenomena by Libchaber, Fauve, and Laroche (1983). For a Rayleigh-Bénard experiment Libchaber, Fauve, and Laroche (1983) meticulously determined the temperature differences between two plates at which convective cells add an extra frequency. They calculated Feigenbaum's constant to 4.4 ± 0.1 which led to the recognition of Feigenbaum's numbers as universal constants. Astonishingly, our simple analysis of large-scale stream bifurcations comes closest to Feigenbaum's delta as $4.669719\ldots$ (cf. Fig. 4.21a) which differs less than 0.1% from the theoretical value. For mean ratios of stream lengths, the closest value to Feigenbaum's alpha we found to be 2.312379 (cf. Fig. 4.21c) which is still below 8% of difference to the theoretical value, however there are some individual river basins for which the difference is even smaller (cf. Appendix A.3.7).

That there is a link between catchment evolution and nonlinear dynamical systems has also been observed by others. For example, Hooshyar et al. (2020) have recently brought forward a similar hypothesis, pointing out that equilibrium profiles of landscapes are remarkably similar to mean flow velocity profiles of turbulent flow, which is probably the archetype of a nonlinear dynamical system (Frisch (1995)). The best model of turbulent flow is still represented by the Navier Stokes equations, which Frisch (1995) showed can be rewritten as the "poor man's Navier Stokes equations" so that they essentially convey the
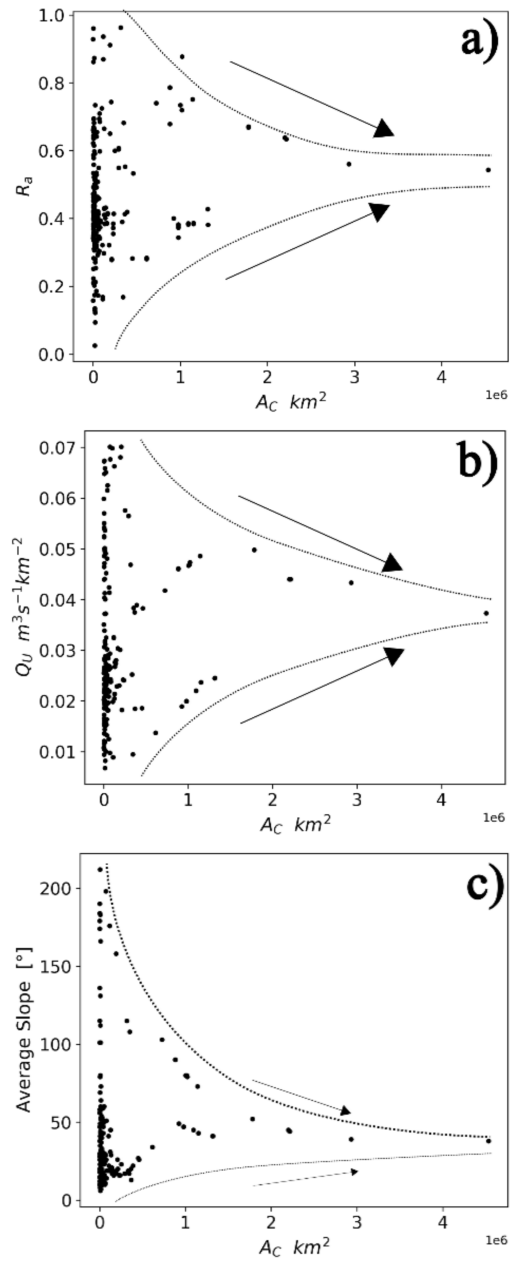
Figure 4.23: a) Mean annual runoff coefficient R_a, b) Mean annual unit discharge Q_U, and c) Mean slope of the Amazon Basin as a function of upslope draingage area

properties of the logistic map (Eq. 4.13, and Appendix A.3.6). However, we should also note that it is not exactly clear up to which degree turbulence is chaotic and chaos is turbulent (Ottino (1990)). Nevertheless, the similarities between chaos and turbulence are evident and if turbulence relates to equilibrium structures of hydrological systems, so does chaos.

4.5   CONCLUSION

In this chapter we challenge the classical perspective of surface runoff from river basins as being a predictable deterministic system. In the literature over the last centuries, a river is typically seen as an entity which is fed from rainfall and merely provides the means for the transport of water and solid matter (Horton (1945)), knowledge of the boundaries of the system should therefore suffice to predict the systems internal dynamics in accordance with mass and momentum balances. However, from a thermodynamic point of view the actual cause of runoff is the conversion of free energy into heat (Leopold and Langbein (1962)) and entropy. In the first part of this chapter, we have shown that a river's energy dynamics are highly complex, as along a flow path energy is not only dissipated into heat but also accumulated through the influx of mass. This leads to a section where free energy builds up, which is after some distance followed by a section where free energy is depleted. For the Amazonas River Basin we have shown that a peak of free energy is reached at approximately 50% of the flow path distance. At the same time decreases efficiency with increasing upslope area of the system, which means that relatively less free energy from rainfall is converted into free energy of runoff for a location farther downstream. We argue that this is equivalent to a maximization of entropy production in downstream direction, and we conclude that a distinction should be made for local vs. global energy dynamics of surface runoff. In the second part of this chapter, we show that the interaction between runoff and landscape leads to feedbacks which result in a dynamical equilibrium. Locally this state can be described e.g., by a limiting sinuosity of π and a mean vertical profile that decreases exponentially. Globally, we hypothesize that due to the nonlinearity of the energy fluxes the equilibrium of the entire river network is in fact better described by an attractor of a nonlinear system in phase space. We hypothesize that the well-known Horton-Strahler ratios of Stream area and stream length are directly linked to the Feigenbaum numbers δ and α of one-dimensional nonlinear maps. We believe that the here presented analysis of the largest terrestrial river networks presents evidence for our claim, however more research is needed for a sound theoretical foundation of our finding. One step forward might be to use theoretical landscape evolution models and

analyse bifurcation patterns with regard to different parametrizations of the underlying system equations.

Part V

SUMMARY AND SYNTHESIS

SUMMARY AND SYNTHESIS

5.1 KEY FINDINGS

In this presented work we foremost tackled an omnipresent problem hydrological research is facing when dealing with mass and momentum dynamics of the water cycle: In essence every approximated water flux is based on semi-empirical parameters which have to be derived from observations or need to be estimated (by inter- or extrapolation). For hillslope-scale surface and subsurface runoff we speak of conductivities that relate to physical and structural properties of the material the water flux is interacting with (Emmett (1970); Dunne and Dietrich (1980); Germann and Di Pietro (1999)), and for catchment-scale water fluxes we incorporate parameters which represent geology and climate (Horton (1945); Bonetti et al. (2020)). The classical physics-based recipe to make predictions of e.g., ungauged basins (Hrachowitz et al. (2013)), is therefore to somehow measure or estimate these (physical, chemical, or structural) properties and subsequently derive the water fluxes based on conservation of mass and momentum at the desired scale. Research has shown that these parameters can be highly dynamic in space and time (e.g. Abrahams, Parsons, and Wainwright (1994); Ali et al. (2012), Phelps (1975)) and are often not uniquely identifiable. In engineering practice however, they are more than often taken as static and whole feasibility studies of large-scale infrastructure projects can be underpinned with tables of estimated parameters for water fluxes (such as roughness parameters for hydraulic calculations or land use classes for derivation of stomata resistances for plant-transpiration as part of a hydrological study).

In this thesis we outlined the notion that there lies untapped potential in the identification and estimation of these parameters. We base this on the idea that essentially all physical processes of the water cycle can be unified under the banner of thermodynamic theory. The physical concept of energy, and its separation into free vs. bound energy can be applied to any quantitative flux and we therefore hypothesized that a closer look at the energy balance (1st law of thermodynamics) and the role of dissipation (which is the transformation of free into bound energy, cf. 2nd law of thermodynamics) holds potential for our understanding of the water cycle and beyond in geoscience. We put special focus on so-called dissipative structures which emerge at any scale of the water cycle (cf. Kleidon (2016)). Consequently, all three chapters (chapter II, chapter III and chapter IV) represent an analysis of structural properties that relate to surface runoff on different spatial

and temporal scales.

In the following we provide a brief resume of our approach and a short follow up on how the spatial and temporal scales interrelate to each other.

5.1.1   *Part II: Steady state surface runoff on hillslopes*

In chapter II of this thesis we analysed steady state surface runoff on hillslopes. We did this theoretically by using an empirical equation developed by Nearing et al. () that allowed the exclusion of a roughness parameter, but we also analyzed observed steady state runoff experiments from Gerlinger (1996). Both approaches confirmed our hypothesis that a) runoff and particularly dissipation rates are indeed spatially organized, and b) when separating surface runoff into sheet- and rill-flow (cf. Dunne and Dietrich (1980)) the resulting steady state dissipation rates resemble a maximum power configuration, which is typically observed in flow of electrical currents.

For the presented analysis of surface runoff, we applied the energy balance in its steady state form, reducing water dynamics to constant energy fluxes across the boundaries of a control volume. The main benefit of this approach is that the flow of water can be framed into a thermodynamic view, where free energy dissipates into bound energy, increasing the entropy of the surrounding environment. On the one hand this helps to explain the flow direction (from higher to lower geopotential; cf. Loritz et al. (2019) and Zehe et al. (2014)) and on the other hand it can be used to analyze the development of the system and its structures. For the case of surface runoff as sheet- and rill-flow this means that runoff minimizes along its flow path frictional loss of free energy but also maximizes overall dissipation along the whole flow path. On first sight this seems like a contradiction but can explained by highlighting the vastly different magnitudes on which minimizing local loss of energy and maximizing dissipation of the system operate. Loss of free energy is related to kinetic energy of the flow, while the system's entropy export relates to potential energy of the water. In this analysis we have shown, that for small scale hillslope plot experiments potential energy is on average by a factor of 103 larger than kinetic energy of surface runoff. This implies that even if kinetic energy of the flow would enlarge by significant amounts, this increase would hardly affect the overall energy balance as 99.9% of the potential energy is not converted into kinetic energy in the first place but was already exported as entropy from the system into the surrounding environment.

In the end we also wanted to highlight that the use of empirical parameters is useful to understand dissipation rates and the organization of structure of a system. A parameter such as Manning's *n* is not a physical property but the sum of a cascade of energy conversion processes

(e.g., Abrahams, Parsons, and Wainwright (1994)) which adhere in accordance with the second law of thermodynamics to the generation of entropy. This is also the reason why we highlighted in this chapter, that surface runoff undergoes a transition from laminar to turbulent flow regime from upslope to downslope. Laminar flow has explicitly a less frictional character, the water molecules are theoretically flowing in the form of vertically stratified layers into downstream direction, allowing for little transfer of free energy to heat. We therefore hypothesize that laminar flow relates to an increase of free energy along the flow path. With more free energy accumulating along the flow path, the gradient to zero geopotential also increases, which from a thermodynamic perspective leads to the necessity of more geopotential energy to be dissipated. We therefore argue that the transitioning from laminar to turbulent flow provides the necessary means to dissipate more free energy, faster.

All in all, chapter II is but a small step towards a less parameterized understanding of the governing physics of surface runoff. The presented empirical formula from Nearing et al. (2017) implies that fluxes (discharge) and their driving gradients (terrain slope) are interdependent, making the use of a roughness parameter more of a practical choice instead of necessity. Our findings support this theory for the steady state case, but we recognize that more evidence, especially for the transient case is needed for a conclusive argument.

5.1.2 *Part III: Transient surface runoff events*

Part III represents an extension of the preceding part II. We put again hillslope-scale surface runoff into a thermodynamic perspective of a system which exports entropy through dissipation of the free energy from water. The main difference to the preceding chapter II is that we release the steady state assumption and analyze transient events of surface runoff at the catchment scale. This idea stems originally from Wolman M. G. and Miller J. P. (1960), who pointed out that most (geomorphological) work (and therefore dissipation and export of entropy) within a catchment relates to events which have an intermediate range of recurrence. This is because work in the long run is not only dependent on magnitude, but also frequency of the event (cf. Beven (1981)). For a study of the interaction between runoff and landscape it is therefore an imperative to consider intermittency of the land-water system. We started by outlining different hillslope profiles which are typically observed in natural catchments and presented the original, still valid theoretical derivation of those by Kirkby (1971). On the basis of these structurally different hillslopes we then defined three rainfall-surface-runoff scenarios which we computed numerically by solving the full Saint-Venant equations (cf. Eq.1.6) in one dimension with a Mac-Cormack algorithmic scheme (Liang, Falconer, and Lin (2006)).

For a thermodynamic analysis we defined the concept of relative dissipation, which represents the ratio of free energy which has dissipated during a given time interval and within defined spatial boundaries (in this case the hillslopes that start at the drainage divide and end at the riverbank). For the defined scenarios we found that hillslope structures which relate to more diffusive erosion processes and where less surface runoff has occurred allow relatively more free energy to be conserved than hillslopes which relate to advective erosion processes. We concluded therefore that surface runoff and the induced erosion, lead to a hillslope-runoff system where the structures evolve towards a state of maximum dissipation. In this state the free energy influx by rainfall is depleted as fast as possible, in terms of energy efficiency this is equal to a system which evolves towards smaller energy efficiency. This is in line with any real-world machine, which over time loses some of its efficiency due to a relative increase in dissipation, e.g., through slow deterioration of individual machine components.

In the second part of the chapter, we included sediment erosion and transport into our analysis as some of the expanded energy from surface runoff is not immediately dissipated but instead is converted into free energy of the sediment particles. We proposed a formula which approximates this free energy transfer from water to sediments on an event-scale, by computing the theoretically necessary kinetic energy for the transport of the eroded sediment mass. To test our theory, we used the physics based Catflow model (Zehe et al. (2001)) which has been calibrated to simulate observed surface runoff and erosion events (Scherer et al. (2012)). The results thereof allowed a spatio-temporal analysis of energy efficiency in the Weiherbach catchment and confirmed our hypothesis that hillslope structures which relate to advective erosion processes tend to decrease energy efficiency of surface runoff. We find that most geomorphological work is done on hillslopes with specific structural patterns, this is similar to the results from Wolman and Gerson (1978) but in addition to their argument of maximum work being related to the frequency and magnitude of an event we also consider the structure of the system at hand. Our results suggest that a hillslope system adjusts its internal structures (macro- and micro topography) towards a state where the free energy influx is depleted as fast as possible. This state corresponds to a maximum power configuration (Kleidon et al. (2013)) and means that the dynamics of the system were stepwise downregulated through erosion and sediment export. The latter becomes evident by comparing relative dissipation rates and free energy transfer to sediment particles. Hillslopes with larger relative dissipation rates are less energy efficient, meaning less energy is transferred to sediment.

Finally, the hillslope system reaches a state which has been described by others as dynamic equilibrium (e.g. Gilbert (1876); Thorn and Welford (1994)). At this state the intermittent rainfall- runoff events

are damped, and quasi-steady, metastable configurations may emerge, as proposed e.g., by Howard (1990), Rodriguez-Iturbe et al. (1992) or Nearing et al. (2017). In chapter III we wanted to highlight that there is a clear link between the overshoot in power of intermittent, transient events and the evolution of a hydrological system towards a steady state configuration. The pathway of this evolution can be described by structural formations of the system, on a microscale e.g. in the form of rills (cf. Schroers et al. (2022)), then on the next larger scale in the form of hillslope profiles (this chapter) and finally it also becomes evident on the catchment scale, which we explored in the subsequent chapter IV.

5.1.3 *Part IV: Rivers and drainage networks*

In chapter IV we rescaled our perspective to energy dynamics of surface runoff of entire catchments. Just as on hillslopes, surface runoff in drainage networks and individual rivers is driven by an influx of free energy and dissipate this energy through a cascade of energy conversion processes. At this scale we assumed the catchments to be largely in dynamic equilibrium where geological uplift and fluvial sediment erosion are balanced (cf. Kleidon et al. (2013)). Some authors suggest that especially the largest of all terrestrial watersheds, the Amazon basin has evolved over time into a state of geomorphological, biological, and chemical equilibrium (Salati and Vose (1984)). Also, Latrubesse (2008) describes its anabranching main channel (the Solimoes River) as the ultimate end member adjustment of so-called mega rivers, which supports the idea that foremost the largest rivers (basins) in the world are found to be in some equilibrium state of energy fluxes.
In the first part of this chapter, we therefore focused on the free energy dynamics, dissipation, and work of surface runoff in the AB. First, we recollected available data about discharge and sediment transport from national databases and scientific datasets, which we then merged into a single product. We showed that like hillslopes, individual flow paths (rivers) of the catchment show first an increase of free energy, which peaks at some distance and then decreases until the watershed outlet at the Atlantic Ocean. We also showed how mass and momentum dynamics of surface runoff in a large basin such as the AB can be framed into an energy centered concept. When deriving separately the efficiencies of energy conversions from free energy of rainfall to potential energy of discharge (1), to kinetic energy of discharge (2), and finally to kinetic energy of the sediment (3) we show that these three efficiencies directly relate to the runoff coefficient (1), to the hydraulic radius of the river cross-section (2), and to the sediment concentration of the discharge (3). We found that each of the three energy efficiencies shows a very different spatial pattern in the AB: 1) The runoff coefficient decreases along the flow path, in line with the idea that

energy efficiency of surface runoff decreases; 2) The hydraulic radius linearly increases along the flow path, meaning more kinetic energy can be created from less geopotential gradient closer to the outlet; and 3) sediment concentrations peak at an intermediate flow path length. The results show that energy dynamics of the watershed scale with accumulated drainage area, whereas an analysis along the flow path reveals intervals of energy increase and intervals of energy decrease. The reason for this surprising behaviour could lie within Hack's law (Hack J. T. (1957)), which implies that drainage networks are fractal objects (Tarboton, Bras, and Rodriguez-Iturbe (1988); Marani, Rigon, and Rinaldo (1991)) as the relation between the measure of a network set (e.g., drainage area) and the unit of measure (e.g., flow path length) can be described by a power law (cf. Mandelbrot (1983)).

In the second part of chapter IV, we show that the structure of drainage networks can be described by transcendental numbers, which also relate to fractal objects. We extracted from a global dataset the largest terrestrial drainage basins and their drainage networks, and calculated the Horton laws of stream number, stream area and stream length, as well as patterns of sinuosity and average vertical river profiles. Our results indicate that the ratio of drainage areas (as well as stream number, cf. Marani, Rigon, and Rinaldo (1991)) corresponds to the Feigenbaum constant δ and the ratio of stream lengths corresponds to the Feigenbaum constant α. At the upstream part of the drainage networks up to a Horton-Strahler order of 4 to 5 we find δ within 0.1% and α within 8% of difference to the theoretical values of one-dimensional maps (Feigenbaum (1978)). Similarly, Stølum (1996) showed that sinuosity of a river is attracted to the value Π, a finding which we confirmed for the analyzed river networks with 0.1% difference to the precise value (all referred irrational numbers we truncated to 10 significant digits).We believe that this is due to the fractal nature of drainage basins, Π, α, and δ are an integral part of the Mandelbrot set (Mandelbrot (1983)). We close this chapter by arguing that the formation of structures at the watershed scale in the form of drainage networks is related to chaos theory, models of landscape evolution show that water and earth material form a non-linear feedback system- which are the basic ingredients for chaos. We elaborate on this hypothesis in the next section.

5.2 DISCUSSION AND OUTLOOK

In this thesis we have elaborated on the dynamics of surface runoff from hillslopes to rivers and their drainage networks. Historically the movement of water and its interaction with sediment were mostly treated as different processes which were therefore independently classified and analysed. Inspired by the work from Leopold and Langbein (1962), but also by more recent work from Kleidon et al. (2013) we came to the conviction that the interaction of surface runoff and the landscape has more to offer than the derivation of empirical parameters which can replicate the observed processes. As dynamics implies rates of a liquid or solid substance rather than static forces, thermodynamic theory seems very appealing to deal with evolving systems for an analysis of the individual units of the water cycle. However, as also pointed out by Thorn and Welford (1994), many concepts such as the idea of a dynamic equilibrium or the classification of a system itself is not always well defined. The confusion stems from the broad spectra of disciplines which applied thermodynamic concepts and developed ideas which that subsequently were transferred to hydrology and geomorphology without rigorous reframing. Leopold and Langbein (1962) themselves compared the flow of water to the flow of heat, leaving aside the nitty-gritty details of why geopotential energy should follow the same thermodynamic laws as temperature (cf. Eq. 14 in Leopold and Langbein (1962)). In general, we find that many ideas which surge in at the interface of geomorphology and hydrology have been lend borrowed from very different disciplines such as medicine (West, Brown, and Enquist (1997)), biology (May (1976)), economics (Lotka (1922)) or chemistry (Prigogine (1955)). In the following final sections paragraphs of this work, we therefore outline why and how we used these terms concepts and where we see potential for further developments.

5.2.1 *Dissipation as an agent of order*

As Kleidon (2016) points out, the dynamics of the water cycle can only be represented by open systems which are far from thermodynamic equilibrium. This means that free energy gradients are maintained rather than completely depleted, fuelling a cascade of energy conversions. As we have shown in this thesis, each conversion of one type of energy to the next creates entropy, which is exported from the system. The system therefore increases the entropy of its surroundings, meaning total entropy of the universe increases. The locked-in open system itself (e.g., the watershed) has been proclaimed to be attracted towards an equilibrium state where the rate at which this entropy is generated is maximized (cf. Kleidon et al. (2013); Berkowitz and Zehe (2020); Schroers et al. (2022)). This maximization is due to the opposing

processes of an increase of some variable that feeds back on its driving gradient. If entropy is generated by dissipation (as usually argued), the expression maximum dissipation (maximum entropy production, cf. Kleidon (2016)) is misleading as it implies that maximum quantities of free energy are converted into heat, which does not seem to be the case (cf. chapter III). Here we argue that an open system rather develops towards a state where the total free energy that is converted into heat decreases. In this state the system's internal structures have self-organized in such a way that the given gradient is depleted at the maximum rate (cf. chapter II, III). We therefore argue that in the case of real-world open systems it would be thermodynamically more adequate to speak of a maximization of relative dissipation rates instead of a maximization of absolute dissipation rates. In the universe absolute dissipation rates might be maximized but the earth's open systems seem to strive towards a state where an ever-smaller amount of energy is dissipated at the maximum rate. The accompanied structural self-organization and the resulting maximum relative dissipation rates depend on physical thresholds as well as the degrees of freedom of the system. Lovelock (1972) e.g., theorized that earth itself is an evolving open system (Gaia hypothesis) that is believed to maximize entropy production (Kleidon and Lorenz (2005)). To do so, the internal structures of the earth are evolving in a direction towards more entropy output, e.g., the growth of cities and the related conversion of low entropy energy sources such as gas or oil into high entropy radiation energy. Obviously, this growth is limited by the gradient (the availability of oil and gas) but also by thresholds, such as the invention of more powerful machines which can convert more energy of oil and gas at a faster rate into radiation. The resulting structures which these machines enable us to build and run (bigger and more free energy consuming cities) then maintain this higher flux of low entropy energy to high entropy energy. It is therefore an astonishing and a perplex situation, somehow it seems that although open systems far from thermodynamic equilibrium maximize entropy production, which is a measure of disorder, they do so by maximization of internal order. Or as Lorenz (cited in Gleick (1988)) put it, dissipation seems to be an agent of order and vice-versa. Conceptually, these findings almost resemble Heisenberg's uncertainty principle (Heisenberg (1927); also results in Zehe et al. (2021)), the increase of disorder (entropy) in space-time of the universe, is accompanied by the internal decrease of disorder (the growth of structures).

5.2.2 *Entropy, chaos, and equilibrium*

In this thesis we have used thermodynamic concepts principally from physics and chemistry to explain the richness of structure that is related to surface runoff in hydrological systems. Therefore, we often

referred to equilibrium conditions of the system. Thorn and Welford (1994) have already pointed out that depending on the scientific discipline, different types of equilibria can be defined. Here we referred to equilibrium as a situation where the rates of energy and mass exchange with the surrounding environment of the system are close to being constant over some characteristic time horizon. In chapter II we represented this time horizon as some steady state infiltration excess runoff that corresponds to an extraordinary return period, in chapter III it is a transient event of surface runoff, while in chapter IV the horizon is a hydrological year. Consequently, it becomes evident that in fact there is no well-defined single equilibrium state of the runoff system, but rather a multidimensional attractor, where fluctuations occur around some mean orbit. We have mentioned the idea of an attractor in this thesis, as we believe that the dynamics of a hydrological system are best described in phase space (cf. Sivakumar (2017)). In this sense, a process which has many degrees of freedom might result in a more complex attractor (e.g. the Lorenz attractor, cf. Lorenz (1963); or a double pendulum), while a system with few degrees of freedom will result in a simpler attractor (e.g. a single pendulum). The degrees of freedom in our system are defined by physical constraints, such as geological material of the watershed, but also by structural adaptations of the system. A system with fewer degrees of freedom then corresponds to more structure and the associated dynamics in phase space are therefore less complex. For the example of a drainage network in chapter IV, we showed that the complexity of the dynamics within a catchment decrease with increasing drainage area (Fig. 4.22). We interpret this as the damping of a dynamical system through the growth of structure, somehow dissipation bleeds a complex system of many conflicting motions (Gleick (1988)). From a thermodynamic standpoint this corresponds to a decrease of the system's entropy through maximization of entropy export. Or in line with the Gaia hypothesis of the earth as a living organism, we could adapt the perspective of Erwin Schrödinger (cited in Gleick (1988)) who famously said: "A living organism has the astonishing gift of concentrating a stream of order on itself and thus escaping the decay into atomic chaos".

Part VI

APPENDIX

A

A.1 APPENDIX CHAPTER II

A.1.1 *Energy flux between thermodynamic sub systems*

For each OTS_{sub} we apply Eq. 2.1 where potential and kinetic energy of the system do not change with time, so that:

$$0 = J_{f,net}^{pe}(x) + J_{f,net}^{ke}(x) + J_{Peff}^{pe}(x) - D_f(x) \tag{A1.1}$$

For potential energy conversion we obtain:

$$J_{f,net}^{pe}(x) + J_{Peff}^{pe}(x) = P_f(x) \tag{A1.2}$$

While kinetic energy conversion is as follows:

$$P_f(x) = D_f(x) - J_{f,net}^{ke}(x) \tag{A1.3}$$

To relate the spatial distribution of energy with energy fluxes we recall that the downslope mass flux is associated with downslope flux of kinetic and potential energy. The net fluxes correspond to the divergence of the kinetic and potential energy flow. $J_f^{pe/ke}$ in *watt* is here defined as the advective energy flux, which is the product of specific energy E_{sp} in *joule kg^{-1}* and flow rate ρQ in *kg s^{-1}*. As per definition of Eq. A1.4, $J_{f,net}$ is positive for a decrease of energy flux over the control volume and therefore has the opposite sign to change in energy:

$$J_{f,net}^{pe/ke} = -div(J_f^{pe/ke}(x)) \tag{A1.4}$$

$$J_f^{pe} = E_{sp}^{pe}(x)Q(x) = gh(x)\rho Q(x) \tag{A1.5a}$$

$$J_f^{ke} = E_{sp}^{ke}(x)Q(x) = (v(x)^2)/2\rho Q(x) \tag{A1.5b}$$

$$J_{Peff}^{pe}(x) = \rho I(x)gh(x)b(x)/(3.6 * 10^6) \tag{A1.6}$$

Inserting the expressions for specific potential and kinetic energy (Eq. A1.5a to Eq. A1.6) into Eq. A1.2 and Eq. A1.3, we get power (Eq. A1.7) and dissipation (Eq. A1.8) of flow energy per unit length in *watt m^{-1}*:

$$P_f(x) = J_{f,net}^{pe}(x) + J_{Peff}^{pe}(x) =$$
$$\rho g \left(-\frac{dQ(x)}{dx}h(x) - \frac{dh(x)}{dx}Q(x) + P_{eff}(x)h(x)b(x) \right) \tag{A1.7}$$

$$D_f(x) = P_f(x) + J^{ke}_{f,net}(x) =$$

$$\rho g \left(-\frac{dQ(x)}{dx}h(x) - \frac{dh(x)}{dx}Q(x) + I(x)h(x)b(x)/(3.6*10^6) \right)$$

$$-\frac{1}{2}\rho \left(\frac{dQ(x)}{dx}v(x)^2 + 2v(x)\frac{dv(x)}{dx}Q(x) \right)$$

(A1.8)

For the transient case we additionally define potential- and kinetic energy per unit flow length $E^{pe/ke}_f$ as:

$$E^{pe}_f = \rho g \frac{Q(x,t)}{v(x,t)}h(x,t) \tag{A1.9}$$

$$E^{ke}_f = \frac{\rho}{2}Q(x,t)v(x,t) \tag{A1.10}$$

which leads to the transient version of A1.8:

$$D_f(x) =$$

$$\rho g \left(-\frac{dQ(x,t)}{dx}h(x,t) - \frac{dh(x,t)}{dx}Q(x,t) + I(x,t)h(x,t)\frac{b(x)}{3.6*10^6} \right)$$

$$-\frac{1}{2}\rho \left(\frac{dQ(x,t)}{dx}v(x,t)^2 + 2v(x,t)\frac{dv(x,t)}{dx}Q(x,t) \right)$$

$$-\rho g \left((\frac{dQ(x,t)}{dtv(x,t)} + Q(x,t)\frac{-\frac{dv(x,t)}{dt}}{v(x,t)^2})h(x,t) + \frac{Q(x,t)}{v(x,t)}\frac{dh(x,t)}{dt} \right)$$

$$-\frac{\rho}{2} \left(Q(x,t)\frac{dv(x,t)}{dt} + \frac{dQ(x,t)}{dt}v(x,t) \right)$$

(A1.11)

A.1.2 *Correlation of Manning's n, ratio of sheet to rill velocity, slope and C_f*

The Figures A.1a to A.1d are based on values derived from measurements (Manning's n, v_{RF}, v_{SF}, slope) and calibrated (C_f) values for all 31 analysed rainfall simulation experiments (cf. Gerlinger (1996); **??**). Correlation was expressed by a power law which was fitted to mean bin values containing at least 2 values or more.
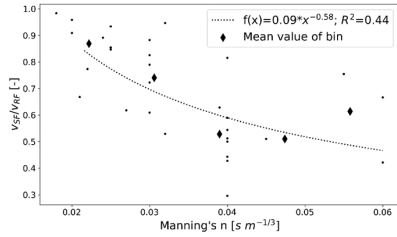
(a) Manning's n vs. ratio of sheet to rill flow velocity
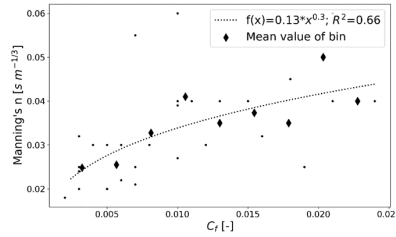
(b) Calibrated flow accumulation C_f vs. Manning's n
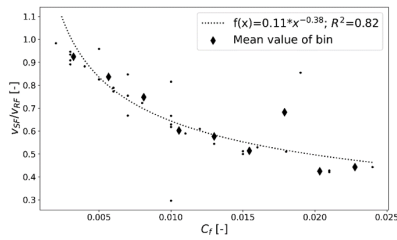
(c) Calibrated flow accumulation C_f vs. ratio of sheet to rill flow velocity
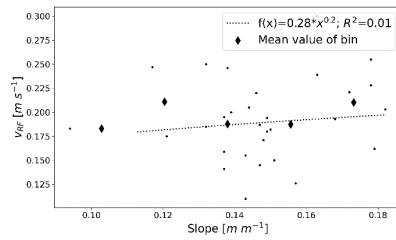
(d) Slope of experiment plots vs. rill flow velocity

Figure A.1: Correlation of hydraulic parameters

A.1.3 *Maximum power in rill domain*

Flow on hillslope equivalent to current in circuit: With: Therefore,

	Hillslope	Electrical circuit
Flow	$Q = K_{ch}\left(I_0\right)^{0.5}$	$I_{el} = \frac{1}{R_{el}}V_{el}$
Power	$P = Q^2 \frac{1}{K_{ch}}\rho g$	$P_{el} = (I_{el})^2 R_{el}$

Symbol	Unit	Description
I_{el}	Ampere	Electrical current
R_{el}	Ohm	Resistance
V_{el}	Volt	Voltage
P_{el}	Watt	External power of the circuit
K_{ch}	$m^3\ s^{-1}$	Conveyance of the channel $K_{ch} = \frac{1}{n}AR^{2/3}$
R_{ch}	$m^3\ s^{-1}$	Resistance to flow: $R_{ch} = \frac{1}{K_{ch}}$

channel conveyance is the inverse of the resistance of the channel to transport flow. If water is mainly falling on sheet flow area and flows therefore first on sheet-flow area with R_{ch}^{SF} and then accumulates in a channel with R_{ch}^{RF} the total resistance to flow is:

$$R_{ch} = R_{ch}^{SF} + R_{ch}^{RF} \tag{A1.12}$$

Here we assume that R_{ch}^{SF} is fixed and that mainly resistance to flow of the rill adapts. Total power in the rill is then:

$$P^{RF} = Q^2 \frac{1}{R_{ch}^{RF}}\rho g =$$

$$\left((R_{ch}^{SF} + R_{ch}^{RF})^{-2}I_0\right)R_{ch}^{RF}\rho g = \tag{A1.13}$$

$$I_0\rho g \left(\underbrace{R_{ch}^{RF} + 2R_{ch}^{SF} + \frac{(R_{ch}^{SF})^2}{R_{ch}^{RF}}}_{T}\right)^{-1}$$

A1.13 becomes maximum if the term T becomes minimum:

$$\frac{dT}{dR_{ch}^{RF}} = 1 - \left(\frac{R_{ch}^{SF}}{R_{ch}^{RF}}\right)^2 \tag{A1.14}$$

The derivative A1.11 becomes zero if:

$$R_{ch}^{SF} = R_{ch}^{RF} \tag{A1.15}$$

Or equivalently:

$$K_{ch}^{SF} = K_{ch}^{RF} \qquad (A1.16)$$

A.1.4   *Supplemental material: Rainfall simulations experiments by Gerlinger (1996)*

	no	width	length	I	I_0	n	vrf_{mess}	vsf_mess	d_{50}	c_{sed}	vrf_{sim}	vsf_{sim}	SS_Q	SS_{Csed}	CF
0	fk1_1	2.0	12.0	62.4	0.138	0.027	0.246	0.152	33.015	69.366	0.237	0.147	1.0	0.0	0.01
1	fk1_2	2.0	12.0	62.4	0.172	0.022	0.221	0.171	29.387	63.879	0.218	0.178	1.0	0.0	0.006
2	fk1_3	2.0	12.0	62.4	0.117	0.021	0.247	0.165	31.176	67.618	0.248	0.161	1.0	0.0	0.007
3	fk3_1	2.0	12.0	62.4	0.121	0.024	0.175	0.156	35.261	74.786	0.177	0.159	1.0	1.0	0.003
4	lek_1	2.0	12.0	62.4	0.163	0.04	0.3	0.133	38.39	81.14	0.298	0.104	1.0	0.0	0.024
5	lek_2	2.0	12.0	62.4	0.163	0.045	0.239	0.122	34.339	53.066	0.24	0.106	1.0	1.0	0.018
6	oek2_1	2.0	12.0	60.3	0.094	0.018	0.183	0.18	26.525	27.28	0.181	0.167	1.0	0.0	0.002
7	oek2_2	2.0	12.0	63.3	0.139	0.04	0.2	0.118	21.947	42.702	0.203	0.106	1.0	0.0	0.011
8	oek2_31	2.0	12.0	34.4	0.137	0.04	0.141	0.115	24.97	19.683	0.141	0.082	1.0	1.0	0.01
9	oek2_32	2.0	12.0	62.4	0.137	0.03	0.195	0.141	24.97	48.84	0.197	0.13	0.0	1.0	0.008
10	oek2_33	2.0	12.0	44.6	0.137	0.039	0.159	0.1	24.97	35.92	0.157	0.091	1.0	1.0	0.01
11	oek2_4	2.0	12.0	62.4	0.151	0.032	0.15	0.142	30.6	108.89	0.149	0.139	1.0	0.0	0.0032
12	ok2_1	2.0	12.0	60.6	0.157	0.06	0.126	0.084	23.69	22.226	0.124	0.078	1.0	0.0	0.01
13	ok2_31	2.0	12.0	60.6	0.143	0.03	0.155	0.128	24.676	34.188	0.154	0.126	1.0	0.0	0.005
14	ok2_32	2.0	12.0	60.6	0.143	0.055	0.11	0.083	23.722	23.517	0.113	0.081	1.0	0.0	0.007
15	ok2_41	2.0	12.0	60.6	0.147	0.02	0.187	0.17	31.61	43.186	0.184	0.17	1.0	0.0	0.003
16	ok2_42	2.0	12.0	60.6	0.147	0.03	0.145	0.128	30.562	27.056	0.144	0.127	1.0	0.0	0.004
17	ok2_5	2.0	12.0	60.6	0.146	0.04	0.22	0.11	33.267	71.408	0.219	0.101	1.0	0.0	0.015
18	ok3_1	2.0	12.0	61.2	0.146	0.074	0.19	0.06	24.128	37.922	0.19	0.024	0.0	0.0	0.139
19	ok3_2	2.0	12.0	60.6	0.144	0.04	0.205	0.105	24.827	31.189	0.207	0.095	0.0	1.0	0.015
20	ok4_11	2.0	12.0	60.6	0.132	0.06	0.185	0.078	25.744	41.857	0.188	0.059	1.0	0.0	0.021
21	ok4_12	2.0	12.0	60.6	0.132	0.04	0.25	0.107	25.739	45.682	0.25	0.082	1.0	1.0	0.021
22	ok4_31	2.0	12.0	63.0	0.149	0.04	0.18	0.098	31.421	82.021	0.181	0.094	1.0	0.0	0.013
23	ok4_32	2.0	12.0	59.9	0.149	0.02	0.194	0.186	30.877	56.982	0.196	0.162	1.0	1.0	0.005
24	ok5_1	2.0	12.0	60.6	0.179	0.04	0.162	0.048	37.526	72.786	0.165	0.111	0.0	0.0	0.01
25	ok6_11	2.0	12.0	60.6	0.178	0.032	0.255	0.135	36.703	87.863	0.255	0.129	1.0	0.0	0.016
26	ok6_12	2.0	12.0	62.3	0.178	0.03	0.228	0.139	36.703	60.703	0.226	0.137	1.0	1.0	0.012
27	ok6_22	2.0	12.0	59.2	0.182	0.025	0.203	0.172	40.406	200.881	0.202	0.16	1.0	0.0	0.007
28	ok6_32	2.0	12.0	64.8	0.148	0.03	0.171	0.135	36.633	165.179	0.173	0.135	1.0	0.0	0.006
29	sk1_2	2.0	12.0	62.4	0.15	0.025	0.182	0.17	41.291	134.24	0.179	0.167	1.0	0.0	0.003
30	sk2_2	2.0	12.0	62.4	0.168	0.025	0.193	0.165	67.628	98.487	0.192	0.084	1.0	0.0	0.019

symbol (header)	unit	description
no	-	Location identifier
width	m	Width of experimental plot
length	m	Length of experimental plot
I	$mm\ h^{-1}$	Steady rainfall rate
I_0	$m\ m^{-1}$	Slope of experimental plot
n	$m^{-1/3}\ s$	Manning's n
vrf_{mess}	$m\ s^{-1}$	Measured rill flow velocity
vsf_{mess}	$m\ s^{-1}$	Measured sheet flow velocity
d_{50}	µm	Mean particle diameter of eroded top soil
c_{sed}	$kg\ m^{-3}$	Steady state sediment concentration
toprule vrf_{sim}	$m\ s^{-1}$	Simulated rill flow velocity (cf. main article)
vsf_{sim}	$m\ s^{-1}$	Simulated sheet flow velocity (cf. main article)
SS_Q	-	Index for steady state discharge: 1==yes; 0== no
SS_{Csed}	-	Index for steady state sediment concentration: 1==yes; 0== no
CF	-	Flow accumulation parameter for rill flow model

A.2 APPENDIX CHAPTER III

A.2.1 *Python code example of transient surface runoff*

```python
# -*- coding: utf-8 -*-
"""
Created on Mon Sep 12 11:26:07 2022
@author: shmul
Implementation of a McCormack Scheme for solving 1D Shallow Water
    Equations, including a mass source term for accumulation of
    rainfall along the flow path.
A description of the scheme can be found in
- Liang D., Lin B., Flaconer R. A., Simulation of rapidly varying
    flow using an efficient TVD-MacCormack scheme, int. journal
    for numerical methods in fluids 2007; 53:811-826 (2007)
"""
#%% import libraries and functions from 'functions.py'
import numpy as np
import matplotlib.pyplot as plt
import sys
# adjust path to the directory you are woking in...
path=r'C:\Users\...\SWE_example'
sys.path.append(path)
import functions as F


#%% Scenario definition

# 1) define spatial domain

## horizontal
N=50 #number of computation segments
L=10     #length of hillslope in meters
x=np.linspace(1,L+1,num=N)
xp=np.linspace(1-(x[1]-x[0]),L+1+(x[-1]-x[-2]),num=N+2)   # incl.
    ghost points

## vertical
### create Kirkby Soil Creep and Soil Wash slopes (compare https
    ://doi.org/10.5194/hess-26-3125-2022)
xl=xp[-1]-xp[0]
xf=xp-xp[0]
YC={}
Ytyp=["Soil Creep","Rainsplash","Soil Wash","Rivers"]
ytyp=iter(Ytyp)
for mn in [(0.2,0.82),(1.0,1.11),(1.7,1.45),(2.5,1.97)]:
    m=mn[0]
    n=mn[1]
    y0=0.5     # Hillslope height (m) at uppermost point
    nt=next(ytyp)
    YC[nt]=y0*(1-(xf/xl)**((1-m)/n+1))
    plt.plot(xf,YC[nt],label=mn)
plt.legend()
```

```python
# 2) define time domain

tend=1800    #end of calculations in seconds
pend=0.2*tend   #end of block-rainfall in seconds

# 3) define rainfall input

Peff=100/3600/1000
tss=np.linspace(0,tend,num=tend+1)
Pts=np.zeros(len(tss))
Pts[0:int(len(tss)*pend)+1]=Peff

#%% Run code

# define the output directory and a name for the run
path_out=r"C:\Users\\"
name='test'

t,Q,H=F.SWE(oldrun=False,path_in=path_out,tname="tsave_"+name+"_n
    ",Hname="Hsave_"+name+"_n",Qname="Qsave_"+name+"_n",name=name
    ,x=x,hini=.0001,tend=tend,ts=5,tss=tss,Pts=Pts,crstart=0.5,
    dtmax=0.01,hgp=YC['Soil Creep'],n=0.1,hmin=0.0001,save=True,
    path_out=path_out, rst=-99, plotQ=True)
```

A.2.2 *Python code MC-Cormack numerical scheme*

```python
#%% Functions
import numpy as np
import matplotlib.pyplot as plt
import time

# bed level functions
def flin(x,zmax,L):
    y1=(zmax-zmax/L*x)
    return(y1)
def fsin(x,zmax,L):
    y2=(zmax/2+zmax/2*np.cos(x/L*np.pi))
    return(y2)
def fexp(x,zmax,L,f):
    y3=(np.exp(-x*2*f)*zmax*(1-x/L))
    return(y3)
def fnexp(x,zmax,L,f):
    y4=(-np.exp(x*f))*(-zmax)*(1-x/L)
    return(y4)
def fElinexp(Zmax,Epot,XHS,f):
    for i in np.linspace(Zmax/5,Zmax*5,num=10000):
        zexp=fexp(x,i,XHS,f)
        di=Epot-np.round(zexp.cumsum()[-1],2)/XHS
        #print(di)
        if abs(di)<0.01:
            zfinal=i
    return(zfinal)
def fElinnexp(Zmax,Epot,XHS,f):
    for i in np.linspace(Zmax/5,Zmax*5,num=10000):
        zexp=fnexp(x,i,XHS,f)
        di=Epot-np.round(zexp.cumsum()[-1],2)/XHS
        #print(di)
        if abs(di)<0.01:
            zfinal=i
    return(zfinal)


def SWE(oldrun,path_in,tname,Hname,Qname,name,x,hini,
        tend,ts,tss,Pts,crstart,dtmax,
        hgp,n,hmin,save,path_out,rst,plotQ):

    #variables
    ## oldrun == True or False (if a previous run has been saved
        and should be continued)
    ## path_in== STRING (absolute path to saved runs)
    ## tname,Hname,Qname== STRING (names of .npy dics)
    ## x== NUMPY ARRAY (horizontal resolution of numeric grid/
        computation points)
    ## hini== FLOAT (initial water depth, everywhere equal)
    ## tend== FLOAT (End computation point in time in seconds)
    ## ts== FLOAT (timestep for saving and plotting, in seconds)
    ## dtmax== FLOAT (maximum allowable timestep)
```

```python
## hgp== NUMPY ARRAY (vertical distribution of computational
    points)
## tss== NUMPY ARRAY (timestamps in seconds of rainfall time
    series)
## Pts== NUMPY ARRAY (rainfall intensities at tss in m/s)
## crstart== FLOAT (usually 0.5, see Liang et al. 2006)
## n== FLOAT (Manning's n)
## hmin== FLOAT (minimum allowable water depth)
## beta== FLOAT (usually 1.0, vertical distribution of
    velocity)
beta=1
## save== LOGICAL (save results or not)
## path_out== STRING (Absolute path to directory to save)
## plotQ== Logical (if true then Q at the lower end of the
    hillslope will be plotted every ts seconds)

dx=x[-1]/(len(x)-1)
dh=abs((hgp[2:]-hgp[0:-2])/(2*dx))
dl=dx/np.cos(np.arctan(dh/dx))
dl=np.concatenate(([dl[0]],dl,[dl[-1]]))

Qout=[]
tout=[]
tout.append(0)

###### first we define functions which are called during the
    time marching:
def dtcalc(dl,q,H,Crpreset):
    dt=Crpreset*dl/np.nanmax(q/H+np.sqrt(9.81*H))
    return(dt)

def Fcalc(X1,X2):
    F1P=X2
    F2P=beta*X2**2/X1+9.81*X1**2/2
    return(F1P,F2P)

def Scalc(X1,X2,P,typ):
    S1P=np.zeros(len(X1))+P
    dhdx=abs((hgp[2:]-hgp[0:-2])/(2*dx))  #central
        differences
    if typ=="forward":
        dhdx=np.concatenate(([dhdx[0]],dhdx,[dhdx[-1]]))
    elif typ=="backward":
        dhdx=np.concatenate(([dhdx[0]],dhdx,[dhdx[-1]]))
    Ix=dhdx*X1
    Ie=n**2*X2**2/X1**(7/3)
    dI=Ix-Ie
    S2P=9.81*(dI)
    return(S1P,S2P)

def TVD(x1,x2,Cr):
    X=np.array((x1,x2))
```

```python
    rpos=np.zeros(len(x1)-2)
    rneg=rpos.copy()
    dXus=X[:,2:]-X[:,1:-1]    #take both rows but not all
        columns (ghost points)
    dXds=X[:,1:-1]-X[:,:-2]
    dXus[dXus==0]=1e-99
    dXds[dXds==0]=1e-99
    for i in range(len(dXus[0])):
        rpos[i]=np.dot(dXus[:,i],dXds[:,i])/np.dot(dXus[:,i],
            dXus[:,i])
        rneg[i]=np.dot(dXus[:,i],dXds[:,i])/np.dot(dXds[:,i],
            dXds[:,i])
        if np.isnan(rpos[i]):
            pass
    rposminus=np.append(rpos[0],rpos[0:-1])
    rnegplus=np.append(rpos[1:],rpos[-1])
    tvd=(fG(rpos,Cr)+fG(rnegplus,Cr))*dXus-(fG(rneg,Cr)+fG(
        rposminus,Cr))*dXds
    return(tvd)


def fCr(H,q,dtoverdx):
    Cr=(abs(q/H)+np.sqrt(9.81*H))*dtoverdx
    return(Cr)


def fG(r,Cr):
    phi=np.zeros(len(r))
    for i in range(len(r)):
        phi[i]=np.nanmax(np.append(0,np.nanmin(np.append(2*r[
            i],1))))
    C=np.where(Cr<=0.5,Cr*(1-Cr),0.25)
    G=0.5*C*(1-phi)    #do not include ghost points
    return(G)


if oldrun:
    tsave=np.load(path_in+tname+".npy",allow_pickle=True).
        item()
    Hsave=np.load(path_in+Hname+".npy",allow_pickle=True).
        item()
    Qsave=np.load(path_in+Qname+".npy",allow_pickle=True).
        item()
    x=np.load(path_in+"x_"+"n"+".npy",allow_pickle=True)
    hgp=np.load(path_in+"Z_"+"n"+".npy",allow_pickle=True)
    if rst<0:
        dtno=list(tsave)[-1]
    else:
        dtno=rst
    t=tsave[dtno]
    print("Restart at {}".format(t))
    H0=Hsave[dtno]
    Q0=Qsave[dtno]
    told=t
    count=0
```

```python
        countn=dtno+1
    else:
        H0=np.ones((len(x)))*hini
        Q0=H0*0
        t=0
        Hsave={}
        Qsave={}
        tsave={}
        told=0
        count=0
        countn=0

    # Time marching
    H=H0.copy()
    Q=Q0.copy()
    tmon0=time.time()
    while t<tend:
        tmonact=time.time()
        dtmon=tmonact-tmon0
        P=np.interp(t,tss,Pts)
        qini=0 #no flow from upstream of first point

        count=count+1
        #set boundary values at ghost points
        dH=(H[-1]-H[-2])
        dQ=(Q[-1]-Q[-2])
        H=np.concatenate(([H[0]],H,[H[-1]+dH]))
        Q=np.concatenate(([qini],Q,[Q[-1]+dQ]))
        dtorg=np.min(dtcalc(dl,abs(Q),abs(H),crstart))

        if dtorg>dtmax:
            dt=dtmax
        else:
            dt=dtorg

        dtoverdl=dt/dl
        dtoverdx=dt/dx

        F1,F2=Fcalc(abs(H),abs(Q))
        S1,S2=Scalc(H,Q,P,typ="forward")
        S1[0]=0
        S1[-1]=0
        #forward differences
        dF1=F1[2:]-F1[1:-1]
        dF2=F2[2:]-F2[1:-1]

        # 1) predictor step
        HP=H[1:-1]-dtoverdx*dF1+S1[1:-1]*dt
        qP=Q[1:-1]-dtoverdx*dF2+S2[1:-1]*dt

        #set boundary values at ghost points
        dH=(HP[-1]-HP[-2])
```

```python
dQ=(qP[-1]-qP[-2])
HP=np.concatenate(([HP[0]],HP,[HP[-1]+dH]))
QP=np.concatenate(([qini],qP,[qP[-1]+dQ]))

HP[HP<hmin]=hmin
QP[np.where(HP<hmin)]=0

#insert XP into F,S to get FP,SP:
F1P,F2P=Fcalc(abs(HP),abs(QP))
S1P,S2P=Scalc(HP,QP,P,typ="backward")
S1P[0]=0
S1P[-1]=0

dF1P=F1P[1:-1]-F1P[0:-2]
dF2P=F2P[1:-1]-F2P[0:-2]

# 2) corrector step
HC=H[1:-1]-dtoverdx*dF1P+S1P[1:-1]*dt
qC=Q[1:-1]-dtoverdx*dF2P+S2P[1:-1]*dt

#calculate local courantnumbers
Cr=fCr(H,Q,dtoverdl)

#set boundary values at ghost points
dH=(HC[-1]-HC[-2])
dQ=(qC[-1]-qC[-2])
HC=np.concatenate(([HC[0]],HC,[HC[-1]+dH]))
QC=np.concatenate(([qini],qC,[qC[-1]+dQ]))

HC[HC<hmin]=hmin
QC[np.where(HC<hmin)]=0

#Final value not incl. ghost points
TVDX1=TVD(H,Q,Cr[1:-1])[0,:]
TVDX2=TVD(H,Q,Cr[1:-1])[1,:]

HF=(HP[1:-1]+HC[1:-1])/2
QF=(QP[1:-1]+QC[1:-1])/2
HF[2:-1]=HF[2:-1]+TVDX1[2:-1]
QF[2:-1]=QF[2:-1]+TVDX2[2:-1]

HF[np.isnan(HF)]=hmin

H=HF.copy()
Q=QF.copy()
t=t+dt

print("Steps:{} time:{} dt:{} Hmax:{} Hmin:{}".format(
    count,np.round(t,6),np.round(dt,6),np.round(np.max(HF
    ),6),np.round(np.min(HF),6)))
if t>=told+ts or told==0:
```

```python
            print("saved at {} seconds; seconds computated:{}".
                format(round(t,4),round(dtmon,2)))
            tsave[countn]=t
            Qsave[countn]=QF
            Hsave[countn]=HF
            countn=countn+1
            told=t

            if (plotQ):
                Qout.append(QF[-1])
                tout.append(t)
                plt.scatter(tout[1:],Qout)
                plt.draw()
                plt.pause(0.01)
                #print(dtorg)

    if save:
        #save result dicts to folder
        np.save(path_out+tname+"_n"+".npy",tsave)
        np.save(path_out+Qname+"_n"+".npy",Qsave)
        np.save(path_out+Hname+"_n"+".npy",Hsave)
        np.save(path_out+"x"+name+"_n"+".npy",x)
        np.save(path_out+"Z"+name+"_n"+".npy",hgp)
        np.save(path_out+"t"+name+"_n"+".npy",tss)
        np.save(path_out+"P"+name+"_n"+".npy",Pts)
        f=open(path_out+"Run_out_"+tname+"_n.txt","w")
        if oldrun:
            f.write("restarted from "+tname+"\n")
            f.write("started at: {}".format(tsave[dtno])+"\n")
        else:
            f.write("initial Run: "+tname+"\n")
            f.write("started at: o\n")
        f.write("dt save: "+str(ts)+"\n")
        f.write("Mannings n: {}".format(n)+"\n")
        f.write("ended at: {}".format(tend)+"\n")
        f.write("total runtime: {}".format(dtmon)+"\n")
        f.close()

    return(tsave,Qsave,Hsave)
```

A.3 APPENDIX CHAPTER IV

A.3.1 *Assimilated data of Amazonas discharge stations*

	LAT	LON	HYRIV_ID	DIS_AV_CMS	DIST_DN	UPLAND	PRE	ELE	ELE_CMN	SOURCE
	-	-	-	$m^3\ s^{-1}$	km	km^2	$mm\ hr^{1}\ yr^{-1}$	masl.	masl.	-
0	1.200	-76.630	60339739	22	4009	354	2528	2182	682	GRDC
1	1.600	-75.600	60318766	27	3913	453	2414	1134	250	GRDC
2	1.930	-67.120	60338979	5064	2606	74840	3139	234	79	GRDC
3	-11.060	-64.080	61051833	48	2868	1027	1863	454	162	GRDC
4	-10.793	-65.348	61041457	8415	2672	614043	1442	537	118	GRDC
5	-10.918	-65.043	61047150	88	2724	4403	1737	243	130	GRDC
6	-11.067	-64.083	61051833	48	2868	1027	1863	454	162	GRDC
7	-15.200	-59.330	61195782	43	3910	4108	1542	433	217	GRDC
8	-12.851	-62.899	61122787	982	3247	110468	1530	288	142	GRDC
9	-12.830	-62.930	61122787	982	3247	110468	1530	288	142	GRDC
10	-12.427	-64.425	61106352	3253	3000	342866	1317	301	129	GRDC
11	-13.486	-61.050	61145835	699	3586	55979	1589	344	168	GRDC
12	-15.009	-59.958	61188983	230	3845	22860	1427	307	196	GRDC
13	-15.215	-59.354	61195416	26	3932	2455	1554	501	227	GRDC
14	-11.931	-62.153	61086417	22	3373	1410	1745	400	227	GRDC
15	-0.482	-64.827	60432570	16593	2078	293720	3141	165	29	GRDC
16	-0.201	-66.802	60413528	13218	2336	194159	3208	188	50	GRDC
17	0.372	-67.313	60383263	8245	2448	124380	3232	194	74	GRDC
18	1.215	-66.853	60300059	5016	2702	71548	3133	240	81	GRDC
19	1.074	-67.595	60346096	1537	2556	23605	3391	161	81	GRDC
20	1.339	-68.686	60332135	303	2763	4670	3368	165	102	GRDC
21	0.209	-69.378	60391755	308	2712	4579	3275	157	96	GRDC
22	0.249	-69.785	60388777	132	2768	1963	3226	174	104	GRDC
23	-0.246	-67.009	60417154	875	2368	13275	3382	107	66	GRDC
24	0.884	-62.622	60356264	456	2122	17859	1951	217	53	GRDC
25	1.821	-61.124	60307232	2703	2072	126162	1755	350	44	GRDC
26	-0.859	-60.520	60454857	243	1918	7175	2070	117	49	GRDC
27	4.631	-60.471	60166241	99	2524	3241	1439	957	633	GRDC
28	4.168	-60.528	60190278	155	2425	5915	1258	764	106	GRDC
29	4.196	-60.794	60189604	51	2439	2336	1540	558	119	GRDC
30	3.208	-60.571	60238241	1311	2272	49590	2031	418	64	GRDC
31	3.438	-61.037	60226269	1095	2352	36268	2179	494	74	GRDC
32	3.550	-63.169	60221678	616	2665	15376	2436	719	317	GRDC
33	2.871	-61.441	60253128	319	2294	12543	1908	396	76	GRDC
34	2.732	-62.017	60259554	275	2404	9657	1931	449	175	GRDC
35	1.750	-62.283	60310771	150	2135	6178	1837	293	106	GRDC
36	0.477	-69.128	60377085	2453	2718	39876	3046	216	105	GRDC
37	0.130	-68.539	60395966	2755	2589	44069	3091	207	77	GRDC
38	-3.102	-67.936	60606185	48330	2532	1020953	2026	1134	47	GRDC
39	-1.821	-66.600	60517739	14453	2331	250910	2940	274	41	GRDC
40	-1.395	-69.428	60494179	14537	2705	207334	2851	310	63	GRDC
41	-3.450	-68.750	60626828	47713	2649	1016431	2022	1139	54	GRDC
42	-4.221	-67.893	60680730	1715	2695	35671	2632	147	61	GRDC
43	-5.383	-68.998	60751554	445	3007	10775	2567	160	101	GRDC
44	-4.326	-67.344	60687549	483	2671	10946	2569	119	65	GRDC
45	-4.292	-65.202	60684429	680	2123	13774	2662	96	45	GRDC
46	-5.109	-63.985	60733816	413	1933	8228	2690	85	39	GRDC
47	-4.058	-63.028	60669693	88791	1735	1783039	2317	736	19	GRDC
48	-3.311	-60.609	60620519	97470	1387	2214552	2302	620	7	GRDC
49	-3.063	-59.648	60604044	127020	1287	2932890	2360	509	7	GRDC
50	-1.438	-57.827	60493402	366	1073	9847	2287	157	27	GRDC
51	-2.109	-59.335	60538147	747	1259	20083	2435	109	18	GRDC
52	-1.938	-59.483	60527044	706	1288	18927	2434	108	23	GRDC
53	-6.750	-58.930	60832047	405	1761	12736	2254	170	41	GRDC
54	-6.796	-59.042	60832047	405	1761	12736	2254	170	41	GRDC
55	-7.101	-59.683	60849137	237	1862	5034	2205	179	90	GRDC
56	-1.503	-54.873	60498430	300	717	19799	2084	357	18	GRDC
57	-1.779	-54.397	60527635	119	477	14503	1784	314	9	GRDC
58	-3.677	-53.554	60644771	64	692	2943	1700	209	85	GRDC
59	-0.568	-52.569	60436523	1022	364	52010	2270	276	31	GRDC
60	-0.552	-52.570	60436522	99	366	4461	2416	246	42	GRDC

	LAT	LON	HYRIV_ID	DIS_AV_CMS	DIST_DN	UPLAND	PRE	ELE	ELE_CMN	SOURCE
	-	-	-	m^3s^{-1}	km	km^2	$mmhr^1yr^{-1}$	masl.	masl.	-
61	-0.417	-53.700	60427139	445	476	29051	2057	353	123	GRDC
62	1.221	-54.657	60338167	97	825	7070	1983	397	297	GRDC
63	-4.341	-70.906	60688595	2615	3131	61704	2453	155	76	GRDC
64	-5.139	-72.814	60736332	479	3526	16615	2399	171	103	GRDC
65	-4.579	-71.413	60701603	1148	3270	25389	2424	164	93	GRDC
66	-4.733	-70.300	60711845	950	3030	19347	2458	158	85	GRDC
67	-4.733	-70.300	60711845	950	3030	19347	2458	158	85	GRDC
68	-7.447	-73.664	60867473	44	4413	1010	2335	301	222	GRDC
69	-4.839	-66.851	60718341	4993	2735	164381	2169	225	65	GRDC
70	-6.440	-68.246	60812668	4036	3260	144049	2124	239	91	GRDC
71	-6.684	-69.881	60825513	1873	3693	77204	2115	241	114	GRDC
72	-7.056	-71.689	60846857	1358	4071	55731	2062	255	147	GRDC
73	-7.633	-72.662	60878108	957	4269	38099	1992	272	167	GRDC
74	-8.934	-72.789	60950081	425	4511	16248	1849	310	209	GRDC
75	-9.410	-72.716	60969010	237	4572	8459	1887	324	230	GRDC
76	-7.428	-70.023	60866381	1423	3830	50071	2037	261	133	GRDC
77	-8.146	-70.715	60906091	379	4008	15749	1933	287	162	GRDC
78	-8.164	-70.356	60906790	491	3979	17325	1918	286	152	GRDC
79	-7.951	-71.482	60894632	37	4072	2128	1985	275	191	GRDC
80	-11.000	-68.762	61049602	96	3989	7054	1750	302	192	GRDC
81	-10.944	-69.566	61046937	45	4100	3739	1809	324	235	GRDC
82	-10.651	-68.506	61035009	120	3926	8326	1745	292	167	GRDC
83	-9.975	-67.801	61003813	368	3772	23587	1797	251	132	GRDC
84	-9.067	-67.397	60956865	573	3622	34841	1850	228	110	GRDC
85	-7.550	-67.550	60872528	642	3454	23468	2430	178	97	GRDC
86	-8.768	-65.884	60941469	415	3168	17323	1898	159	79	GRDC
87	-6.319	-64.886	60805627	916	2543	38376	2525	114	44	GRDC
88	-6.538	-64.384	60819554	5716	2577	237352	2057	190	46	GRDC
89	-7.258	-64.798	60857082	5512	2787	227893	2046	195	52	GRDC
90	-7.716	-67.000	60882838	3546	3317	154892	2043	226	83	GRDC
91	-8.653	-67.375	60934558	2102	3548	105914	1914	251	92	GRDC
92	-9.044	-68.577	60955471	1389	3810	63375	1937	275	125	GRDC
93	-8.884	-69.268	60947250	880	4006	32854	1935	307	142	GRDC
94	-9.374	-68.724	60973355	135	3881	11314	1836	281	148	GRDC
95	-9.110	-68.993	60959079	121	3882	6153	1957	223	149	GRDC
96	-7.465	-64.243	60868458	118	2710	5689	2132	94	58	GRDC
97	-5.817	-61.302	60775757	27257	1648	1149980	1692	566	23	GRDC
98	-7.503	-63.018	60870923	24034	1997	1092012	1651	592	40	GRDC
99	-8.748	-63.917	60940271	19545	2255	978973	1606	638	54	GRDC
100	-9.703	-65.365	60990417	17489	2523	923307	1591	667	91	GRDC
101	-8.770	-63.920	60940778	19543	2258	978964	1606	638	54	GRDC
102	-9.785	-65.528	60994334	723	2537	31079	1792	174	96	GRDC
103	-7.958	-62.043	60895382	209	2115	3851	2250	91	68	GRDC
104	-9.926	-63.071	61000813	408	2419	8206	2229	231	97	GRDC
105	-8.799	-63.711	60942421	665	2251	12405	2229	155	68	GRDC
106	-9.179	-62.952	60962893	60	2290	1062	2341	131	87	GRDC
107	-9.556	-62.951	60982759	62	2392	1131	2226	151	104	GRDC
108	-9.761	-63.288	60992986	48	2414	913	2404	190	112	GRDC
109	-9.887	-62.985	60999608	54	2423	1028	2144	167	102	GRDC
110	-8.932	-62.056	60949685	1624	2241	60410	1895	239	73	GRDC
111	-10.874	-61.936	61044421	721	2598	33014	1845	285	133	GRDC
112	-11.653	-61.215	61075179	386	2757	16333	1806	334	177	GRDC
113	-9.347	-61.935	60971821	187	2328	4628	2083	168	102	GRDC
114	-10.446	-62.466	61026228	104	2565	3990	1976	241	142	GRDC
115	-11.684	-61.192	61076823	224	2761	10101	1736	324	175	GRDC
116	-11.670	-61.181	61076317	161	2761	6166	1921	352	175	GRDC
117	-11.749	-60.868	61080555	116	2803	4367	1917	389	187	GRDC
118	-9.817	-60.692	60995862	616	2200	24484	1941	312	102	GRDC
119	-7.593	-60.709	60875968	1565	1845	59569	2023	230	38	GRDC
120	-10.168	-59.464	61013681	409	2312	15350	1902	340	126	GRDC

	LAT	LON	HYRIV_ID	DIS_AV_CMS	DIST_DN	UPLAND	PRE	ELE	ELE_CMN	SOURCE
	-	-	-	m^3s^{-1}	km	km^2	$mmhr^1yr^{-1}$	masl.	masl.	-
121	-7.208	-60.650	60855075	3516	1798	131326	2072	215	27	GRDC
122	-7.707	-60.587	60881711	2070	1865	70449	2105	204	35	GRDC
123	-7.739	-60.576	60883522	508	1870	16273	2199	150	55	GRDC
124	-1.101	-56.040	60471885	461	818	34822	2136	319	11	GRDC
125	2.224	-55.956	60288506	10	1343	859	1743	432	332	GRDC
126	-1.088	-57.047	60471022	2071	904	78008	2251	243	9	GRDC
127	-1.065	-57.061	60469554	1384	909	52058	2251	246	12	GRDC
128	-0.998	-57.043	60464577	947	918	39176	2213	263	25	GRDC
129	-1.101	-57.057	60470117	686	908	25903	2249	238	10	GRDC
130	-0.695	-57.975	60444893	557	1063	21688	2218	258	83	GRDC
131	-6.045	-57.643	60789732	13656	1181	364434	2075	343	60	GRDC
132	-5.153	-56.854	60738023	15102	1031	388268	2087	335	41	GRDC
133	-7.340	-58.155	60861813	8420	1402	333783	2053	357	99	GRDC
134	-11.358	-58.343	61064043	1481	1989	55945	1924	480	238	GRDC
135	-7.731	-58.281	60883777	4210	1459	182816	1974	379	101	GRDC
136	-6.820	-56.852	60833446	311	1367	6218	2432	274	156	GRDC
137	-13.051	-55.890	61129804	87	2491	5418	1856	459	367	GRDC
138	-8.858	-57.402	60946188	3632	1631	131499	2121	353	133	GRDC
139	-9.643	-56.018	60986880	1948	1849	81836	2020	377	228	GRDC
140	-10.113	-55.570	61011270	954	1941	52377	1869	391	238	GRDC
141	-11.646	-55.702	61075848	674	2263	34780	1824	424	298	GRDC
142	-12.674	-55.792	61115617	273	2448	14197	1738	459	324	GRDC
143	-13.556	-55.332	61147533	215	2576	10908	1711	474	347	GRDC
144	-7.615	-57.950	60876862	3811	1447	139157	2134	344	104	GRDC
145	-10.183	-55.367	61013699	349	1962	17505	2276	365	243	GRDC
146	-9.817	-54.886	60995706	26	2065	1015	2415	447	298	GRDC
147	-9.342	-54.908	60971856	13	2123	496	2446	545	461	GRDC
148	-11.764	-58.036	61080573	532	2058	24913	1968	393	241	GRDC
149	-11.536	-57.423	61071010	829	2070	37166	1959	378	237	GRDC
150	-3.731	-51.568	60649215	462	527	24854	1905	206	84	GRDC
151	-3.215	-52.212	60615164	8346	574	449461	2000	315	86	GRDC
152	-6.736	-51.995	60830247	3855	1088	211161	1945	351	184	GRDC
153	-4.528	-54.013	60699951	2511	888	122654	2217	293	156	GRDC
154	-5.697	-54.246	60769548	1228	1121	58834	2269	317	187	GRDC
155	-6.745	-51.774	60831613	772	1115	42549	1962	351	190	GRDC
156	-5.650	-54.521	60767901	852	1108	35772	2310	296	187	GRDC
157	-6.570	-54.820	60827448	573	1271	22037	2389	320	198	GRDC
158	-13.141	-54.445	61133565	64	2150	3872	1682	468	321	GRDC
159	-14.611	-53.999	61180368	28	2404	1089	1926	654	463	GRDC
160	-0.303	-77.775	60420503	100	4296	2526	1593	3137	1405	GRDC
161	-1.390	-78.421	60490152	179	4619	7927	767	3473	1752	GRDC
162	-2.891	-78.966	60591848	23	4593	1258	918	3362	2437	GRDC
163	-2.867	-79.067	60591512	6	4605	309	988	3687	2628	GRDC
164	-10.664	-73.823	61035697	5770	4902	191810	1123	2917	200	HYBAM
165	-4.472	-77.550	60695337	3723	4147	114634	1456	2143	163	HYBAM
166	-0.475	-76.981	60430718	1016	4123	12279	3133	1401	247	HYBAM
167	-4.121	-70.036	60673609	40626	2910	880909	1949	1291	64	HYBAM
168	-4.218	-69.962	60679927	40633	2894	881319	1949	1291	63	HYBAM
169	-7.252	-64.811	60857081	5510	2790	227793	2046	195	51	HYBAM
170	-3.312	-60.630	60622464	96821	1407	2199160	2301	624	7	HYBAM
171	-0.485	-64.829	60432570	16593	2078	293720	3141	165	29	HYBAM
172	1.814	-61.124	60307232	2703	2072	126162	1755	350	44	HYBAM
173	-14.441	-67.535	61175575	686	3533	70224	1300	2171	193	HYBAM
174	-8.800	-63.946	60942418	19534	2263	978857	1606	638	55	HYBAM
175	-4.378	-59.623	60689177	32359	1350	1318684	1752	517	11	HYBAM
176	-1.923	-55.675	60525925	169174	691	4533910	2178	485	1	HYBAM
177	-4.288	-55.996	60684706	17605	854	459980	2123	320	8	HYBAM
178	-4.003	-73.161	60666383	30286	3413	725173	1740	1482	88	ANA_P
179	-4.600	-74.200	60704730	14882	3606	317328	1764	1381	95	ANA_P
180	-5.042	-73.838	60729473	13387	3608	349140	1563	1793	93	ANA_P

	LAT	LON	HYRIV_ID	DIS_AV_CMS	DIST_DN	UPLAND	PRE	ELE	ELE_CMN	SOURCE
	-	-	-	m^3s^{-1}	km	km^2	$mmhr^1yr^{-1}$	masl.	masl.	-
181	-3.472	-73.057	60631573	7032	3385	100652	2960	551	86	ANA_P
182	-4.450	-77.450	60694575	3746	4131	115048	1460	2136	150	ANA_P
183	-6.569	-76.112	60819974	2987	4217	69018	1359	1771	181	ANA_P
184	-11.800	-75.487	61082302	243	5746	9208	898	4358	3349	ANA_P
185	-7.255	-76.478	60857454	321	4340	5963	2006	994	257	ANA_P
186	-5.756	-78.432	60772627	141	4445	5764	994	2423	424	ANA_P
187	-13.183	-72.534	61133610	187	5496	9653	764	4192	2281	ANA_P
188	-5.896	-79.331	60780930	34	4552	2467	812	2417	1090	ANA_P
189	-5.890	-78.189	60783586	18	4482	764	930	2369	708	ANA_P
190	-6.471	-76.378	60816901	12	4261	335	1370	683	237	ANA_P
191	-7.221	-78.404	60856113	7	4785	782	1009	3310	2535	ANA_P
192	-5.933	-79.433	60786440	2	4559	218	918	2984	1669	ANA_P
193	-5.917	-79.317	60785980	3	4549	269	873	2817	1079	ANA_P
194	-8.330	-51.460	60917278	104	1409	6851	1909	369	258	ANA_B
195	-6.740	-52.000	60830247	3855	1088	211161	1945	351	184	ANA_B
196	-13.570	-53.080	61147859	282	2226	11659	1735	469	320	ANA_B
197	-1.780	-54.400	60517232	85	500	12487	1805	351	15	ANA_B
198	-5.650	-54.520	60767901	852	1108	35772	2310	296	187	ANA_B
199	-1.500	-54.870	60498430	300	717	19799	2084	357	18	ANA_B
200	-9.640	-56.020	60986880	1948	1849	81836	2020	377	228	ANA_B
201	-1.100	-56.040	60471885	461	818	34822	2136	319	11	ANA_B
202	-11.540	-57.420	61071842	828	2076	37133	1959	378	236	ANA_B
203	-13.030	-58.190	61128321	201	2223	7103	1810	582	361	ANA_B
204	-11.360	-58.340	61064043	1481	1989	55945	1924	480	238	ANA_B
205	-1.680	-58.530	60509501	809	1239	24901	2151	177	19	ANA_B
206	-13.460	-59.010	61144217	113	2306	4386	1752	627	461	ANA_B
207	-6.800	-59.040	60833426	387	1765	12277	2252	171	44	ANA_B
208	-15.220	-59.350	61195498	32	3924	3068	1551	473	224	ANA_B
209	-10.170	-59.470	61013682	408	2319	15313	1902	340	216	ANA_B
210	3.380	-59.810	60229642	192	2397	10039	1650	189	81	ANA_B
211	-4.900	-60.030	60721946	32195	1441	1314795	1750	519	12	ANA_B
212	3.320	-60.340	60232010	868	2296	41426	1420	374	67	ANA_B
213	4.170	-60.530	60190278	155	2425	5915	1258	764	106	ANA_B
214	3.210	-60.570	60238241	1311	2272	49590	2031	418	64	ANA_B
215	-7.710	-60.580	60883092	1574	1868	53992	2075	221	35	ANA_B
216	-3.310	-60.610	60622464	96821	1407	2199160	2301	624	7	ANA_B
217	-7.210	-60.650	60855075	3516	1798	131326	2072	215	27	ANA_B
218	-7.590	-60.710	60875968	1565	1845	59569	2023	230	38	ANA_B
219	-11.750	-60.870	61079704	117	2796	4392	1917	388	183	ANA_B
220	3.440	-61.040	60226269	1095	2352	36268	2179	494	74	ANA_B
221	1.820	-61.120	60307232	2703	2072	126162	1755	350	44	ANA_B
222	-11.680	-61.190	61076823	224	2761	10101	1736	324	175	ANA_B
223	-5.820	-61.300	60776872	27258	1648	1149975	1692	566	23	ANA_B
224	2.870	-61.440	60253128	319	2294	12543	1908	396	76	ANA_B
225	-10.870	-61.940	61044421	721	2598	33014	1845	285	133	ANA_B
226	-8.930	-62.060	60949210	1627	2239	60453	1895	239	77	ANA_B
227	-4.730	-62.150	60712169	6784	1726	367736	2204	154	16	ANA_B
228	-12.850	-62.900	61122787	982	3247	110468	1530	288	142	ANA_B
229	-7.500	-63.020	60870923	24034	1997	1092012	1651	592	40	ANA_B
230	-4.060	-63.030	60669693	88791	1735	1783039	2317	736	19	ANA_B
231	-9.930	-63.070	61001028	151	2422	3109	2182	197	99	ANA_B
232	-8.750	-63.920	60940271	19545	2255	978973	1606	638	54	ANA_B
233	-7.260	-64.800	60857082	5512	2787	227893	2046	195	52	ANA_B
234	-0.480	-64.830	60432570	16593	2078	293720	3141	165	29	ANA_B
235	-6.320	-64.890	60805627	916	2543	38376	2525	114	44	ANA_B
236	-10.790	-65.350	61041457	8415	2672	614043	1442	537	118	ANA_B
237	-4.840	-66.850	60717858	4999	2731	164471	2169	224	64	ANA_B
238	1.220	-66.850	60338979	5064	2606	74840	3139	234	79	ANA_B
239	-7.720	-67.000	60882838	3546	3317	154892	2043	226	83	ANA_B
240	-3.340	-67.490	60622667	2672	2488	64620	2633	132	48	ANA_B
241	-9.970	-67.800	61003813	368	3772	23587	1797	251	132	ANA_B
242	-3.100	-67.940	60604815	55517	2529	1142077	2122	1039	47	ANA_B
243	0.130	-68.540	60395966	2755	2589	44069	3091	207	77	ANA_B
244	-9.040	-68.580	60955471	1389	3810	63375	1937	275	125	ANA_B
245	-3.460	-68.910	60629316	46773	2668	1001919	2013	1153	52	ANA_B
246	-4.360	-69.730	60689361	40595	2863	881991	1950	1290	61	ANA_B
247	0.250	-69.780	60389551	135	2766	2008	3227	173	104	ANA_B
248	-6.680	-69.880	60825513	1873	3693	77204	2115	241	114	ANA_B
249	-8.160	-70.360	60906790	491	3979	17325	1918	286	152	ANA_B
250	-8.150	-70.720	60906091	379	4008	15749	1933	287	162	ANA_B
251	-7.630	-72.660	60878108	957	4269	38099	1992	272	167	ANA_B
252	-8.270	-72.740	60912919	533	4392	22361	1852	294	188	ANA_B
253	-5.140	-72.810	60736332	479	3526	16615	2399	171	103	ANA_B

A.3.2   *Assimilated data of Amazonas sediment loads*

	citation	lat	lon	Qa	Qsa	HYRIV_ID	DIST_DN_KM	UPLAND_SKM	ele_mt_cmn
	-	-	-	$m^3 s^{-1}$	Mt yr^{-1}	-	km	km^2	masl.
1	Armijos et al., 2020	-4.000	-73.160	28090	726.00	60666383	3413	725173	88
2	Armijos et al., 2020	-3.310	-60.610	102470	956.00	60620519	1387	2214552	7
3	Armijos et al., 2020	-8.750	-63.920	18600	476.00	60940271	2255	978973	54
4	Armijos et al., 2020	-4.900	-60.030	27940	445.00	60689177	1350	1318684	11
5	Armijos et al., 2020	1.820	-61.120	2880	4.00	60307232	2072	126162	44
6	Armijos et al., 2020	-1.923	-55.675	170000	1122.00	60525925	691	4533910	1
7	Armijos et al., 2013	-4.470	-77.550	5018	149.00	60695337	4147	114634	163
8	Armijos et al., 2013	-6.570	-76.120	2984	51.00	60819974	4217	69018	181
9	Armijos et al., 2013	-4.320	-74.290	2187	9.00	60686630	3621	42058	97
10	Armijos et al., 2013	-10.610	-73.870	6544	378.00	61032824	4892	191985	194
11	Armijos et al., 2013	-4.900	-73.670	11415	359.00	60729473	3608	349140	93
12	Armijos et al., 2013	-4.510	-73.950	16175	173.00	60704730	3606	317328	95
13	Armijos et al., 2013	-4.000	-73.160	28090	556.00	60666383	3413	725173	88
14	Armijos et al., 2013	-0.920	-75.390	2226	19.00	60458920	3902	27489	175
15	Armijos et al., 2013	-3.480	-73.080	6609	45.00	60631573	3385	100652	86
16	Filizola and Guyot, 2009	-5.140	-72.810	640	1.34	60736332	3526	16615	103
17	Filizola and Guyot, 2009	-4.360	-69.730	44200	434.56	60689361	2863	881991	61
18	Filizola and Guyot, 2009	-3.460	-68.910	46540	343.92	60626828	2649	1016431	54
19	Filizola and Guyot, 2009	-3.100	-67.940	54940	473.15	60606185	2532	1020953	47
20	Filizola and Guyot, 2009	-4.326	-67.344	410	2.68	60687549	2671	10946	65
21	Filizola and Guyot, 2009	-7.630	-72.660	910	12.30	60878108	4269	38099	167
22	Filizola and Guyot, 2009	-6.680	-69.880	1780	11.78	60825513	3693	77204	114
23	Filizola and Guyot, 2009	-4.840	-66.850	4750	25.45	60718341	2735	164381	65
24	Filizola and Guyot, 2009	-1.395	-69.428	13720	26.44	60494179	2705	207334	63
25	Filizola and Guyot, 2009	-4.060	-63.030	84010	509.90	60669693	1735	1783039	19
26	Filizola and Guyot, 2009	-9.970	-67.800	330	4.21	61003813	3772	23587	132
27	Filizola and Guyot, 2009	-7.720	-67.000	3650	102.66	60882838	3317	154892	83
28	Filizola and Guyot, 2009	-7.260	-64.800	5520	68.41	60857082	2787	227893	52
29	Filizola and Guyot, 2009	-6.320	-64.890	1490	7.44	60805627	2543	38376	44
30	Filizola and Guyot, 2009	-4.730	-62.150	10720	24.65	60712169	1726	367736	16
31	Filizola and Guyot, 2009	-3.310	-60.610	98750	402.75	60620519	1387	2214552	7
32	Filizola and Guyot, 2009	1.220	-66.850	4840	0.97	60300059	2702	71548	81
33	Filizola and Guyot, 2009	0.619	-66.135	1880	0.27	60346096	2556	23605	81
34	Filizola and Guyot, 2009	0.130	-68.540	2760	0.70	60395966	2589	44069	77
35	Filizola and Guyot, 2009	0.250	-69.780	130	0.02	60388777	2768	1963	104
36	Filizola and Guyot, 2009	-0.480	-64.830	16070	3.89	60432570	2078	293720	29
37	Filizola and Guyot, 2009	-0.301	-62.762	530	0.28	60419913	1918	22056	31
38	Filizola and Guyot, 2009	3.440	-61.040	1020	1.00	60226269	2352	36268	74
39	Filizola and Guyot, 2009	2.870	-61.440	280	0.34	60253128	2294	12543	76
40	Filizola and Guyot, 2009	1.820	-61.120	2900	2.74	60307232	2072	126162	44
41	Filizola and Guyot, 2009	-15.220	-59.350	60	0.09	61195782	3910	4108	217
42	Filizola and Guyot, 2009	-13.486	-61.050	530	0.24	61145835	3586	55979	168
43	Filizola and Guyot, 2009	-12.850	-62.900	910	0.14	61122787	3247	110468	142
44	Filizola and Guyot, 2009	-10.790	-65.350	8400	56.45	61041457	2672	614043	118
45	Filizola and Guyot, 2009	-8.750	-63.920	19360	277.48	60940271	2255	978973	54
46	Filizola and Guyot, 2009	-11.750	-60.870	110	0.08	61080555	2803	4367	187
47	Filizola and Guyot, 2009	-11.680	-61.190	210	0.13	61076823	2761	10101	175
48	Filizola and Guyot, 2009	-10.870	-61.940	720	1.53	61044421	2598	33014	133
49	Filizola and Guyot, 2009	-9.347	-61.935	130	0.03	60971821	2328	4628	102
50	Filizola and Guyot, 2009	-7.210	-60.650	3380	2.57	60855075	1798	131326	27
51	Filizola and Guyot, 2009	-4.900	-60.030	31250	244.28	60689177	1350	1318684	11
52	Filizola and Guyot, 2009	-1.680	-58.530	640	0.33	60509501	1239	24901	19
53	Filizola and Guyot, 2009	-1.101	-57.057	730	0.60	60470117	908	25903	10
54	Filizola and Guyot, 2009	-1.100	-56.040	520	0.18	60471885	818	34822	11
55	Filizola and Guyot, 2009	-1.923	-55.675	169480	555.93	60525925	691	4533910	1
56	Filizola and Guyot, 2009	-5.153	-56.854	10780	4.25	60738023	1031	388268	41
57	Filizola and Guyot, 2009	-2.816	-54.302	56000	0.18	60586830	539	16646	14
58	Filizola and Guyot, 2009	-1.780	-54.400	120	0.12	60527635	477	14503	9
59	Filizola and Guyot, 2009	-0.417	-53.688	490	0.26	60427139	476	29051	123
60	Filizola and Guyot, 2009	-6.745	-51.774	830	1.37	60831613	1115	42549	190
61	Filizola and Guyot, 2009	-5.393	-52.877	5170	5.95	60751424	871	281596	162
62	Filizola and Guyot, 2009	-4.528	-54.013	2690	2.56	60699951	888	122654	156
63	Filizola and Guyot, 2009	-3.200	-52.217	8720	5.80	60615164	574	449461	86
64	Filizola and Guyot, 2009	-0.569	-52.569	1010	0.43	60436523	364	52010	31
65	Dunne et al., 1998	-3.460	-68.910	45600	616.00	60626828	2649	1016431	54
67	Dunne et al., 1998	-3.100	-67.940	55600	642.00	60606185	2532	1020953	47
68	Dunne et al., 1998	-2.610	-67.092	56000	646.00	60572993	2398	1149426	44
69	Dunne et al., 1998	-2.576	-65.784	60700	678.00	60569848	2161	1233289	36
70	Dunne et al., 1998	-3.597	-64.290	63200	738.00	60640356	1905	1732899	24

	citation	lat	lon	Qa	Qsa	HYRIV_ID	DIST_DN_KM	UPLAND_SKM	ele_mt_cmn
	-	-	-	m^3s^{-1}	Mt yr^{-1}	-	km	km^2	masl.
71	Dunne et al., 1998	-4.060	-63.030	85800	731.00	60669693	1735	1783039	19
72	Dunne et al., 1998	-3.773	-61.623	86900	706.00	60651432	1546	1815284	12
73	Dunne et al., 1998	-3.310	-60.610	101400	697.00	60620519	1387	2214552	7
74	Dunne et al., 1998	-3.285	-58.890	98200	783.00	60619410	1188	2937365	5
75	Dunne et al., 1998	-2.382	-57.491	154700	1197.00	60556771	975	4392306	4
76	Dunne et al., 1998	-1.923	-55.675	170100	1239.00	60525925	691	4533910	1
77	Dunne et al., 1998	-3.132	-68.057	7100	24.00	60608498	2547	120776	47
78	Dunne et al., 1998	-2.808	-66.890	4000	2.20	60586190	2360	77385	43
79	Dunne et al., 1998	-2.631	-65.778	4900	28.00	60573575	2160	189713	37
80	Dunne et al., 1998	-2.266	-65.174	14000	30.00	60551074	2108	265162	30
81	Dunne et al., 1998	-3.918	-61.421	11100	25.00	60661217	1562	377901	11
82	Dunne et al., 1998	-3.065	-60.245	29600	7.50	60604329	1364	712061	8
83	Dunne et al., 1998	-3.450	-58.882	-	29	60631125.00	1191	1322145	6

A.3.3   *Processed data of national Brazilian dataset (ANA Brazil)*

	Lat	Lon	Qa_{mean}	Wa	Da	Va	RHa	HYRIV_ID	DIST_DN_KM
0	-5.14	-72.81	651	108.45	7.46	0.8	6.57	60736332	3526
1	-4.36	-69.73	36997	1770.35	15.34	1.31	15.16	60689361	2863
2	-3.46	-68.91	46983	1574.51	19.08	1.57	18.62	60629316	2668
3	-3.1	-67.94	57731	2205.79	17.86	1.49	17.28	60604815	2529
4	-3.34	-67.49	2479	438.03	7.56	0.75	7.3	60622667	2488
5	-8.27	-72.74	591	179.14	3.54	0.98	3.38	60912919	4392
6	-7.63	-72.66	944	181	5.33	0.98	5.01	60878108	4269
7	-6.68	-69.88	1767	191.26	9.57	0.95	8.71	60825513	3693
8	-8.15	-70.72	436	136.19	3.12	1.03	2.97	60906091	4008
9	-8.16	-70.36	451	106.58	4.2	0.98	3.9	60906790	3979
10	-4.84	-66.85	4672	374.42	13.22	0.97	12.36	60717858	2731
11	-4.06	-63.03	87554	1165.55	40.8	1.91	37.96	60669693	1735
12	-9.04	-68.58	1351	171.37	8.07	0.99	7.34	60955471	3810
13	-9.97	-67.8	364	83.95	4.65	0.89	4.11	61003813	3772
14	-7.72	-67	3877	316.91	10.8	1.09	10.08	60882838	3317
15	-7.26	-64.8	5693	434.82	11.86	1.06	11.24	60857082	2787
16	-6.32	-64.89	1512	296.78	7.4	0.69	7.04	60805627	2543
17	-4.73	-62.15	14211	714.81	21.22	0.94	20.02	60712169	1726
18	-3.31	-60.61	102418	3197.76	24.34	1.32	23.93	60622464	1407
19	1.22	-66.85	5107	668.73	8.46	0.9	8.26	60338979	2606
20	0.13	-68.54	2829	626.05	7.32	0.61	7.19	60395966	2589
21	0.25	-69.78	132	65.67	3.77	0.54	3.38	60389551	2766
22	-0.48	-64.83	17771	1891.53	10.89	0.87	10.77	60432570	2078
23	3.44	-61.04	1159	408.22	2.84	1.02	2.74	60226269	2352
24	3.21	-60.57	1482	421.72	4.54	0.75	4.55	60238241	2272
25	3.38	-59.81	200	131.47	3.76	0.38	3.57	60229642	2397
26	4.17	-60.53	154	112.97	2.19	0.59	2.14	60190278	2425
27	3.32	-60.34	621	258.27	4.02	0.52	4.51	60232010	2296
28	2.87	-61.44	315	219.41	2.14	0.69	2.09	60253128	2294
29	1.82	-61.12	3020	599.44	6.37	0.75	6.37	60307232	2072
30	-15.22	-59.35	56	37.48	2.3	0.67	2.04	61195498	3924

	Lat	Lon	Qa_{mean}	Wa	Da	Va	RHa	HYRIV_ID	DIST_DN_KM
31	-12.85	-62.9	904	287.57	5.65	0.56	5.39	61122787	3247
32	-10.79	-65.35	7975	869.83	10.29	0.95	10.04	61041457	2672
33	-8.75	-63.92	19059	780.95	19.65	1.29	18.42	60940271	2255
34	-9.93	-63.07	185	74.65	3.18	0.74	2.9	61001028	2422
35	-11.75	-60.87	117	62.64	1.89	0.92	1.79	61079704	2796
36	-11.68	-61.19	229	80.25	3.13	0.87	2.88	61076823	2761
37	-10.87	-61.94	754	242.91	4.12	0.74	3.94	61044421	2598
38	-8.93	-62.06	1500	290.11	7.51	0.7	7.06	60949210	2239
39	-7.5	-63.02	21875	1192.81	13.3	1.36	12.96	60870923	1997
40	-5.82	-61.3	23672	835.4	19.93	1.34	19.05	60776872	1648
41	-10.17	-59.47	301	165.67	4.42	0.42	4.2	61013682	2319
42	-7.71	-60.58	1441	301.39	8.03	0.59	7.62	60883092	1868
43	-7.59	-60.71	1444	437.52	4.69	0.68	4.58	60875968	1845
44	-7.21	-60.65	3322	451.89	9.38	0.78	8.99	60855075	1798
45	-4.9	-60.03	31187	1348.89	18.75	1.24	18.27	60721946	1441
46	-6.8	-59.04	456	128.82	5.53	0.62	5.07	60833426	1765
47	-1.68	-58.53	781	143.41	7.16	0.76	6.37	60509501	1239
49	-1.5	-54.87	177	105.44	4.13	0.41	3.86	60498430	717
50	-13.46	-59.01	141	47.5	5	0.59	4.15	61144217	2306
51	-13.03	-58.19	178	59.46	4.76	0.63	4.11	61128321	2223
52	-11.36	-58.34	1431	363.68	5.27	0.76	4.97	61064043	1989
53	-11.54	-57.42	741	214.41	4.2	0.81	4.03	61071842	2076
54	-9.64	-56.02	2042	397.21	7.04	0.71	6.71	60986880	1849
55	-1.78	-54.4	145	71.94	5.66	0.46	4.85	60517232	500
56	-13.57	-53.08	197	86.91	3.46	0.62	3.22	61147859	2226
57	-6.74	-52	3648	756.16	7.21	0.67	7.03	60830247	1088
58	-8.33	-51.46	141	89.42	3.68	0.42	3.37	60917278	1409
59	-5.65	-54.52	833	382.4	3.59	0.62	3.51	60767901	1108

A.3.4   *Energy dynamics of the Amazonas basin*
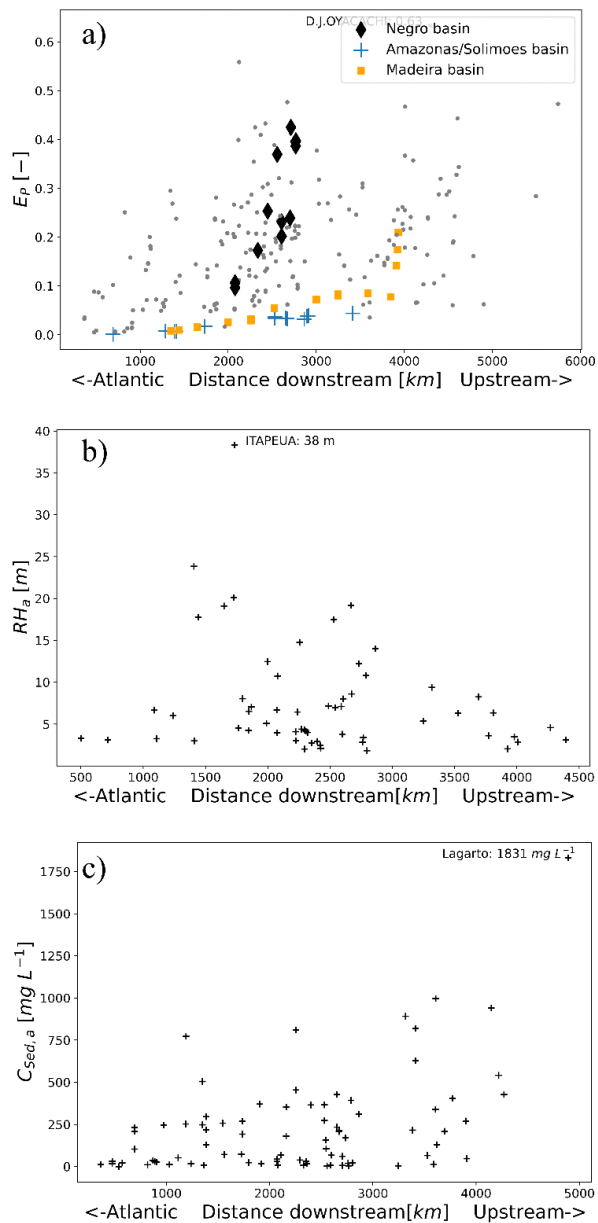
Figure A.2: Energy efficiencies of the Amazon Basin

A.3.5   *Exponential river profiles*
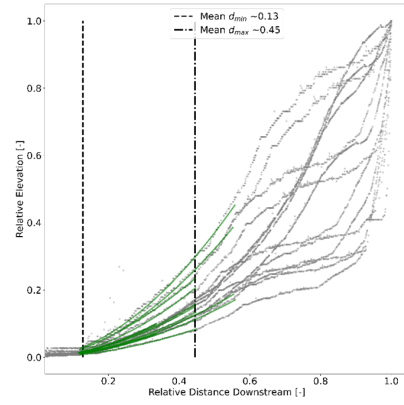
(a) Profiles for flow paths of the Amur River
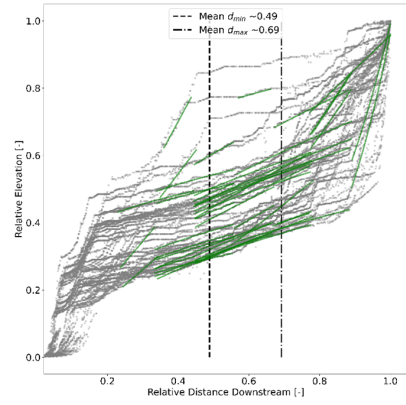
(b) Profiles for flow paths of the Congo River
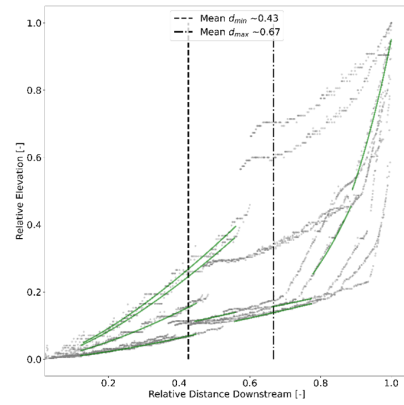
(c) Profiles for flow paths of the Danube River
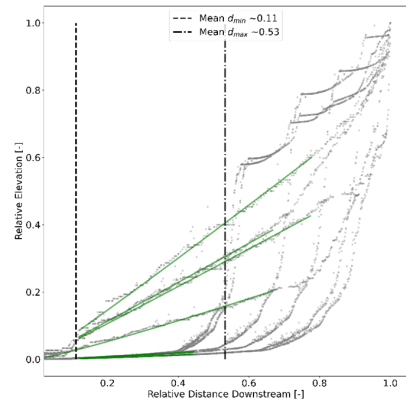
(d) Profiles for flow paths of the Ganges-Brahmaputra River

Figure A.3: Exponential river profiles 1
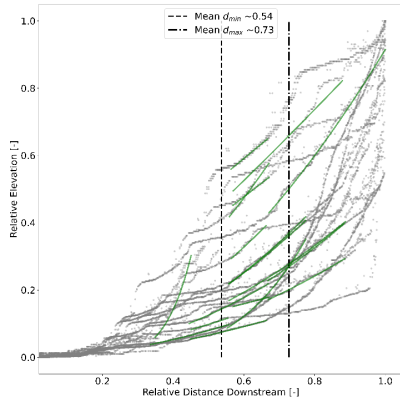
(a) Profiles for flow paths of the Mekong River
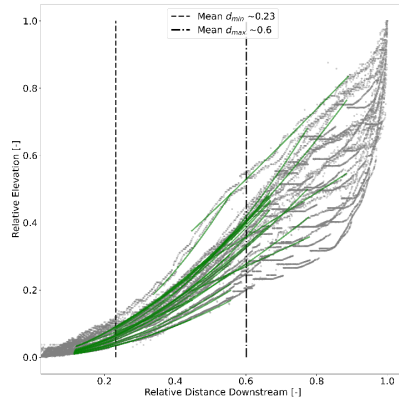
(b) Profiles for flow paths of the Mississippi River
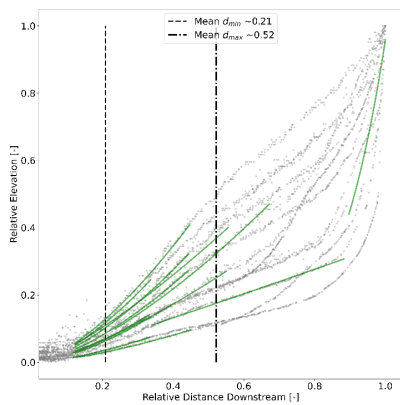
(c) Profiles for flow paths of the Murray River
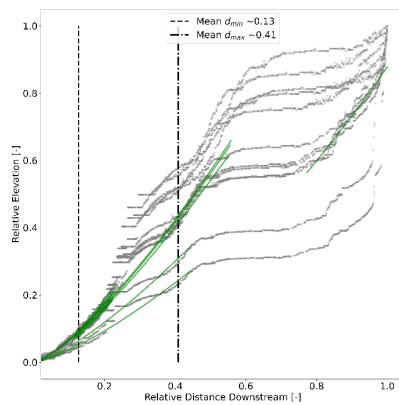
(d) Profiles for flow paths of the Niger River

Figure A.4: Exponential river profiles 2
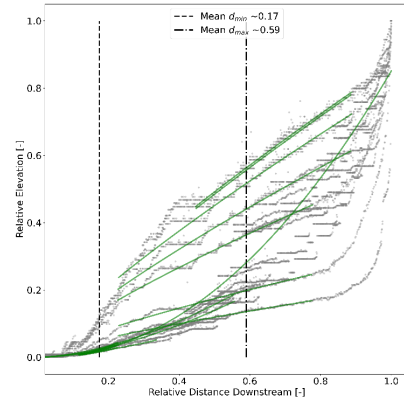
(a) Profiles for flow paths of the Rio de la Plata
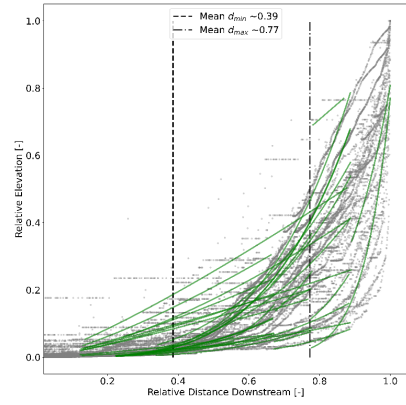
(b) Profiles for flow paths of the Yangtze River
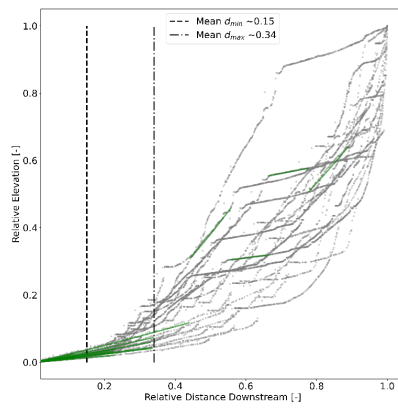
(c) Profiles for flow paths of the Yellow River

Figure A.5: Exponential river profiles 3

A.3.6 *The catchment as a simple non-linear system*

A catchment is a system of which its dynamics can be described by a set of nonlinear equations. We argue that these equations can be represented by an equation which is essentially the logistic map. Similarly, Frisch (1995) has pointed out that the Navier-Stokes equations can be rewritten as the "poor man's Navier Stokes equations", therefore conveying all the necessary ingredients for a set of deterministic equations which can lead to chaos. While May's population model becomes chaotic once the reproduction rate exceeds a critical threshold, flow of a substance becomes chaotic (turbulent) when the e.g. the Reynolds or the Rayleigh number exceeds a characteristic threshold value (Ruelle and Takens (1971)). Bonetti et al. (2020) as well as Perron, Kirchner, and Dietrich (2009) have shown that similar dimensionless numbers can be used to define thresholds between different drainage network patterns. The equations which describe population growth, flow of a viscous fluid and landscape evolution are written in parallel with their nonlinear and linear terms:

	Evolution in time		Nonlinear term	Linear term
Logistic map	$X_{n+1} - X_n$	=	rX_n^2	$-rX_n - X_n$
Navier Stokes	$d_t \vec{v}$	=	$-(\vec{v}\nabla\vec{v} + \nabla p)$	$+\nu\nabla^2\vec{v} + f$
LEM	dz/dt	=	$-KA^m|\nabla z|^n$	$+D\nabla^2 z + U$

A.3.7   *Horton-Strahler numbers per stream network*
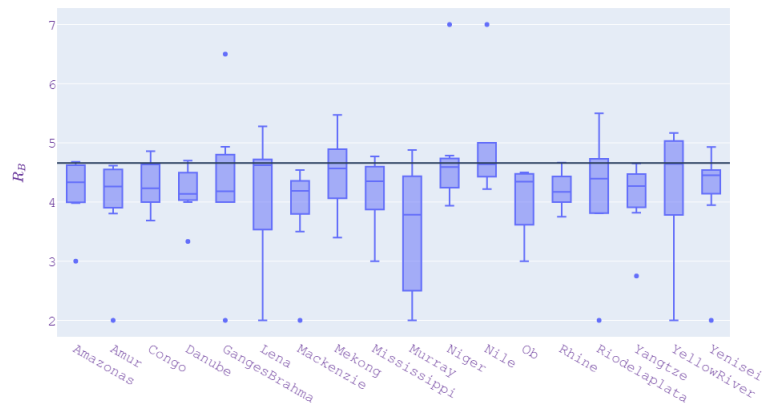
Figure A.6: Bifurcation ratios R_B
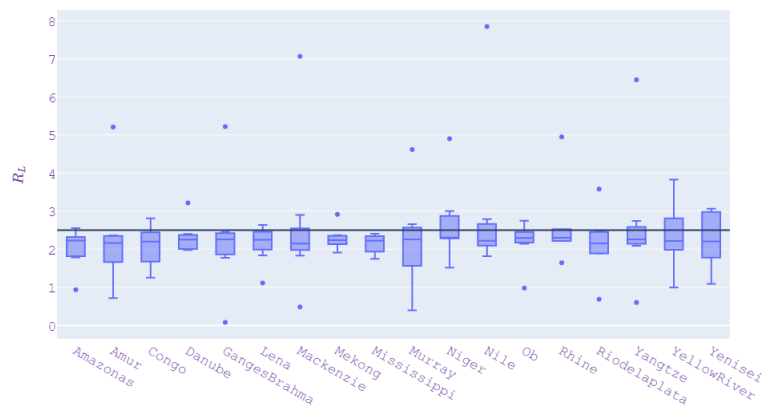
Figure A.7: Length ratios R_L
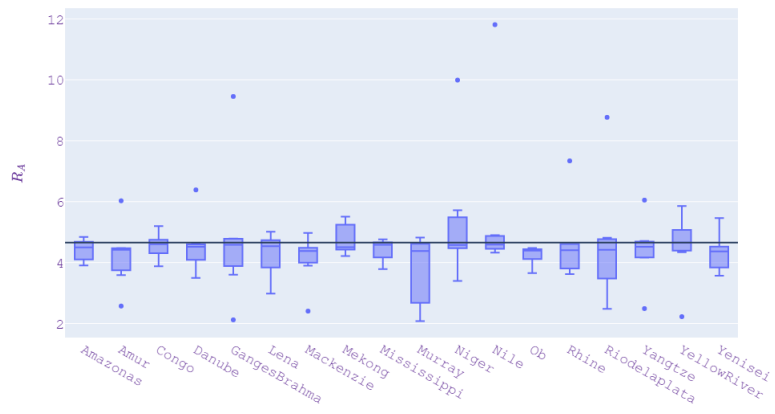
Figure A.8: Accumulated area ratios R_A

Abrahams, A. D., A. J. Parsons, and L. Shiu-Hung (1990). "Field experiments on the resistance to overland flow on desert hillslopes." In: *Erosion, Transport and Deposition Processes* 189.

Abrahams, A. D., J. D. Parsons, and J. Wainwright (1994). "Resistance to overland flow on semiarid grassland and shrubland hillslopes, Walnut Gulch, southern Arizona." In: *Journal of Hydrology* 156, pp. 431–446. ISSN: 00221694.

Achten, W. M. J., S. Dondeyne, S. Mugogo, E. Kafiriti, J. Poesen, J. Deckers, and B. Muys (2008). "Gully erosion in South Eastern Tanzania: spatial distribution and topographic thresholds." In: *Zeitschrift für Geomorphologie* 52.2, pp. 225–235. ISSN: 03728854. DOI: 10.1127/0372-8854/2008/0052-0225.

Ali, M., G. Sterk, M. Seeger, M. Boersema, and P. Peters (2012). "Effect of hydraulic parameters on sediment transport capacity in overland flow over erodible beds." In: *Hydrol. Earth Syst. Sci.* 16.2, pp. 591–601. DOI: 10.5194/hess-16-591-2012.

Armijos, E. et al. (2020). "Rainfall control on Amazon sediment flux: synthesis from 20 years of monitoring." In: *Environmental Research Communications* 2.5, p. 051008. DOI: 10.1088/2515-7620/ab9003.

Arndt, J. and C. Haenel (2001). *Pi – Unleashed*. Berlin, Heidelberg: Springer Berlin Heidelberg. ISBN: 978-3-642-56735-3.

Asselman, N. E. M. (1999). "Suspended sediment dynamics in a large drainage basin: the River Rhine." In: *Hydrological Processes* 13.10, pp. 1437–1450. ISSN: 08856087. DOI: 10.1002/(SICI)1099-1085(199907)13:10{\textless}1437::AID-HYP821{\textgreater}3.0.CO;2-J.

Bagnold, R. A. (1966). "An approach to the sediment transport problem from general physics." In: *US. geol. Surv. Prof. Paper* 422-I. URL: https://pubs.usgs.gov/pp/0422i/report.pdf.

Beighley, R. E., K. G. Eggert, T. Dunne, Y. He, V. Gummadi, and K. L. Verdin (2009). "Simulating hydrologic and hydraulic processes throughout the Amazon River Basin." In: *Hydrological Processes* 23.8, pp. 1221–1235. ISSN: 08856087. DOI: 10.1002/hyp.7252.

Bejan, A. and S. Lorente (2010). "The constructal law of design and evolution in nature." In: *Philosophical transactions of the Royal Society of London. Series B, Biological sciences* 365.1545, pp. 1335–1347. DOI: 10.1098/rstb.2009.0302.

Berger, C., M. Schulze, D. H. Rieke-Zapp, and F. Schlunegger (2010). "Rill development and soil erosion: a laboratory study of slope and rainfall intensity." In: *Earth. Surf. Process. Landforms* 35, pp. 1456–1467.

Berkowitz, B. and E. Zehe (2020). "Surface water and groundwater: unifying conceptualization and quantification of the two "water worlds"." In: *Hydrology and Earth System Sciences* 24.4, pp. 1831–1858. DOI: 10.5194/hess-24-1831-2020.

Beven, K. J. (1981). "The effect of ordering on the geomorphic effectiveness of hydrologic events." In: *Intl. Assoc. Hydrol. Sci. Pub.* 132, pp. 510–526.

– (1996). *Equifinality and uncertainty in geomorphological modelling*. The Scientific Nature of Geomorphology. Rhoads, B. L. and Thorn, C. E., Wiley, Chichester. ISBN: 0-471-96811-0.

– (2004). "Robert E. Horton's perceptual model of infiltration processes." In: *Hydrol. Process.* 18.17, pp. 3447–3460. DOI: 10.1002/hyp.5740.

– (2006). "Searching for the Holy Grail of scientific hydrology: Qt=f(S, R, dt)A as closure." In: *Hydrology and Earth System Sciences* 10.5, pp. 609–618. DOI: 10.5194/hess-10-609-2006.

Beven, K. J. and M. J. Kirkby (1979). "A physically based, variable contributing area model of basin hydrology." In: *Hydrological Sciences Bulletin* 24.1, pp. 43–69. ISSN: 0303-6936. DOI: 10.1080/02626667909491834.

Beven, K. J., M. J. Kirkby, J. E. Freer, and R. Lamb (2021). "A history of TOPMODEL." In: *Hydrology and Earth System Sciences* 25.2, pp. 527–549. DOI: 10.5194/hess-25-527-2021.

Blatter, A. S., J. Liebert, P. A. Preuss, J. Szabadics, and J. Ihringer (2007). "Information system "BW_Abfluss": regionalisation of flood, mean and low flow parameters." In: *Advances in Geosciences*. Copernicus GmbH, pp. 57–61. ISBN: 1680-7340. DOI: 10.5194/adgeo-11-57-2007. URL: https://adgeo.copernicus.org/articles/11/57/2007/.

Blöschl, G. et al. (2019). "Twenty-three unsolved problems in hydrology (UPH) – a community perspective." In: *Hydrological Sciences Journal* 64.10, pp. 1141–1158. ISSN: 0262-6667. DOI: 10.1080/02626667.2019.1620507.

Bonetti, S., M. Hooshyar, C. Camporeale, and A. Porporato (2020). "Channelization cascade in landscape evolution." In: *Proceedings of the National Academy of Sciences of the United States of America* 117.3, pp. 1375–1382. DOI: 10.1073/pnas.1911817117.

Boyer, C. B. and U. C. Merzbach (1991). *A history of mathematics*. 2., rev. ed. New York: Wiley. ISBN: 978-0-471-54397-8.

Brown, G. O. (2002). "Henry Darcy and the making of a law." In: *Water Resources Research* 38.7, pp. 11–1–11–12. ISSN: 00431397. DOI: 10.1029/2001WR000727.

Causon, D. M. and C. G. Mingham (2010). *Introductory finite difference methods for PDEs*. Ventus Publishing ApS. ISBN: 978-87-7681-642-1.

Celia, M. A., E. T. Bouloutas, and R. L. Zarba (1990). "A general mass-conservative numerical solution for the unsaturated flow equation." In: *Water Resources Research* 26.7, pp. 1483–1496. ISSN: 00431397. DOI:

10.1029/WR026i007p01483. URL: https://agupubs.onlinelibrary.
wiley.com/doi/10.1029/WR026i007p01483.

Chanson, H. (2004). *Environmental hydraulics of open channel flows*. Amsterdam [The Netherlands]: Elsevier Butterworth-Heinemann. ISBN: 0750661658.

Chen, A., J. Darbon, and J.-M. Morel (2014). "Landscape evolution models: A review of their fundamental equations." In: *Geomorphology* 219, pp. 68–86. ISSN: 0169555X. DOI: 10.1016/j.geomorph.2014.04.037.

Cheraghi, M., A. Rinaldo, G. C. Sander, P. Perona, and D. A. Barry (2018). "Catchment Drainage Network Scaling Laws Found Experimentally in Overland Flow Morphologies." In: *Geophysical Research Letters* 45.18, pp. 9614–9622. ISSN: 0094-8276. DOI: 10.1029/2018GL078351.

Chow, V. T. (1959). *Open channel hydraulics*. McGraw-Hill. ISBN: 9780070859067.

Constantine, J. A., T. Dunne, J. Ahmed, C. Legleiter, and E. D. Lazarus (2014). "Sediment supply as a driver of river meandering and floodplain evolution in the Amazon Basin." In: *Nature Geoscience* 7.12, pp. 899–903. ISSN: 1752-0894. DOI: 10.1038/ngeo2282.

Conte, L., M. Renner, P. Brando, C. Oliveira dos Santos, D. Silvério, O. Kolle, S. E. Trumbore, and A. Kleidon (2019). "Effects of tropical deforestation on surface energy balance partitioning in southeastern Amazonia estimated from maximum convective power." In: *Geophysical Research Letters* 46.8, pp. 4396–4403. ISSN: 0094-8276. DOI: 10.1029/2018GL081625.

Das, S. K. and J. Bagheri (2015). "Modelling of shallow-water equations by using compact MacCormack-Type schemes with application to dam-break problem." In: *Int. J. Adv. Appl. Math. and Mech.* 2.3, pp. 60–71.

Dietrich, W. E., T. Dunne, N. F. Humphrey, and L. M. Reid (1982). "Construction of sediment budgets for drainage basins." In: *Sediment Budgets and Routing in Forested Drainage Basins: Proceedings of the Symposium* PNW-141. URL: https://www.fs.usda.gov/treesearch/pubs/7749.

Dietrich, W. E., C. J. Wilson, and S. L. Reneau (1986). *Hollows, colluvium, and landslides in soil-mantled landscapes: Hillslope Processes*. ISBN: 9781003028840.

Dingman, S. L. (2015). *Physical hydrology*. 3. ed. Long Grove, Ill.: Waveland Press. ISBN: 1-4786-1118-9.

Dodds, P. S. and D. H. Rothman (2000). "Scaling, Universality, and Geomorphology." In: *Annual Review of Earth and Planetary Sciences* 28.1, pp. 571–610. ISSN: 0084-6597. DOI: 10.1146/annurev.earth.28.1.571.

Döll, P., F. Kaspar, and B. Lehner (2003). "A global hydrological model for deriving water availability indicators: model tuning and valida-

tion." In: *Journal of Hydrology* 270.1-2, pp. 105–134. ISSN: 00221694. DOI: 10.1016/S0022-1694(02)00283-4.

Dunne, T. and R. D. Black (1970). "An experimental investigation of runoff production in permeable soils." In: *Water Resour. Res.* 6.2, pp. 478–490. DOI: 10.1029/WR006i002p00478.

Dunne, T. and W. E. Dietrich (1980). "Experimental investigation of Horton overland flow on tropical hillslopes: Part II: Hydraulic characteristics and hillslope hydrographs." In: *Zeitschrift für Geomorphologie* Supplement Band 35, pp. 60–80.

Dunne, T., L. A. K. Mertes, R. H. Meade, J. E. Richey, and B. R. Forsberg (1998). "Exchanges of sediment between the flood plain and channel of teh Amazon River in Brazil." In: *Geol. Society of America Bulletin* 110.4, pp. 450–467. DOI: 10.1130/0016-7606.

Emmett, W. W. (1970). "The Hydraulics of Overland Flow on Hillslopes." In: *US. geol. Surv. Prof. Paper* 662. URL: https://pubs.usgs.gov/pp/0662a/report.pdf.

Engelund, F. and E. Hansen (1967). "A monograph on sediment transport in alluvial streams: Hydraulic Engineering Reports." In: URL: http://resolver.tudelft.nl/uuid:81101b08-04b5-4082-9121-861949c336c9.

Engman, T. E. (1986). "Roughness coefficients for routing surface runoff." In: *Journal of Irrigation and Drainage Engineering* 112, pp. 39–53.

Espinoza Villar, J. C., J. Ronchail, J. L. Guyot, G. Cochonneau, N. Filizola, W. Lavado, E. de Oliveira, R. Pombosa, and P. Vauchel (2009a). "Spatio-temporal rainfall variability in the Amazon basin countries (Brazil, Peru, Bolivia, Colombia, and Ecuador)." In: *International Journal of Climatology* 29.11, pp. 1574–1594. ISSN: 08998418. DOI: 10.1002/joc.1791.

Espinoza Villar, Jhan Carlo, Jean Loup Guyot, Josyane Ronchail, Gérard Cochonneau, Naziano Filizola, Pascal Fraizy, David Labat, Eurides de Oliveira, Juan Julio Ordoñez, and Philippe Vauchel (2009b). "Contrasting regional discharge evolutions in the Amazon basin (1974–2004)." In: *Journal of Hydrology* 375.3-4, pp. 297–311. ISSN: 00221694. DOI: 10.1016/j.jhydrol.2009.03.004.

Evans, R. and J. Taylor (1995). "Some methods of directly assessing water erosion of cultivated land - a comparison of measurements made on plots and in fields." In: *Progress in Physical Geography* 19, pp. 115–129.

Fassoni-Andrade, A. C. et al. (2021). "Amazon Hydrology From Space: Scientific Advances and Future Challenges." In: *Reviews of Geophysics* 59.4. ISSN: 8755-1209. DOI: 10.1029/2020RG000728.

Faulkner, H. (2008). "Connectivity as a crucial determinant of badland morphology and evolution." In: *Geomorphology* 100.1-2, pp. 91–103. ISSN: 0169555X. DOI: 10.1016/j.geomorph.2007.04.039.

Feigenbaum, M. J. (1978). "Quantitative universality for a class of nonlinear transformations." In: *Journal of Statistical Physics* 19.1, pp. 25–52. ISSN: 0022-4715. DOI: 10.1007/BF01020332.

Fick, A. (1855). "On liquid diffusion." In: *Philos. Mag.* 4.10, pp. 30–39. DOI: 10.1016/0376-7388{\%}2894{\%}2900230-V.

Figueroa, S. N. and C. A. Nobre (1990). "Precipitation Distribution over Central and Western Tropical South America." In: *Climanálise* 5.6, pp. 36–45.

Filizola, N. and J. L. Guyot (2009). "Suspended sediment yields in the Amazon basin: an assessment using the Brazilian national data set." In: *Hydrological Processes* 23.22, pp. 3207–3215. ISSN: 08856087. DOI: 10.1002/hyp.7394.

Frings, R. M., G. Hillebrand, N. Gehres, K. Banhold, S. Schriever, and T. Hoffmann (2019). "From source to mouth: Basin-scale morphodynamics of the Rhine River." In: *Earth-Science Reviews* 196, p. 102830. ISSN: 00128252. DOI: 10.1016/j.earscirev.2019.04.002.

Frisch, U. (1995). *Turbulence: The legacy of A.N. Kolmogorov*. Cambridge University Press. ISBN: 9780521451031. DOI: 10.1017/CBO9781139170666.

Gauch, M., F. Kratzert, D. Klotz, G. Nearing, J. Lin, and S. Hochreiter (2021). "Rainfall–runoff prediction at multiple timescales with a single Long Short-Term Memory network." In: *Hydrology and Earth System Sciences* 25.4, pp. 2045–2062. DOI: 10.5194/hess-25-2045-2021.

Gerlinger, K. (1996). *Erosionsprozesse auf Lössböden: Experimente und Modellierung: Dissertation*. Vol. 194. Mitteilungen des Institutes für Wasserbau und Kulturtechnik der Universität Karlsruhe (TH).

Germann, P. F. and L. Di Pietro (1999). "Scales and dimensions of momentum dissipation during preferential flow in soils." In: *Water Resources Research* 35.5, pp. 1443–1454. ISSN: 00431397. DOI: 10.1029/1998WR900112.

Gibbs, R. J. (1967). "The Geochemistry of the Amazon River System: Part I. The Factors that Control the Salinity and the Composition and Concentration of the Suspended Solids." In: *Geological Society of America Bulletin* 78.10, p. 1203. ISSN: 00167606. DOI: 10.1130/0016-7606(1967)78[1203:TGOTAR]2.0.CO;2.

Gilbert, G. K. (1876). "The Colorado plateau province as a field for geological study." In: *American Journal of Science* s3-12.67, pp. 16–24. ISSN: 0002-9599. DOI: 10.2475/AJS.S3-12.67.16.

Gillett, S. L. (2006). "Entropy and its misuse, I. Energy, free and otherwise." In: *Ecological Economics* 56.1, pp. 58–70. ISSN: 09218009. DOI: 10.1016/j.ecolecon.2004.12.019.

Giménez, R. and G. Govers (2002). "Flow detachment by concentrated flow on smooth and irregular beds." In: *Soil Science Society of America Journal* 66.5, pp. 1475–1483. ISSN: 03615995. DOI: 10.2136/sssaj2002.1475.

Gleick, J. (1988). *Chaos: Making a new science*. New York: Viking. ISBN: 0670811785.

Gob, F., J. P. Bravard, and F. Petit (2010). "The influence of sediment size, relative grain size and channel slope on initiation of sediment motion in boulder bed rivers. A lichenometric study." In: *Earth Surface Processes and Landforms* 35.13, pp. 1535–1547. ISSN: 01979337. DOI: 10.1002/esp.1994.

Gomez, J. A., F. Darboux, and M. A. Nearing (2003). "Development and evolution of rill networks under simulated rainfall." In: *Water Resour. Res.* 6.

Govers, G. (1992). "Relationship between discharge, velocity and flow area for rills eroding loose, non-layered materials." In: *Earth. Surf. Process. Landforms* 17, pp. 515–528.

Govers, G., I. Takken, and K. Helming (2000). "Soil roughness and overland flow." In: *Agronomie* 20, pp. 131–146. DOI: 10.1016/0304-1131(75)90001-6.

Graeff, T., E. Zehe, D. Reusser, E. Lück, B. Schröder, G. Wenk, H. John, and A. Bronstert (2009). "Process identification through rejection of model structures in a mid-mountainous rural catchment: observations of rainfall-runoff response, geophysical conditions and model inter-comparison." In: *Hydrological Processes* 23.5, pp. 702–718. ISSN: 08856087. DOI: 10.1002/hyp.7171.

Grau Galofre, A. and A. M. Jellinek (2017). "The geometry and complexity of spatial patterns of terrestrial channel networks: Distinctive fingerprints of erosional regimes." In: *Journal of Geophysical Research: Earth Surface* 122.4, pp. 1037–1059. ISSN: 21699003. DOI: 10.1002/2016JF003825.

Guyot, J. L. (1993). *Hydrogéochimie des fleuves de l'Amazonie bolivienne*. Collection Etudes et thèses. Paris: Editions de l'ORSTOM. ISBN: 978-2709911573.

Hack J. T. (1957). "Studies of longitudinal stream profiles in Virginia and Maryland." In: *US. geol. Surv. Prof. Paper* 294-B. URL: https://pubs.usgs.gov/pp/0294b/report.pdf.

Heisenberg, W. (1927). "ber den anschaulichen Inhalt der quantentheoretischen Kinematik und Mechanik." In: *Zeitschrift fr Physik* 43.3-4, pp. 172–198. ISSN: 1434-6001. DOI: 10.1007/BF01397280.

Hijmans, R. J., S. E. Cameron, J. L. Parra, P. G. Jones, and A. Jarvis (2005). "Very high resolution interpolated climate surfaces for global land areas." In: *International Journal of Climatology* 25.15, pp. 1965–1978. ISSN: 08998418. DOI: 10.1002/joc.1276.

Hooshyar, M., S. Bonetti, A. Singh, E. Foufoula-Georgiou, and A. Porporato (2020). "From turbulence to landscapes: Logarithmic mean profiles in bounded complex systems." In: *Physical review. E* 102.3-1, p. 033107. DOI: 10.1103/PhysRevE.102.033107.

Horton, R. E. (1931). "The field, scope, and status of the science of hydrology." In: *Transactions, American Geophysical Union* 12.1, p. 189. ISSN: 0002-8606. DOI: 10.1029/TR012i001p00189-2.

– (1945). "Erosional development of streams and their drainage basins; Hydrophysical approach to quantitive morphology." In: *Bulletin of the Geological Soc. of America* 56, pp. 275–370.

Howard, A. D. (1990). "Theoretical model of optimal drainage networks." In: *Water Resources Research* 26.9, pp. 2107–2117. ISSN: 00431397. DOI: 10.1029/WR026i009p02107. URL: https://agupubs.onlinelibrary.wiley.com/doi/10.1029/WR026i009p02107.

Hrachowitz, M. et al. (2013). "A decade of Predictions in Ungauged Basins (PUB)—a review." In: *Hydrological Sciences Journal* 58.6, pp. 1198–1255. ISSN: 0262-6667. DOI: 10.1080/02626667.2013.803183.

Ijjasz Vasquez, E. J., R. L. Bras, I. Rodriguez-Iturbe, R. Rigon, and A. Rinaldo (1993). "Are river basins optimal channel networks?" In: *Advances in Water Resources* 16, pp. 69–79.

Junghänel, T., H. Ertel, and T. Deutschländer (2010). "KOSTRA-DWD-2010R- Bericht zur Revision der koordinierten Starkregenregionalisierung und -auswertung des Deutschen Wetterdienstes: Version 2010." In: URL: https://www.dwd.de/DE/leistungen/kostra_dwd_rasterwerte/download/bericht_kostra_dwd_2010_pdf.pdf.

Kinnell, P. I. A. (2020). "The influence of time and other factors on soil loss produced by rain-impacted flow under artificial rainfall." In: *Journal of Hydrology* 587, p. 125004. ISSN: 00221694. DOI: 10.1016/j.jhydrol.2020.125004. URL: https://www.sciencedirect.com/science/article/pii/S0022169420304649.

Kirchner, J. W. (2006). "Getting the right answers for the right reasons: Linking measurements, analyses, and models to advance the science of hydrology." In: *Water Resources Research* 42.3. ISSN: 00431397. DOI: 10.1029/2005WR004362.

– (2009). "Catchments as simple dynamical systems: Catchment characterization, rainfall-runoff modeling, and doing hydrology backward." In: *Water Resources Research* 45.2. ISSN: 00431397. DOI: 10.1029/2008WR006912.

Kirkby, M. J. (1971). "Hillslope process-response models based in the continuity equation." In: *Special Publication Institute of British Geographers* 3, pp. 15–30.

– (1975). *Hydrograph modelling strategies*. Processes in Human and Physical Geography. London: Heinemann.

Kleidon, A. (2016). *Thermodynamic foundations of the Earth system*. New York NY: Cambridge University Press. ISBN: 9781107029941.

Kleidon, A. and R. Lorenz (2005). *Non-equilibrium thermodynamics and the production of entropy: Life, Earth and beyond*. Springer complexity. Berlin: Springer. ISBN: 978-3-642-06135-6.

Kleidon, A. and M. Renner (2018). "Diurnal land surface energy balance partitioning estimated from the thermodynamic limit of a cold

heat engine." In: *Earth System Dynamics* 9.3, pp. 1127–1140. DOI: 10.5194/esd-9-1127-2018.

Kleidon, A., M. Renner, and P. Porada (2014). "Estimates of the climatological land surface energy and water balance derived from maximum convective power." In: *Hydrology and Earth System Sciences* 18.6, pp. 2201–2218. DOI: 10.5194/hess-18-2201-2014.

Kleidon, A., E. Zehe, U. Ehret, and U. Scherer (2013). "Thermodynamics, maximum power, and the dynamics of preferential river flow structures at the continental scale." In: *Hydrology and Earth System Sciences* 17.1, pp. 225–251. DOI: 10.5194/hess-17-225-2013.

Knighton, D. (1998). *Fluvial Forms and Processes*. Routledge. ISBN: 9781444165753. DOI: 10.4324/9780203784662.

Kondepui, D. and I. Prigogine (1952). *Modern thermodynamics: From heat engines to dissipative structures*. John Wiley & Sons, Ltd. ISBN: 0471973939.

Kratzert, F., D. Klotz, G. Shalev, G. Klambauer, S. Hochreiter, and G. Nearing (2019). "Towards learning universal, regional, and local hydrological behaviors via machine learning applied to large-sample datasets." In: *Hydrology and Earth System Sciences* 23.12, pp. 5089–5110. DOI: 10.5194/hess-23-5089-2019.

Krylova, A. I., D. V. Antipova, and D. V. Perevozkin (2017). "The derivation of the Saint-Venant equations." In: *Bull.Nov.Comp.Center, Num.Model. in Atmosph.* 16, pp. 21–35.

LUBW (2022). *Hochwasservorhersagezentrale*. URL: https://hvz.lubw.baden-wuerttemberg.de/map_peg.html.

Langbein, W. B. (1964). "Profiles of rivers of uniform discharge." In: *US. geol. Surv. Prof. Paper* 501.B, pp. 119–122. URL: https://pubs.usgs.gov/pp/0501b/report.pdf.

Latrubesse, E. M. (2008). "Patterns of anabranching channels: The ultimate end-member adjustment of mega rivers." In: *Geomorphology* 101.1-2, pp. 130–145. ISSN: 0169555X. DOI: 10.1016/j.geomorph.2008.05.035.

Lawrence, D. S. L. (1997). "Macroscale surface roughness and frictional resistance in overland flow." In: *Earth. Surf. Process. Landforms* 22, pp. 365–382.

Lehner, B., K. Verdin, and A. Jarvis (2008). "New Global Hydrography Derived From Spaceborne Elevation Data." In: *Eos, Transactions American Geophysical Union* 89.10, p. 93. ISSN: 0096-3941. DOI: 10.1029/2008EO100001.

Leopold, L. B. and W. B. Langbein (1962). "The concept of entropy in landscape evolution." In: *US. geol. Surv. Prof. Paper* 500-A. URL: https://pubs.usgs.gov/pp/0500a/report.pdf.

Leopold, L. B. and Maddock T. (1953). "The hydraulic geometry of stream channels and some physiographic implications." In: *US. geol. Surv. Prof. Paper* 252. DOI: 10.3133/pp252. URL: https://pubs.usgs.gov/pp/0252/report.pdf.

Liang, D., R. A. Falconer, and B. Lin (2006). "Comparison between TVD-MacCormack and ADI-type solvers of the shallow water equations." In: *Advances in Water Resources* 29.12, pp. 1833–1845. DOI: 10.1016/j.advwatres.2006.01.005. URL: https://www.sciencedirect.com/science/article/pii/S0309170806000108.

Liang, D., B. Lin, and R. A. Falconer (2007). "Simulation of rapidly varying flow using an efficient TVD–MacCormack scheme." In: *International Journal for Numerical Methods in Fluids* 53.5, pp. 811–826. ISSN: 02712091. DOI: 10.1002/fld.1305. URL: https://onlinelibrary.wiley.com/doi/10.1002/fld.1305.

Libchaber, A., S. Fauve, and C. Laroche (1983). "Two-parameter study of the routes to chaos." In: *Physica D: Nonlinear Phenomena* 7.1-3, pp. 73–84. ISSN: 01672789. DOI: 10.1016/0167-2789(83)90117-3.

Linke, S. et al. (2019). "Global hydro-environmental sub-basin and river reach characteristics at high spatial resolution." In: *Scientific data* 6.1, p. 283. DOI: 10.1038/s41597-019-0300-6.

Lorenz, E. N. (1963). "Deterministic Nonperiodic Flow." In: *Journal of the Atmospheric Sciences* 20.2, pp. 130–141. ISSN: 0022-4928. DOI: 10.1175/1520-0469{\%}281963{\%}29020{\%}3C0130{\%}3ADNF{\%}3E2.0.CO{\%}3B2.

Loritz, R., S. K. Hassler, C. Jackisch, N. Allroggen, L. van Schaik, J. Wienhöfer, and E. Zehe (2017). "Picturing and modeling catchments by representative hillslopes." In: *Hydrology and Earth System Sciences* 21.2, pp. 1225–1249. DOI: 10.5194/hess-21-1225-2017.

Loritz, R., A. Kleidon, C. Jackisch, M. Westhoff, U. Ehret, H. Gupta, and E. Zehe (2019). "A topographic index explaining hydrological similarity by accounting for the joint controls of runoff formation." In: *Hydrology and Earth System Sciences* 23.9, pp. 3807–3821. DOI: 10.5194/hess-23-3807-2019.

Lotka, A. J. (1922). "Contribution to the energetics of evolution." In: *Biology* 8, pp. 147–151. DOI: 10.1073/pnas.8.6.147. URL: https://doi.org/10.1073/pnas.8.6.147.

Lovelock, J. (1972). *Gaia: A New Look at Life on Earth*. Oxford University Press, USA. ISBN: 978-0198784883.

MacCormack, R. W. (1969). "The effect of viscosity in hypervelocity impact cratering." In: *Journal of Spacecraft and Rockets* 69.354. ISSN: 0022-4650. DOI: 10.2514/2.6901.

Macklin, M. G. and J. Lewin (2015). "The rivers of civilization." In: *Quaternary Science Reviews* 114, pp. 228–244. ISSN: 02773791. DOI: 10.1016/j.quascirev.2015.02.004.

Mandelbrot, B. B. (1983). *The fractals geometry of nature*. Vol. 173. Einaudi paperbacks. San Francisco, Calif.: Freeman. ISBN: 9780716711865.

Marani, A., R. Rigon, and A. Rinaldo (1991). "A Note on Fractal Channel Networks." In: *Water Resources Research* 27.12, pp. 3041–3049. ISSN: 00431397. DOI: 10.1029/91WR02077.

Marengo, J. A. (1992). "Interannual variability of surface climate in the Amazon basin." In: *International Journal of Climatology* 12.8, pp. 853–863. ISSN: 08998418. DOI: 10.1002/joc.3370120808.

Maurer, T. (1997). *Physikalisch begründete, zeitkontinuierliche Modellierung des Wassertransports in kleinen ländlichen Einzugsgebieten*. Vol. 61. Hochschulschrift. Universität Karlsruhe (TH). DOI: 10.5445/IR/65797.

May, R. M. (1976). "Simple mathematical models with very complicated dynamics." In: *Nature* 261.5560, pp. 459–467. ISSN: 0028-0836. DOI: 10.1038/261459a0.

Meade, R. H., T. Dunne, J. E. Richey, U. de M Santos, and E. Salati (1985). "Storage and remobilization of suspended sediment in the lower Amazon river of Brazil." In: *Science (New York, N.Y.)* 228.4698, pp. 488–490. ISSN: 0036-8075. DOI: 10.1126/science.228.4698.488.

Mu, Q., F. A. Heinsch, M. Zhao, and S. W. Running (2007). "Development of a global evapotranspiration algorithm based on MODIS and global meteorology data." In: *Remote Sensing of Environment* 111.4, pp. 519–536. ISSN: 00344257. DOI: 10.1016/j.rse.2007.04.015.

Mualem, Y. (1976). "A new model for predicting the hydraulic conductivity of unsaturated porous media." In: *Water Resour. Res.* 12, pp. 513–522. DOI: 10.1029/WR012i003p00513.

Nearing, M. A., A. Kimoto, M. H. Nichols, and J. C. Ritchie (2005). "Spatial patterns of soil erosion and deposition in two small, semiarid watersheds." In: *Journal of Geophysical Research: Earth Surface* 110.F4, n/a–n/a. ISSN: 01480227. DOI: 10.1029/2005JF000290.

Nearing, M. A., L. D. Norton, D. A. Bulgakov, G. A. Larionov, L. T. West, and K. M. Dontsova (1997). "Hydraulics and erosion in eroding rills." In: *Water Resources Research* 33.4, pp. 865–876. ISSN: 00431397. DOI: 10.1029/97WR00013. URL: https://agupubs.onlinelibrary.wiley.com/doi/10.1029/97WR00013.

Nearing, M. A., V. O. Polyakov, M. H. Nichols, M. Hernandez, L. Li, Y. Zhao, and G. Armendariz (2017). "Slope–velocity equilibrium and evolution of surface roughness on a stony hillslope." In: *Hydrology and Earth System Sciences* 21.6, pp. 3221–3229. DOI: 10.5194/hess-21-3221-2017.

Ochoa-Tocachi, B. F. et al. (2019). "Potential contributions of pre-Inca infiltration infrastructure to Andean water security." In: *Nature Sustainability* 2.7, pp. 584–593. DOI: 10.1038/s41893-019-0307-1.

Ottino, J. M. (1990). "Mixing, Chaotic Advection, and Turbulence." In: *Annual Review of Fluid Mechanics* 22.1, pp. 207–254. ISSN: 0066-4189. DOI: 10.1146/annurev.fl.22.010190.001231.

Paik, K. and P. Kumar (2010). "Optimality approaches to describe characteristic fluvial patterns on landscapes." In: *Philosophical transactions of the Royal Society of London. Series B, Biological sciences* 365.1545, pp. 1387–1395. DOI: 10.1098/rstb.2009.0303.

Paltridge, G. W. (1979). "Climate and thermodynamic systems of maximum dissipation." In: *Nature* 279.5714, pp. 630–631. ISSN: 0028-0836. DOI: 10.1038/279630a0.

Parsons, A. J., A. D. Abrahams, and S. H. Luk (1990). "Hydraulics of interrill overland flow on a semi-arid hillslope, Arizona." In: *Journal of Hydrology* 117, pp. 255–273. ISSN: 00221694.

Penman, H. L. (1948). "Natural evaporation from open water, hare soil and grass." In: *Proceedings of the Royal Society of London. Series A, Mathematical and physical sciences* 193.1032, pp. 120–145. ISSN: 0950-1207. DOI: 10.1098/rspa.1948.0037.

Perron, J. T., W. E. Dietrich, and J. W. Kirchner (2008). "Controls on the spacing of first-order valleys." In: *Journal of Geophysical Research* 113.F4. ISSN: 0148-0227. DOI: 10.1029/2007JF000977.

Perron, J. T., J. W. Kirchner, and W. E. Dietrich (2009). "Formation of evenly spaced ridges and valleys." In: *Nature* 460.7254, pp. 502–505. ISSN: 0028-0836. DOI: 10.1038/nature08174.

Phelps, H. O. (1975). "Friction coefficients for laminar sheet flow over rough surfaces." In: *Proceedings of the Institution of Civil Engineers* 59, pp. 21–41. DOI: 10.1680/iicep.1975.3840.

Plate, E. and E. Zehe (2008). *Hydrologie und Stoffdynamik kleiner Einzugsgebiete: Prozesse und Modelle*. Stuttgart: Schweizerbart Science Publishers. ISBN: 978-3-510-65238-9.

Popovic, M. (2017). *Researchers in an entropy wonderland: A review of the entropy concept*. URL: https://arxiv.org/pdf/1711.07326.

Prigogine, I. (1955). *Introduction to thermodynamics of irreversible processes*. 3d ed. New York: Interscience Publishers. ISBN: 978-0470699287.

– (1978). "Time, structure, and fluctuations." In: *Science (New York, N.Y.)* 201.4358, pp. 777–785. ISSN: 0036-8075. DOI: 10.1126/science.201.4358.777.

Prigogine, I. and J. M. Wiame (1946). "Biologie et thermodynamique des phenomenes irreversibles." In: *Experientia* 2, pp. 451–453. DOI: 10.1007/BF02153597.

Ribeiro, M. L., K. Blanckaert, A. G. Roy, and A. J. Schleiss (2012). "Flow and sediment dynamics in channel confluences." In: *Journal of Geophysical Research* 117. DOI: 10.1029/2011JF002171.

Rieke-Zapp, D. H. and M. A. Nearing (2005). "Slope shape effects on erosion: a laboratory study." In: *Soil Sci. Soc. Am. J.* 69, pp. 1463–1471. DOI: 10.2136/sssaj2005.0015.

Riggs, H. C. (1976). "A simplified slope-area method for estimating flood discharges in natural channels." In: *Journal of Research of the U.S. Geological Survey* 4.3. URL: https://pubs.usgs.gov/journal/1976/vol4issue3/report.pdf.

Robinson, N., J. Regetz, and R. P. Guralnick (2014). "EarthEnv-DEM90: A nearly-global, void-free, multi-scale smoothed, 90m digital elevation model from fused ASTER and SRTM data." In: *ISPRS Journal*

of Photogrammetry and Remote Sensing 87, pp. 57–67. ISSN: 09242716. DOI: 10.1016/j.isprsjprs.2013.11.002.

Rodriguez-Iturbe, I., M. Marani, R. Rigon, and A. Rinaldo (1994). "Self-organized river basin landscapes: Fractal and multifractal characteristics." In: *Water Resources Research* 30.12, pp. 3531–3539. ISSN: 00431397. DOI: 10.1029/94WR01493.

Rodriguez-Iturbe, I., A. Rinaldo, R. Rigon, R. L. Bras, A. Marani, and E. Ijjasz-Vasquez (1992). "Energy dissipation, runoff production, and the threedimensional structure of river basins." In: *Water Resour. Res.* 4, pp. 1095–1103. DOI: 10.1029/91WR03034.

Ruelle, David and Floris Takens (1971). "On the nature of turbulence." In: *Communications in Mathematical Physics* 20.3, pp. 167–192. ISSN: 0010-3616. DOI: 10.1007/BF01646553.

Salati, E. and P. B. Vose (1984). "Amazon basin: a system in equilibrium." In: *Science (New York, N.Y.)* 225.4658, pp. 129–138. ISSN: 0036-8075. DOI: 10.1126/science.225.4658.129.

Schäfer, D. (1999). *Bodenhydraulische Eigenschaften eines Kleineinzugsgebietes- Vergleich und Bewertung unterschiedlicher Verfahren. Dissertation.*

Scherer, U., E. Zehe, K. Träbing, and K. Gerlinger (2012). "Prediction of soil detachment in agricultural loess catchments: Model development and parameterisation." In: *CATENA* 90, pp. 63–75. ISSN: 03418162. DOI: 10.1016/j.catena.2011.11.003.

Scherer, Ulrike (2008). *Prozessbasierte Modellierung der Bodenerosion in einer Lösslandschaft: Karlsruhe, Univ., Diss.* Vol. 129. Schriftenreihe SWW.

Schierholz, I., D. Schäfer, and O. Kolle (2000). "The Weiherbach data set: An experimental data set for pesticide model testing in the field scale." In: *Agricultural Water Management* 44, pp. 43–61. DOI: 10.1016/S0378-3774(99)00083-9.

Schlichting, H. and K. Gersten (2017). *Boundary-Layer Theory.* Berlin, Heidelberg: Springer Berlin Heidelberg. DOI: 10.1007/978-3-662-52919-5.

Schmidt, G. W. (1972). "Amounts of suspended solids and dissolved substances in the middle reaches of the Amazon over the course of one year (August, 1969 - July, 1970)." In: *Amazoniana: Limnologia et Oecologia Regionalis Systematis Fluminis Amazonas* 3.2, pp. 208–223.

Schmidt, J. (1996). *Entwicklung und Anwendung eines physikalisch begründeten Simulationsmodells für die Erosion geneigter landwirtschaftlicher Nutzflächen.* Selbstverl. des Inst. für Geograph. Wiss., Berlin. ISBN: 3-88009-062-9. DOI: 10.23689/fidgeo-3199. URL: https://e-docs.geo-leo.de/handle/11858/7519?locale-attribute=en.

Schroers, S., O. Eiff, A. Kleidon, U. Scherer, J. Wienhöfer, and E. Zehe (2022). "Morphological controls on surface runoff: an interpretation of steady-state energy patterns, maximum power states and dissipation regimes within a thermodynamic framework." In: *Hydrology and Earth System Sciences* 26.12, pp. 3125–3150. DOI: 10.5194/hess-

26-3125-2022. URL: https://hess.copernicus.org/articles/26/3125/2022/.

Schumm, S. A., M. D. Harvey, and C. C. Watson (1984). *Incised Channels: Morphology, Dynamics and Control*. Water Resources Publications. ISBN: 09-183-3453.

Seibert, S., K. Auerswald, P. Fiener, M. Disse, W. Martin, A. M. Haider, and K. Gerlinger (2011). "Surface runoff from arable land- a homogenized data base of 726 rainfall simulation experiments: CRC/TR32 Database (TR32DB)." In: DOI: 10.1594/GFZ.TR32.2,\%00202011.

Shih, H. M. and C. T. Yang (2009). "Estimating overland flow erosion capacity using unit stream power." In: *International Journal of Sediment Research* 24.1, pp. 46–62. DOI: 10.1016/S1001-6279(09)60015-9.

Shreve, R. L. (1966). "Statistical Law of Stream Numbers." In: *The Journal of Geology* 74.1, pp. 17–37. ISSN: 0022-1376. DOI: 10.1086/627137.

Singh, V. P. (2003). "On the theories of hydraulic geometry." In: *International Journal of Sediment Research* 18, pp. 196–218.

Sioli, H. (1957). "Sedimentation im Amazonasgebiet." In: *Geologische Rundschau* 45.3, pp. 608–633. ISSN: 0016-7835. DOI: 10.1007/BF02296856.

Sivakumar, B. (2017). *Chaos in Hydrology*. Dordrecht: Springer Netherlands. ISBN: 978-90-481-2551-7. DOI: 10.1007/978-90-481-2552-4.

Smart, J. S. (1972). "Channel networks." In: *Advances in Hydroscience* 8, pp. 305–345.

Stepinski, T. F., M. M. Marinova, P. J. McGovern, and S. M. Clifford (2002). "Fractal analysis of drainage basins on Mars." In: *Geophysical Research Letters* 29.8, pp. 30–1–30–4. ISSN: 0094-8276. DOI: 10.1029/2002GL014666.

Stølum, H.-H. (1998). "Planform geometry and dynamics of meandering rivers." In: *Geological Society of America Bulletin* 110.11, p. 1485. ISSN: 00167606. DOI: 10.1130/0016-7606(1998)110{\%}3C1485:PGADOM{\%}3E2.3.CO;2.

Stølum, Hans-Henrik (1996). "River Meandering as a Self-Organization Process." In: *Science (New York, N.Y.)* 271.5256, pp. 1710–1713. ISSN: 0036-8075. DOI: 10.1126/science.271.5256.1710.

Strahler, Arthur N. (1957). "Quantitative analysis of watershed geomorphology." In: *Transactions, American Geophysical Union* 38.6, p. 913. ISSN: 0002-8606. DOI: 10.1029/TR038i006p00913.

Tanner, W. F. (1971). "The river profile." In: *The Journal of Geology* 79.4, pp. 482–492. ISSN: 0022-1376. URL: http://www.jstor.org/stable/30063062.

Tarboton, D. G., R. L. Bras, and I. Rodriguez-Iturbe (1988). "The fractal nature of river networks." In: *Water Resources Research* 24.8, pp. 1317–1322. ISSN: 00431397. DOI: 10.1029/WR024i008p01317.

Tarboton, D. G., R. L. Bras, and I. Rodriguez-Iturbe (1992). "A physical basis for drainage density." In: *Geomorphology* 5.1-2, pp. 59–76. ISSN: 0169555X. DOI: 10.1016/0169-555X(92)90058-V.

Tennekes, H. and J. L. Lumley (1972). *A first course in turbulence*. Cambridge Mass.: MIT Press.

Thorn, C. E. and M. R. Welford (1994). "The Equilibrium Concept in Geomorphology." In: *Annals of the Association of American Geographers* 84.4, pp. 666–696. ISSN: 00045608. URL: http://www.jstor.org/stable/2564149.

Tribus, M. and E. C. McIrvine (1971). "Energy and information." In: *Scientific American* 224, pp. 179–188. DOI: 10.1038/scientificamerican0971-179.

Tulla, J. G. (1825). "Ueber die Rektifikation des Rhein von seinem Austritt aus der Schweiz bis zu seinem Eintritt in das Gro-herzugtum Hessen." In.

Vincent, S., J.-P. Caltagirone, and P. Bonneton (2001). "Numerical modelling of bore propagation and run-up on sloping beaches using a MacCormack TVD scheme." In: *Journal of Hydraulic Research* 39.1, pp. 41–49. ISSN: 0022-1686. DOI: 10.1080/00221680109499801.

Vollmer S. and Goelz E. (2006). "Sediment monitoring and sediment management in the Rhine River." In: *Sediemtn Dynamics and the Hydromorphology of Fluvial Systems. IAHS Publ.* 306.

West, G. B., J. H. Brown, and B. J. Enquist (1997). "A general model for the origin of allometric scaling laws in biology." In: *Science (New York, N.Y.)* 276.5309, pp. 122–126. ISSN: 0036-8075. DOI: 10.1126/science.276.5309.122.

Willgoose, Garry, Rafael L. Bras, and Ignacio Rodriguez-Iturbe (1991). "A coupled channel network growth and hillslope evolution model: 1. Theory." In: *Water Resources Research* 27.7, pp. 1671–1684. ISSN: 00431397. DOI: 10.1029/91WR00935.

Wischmeier, W. H. and Smith D.D. (1978). "Predicting rainfall erosion losses: a guide to conservation planning." In: *Agriculture Handbook, US Department of Agriculture* 537.

Wolman M. G. and Miller J. P. (1960). "Magnitude and frequency of forces in geomorphic processes." In: *The Journal of Geology* 68.1, pp. 54–75. ISSN: 0022-1376. URL: http://www.jstor.org/stable/30058255.

Wolman, M. G. and R. Gerson (1978). "Relative scales of time and effectiveness of climate in watershed geomorphology." In: *Earth. Surf. Process. and Landforms* 3.2, pp. 189–208. URL: https://doi.org/10.1002/esp.3290030207.

Wooding, R. A. (1965). "A hydraulic model for the catchment-stream problem." In: *Journal of Hydrology* 3, pp. 254–267. ISSN: 00221694. DOI: 10.1002/9781118925935.ch2.

Woolderink, H.A.G., K. M. Cohen, C. Kasse, M. G. Kleinhans, and R. T. van Balen (2021). "Patterns in river channel sinuosity of the Meuse,

Roer and Rhine rivers in the Lower Rhine Embayment rift-system, are they tectonically forced?" In: *Geomorphology* 375, p. 107550. ISSN: 0169555X. DOI: 10.1016/j.geomorph.2020.107550.

Yang, C. T. (1971). "Potential Energy and Stream Morphology." In: *Water Resour. Res.* 7, pp. 311–322. DOI: 10.1029/WR007i002p00311.

– (1976). "Minimum Unit Stream Power and Fluvial Hydraulics." In: *Journal of the Hydraulics Division* 102.

Zehe, E. (1999). *Stofftransport in der ungesättigten Bodenzone auf verschiedenen Skalen*. Vol. 64. Hochschulschrift. Universität Karlsruhe (TH). DOI: 10.5445/IR/60999.

Zehe, E., R. Becker, A. Bárdossy, and E. Plate (2005). "Uncertainty of simulated catchment runoff response in the presence of threshold processes: Role of initial soil moisture and precipitation." In: *Journal of Hydrology* 315.1-4, pp. 183–202. ISSN: 00221694. DOI: 10.1016/j.jhydrol.2005.03.038.

Zehe, E. and G. Blöschl (2004). "Predictability of hydrologic response at the plot and catchment scales: Role of initial conditions." In: *Water Resources Research* 40.10. ISSN: 00431397. DOI: 10.1029/2003WR002869.

Zehe, E., T. Blume, and G. Blöschl (2010). "The principle of 'maximum energy dissipation': a novel thermodynamic perspective on rapid water flow in connected soil structures." In: *Philosophical transactions of the Royal Society of London. Series B, Biological sciences* 365.1545, pp. 1377–1386. DOI: 10.1098/rstb.2009.0308.

Zehe, E., U. Ehret, T. Blume, A. Kleidon, U. Scherer, and M. Westhoff (2013). "A thermodynamic approach to link self-organization, preferential flow and rainfall–runoff behaviour." In: *Hydrology and Earth System Sciences* 17.11, pp. 4297–4322. DOI: 10.5194/hess-17-4297-2013.

Zehe, E. and H. Flühler (2001a). "Preferential transport of isoproturon at a plot scale and a field scale tile-drained site." In: *Journal of Hydrology* 247.1-2, pp. 100–115. ISSN: 00221694. DOI: 10.1016/S0022-1694(01)00370-5.

– (2001b). "Slope scale variation of flow patterns in soil profiles." In: *Journal of Hydrology* 247.1-2, pp. 116–132. ISSN: 00221694. DOI: 10.1016/S0022-1694(01)00371-7.

Zehe, E., R. Loritz, Y. Edery, and B. Berkowitz (2021). "Preferential pathways for fluid and solutes in heterogeneous groundwater systems: self-organization, entropy, work." In: *Hydrology and Earth System Sciences* 25.10, pp. 5337–5353. DOI: 10.5194/hess-25-5337-2021. URL: https://hess.copernicus.org/articles/25/5337/2021/.

Zehe, E., T. Maurer, J. Ihringer, and E. Plate (2001). "Modeling water flow and mass transport in a loess catchment." In: *Physics and Chemistry of the Earth, Part B: Hydrology, Oceans and Atmosphere* 26.7-8, pp. 487–507. ISSN: 14641909. DOI: 10.1016/S1464-1909(01)00041-7.

Zehe, E. and M. Sivapalan (2009). "Threshold behaviour in hydrological systems as (human) geo-ecosystems: manifestations, controls, implications." In: *Hydrol. Earth Syst. Sci.* 13, pp. 1273–1297.

Zehe, E. et al. (2014). "HESS Opinions: From response units to functional units: a thermodynamic reinterpretation of the HRU concept to link spatial organization and functioning of intermediate scale catchments." In: *Hydrology and Earth System Sciences* 18.11, pp. 4635–4655. DOI: 10.5194/hess-18-4635-2014.

Zemp, D. C., C.-F. Schleussner, H. M. J. Barbosa, M. Hirota, V. Montade, G. Sampaio, A. Staal, L. Wang-E., and A. Rammig (2017). "Self-amplified Amazon forest loss due to vegetation-atmosphere feedbacks." In: *Nature communications* 8, p. 14681. DOI: 10.1038/ncomms14681.

Zhang, Z. and H. G. Savenije (2018). "Thermodynamics of saline and fresh water mixing in estuaries." In: *Earth System Dynamics* 9.1, pp. 241–247. DOI: 10.5194/esd-9-241-2018.

van Genuchten, M. T. (1980). "A closed-form equation for predicting the hydraulic conductivity of unsaturated soils." In: *Soil Sci. Soc. Am. J.* 44, pp. 892–898. DOI: 10.2136/sssaj1980.03615995004400050002x.

van der Ent, Rudi J., Hubert H. G. Savenije, Bettina Schaefli, and Susan C. Steele-Dunne (2010). "Origin and fate of atmospheric moisture over continents." In: *Water Resources Research* 46.9. ISSN: 00431397. DOI: 10.1029/2010WR009127.